Semiconductors, Vol. 37, No. 6, 2003, pp. 617–619. Translated from Fizika i Tekhnika Poluprovodnikov, Vol. 37, No. 6, 2003, pp. 641–643.

ATOMIC STRUCTURE AND NONELECTRONIC PROPERTIES OF SEMICONDUCTORS

Effect of Highly Nonequilibrium Conditions on the Stoichiometry of Cadmium Telluride Layer Obtained by Vapor-Phase Condensation

A. P. Belyaev, V. P. Rubets, M. Yu. Nuzhdin, and I. P. Kalinkin

St. Petersburg Institute of Technology, Zagorodnyi pr. 49, St. Petersburg, 198013 Russia

e-mail: belyaev@tu.spb.ru

Submitted October 29, 2002; accepted for publication November 20, 2002

Abstract—The results of comparison studies of the stoichiometry of cadmium telluride epitaxial films synthesized from the vapor phase in equilibrium and highly nonequilibrium (on cooled substrates) conditions are reported. The data of X-ray microanalysis and atomic-absorption analysis of the films and the vapor phase are given. The stoichiometry of the films is found to increase with lowering the substrate temperature. It is shown that the films obtained in highly nonequilibrium conditions have the best crystal structure. © *2003 MAIK "Nauka/Interperiodica".*

1. INTRODUCTION

It is presently a commonly accepted fact that, for obtaining the best structure of film materials, they should be synthesized under conditions close to equilibrium or, after synthesis, annealed as was suggested, e.g., in [1].

However, in recent years, the possibility of obtaining perfect films with interesting properties in highly nonequilibrium conditions has been demonstrated [2–6]. In this connection, in what follows, we present the results of an investigation of the effect of highly nonequilibrium conditions on the stoichiometry of CdTe films synthesized from the vapor phase.

2. EXPERIMENTAL

Experiments were performed on cadmium telluride films synthesized from the vapor phase under conditions close to equilibrium (the substrate temperature T_S = 773 or 423 K) and on films obtained in highly nonequilibrium conditions (i.e., on a substrate cooled to a temperature of T_S = 180 K). The method of synthesis is described in [3]. The films obtained at T_S = 773 and 180 K had an epitaxial structure (the corresponding electron diffraction patterns are shown in Figs. 1a and 1b). The films synthesized at T_S = 423 K had a texture structure (see electron diffraction pattern in Fig. 1c). The thickness of the samples was about 2 μm. The films were synthesized from CdTe powder with excess tellurium, 5.0×10^{-3} at %.

The excess component was determined by an X-ray microanalyzer based on a JSM-35 scanning electron microscope and by the atomic-absorption method. In the latter case, the sample was sublimated; the vapor was extracted into the closed volume of a cell, and its concentration was determined by measuring its optical density.

3. RESULTS

The composition of the vapor phase of cadmium telluride and the stoichiometry of cadmium telluride films synthesized from this vapor in various technological conditions were studied. The main results are given in Fig. 2 and in the table.

The experimental temperature dependence of the vapor pressure above the CdTe powder is shown in Fig. 2. For comparison, solid lines show the temperature dependence of vapor pressure corresponding to the congruent sublimation (curve *2*) and the boundary of the region of homogeneity of CdTe with respect to tellurium (curve *3*) [7]. From Fig. 2, it can be seen that the evaporation was congruent only at high temperatures. Lowering the temperature led to the enriching of the vapor phase with tellurium.

The table gives the results of studies of the stoichiometry of CdTe films obtained under various technological conditions. From these data, it follows that lowering the temperature T_i of the vaporizer, which contained evaporable powder, from 873 to 823 K resulted in a strong deviation from stoichiometry in the films (the amount of excess Te significantly increased; compare samples 1, 2 and 3, 4). The temperature of the substrate also essentially affected the stoichiometry of the growing film. The stoichiometry was better at lower temperatures. However, the positive effect of lowering the substrate temperature on the stoichiometry, in the case of synthesis on a heated substrate, was accompanied by the violation of epitaxy processes (compare the electron diffraction patterns in Figs. 1a and 1c).

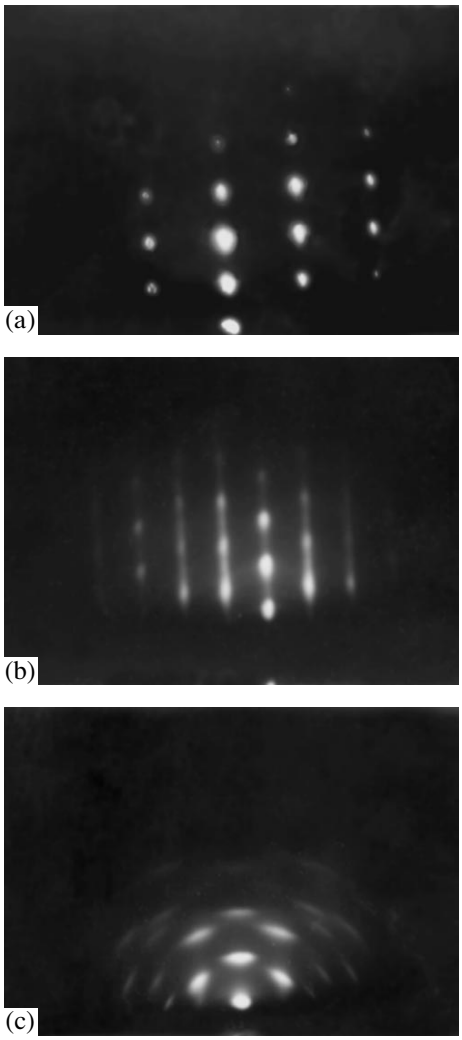

Fig. 1. Electron diffraction patterns of CdTe films synthesized at a substrate temperature T_S = (a) 773, (b) 180, and (c) 423 K.

The films synthesized in highly nonequilibrium conditions had the best crystal structure. Having an epitaxial structure, these films were characterized by the highest stoichiometry, in contrast to the epitaxial films synthesized in equilibrium conditions, which showed essential deviation from the stoichiometric composition.

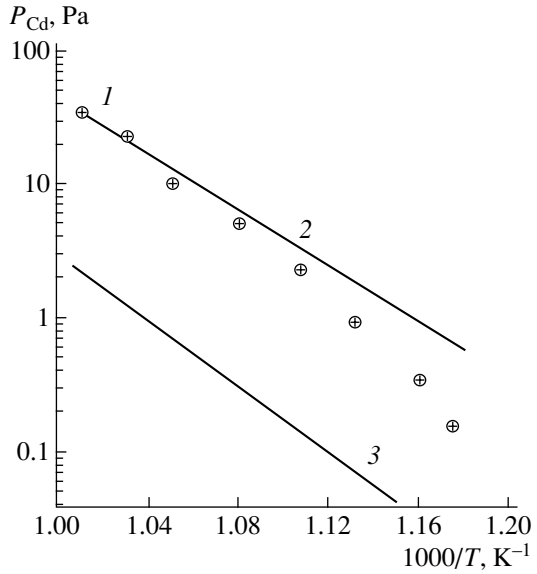

Fig. 2. Temperature dependences of the partial pressure of cadmium vapor above CdTe: (*1*) experimental data, (*2*) theoretical dependence corresponding to congruent vaporization, (*3*) the boundary of the region of homogeneity of CdTe with respect to Te.

4. DISCUSSION

As is known [3], in the conditions close to equilibrium, CdTe films are formed from the vapor phase by normal layer-by-layer growth. The formation of each layer includes nucleation, Ostwald ripening, coalescence, and merging into a continuous layer [8]. The stoichiometry of a film is governed by the first two stages.

Nucleation occurs from the two-dimensional gas of adatoms on a substrate when the density of this gas attains a certain critical value [8, 9]. Initially, the nuclei represent islands consisting of a mixture of tellurium and cadmium, since the characteristic time of involvement of particles in a phase transition t_p is much shorter than the characteristic time t_c of involvement in the chemical reaction for the formation of CdTe ($t_p \approx 10^{-3}$ s, $t_c > 0.2$ s at the activation energy of the reaction $E_c^{CdTe} \approx 24$ kcal/mol [7, 8]). Islands are formed independently of each other. The supply of components from the vapor phase is sufficient for the growth of each

Table

Sample no.	Temperature of vaporizer T_i, K	Temperature of substrate T_S, K	Structure	Stoichiometry, at. %
1	823	773	Epitaxial	Excess of Te, 10.224
2	823	423	Texture	Excess of Te, 7.208
3	873	773	Epitaxial	Excess of Te, 1.200
4	873	423	Texture	Excess of Te, 0.890
5	873	180	Epitaxial	Excess of Te, 0.700

island. As a result, the composition of the islands is close to the composition of the two-dimensional gas of adatoms. The composition of this gas depends on the composition of the adjacent vapor phase.

What is said above is supported by our experiment. Indeed, films synthesized under conditions where the vapor phase contained a large excess of Te (T_i = 823 K) had a high content Δ of excess Te (e.g., at T_S = 773 K, Δ = 10.224 at. %). At the same time, in the films synthesized under the same conditions from the vapor with a composition closer to the stoichiometric one (T_i = 873 K), the amount of excess Te Δ = 1.200 at. %.

Ostwald ripening is a relaxation stage for excess energy caused by the appreciably developed interphase. In the course of ripening, redistribution of mass between islands occurs. At the growth front of each island, the dynamic process of atom exchange takes phase (sorption–desorption). During the exchange process, thermal motion additionally corrects the composition. The probability of particles detaching from the positions corresponding to regular energy minima is lower than the probability of detachment of particles trapped in less deep minima (e.g, in minima corresponding to an interstitial site). Therefore, at relatively low substrate temperatures, it is mainly excess atoms that are subject to revaporization. The experimental studies of the temperature dependence of the partial pressure of vapor above initial CdTe support this idea. It can be seen from Fig. 2 that vaporization is congruent only at high temperatures.

It is evident that the effect of substrate temperature on the vaporization of atoms from the islands of a new phase is similar. At high temperatures, the vaporization from the island surface takes place almost congruently; therefore, Ostwald ripening only slightly changes the composition of the islands of the new phase appearing due to nucleation. Since at lower temperatures excess atoms are predominantly subjected to revaporization, the stoichiometry of islands improves. This is confirmed by our experiments (see table). All samples synthesized at lower substrate temperatures are characterized by a higher stoichiometry.

The formation of oriented films in highly nonequilibrium conditions differs from the processes that occur in equilibrium conditions. In this case, nucleation occurs in the vapor phase. After the condensation, instead of Ostwald ripening the islands orient themselves in the potential field of the substrate. The driving force of this orientation is solitons initiated by the misfit dislocations [3, 5]. Although the temperature of the islands during their orientation remains sufficiently high for some time [10], it is obviously lower than during synthesis on a heated substrate. Therefore, a positive correction of the film composition at the stage of orientation exists. Mainly excess atoms are subjected to revaporization, which actually does exist, according to the results obtained in [10].

5. CONCLUSIONS

The results obtained allow us to make the following conclusions.

(1) Highly nonequilibrium conditions provide the possibility for the synthesis from the vapor phase of perfect crystalline cadmium telluride films with a higher stoichiometry than in samples synthesized in equilibrium conditions.

(2) During the synthesis of films under conditions close to equilibrium, the lowering of the substrate temperature, while exerts a beneficial effect on the stoichiometry of the films, hinders the processes of heteroepitaxy.

ACKNOWLEDGMENTS

This study was supported by the Russian Foundation for Basic Research, project no 02-03-32405.

REFERENCES

1. D. S. Sizov, M. V. Maksimov, A. F. Tsatsul'nikov, *et al.*, Fiz. Tekh. Poluprovodn. (St. Petersburg) **36**, 1097 (2002) [Semiconductors **36**, 1020 (2002)].
2. A. P. Belyaev, V. P. Rubets, and I. P. Kalinkin, Fiz. Tekh. Poluprovodn. (St. Petersburg) **31**, 966 (1997) [Semiconductors **31**, 823 (1997)].
3. A. P. Belyaev, V. P. Rubets, and I. P. Kalinkin, Neorg. Mater. **34**, 283 (1998).
4. A. P. Belyaev and V. P. Rubets, Fiz. Tekh. Poluprovodn. (St. Petersburg) **35**, 294 (2001) [Semiconductors **35**, 279 (2001)].
5. A. P. Belyaev and V. P. Rubets, Fiz. Tekh. Poluprovodn. (St. Petersburg) **36**, 843 (2002) [Semiconductors **36**, 789 (2002)].
6. A. P. Belyaev, V. P. Rubets, and I. P. Kalinkin, Zh. Tekh. Fiz. **71** (4), 133 (2001) [Tech. Phys. **46**, 495 (2001)].
7. *Physics and Chemistry of II–VI Compounds*, Ed. by M. Alen and J. S. Prener (General Electric Research and Development Center, New York, 1967).
8. S. A. Kukushkin and A. V. Osipov, Usp. Fiz. Nauk **168**, 1083 (1998) [Phys. Usp. **41**, 983 (1998)].
9. A. P. Belyaev, S. A. Kukushkin, and V. P. Rubets, Fiz. Tverd. Tela (St. Petersburg) **43**, 577 (2001) [Phys. Solid State **43**, 597 (2001)].
10. A. P. Belyaev, V. P. Rubets, and I. P. Kalinkin, Fiz. Tverd. Tela (St. Petersburg) **39**, 382 (1997) [Phys. Solid State **39**, 333 (1997)].

Translated by A. Zalesskiĭ

Semiconductors, Vol. 37, No. 6, 2003, pp. 620–624. Translated from Fizika i Tekhnika Poluprovodnikov, Vol. 37, No. 6, 2003, pp. 644–648.

ATOMIC STRUCTURE AND NONELECTRONIC PROPERTIES OF SEMICONDUCTORS

Hydrogen-Induced Splitting in Silicon over a Buried Layer Heavily Doped with Boron

D. V. Kilanov*, V. P. Popov*, L. N. Safronov*, A. I. Nikiforov*, and R. Sholz**

**Institute of Semiconductor Physics, Siberian Division, Russian Academy of Sciences, pr. Akademika Lavrent'eva 13, Novosibirsk, 630090 Russia*

***Max Plank Institute of Microstructure Physics, 06120 Halle, Germany*

Submitted November 11, 2002; accepted for publication November 20, 2002

Abstract—Formation of interior hydrogen-passivated surfaces in hydrogen-implanted single-crystal Si containing a buried layer heavily doped with boron is investigated. With the use of the infrared absorption spectroscopy, it is shown that, upon annealing, the composition of hydrogen-containing defects in Si samples containing a buried heavily doped layer is the same as in Si samples that do not have such a layer. However, the presence of a heavily doped layer enhances the blistering and exfoliation of a thin silicon film from the Si sample, and the activation energies of the relevant processes change. Thus, the process of development of cavities in such layers changes upon thermal annealing. The depth at which hydrogen-passivated surfaces are formed corresponds to the projected range of H ions in Si, which also corresponds to the depth at which the B-doped layer is located. When a thin exfoliated film is transferred onto an insulator to form a silicon-on-insulator structure, the surface roughness of the film decreases by a factor of 2–5. © *2003 MAIK "Nauka/Interperiodica".*

1. INTRODUCTION

The change from silicon wafers, including epitaxial structures, to silicon-on-insulator (SOI) structures in the wide-scale production of semiconductor devices and integrated circuits ensures noticeable advantages over conventionally used bulk material. Among these are a significant decrease in the power consumption of devices and an increase in their operating speed. In order to fabricate modern devices based on silicon, the Si films used should have a thickness of 30–50 nm [1]. The use of SOI structures with films of such thickness in the production of integrated circuits and single-electron devices places very heavy demands on the surface quality of the films.

As is known, the implantation of H in heavily B-doped Si leads to the enhanced formation of microcavities in the latter [2]. Consequently, this process enhances the blistering and exfoliation of thin silicon films. It is also known that hydrogen atoms, which have very high chemical activity, interact with dangling bonds in the Si matrix. Taking these facts into account, we studied both the development of microcavities produced in a narrow portion of the implanted region, owing to the formation of a thin layer enriched with impurity atoms, and the effect of B atoms on the exfoliation of an Si film.

The purpose of this study is to investigate the special features of hydrogen-induced splitting in the presence of a heavily B-doped layer at a depth corresponding to the projected range of H ions.

2. EXPERIMENTAL

The experiments were performed with 100-mm-diameter samples of KDB-12 *p*-Si (Si:B, $\rho = 12\ \Omega$ cm) with (100) orientation. A heavily B-doped layer was formed by molecular-beam epitaxy. A 50-nm-thick Si buffer layer was grown on a prepared substrate, i.e., a very narrow (1–2 monolayers) B layer with a sheet concentration of 6×10^{14} cm^{-2} was grown on the buffer layer, and then the B layer was coated with a 500-nm-thick Si layer. The Si wafers were implanted with ionized hydrogen molecules with an energy of 100 keV at a dose of 2.5×10^{16} cm^{-2}. The simulation of the implantation process with the use of the TRIM-200 software package shows that the projected range of H ions R_p = 527 nm and the depth corresponding to the maximum concentration of radiation defects, R_d, is equal to 500 nm. Immediately before implantation, the prepared wafers were oxidized; the oxide thickness was 10 nm.

Investigations of hydrogen-induced splitting were performed with samples cut from the structures obtained by the hydrophilic bonding of the working Si wafers to Si substrates [3]. Before bonding, the thin protective oxide was removed from the wafers. Heat treatments were performed in the temperature range T_{ann} = 80–500°C.

The formation and development of the interior surfaces in the implanted material was studied using an IFS-66-v/S spectrometer operating under the conditions of frustrated total internal reflection. The multiple reflections in the wafer made it possible for the light beam to pass through the Si layer saturated with hydro-

gen about 100 times. The absorption spectra were recorded with a resolution of 1 cm^{-1}.

The surface roughness was measured by atomic-force microscopy (AFM); a Multimode Scanning Probe Microscope (Digital Instruments) was used. The scanned area ranged from 30×30 μm^2 to 100×100 nm^2. A silicon cantilever was used for scanning; the radius of the curvature of the tip was smaller than 10 nm.

3. RESULTS

When H-implanted Si samples are subjected to heat treatment, the system of crystal defects transforms; as a result, various defects and complexes are either formed or annealed out.

Figure 1 shows the transformation of the spectra of infrared (IR) absorption of H-implanted *p*-Si(100) containing a buried B-doped layer at a depth of 500 nm (spectra *a*) and without such a layer (spectra *b*), depending on the time of isothermal annealing at T_{ann} = 400°C.

It can be seen from Fig. 1 that, in the presence of a B-doped layer, no additional hydrogen-containing defects appear. However, a number of features can be distinguished in the IR-absorption spectrum. Immediately before the exfoliation of a thin Si film, new lines appear in the IR-absorption spectrum which correspond to the vibrations of H atoms on the surfaces of the internal cavities formed in the implanted layer. After the exfoliation, some of the lines in the IR-absorption spectrum disappear. For example, in the sample containing a B-doped layer, a line appears at 2098 cm^{-1} in the absorption spectrum due to the vibrations of monohydride complexes on the reconstructed surface Si(100)–(2×1)H [4]. Upon isothermal annealing, this line gradually shifts to the region at 2091 cm^{-1}, which corresponds to the vibrations of dihydride complexes on atomically smooth surfaces Si(100)–2H [4]. For the Si sample without a buried layer, we failed to detect a change in the state of hydrogen on the interior surfaces of Si. In the IR-absorption spectrum, a band only at 2091 cm^{-1} was observed.

Figure 2 shows the dependences of the fraction of hydrogen involved in the formation of Si–H bonds on the implantation dose, in relation to the time of isothermal annealing at 400°C. With the use of the relation [5]

$$N(\text{Si–H}) = 1.1 \times 10^{20} \int_{\omega} \frac{\alpha(\omega)}{\omega} d\omega$$

(where ω is the wave number and α is the absorption coefficient), the concentration of Si–H bonds and, consequently, the concentration of chemically bound H were determined. Previously, we showed that the fraction of chemically bound H ranges from 20 to 70% of the implantation dose [1]. It can be seen from Fig. 2 that, after the implantation, about 50–65% of the implanted H ions are in the form of complexes with Si atoms. In the initial stage of annealing, the fraction of H chemically bonded to Si decreases. With further annealing, the amount of bound hydrogen remains almost constant. After exfoliation, a large fraction of hydrogen-containing complexes (about 30% of the implantation dose) is in the exfoliated film. About 10–20% of the implanted H remains in the wafer in the

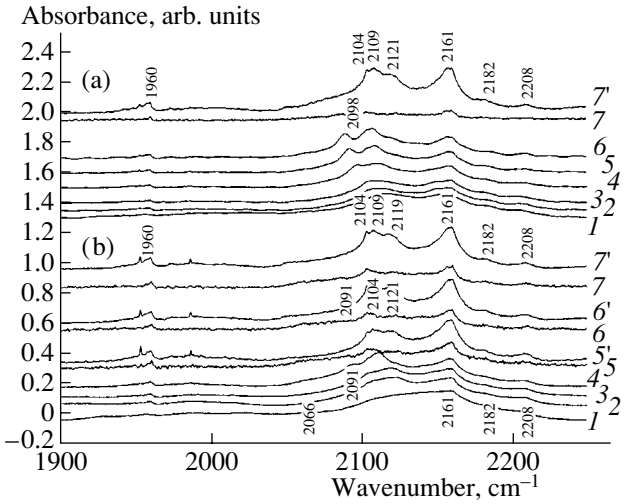

Fig. 1. Transformation of the IR-absorption spectra of an Si(100) sample implanted with ionized hydrogen molecules upon isothermal annealing at T_{ann} = 400°C: (a) the sample contains a buried B-doped layer; (b) the sample contains no buried layers. The spectra were measured under the following conditions: (*1*) immediately after annealing at 200°C for 2 h; after annealing at 400°C, (*2*) 5 min; (*3*) 10 min; (*4*) 20 min; (*5*) working wafer after splitting, 40 min; (*5*') substrate with a film after splitting; (*6*) working wafer, 60 min; (*6*') substrate with a film; (*7*) working wafer, 120 min; and (*7*') substrate with a film, 120 min.

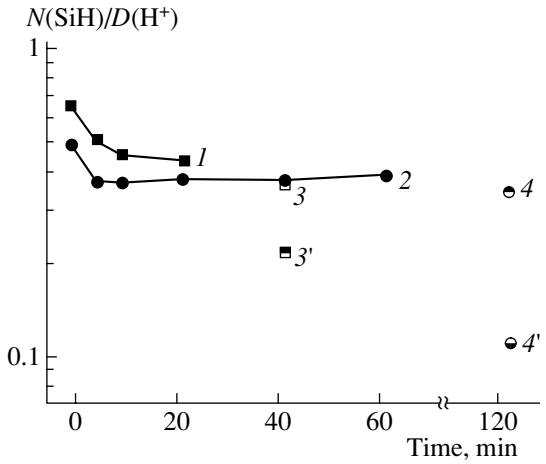

Fig. 2. Fraction of hydrogen involved in the formation of the Si–H bonds in relation to the time of isothermal annealing (400°C) in (*1*) a sample without a buried layer, (*2*) a sample with a buried layer, (*3*) a sample without a buried layer (transferred film), (*3*') a working wafer after splitting, (*4*) a sample with a buried layer (transferred film), and (*4*') a working wafer after splitting.

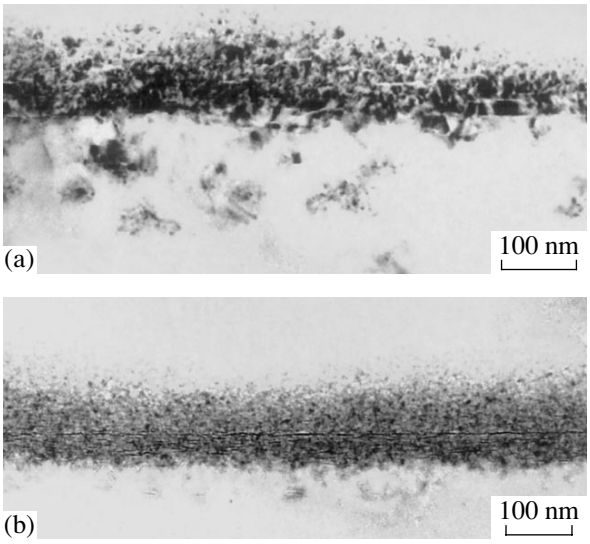

Fig. 3. TEM images of the cross sections of Si(100) wafers (a) without a buried layer and (b) with a B-doped layer at a depth of 500 nm. Both samples were implanted with H ions with an energy of 100 keV and at a dose of 5×10^{16} cm^{-2}.

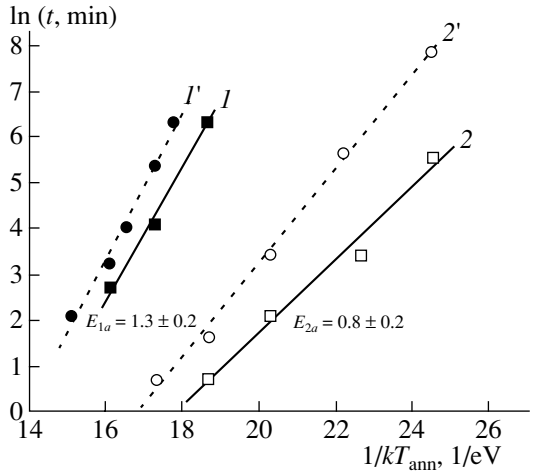

Fig. 4. Dependences of the time t required for blisters to form on the Si surface on the annealing temperature T_{ann}. (*1*, *2*) Blistering and (*1*', *2*') exfoliation of samples implanted with H ions with an energy of 100 keV and at a dose of 5×10^{16} cm^{-2} (*1*, *1*') without a buried layer and (*2*, *2*') with a buried B-doped layer. The numbers near the curves denote the activation energy in eV.

form of SiH complexes, which indicates that the variation in the fraction of H bonding to Si is insignificant during the splitting.

Figures 3a and 3b show images of cross sections of Si samples implanted with H ions; these images were obtained by transmission electron microscopy (TEM). The sample shown in Fig. 3b contains a buried layer doped heavily with B. The images were obtained after implantation with H and annealing at 200°C for two hours. It can be seen from Figs. 3a and 3b that such annealing is sufficient for the formation of microcavities in the implanted layer. The width of the region where microcavities are formed ranges from 100 to 120 nm in both cases. However, in the samples containing a buried layer, microcavities are mainly formed at a depth at which the impurity content is highest. It can also be seen from Fig. 3b that not all of the interior surfaces developing in the sample with a buried layer are parallel to the wafer surface. Formation of microcracks along the [111] direction is also observed, which is in good agreement with the IR-spectroscopy data. Figure 3b shows that, even after annealing at T_{ann} = 200°C for two hours, the microcracks form an almost unified cavity at the depth where the B content is highest.

Figure 4 shows the time t required for blisters to be formed as a function of the annealing temperature T_{ann}. It can be seen from Fig. 4 that the formation of blisters on the surface of an Si sample containing a heavily B-doped layer occurs significantly more rapidly in comparison with the implanted Si samples containing no buried layer. The activation energy of the blister formation on the surface of the H-implanted Si without a buried layer is equal to 1.3 ± 0.2 eV. At the same time, the activation energy of blister formation on the surface of H-implanted Si containing a buried layer is only 0.8 ± 0.2 eV.

Figure 5 shows the AFM images of the surface of an Si film, obtained in the course of splitting of the Si wafers containing a heavily B-doped layer (Figs. 5a, 5c) and of those without such a layer (Figs. 5b, 5d). After conventional hydrogen-induced exfoliation of the Si film, the roughness of the film surface is rather high (the root-mean square roughness is equal to 10.5 nm). It can be seen from Fig. 5 that the roughness of the surface of the Si film transferred from the wafer containing a buried layer onto an insulator substrate is lower by a factor of 2–5 in comparison with the case of conventional exfoliation. Thus, for the windows of 30×30 μm^2 in size, the root-mean square roughness of such surfaces is equal to 5.6 nm.

4. DISCUSSION

The formation of microcavities at a depth of 500 nm in the samples containing a buried layer doped heavily with B is caused by the accumulation of H in the region where the B content is highest. High-temperature annealing during the oxidation of Si at T_{ann} = 900°C for 20 min is not sufficient to obtain a uniform distribution of the B impurity in this region. The enhanced formation of microcavities possibly indicates that centers of their nucleation exist in the samples under study [6] or that the mechanism of accumulation of H in cavities changes from reaction-limited aggregation to diffusion due to a decrease in the incorporation-barrier height (which is confirmed by the decrease in the activation energy).

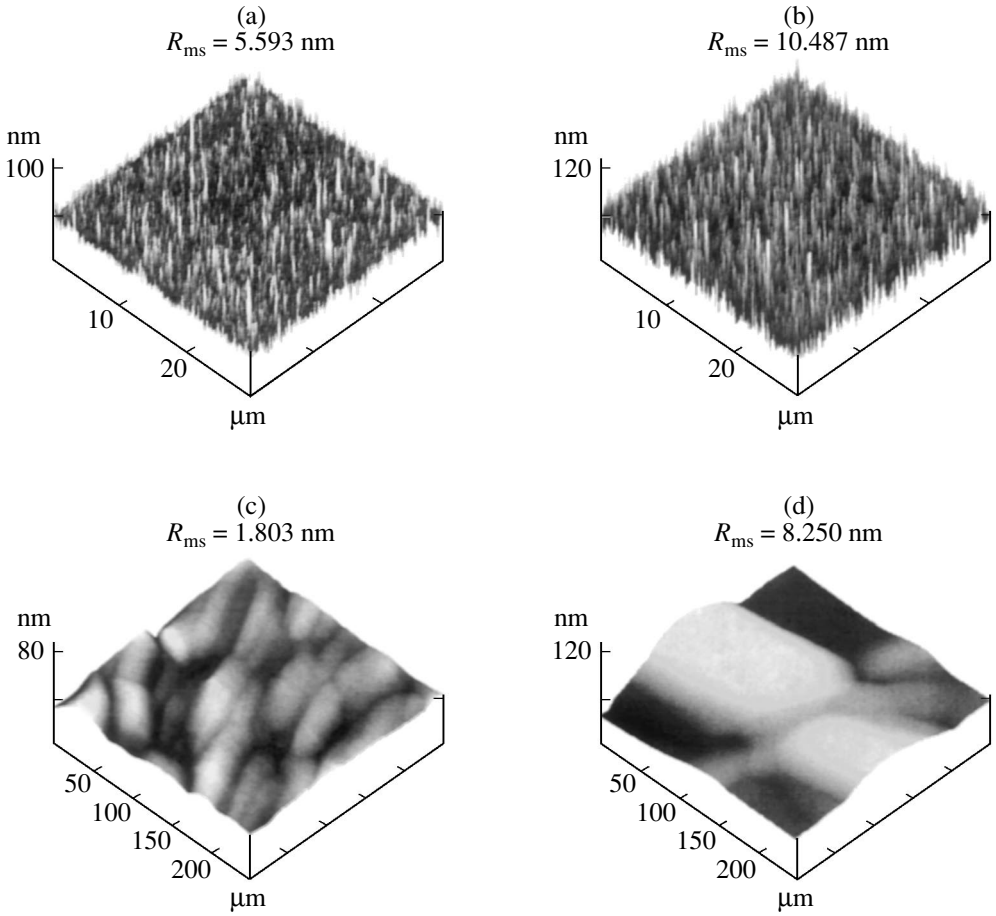

Fig. 5. AFM images of the surfaces of Si films transferred from the wafer (a, c) containing a buried layer and (b, d) from the wafer without a buried layer. The scanned areas are (a, b) 30×30 μm^2 and (c, d) 250×250 nm^2.

Analysis of the IR absorption spectra shows that the composition of hydrogen-containing defects in the Si samples containing a buried layer doped heavily with Band in the samples without such a layer is identical after annealing. It is also possible that the mechanism of development of microcavities due to the accumulation of hydrogen in them also does not change [7]. However, the kinetics and the activation energy of this process change significantly. It is possible that the mechanism of H diffusion to the microcavities changes too.

A mechanism of influence of the high B content on the blistering and exfoliation was suggested previously in [6]. The enhanced formation of microcavities in the region where the B content is highest in attributed to the large number of nucleation centers. Boron atoms can serve as such centers. The significant enhancement of the development of microcavities is due to the enhanced accumulation of gaseous H in these microcavities.

The line at 2091 cm^{-1} in the IR-absorption spectrum of the implanted Si appears immediately before the splitting of the implanted layers and vanishes immediately after the exfoliation. This spectral line corresponds to the state of the surface at which a surface Si atom is bonded to two H atoms. We managed to trace the transformations in the spectrum at the instant when a passivated surface is formed on the Si film; specifically, when the line corresponding to vibrations of the monohydride complexes on the dimerized surface and the appearance of dihydrides in the course of exfoliation completely disappears. Apparently, the disappearance of this line after the exfoliation is caused by the oxidation of the surface. In our opinion, the increase in the content of hydrogen in microcracks, as well as the large concentration of B atoms, which impede the dimerization of Si atoms on the (100) surface (due to the decrease in the number of dangling bonds), facilitates the formation of dihydrides.

Evidently, the increase in the time required to split the sample containing a buried B-doped layer, in comparison with that for the sample without such a layer, is due to the presence of small (1–2 μm) regions in the wafer that remained unimplanted. The real time required to split an H-implanted sample containing a B-doped layer was additionally determined (Fig. 4, curve *2*'). In the presence of a heavily doped layer, the

processes of formation of blisters on the Si surface and exfoliation of a thin Si film are enhanced by approximately a factor of 7–10.

The enhanced formation of microcavities in a narrow portion of the implanted region makes it possible to obtain smoother interior surfaces during annealing, since it is this portion that is responsible for the enhanced trapping of the diffusing hydrogen.

The heavily B-doped region in Si is depleted of intrinsic point defects and enriched with molecular hydrogen [6]. Boron atoms serve as nucleation centers for microcracks in this region. Apparently, these are the reasons for the enhanced formation of cracks in the heavily B-doped region.

The enhanced formation of extended cracks in a sample containing a heavily B-doped layer indicates that such a layer can be used as the formation center for microcavities. In our opinion, the use of a heavily B-doped layer as a boundary over which the splitting of the H-implanted wafer occurs will make it possible to exfoliate very thin films, thus decreasing the implantation energy and the depth at which the heavily doped layer is located.

5. CONCLUSIONS

On the basis of the results obtained, we concluded the following:

(i) The composition of hydrogen-containing defects in the Si samples containing a buried layer doped heavily with B and in the samples without such a layer is the same after annealing. However, the activation energy and the kinetics of the processes of blistering and exfoliation are significantly different in these cases. The presence of a heavily doped layer enhances the processes of formation of blisters on the Si surface and exfoliation of a thin Si film by approximately a factor of 7–10. The enhanced formation of microcavities in the thin layer doped heavily with B makes it possible to decrease the implantation dose of H ions.

(ii) The formation of microcavities in the region near the buried layer significantly affects the roughness of the exfoliated film. The decrease in the surface roughness is due to the fact that film exfoliation is initiated by the microcracks located in the region whose width is considerably smaller than the width of the region within which the boundary of the exfoliated film is formed in the case of conventional hydrogen-induced splitting.

(iii) A line is observed at 2091 cm^{-1} in the IR-absorption spectra. This line appears and disappears within a short period of time corresponding to the exfoliation of a thin Si film. On the basis of an analysis of the absorption spectra, we may state that, at the instant when the surface film is formed, the reconstruction of the surfaces of the interior cavities occurs. In the course of this process, the state of hydrogen changes from Si(100)–(2×1)H to Si(100)–2H.

REFERENCES

1. V. P. Popov, A. I. Antonova, A. A. Frantsuzov, *et al.*, Fiz. Tekh. Poluprovodn. (St. Petersburg) **35**, 1078 (2001) [Semiconductors **35**, 1030 (2001)].
2. Q.-T. Tong, R. Scholz, U. Gosele, *et al.*, Appl. Phys. Lett. **72**, 49 (1998).
3. G. Kissinger and W. Kissinger, Phys. Status Solidi A **123**, 185 (1991).
4. M. K. Weldon, V. E. Marsico, Y. J. Chabal, *et al.*, J. Vac. Sci. Technol. B **15**, 1065 (1997).
5. L. S. Sidhu, T. Kosteski, and S. Zukotynski, J. Appl. Phys. **85**, 2574 (1999).
6. V. P. Popov, V. F. Stas, and I. V. Antonova, MRS Proc. **540**, 499 (1999).
7. A. Agarwal, T. E. Haynes, V. C. Venezia, and O. W. Holland, Appl. Phys. Lett. **72**, 1086 (1998).

Translated by Yu. Sin'kov

Semiconductors, Vol. 37, No. 6, 2003, pp. 625–631. Translated from Fizika i Tekhnika Poluprovodnikov, Vol. 37, No. 6, 2003, pp. 649–656.

ATOMIC STRUCTURE AND NONELECTRONIC PROPERTIES OF SEMICONDUCTORS

A Model of Reduction of Oxidation-Enhanced Diffusion in Heavily Doped Si Layers

O. V. Aleksandrov* and N. N. Afonin**

**St. Petersburg State University of Electrical Engineering, St. Petersburg, 197396 Russia*
e-mail: aleks_ov@mailbox.alkor.ru
***Voronezh State Pedagogical University, Voronezh, 394043 Russia*
e-mail: nafonin@vspu.ac.ru

Submitted December 24, 2001; accepted for publication December 3, 2002

Abstract—A model of reduction of oxidation-enhanced diffusion (OED) in heavily doped Si layers via bulk recombination of self-interstitials at centers associated with the dopant is suggested. The allowance made for the recombination of excess self-interstitials, which are generated upon thermal oxidation, allows one to describe the dependence of OED reduction on the doping level. The experimental data on the OED of B and P impurities in uniformly doped Si layers are analyzed. From the analysis, the recombination-rate constants are determined and capture radii are estimated for various variants of interaction of excess self-interstitials with impurity atoms and impurity–vacancy pairs. *© 2003 MAIK "Nauka/Interperiodica".*

1. INTRODUCTION

Thermal oxidation of Si causes the enhancement of diffusion of a number of substitutional impurities (P, B, Al, Ga, In), which diffuse preferentially via the indirect interstitially mechanism (see reviews [1, 2]). Simultaneously with the oxidation-enhanced diffusion (OED), the growth of extrinsic stacking faults is observed. Both phenomena were explained by Hu [3] as the generation of excess self-interstitials at the Si/SiO_2 interface upon thermal oxidation of Si. For B and P impurities, OED reduction with an increase in the Si doping level above the intrinsic charge-carrier density at the temperature of oxidation annealing is established experimentally [4–8].

Miyake [6] assumed that the reason for the reduction of the OED of B with an increase in the level of uniform doping with P is the recombination of neutral self-interstitials with negatively charged vacancies. It was assumed that the interaction reaction is in equilibrium and that the mass-action law is applicable to it. We show below (in Section 5) that, in this case, the relative concentrations of excess self-interstitials are independent of the doping level. Therefore, equilibrium recombination could not have bee the reason for OED reduction as the doping level increased. It should also be noted that the direct bimolecular recombination of excess self-interstitials with free charged vacancies seems to be considerably less probable than their recombination at the centers. The latter can be the atoms of the dopant or complexes composed of these atoms and vacancies, whose concentrations in heavily doped Si layers considerably exceed the concentration of free vacancies.

Giles [9] attributed the effect of OED reduction to an increase in the doping level to a decrease in relative self-interstitial supersaturation due to an increase in equilibrium concentrations of self-interstitials in charged states according to the shift of the Fermi level. In the framework of the model [9], from an analysis of experimental dependences of the OED on the doping level, the levels of charged self-interstitials in the Si band gap were found in [7–9]. The values found considerably differed from each other. Note that in the framework of the model [9] it is impossible to satisfactorily explain the results obtained in [8]. These results are related to the influence of a lightly doped layer located on the surface of a heavily doped layer on the OED.

In this study, a model of OED reduction in heavily doped Si layers is suggested. The model implies that OED reduction is due to the recombination of excess self-interstitials, which are generated upon thermal oxidation, at the centers associated with the dopant.

2. BASIC CONCEPTS AND EQUATIONS OF THE MODEL

When simulating OED, we will assume that the substitutional impurity under consideration diffuses in the Si lattice via a dual mechanism, i.e., via mixed vacancy and indirect interstitially mechanisms. In this case, the diffusivity is determined by the relationship [2]

$$D = h_E D^*(f_V a_V f_I a_I), \quad (1)$$

where h_E is the coefficient of diffusion enhancement by an internal electric field; D^* is the coefficient of impurity diffusion via intrinsic point defects in equilibrium conditions; f_V and f_I are the relative fractions of impurity diffusion by the vacancy and indirect interstitial mechanisms, respectively ($f_V + f_I = 1$); $a_V = [V]/[V_{eq}]$ and

$a_I = [I]/[I_{eq}]$ are the coefficients of vacancy supersaturation (undersaturation) and self-interstitial supersaturation (undersaturation), respectively; and $[V_{eq}]$, $[I_{eq}]$, and $[V]$, $[I]$ are the equilibrium and nonequilibrium concentrations of vacancies and self-interstitials, respectively. With the proviso of local equilibrium, according to the mass-action law, $a_V = 1/a_I$.

Upon thermal oxidation, the Si/SiO_2 interface serves as a source of excess self-interstitials. The generation rate of self-interstitials at the interface from the Si side is directly proportional to the oxidation rate [3]. Excess self-interstitials generated during oxidation diffuse into the Si bulk, enhancing the diffusion of substitutional impurities according to Eq. (1), migrate to the sinks, and recombine at the bulk centers. In undoped Si, residual impurities and defects act as background bulk sinks. In doped Si, the additional migration of self-interstitials to the centers associated with the dopant is possible. Free charged vacancies, dopant atoms, as well as dopant–vacancy pairs, can serve as such centers. The capture of self-interstitials by these centers occurs according to the following equations:

$$I + V \longrightarrow S, \tag{2a}$$

$$I + A \longrightarrow AI, \tag{2b}$$

$$I + VA \longrightarrow A. \tag{2c}$$

Here, S is the Si atom at a lattice site, A is the dopant atom, and AV is the dopant–vacancy pair.

The equations of joint diffusion of the impurity and self-interstitials take the form

$$\frac{\partial C}{\partial t} = \frac{\partial}{\partial x}\left(D\frac{\partial C}{\partial x}\right), \tag{3}$$

$$\frac{\partial I}{\partial t} = D_I\frac{\partial^2 I}{\partial x^2} - (k_{IA} - k_I)(I - I_{eq}), \tag{4}$$

where x is the coordinate counted from the interface to the Si bulk; t is the current time; C is the concentration of the diffusing impurity; D_I is the diffusivity of self-interstitials; k_I and k_{IA} are the recombination-rate constants for the recombination of excess self-interstitials at the background bulk traps and at the centers associated with the dopant, respectively.

The boundary condition for self-interstitials at the Si/SiO_2 interface at $x = 0$ is the condition for the equality of their surface generation at the interface at the Si side G_I with the sum of the diffusion flux into the Si bulk with the surface-recombination rate at the interface [3]

$$-D_I\frac{\partial I}{\partial x} + \sigma(I - I_{eq}) = G_I. \tag{5}$$

Here, σ is the surface-recombination rate of self-interstitials upon thermal oxidation,

$$G_I = \alpha\gamma V_{ox} N_s, \tag{6}$$

where α is the ratio of the thickness of oxidized Si to the thickness of the dioxide formed W_{ox} ($\alpha = 0.44$); γ is the number of self-interstitials which are formed at the Si side upon formation of one SiO_2 molecule; V_{ox} is the rate of oxidation of Si; and N_S is the concentration of SiO_2 molecules in silicon dioxide ($N_S = 2.2 \times 10^{22}$ cm^{-3}). It was assumed that the concentration of self-interstitials in the sample bulk does not vary and corresponds to its equilibrium value $I = I_{eq}$ for the entire duration of annealing.

The kinetics of oxidation is described by the Deal–Grove linear–parabolic law

$$\frac{W_{ox}^2}{K_p} + \frac{W_{ox}}{K_t} = t, \quad V_{ox} = \frac{K_p}{2W_{ox} + K_p/K_l},$$

in which the linear K_l and parabolic K_p constants of the growth rate of silicon dioxide depend on the concentration for high doping levels [10].

The problem of OED of B and P impurities was solved for the case of uniform doping of Si, which corresponds to experimental conditions [5–8], in which the thickness of the oxidized layer (0.1–0.12 μm) was substantially smaller than the region of localization of impurity distributions (~1 μm). Therefore, segregation effects were disregarded during simulation, and the problem for Eqs. (4) and (5) with a steady-state SiO_2/Si interface was solved. The interface was assumed to be reflective for diffusing impurity atoms, i.e.,

$$\frac{\partial C}{\partial x} = 0 \text{ at } x = 0. \tag{7}$$

3. MODEL PARAMETERS

For high levels of uniform doping, which were used in experiments [5–8], the internal electric field is absent in the diffusion layers, i.e., $h_E \simeq 1$ in relationship (1). The diffusivities of B and P impurities in equilibrium with respect to intrinsic point defects are concentration-dependent [11]:

$$D_B^* = D_B^0 + D_B^+ p/n_i, \tag{8}$$

$$D_P^* = D_P^0 + D_P^- n/n_i + D_P^{2-}(n/n_i)^2, \tag{9}$$

where D_B^r and D_P^r are the partial intrinsic of B and P, respectively, via intrinsic point defects with a charge r ($r = 0, \pm 1$, and -2); p is the hole density; n is the electron density; and n_i is the intrinsic charge-carrier density. For uniform doping by the donor impurity with the concentration C_D ($C_D \gg C_B, C_P$), we have

$$n = \frac{1}{2}(C_D + \sqrt{C_D^2 + 4n_i^2}), \quad p = n_i^2/n.$$

For uniform doping by the acceptor impurity with the concentration C_A ($C_A \gg C_B$, C_P),

$$p = \frac{1}{2}(C_A + \sqrt{C_A^2 + 4n_i^2}), \quad n = n_i^2/p.$$

The relative fraction of the component of B and P diffusion by the indirect interstitially mechanism according to the latest data [2, 12] constitutes $f_I \simeq 0.9$.

The diffusivity of self-interstitials, which has a large spread in the literature (from 10^{-10} to 3×10^{-6} cm^{-2}/s at annealing temperature T_{ann} = 1000°C), is taken from [13]:

$$D_I = 0.335\exp(-1.86/kT);$$

and the equilibrium concentration of self-interstitials was taken from [14]:

$$I_{eq} = 4.76 \times 10^{25}\exp(-3.02/kT).$$

The constant of the recombination rate of excess self-interstitials in undoped Si is controlled by the diffusion length of self-interstitials L_I: $k_I = D_I/L_I^2$. The length L_I, in turn, is controlled by the concentration of residual impurities and defects in the bulk of undoped Si. We assume that $L_I \simeq 1$ μm. The surface-recombination rate of self-interstitials was assumed to be equal to $\sigma = 1.0 \times 10^{-6}$ cm/s [15]. The parameter γ in expression (6) for the surface-generation rate was equal to $\gamma = 4 \times 10^{-3}$. This parameter is independent of both the temperature of oxidation annealing and the type of dopant. Note that the found value of γ lies in the range of literature values from ~0.001 [3] to ~0.02 [16].

The recombination-rate constant of excess self-interstitials recombining at the centers related to the dopant, k_{IA}, depends on the charge state of self-interstitials and a center. Different possible variants of the concentration dependence of the recombination-rate constant of self-interstitials were analyzed in the form

$$k_{IA} = K_m^m C_A p^{m-1}$$

for an acceptor dopant or

$$k_{IA} = K_m^m C_D n^{m-1}$$

for a donor dopant, where m = 1–3.

4. RESULTS OF SIMULATION

The boundary problem for Eqs. (3) and (4) with impurity diffusivities [(1), (8), and (9)] and boundary conditions for self-interstitials and impurity (5)–(7) was solved numerically by the finite difference method using implicit difference schemes [17]. As the initial conditions for the impurity, its experimental distributions after ion implantation and preliminary annealing were used. To determine the form of the concentration dependence k_{IA} and the parameters of the model, we analyzed experimental data [5–8] on the OED of B and P impurities in Si layers uniformly doped with B, P, and As.

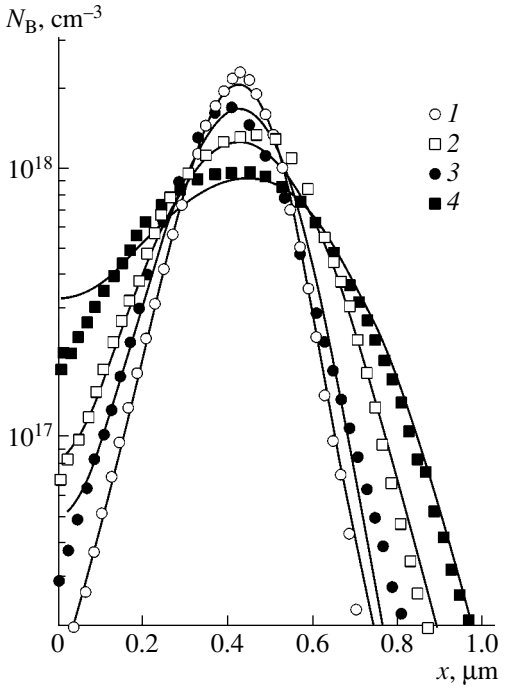

Fig. 1. Distribution of the B concentration N_B in Si after heat treatment (1000°C, 30 min) in (*1*, *2*) nitrogen and (*3*, *4*) dry oxygen. The level of uniform doping with P is (*1*, *3*) 2×10^{14} and (*2*, *4*) 7.4×10^{19} cm^{-3}. Solid lines represent the calculation for $K_2 = 4 \times 10^{-20}$ cm^{-3}/s$^{1/2}$; points represent the experiment [6].

The experimental [6] and calculated B depth distributions in Si after heat treatment in nitrogen and dry oxygen (1000°C, 30 min) for various levels of uniform doping with P are shown in Fig. 1. When carrying out the calculations, we assumed that during annealing in nitrogen (curves *1*, *2*) the generation rate of self-interstitials $G_I = 0$ and the concentration of self-interstitials $I = I_{eq}$. In this case, the impurity redistribution is determined in accordance with the dependence of B diffusivity on concentration (8) under equilibrium with respect to intrinsic point defects. Note that the dependence in the form (8) allows one to describe well the shape of experimental B-distribution curves and make allowance for a decrease in the diffusion broadening of the initial distribution as the level of uniform P doping increases. Upon annealing in oxygen (curves *3*, *4*), the generation rate of excess self-interstitials $G_I \neq 0$ and the concentration of self-interstitials at the Si surface $I_S > I_{eq}$. This leads to larger diffusion broadening of B distributions compared with annealing in nitrogen. The calculation corresponds to the quadratic concentration dependence of the recombination-rate constant of self-interstitials (m = 2).

The calculated concentration depth profiles of self-interstitials in Si, which correspond to B diffusion under conditions of oxidation annealing [6] (1000°C,

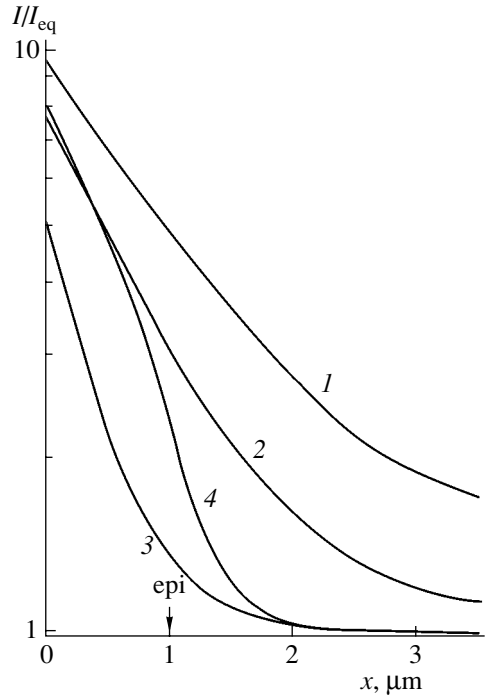

Fig. 2. Calculated depth profiles of self-interstitials in Si upon heat treatment in dry oxygen (1000°C) at the level of uniform doping with phosphorus C_P = (*1*) 2×10^{14}, (*2*) 2.7×10^{19}, (*3*) 7.4×10^{20} cm^{-3}. For curve *4*, $C_P = 2 \times 10^{14}$ in the epilayer 1 μm thick and 7.4×10^{20} in the substrate. The calculation is carried out for $K_2 = 4 \times 10^{-20}$ cm^3/s$^{1/2}$.

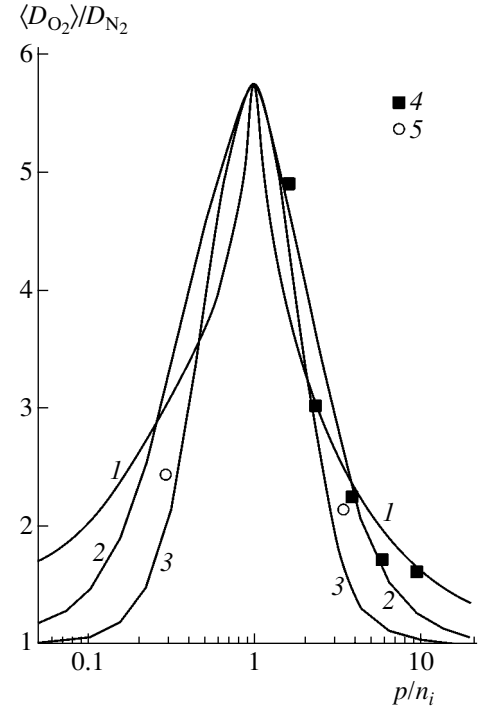

Fig. 3. Concentration dependences of the relative B diffusivity upon heat treatment of the samples in dry oxygen (1000°C). The calculation for the values of m = (*1*) 1, (*2*) 2, and (*3*) 3; point correspond to the experiment: (*4*) [5] and (*5*) [8].

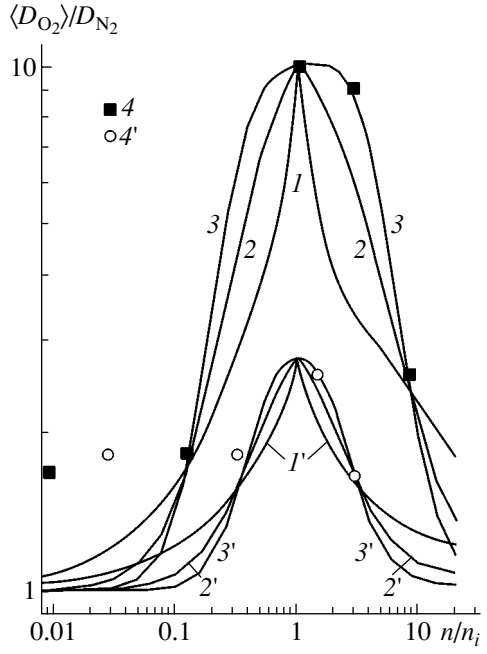

Fig. 4. Concentration dependences of the relative B diffusivity upon heat treatment of the samples in dry oxygen at the temperature T_{ann} = (*1*–*4*) 900 and (*1*'–*4*') 1100°C. Solid lines correspond to the calculation for the values of m = (*1*, *1*') 1, (*2*, *2*') 2, and (*3*, *3*') 3; points (*4*, *4*') correspond to the experiment [7].

30 min) for various levels of uniform doping with P, are shown in Fig. 2 (curves *1*–*3*). The calculated concentration depth profile of self-interstitials in a system that consists of a lightly doped epitaxial layer (epilayer) on the surface of a heavily doped Si substrate is also shown (curve *4*). As can be seen from Fig. 2, with increasing the level of uniform doping, a decrease in the surface concentration of self-interstitials is observed. The presence of the lightly doped layer on the surface of the heavily doped substrate leads to an increase in the surface concentration of self-interstitials (compare curves *3* and *4*).

As can be seen from Figs. 1 and 2, the region of characteristic variation in the concentration of self-interstitials in heavily doped layers is comparable with the region of localization of impurity distributions (<1 μm). Therefore, when carrying out the simulation, the average impurity diffusivity upon annealing in the medium $\langle D_{O_2} \rangle$ over the depth of the solution region was calculated. Then the behavior of the ratio of the diffusivity to the diffusivity upon annealing in the inert medium $\langle D_{O_2} \rangle / D_{N_2}$ with variation in the dopant concentration was analyzed. Figure 3 shows the calculated dependences of the relative B diffusivity, which correspond to different variants of the concentration dependence of the recombination rate of self-interstitials upon annealing in oxygen (T_{ann} = 1000°C, 30 min), in comparison with the experimental data [5] and [8]. The

falloff of the dependences $\langle D_{O_2} \rangle / D_{N_2}$ to both sides with respect to the value of $p/n_i = 1$ corresponds to a decrease in the relative concentration of self-interstitials with an increase in doping level due to an increase in the intensity of their capture at the centers related to the dopant. During the simulation, we aimed for the best agreement between calculations and experimental data for each variant of the concentration dependence of the recombination rate. The best agreement was obtained at the following values of the parameters: $K_1 = 7.5 \times 10^{-20}$ cm^3/s, $K_2 = 4 \times 10^{-20}$ cm^3/s$^{1/2}$, and $K_3 = 5 \times 10^{-20}$ cm^3/s$^{1/3}$ at $T_{ann} = 1000$°C.

The results of simulation of the concentration dependence of the relative P diffusivity upon annealing the samples in oxygen at 900 and 1100°C in comparison with the experimental data [7] are shown in Fig. 4. The calculated dependences are obtained for the following values of the parameters: $K_1 = 5 \times 10^{-20}$ cm^3/s, $K_2 = 3.2 \times 10^{-20}$ cm^3/s$^{1/2}$, and $K_3 = 2.8 \times 10^{-20}$ cm^3/s$^{1/3}$ at $T_{ann} = 900$°C; and $K_1 = 2.5 \times 10^{-19}$ cm^3/s, $K_2 = 6 \times 10^{-20}$ cm^3/s$^{1/2}$, and $K_3 = 4 \times 10^{-20}$ cm^3/s$^{1/3}$ at $T_{ann} = 1100$°C.

5. DISCUSSION

According to the concepts of the model, increasing the level of uniform doping causes the intensity of recombination of excess self-interstitials at the centers related to the dopant to increase. This leads to a decrease in the relative concentration of excess self-interstitials and their contribution to the diffusion transport of impurity and, thus, to OED reduction. According to Eq. (4), OED reduction is controlled by increasing the recombination-rate constant k_{IA}, which is governed by the impurity concentration. At the levels of uniform doping used in [6–8], the characteristic steady-state time constant is controlled by the lifetime of self-interstitials

$$\tau_I = (k_{IA} + k_I)^{-1}$$

and amounts to seconds or fractions of a second. For annealing times $\tau \gg \tau_1$ and constant D_I, k_{IA}, and G_I, Eq. (4) has a steady-state analytical solution [18]:

$$I(x) = (I_S - I_{eq}) \exp(-x/\sqrt{D_I \tau_I}) + I_{eq}, \quad (10)$$

$$I_S = G_I/\sqrt{D_I/\tau_I}, \quad (10a)$$

where I_S is the surface concentration of self-interstitials. Note that, in our case, the Si oxidation rate decreases with increasing time, G_I is not constant, and, therefore, analytical solution (10) turns out to be approximate. It can be seen from solution (10) that recombination affects not only the rate of decrease in the concentration of excess self-interstitials with increasing depth, but also the surface concentration of self-interstitials

$$I_S \propto 1/\sqrt{(k_{IA} + k_I)}.$$

A decrease in the surface concentration of self-interstitials with increasing recombination rate is the main reason for a reduction of OED with increasing doping level.

An increase in the recombination rate of self-interstitials with increasing doping level can be caused by the capture of excess self-interstitials by charged vacancies, ionized dopant atoms (with the subsequent capture of a vacancy), and also by complexes consisting of dopant atoms and vacancies according to reactions (2a)–(2c). We assume that reaction (2a) for the immediate bimolecular recombination of a self-interstitial with a vacancy is less probable than reactions (2b) and (2c). The reason is that the concentration of the dopant, as well as dopant–vacancy complexes, at high doping levels is much higher than the concentration of free charged vacancies. The linear concentration dependence k_{IA} ($m = 1$) can occur upon the capture of neutral self-interstitials by ionized impurity atoms ($k_{IA} \propto C_D^-$ or $k_{IA} \propto C_A^+$). The quadratic dependence of k_{IA} ($m = 2$) can be expected upon the capture of neutral self-interstitials by pairs consisting of ionized impurity atoms and oppositely charged vacancies, as well as upon the capture of charged self-interstitials by oppositely charged impurity atoms ($k_{IA} \propto nC_D^-$ or $k_{IA} \propto pC_A^+$). The cubic dependence k_{IA} ($m = 3$) can take place when charged self-interstitials are captured by pairs composed of ionized impurity atoms and oppositely charged vacancies ($k_{IA} \propto n^2 C_D^-$ or $k_{IA} \propto p^2 C_A^+$). As can be seen from Figs. 3 and 4, each of these three variants of concentration dependences may be used to describe the falloff of relative OED coefficients with respect to the value of $p/n_i = 1$ (or $n/n_i = 1$). From our point of view, for the B diffusion (Fig. 3), the dependences with $m = 1$–2 are more preferable and, for the P diffusion (Fig. 4), the ones with $m = 2$–3 are more preferable. To determine the exponent of the concentration dependence more exactly, the number of experimental points should be increased.

In the case of diffusion-limited capture of neutral self-interstitials by ionized dopant atoms,

$$k_{IA} = 4\pi R D_I C,$$

where R is the capture radius of the self-interstitial; from here we have

$$K_1 = 4\pi R D_I.$$

From the determined values of K_1, found we estimate the radius for this variant of capture $R_1 \simeq (4\text{–}12) \times 10^{-4}$ nm.

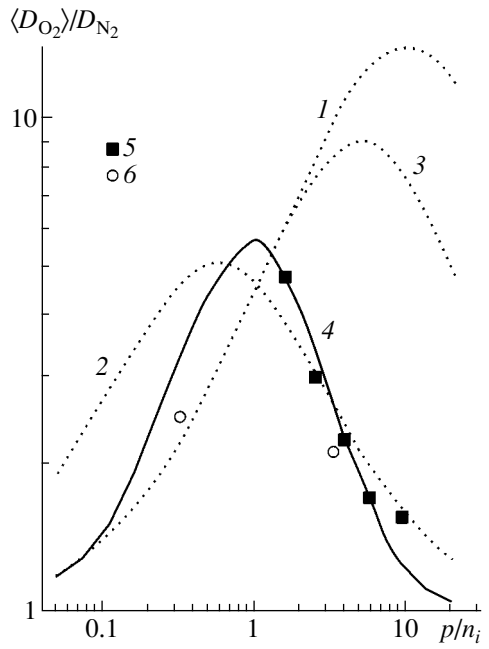

Fig. 5. Concentration dependences of the relative B diffusivity upon heat treatment of the samples in dry oxygen (1000°C), calculated from the model [9] with levels of charged self-interstitials: (*1*) $E_C - 0.11$ eV, $E_V + 0.17$ eV [7]; (*2*) $E_C - 0.35$ eV, $E_V + 0.50$ eV [8]; and (*3*) $E_C - 0.09$ eV, $E_V + 0.34$ eV [9]. Curve *4* corresponds to the calculation according to the suggested model (for $K_2 = 4 \times 10^{-20}$ cm^3/s$^{1/2}$); the points correspond to the experiment: (*5*) [5], and (*6*) [8].

In the case of capture of charged self-interstitials by ionized dopant atoms, we have (for donor doping)

$$k_{IA} = 4\pi R D_I C_D^+ n/n_I,$$

where n_I is the electron density corresponding to the Fermi level coinciding with the level of charged self-interstitials; as a result,

$$K_2^2 = 4\pi R D_I/n_I.$$

Assuming that this level lies close to the midgap ($n_I \simeq n_i$), we can derive the estimation $R_2 \simeq (1.0–1.4) \times 10^{-4}$ nm.

In the case of capture of neutral self-interstitials by the pairs consisting of ionized impurity atoms and oppositely charged vacancies, we have (for donor doping)

$$k_{IA} = 4\pi R D_I k_E C_D^+ V^0 n/n_V,$$

where n_V is the electron density corresponding to the Fermi level, which coincides with the level of the charged vacancy; V^0 is the concentration of neutral vacancies; and k_E is the pair-formation constant:

$$k_E = (4/5) \times 10^{22} \exp(E_B/kT),$$

where E_B is the bonding energy of the pair; as a result, we have

$$K_2^2 = 4\pi R D_I k_E V^0/n_I.$$

For $n_V \simeq n_i$, $E_B \simeq 1.5$ eV, and the value of concentration V^0 taken from [19], we derive the estimate $R_{2E} \simeq$ 0.02–0.65 nm.

For the case of capture of charged self-interstitials by the pairs consisting of ionized impurity atoms and oppositely charged vacancies, we have (for donor doping)

$$k_{IA} = 4\pi R D_I k_E C_D^+ V^0 n^2/(n_V n_I);$$

as a result,

$$K_3^3 = 4\pi R D_I k_E V^0/(n_V n_I)$$

and, for the capture radius, we derive the estimation $R_{3E} \simeq 0.01–0.08$ nm.

The values of R_1 and R_2 are physically unrealistically small; i.e., the most probable centers for the capture of neutral and/or charged self-interstitials are the impurity–vacancy pairs with the radii R_{2E} and R_{3E}, respectively.

Miyake [6] explained a decrease in the OED of B with increasing doping level of P by the recombination of excess self-interstitials at acceptor vacancies V^-. The author arrived at this conclusion using the action-mass law in the form

$$\Delta I V^- = \Delta I_i V_i^-,$$

where the subscript denotes intrinsic doping conditions ($C \ll n_i$), from which the following was derived:

$$\Delta I/\Delta I_i = V_i^-/V^- = n_i/n.$$

However, for the interaction of neutral self-interstitials with the acceptor vacancy

$$I^0 + V^- \longleftrightarrow S + e^-,$$

where e^- is the electron, the action-mass law takes the from

$$I^0 V^-/n = I_i^0 V_i^-/n_i = \text{const};$$

from here,

$$I^0/I_i^0 = (nV_i^-)/(n_i V^-) = 1.$$

It is also easy to obtain similar relationships for any other charge state of recombining self-interstitials and vacancies. Specifically, when the condition for local equilibrium is satisfied, the relative supersaturation of self-interstitials is independent of the doping level and, consequently, the equilibrium recombination can not be the reason for OED reduction with increasing doping level.

Giles [9] explained OED reduction with an increase in the doping level by a decrease in the relative supersaturation of self-interstitials due to increasing the equilibrium concentrations of self-interstitials in the charged states in accordance with the Fermi level shift. In the framework of this model, from an analysis of experimental dependences of OED on the doping level,

the authors [7–9] found the levels of charged self-interstitials in the band gap. In Fig. 5, we plotted the dependences of relative B diffusivity (which were calculated from the model [9] for the levels found in [7–9]) on the doping level. As can be seen from Fig. 5, the levels of self-interstitials found in [8] make it possible to describe B diffusion only for acceptor uniform doping, and the levels of self-interstitials found in [7, 9] allow one to do the same only for donor doping. It should also be noted that it is impossible to satisfactorily explain the results [8] on the influence of a lightly doped layer, positioned on the surface of a heavily doped layer, on the OED in the framework of model [9]. With the presence of a lightly doped epilayer, the OED of P increased by a factor of 2–3, despite the fact that the region of generation of excess self-interstitials, specifically, the Si/SiO_2 interface, was moved away from the doped layer by the epilayer thickness (1 μm). The authors [8] attributed this result to two possible reasons:

(i) An increase in the generation rate of self-interstitials at the Si/SiO_2 interface upon the thermal oxidation of heavily doped layers;

(ii) The emergence of an internal electric field, caused by the gradient of the impurity concentration in a buried doped layer upon growing an epilayer on it, and the influence of this field on an increase in the flux of self-interstitials from the interface.

However, it should be noted that the oxidation rate V_{ox} increases as the Si doping level increases [10]. Therefore, an increase in $G_I \propto V_{ox}$ should be expected rather than a decrease in it. The excess self-interstitials in a lightly doped epilayer are preferentially neutral. Therefore, it can hardly be expected that the internal electric field, which is localized close to the interface between the epilayer and the doped layer, will strongly affect the flux of excess self-interstitials from the interface into the Si bulk.

In the framework of this model, an increase in the OED, when the epilayer is present on the surface, finds a natural explanation. This increase is related to the low concentration of recombination centers in the lightly doped epilayer and, for this reason, to an increase in the surface concentration of excess self-interstitials according to expression (10a), where $I_S \propto \sqrt{\tau_I}$. This result is illustrated in Fig. 2, from which it can be seen that the surface concentration of self-interstitials in the sample with a lightly doped epilayer on a heavily doped substrate (curve *4*) is substantially higher than in the sample with the same doping level of the substrate (curve *3*). At the same time, this concentration is lower than in the sample with a low doping level (curve *1*), which is related to the outflow of self-interstitials from the epilayer surface into the heavily doped substrate, where the recombination rate is high.

6. CONCLUSION

Thus, we have proposed model of reduction of oxidation-enhanced diffusion (OED) in heavily doped Si layers, in which the bulk recombination of excess self-interstitials at the centers related to the dopant is considered as the reason for a decrease in OED. It is shown that an increase in the recombination rate with increasing doping level leads to a decrease in the surface concentration of excess self-interstitials generated at the SiO_2/Si interface upon thermal oxidation of Si. The calculated concentration distributions and dependences of the relative coefficient of OED, $\langle D_{O_2} \rangle / D_{N_2}$, for B and P impurities were compared with experimental data for donor and acceptor uniform doping. From this comparison, the constants of the recombination rate of excess self-interstitials were determined. Estimations of the capture radii show that the most probable centers of capture of self-interstitials are dopant–vacancy pairs. Other models of OED reduction were discussed, and the influence of a lightly doped layer, positioned on the surface of a heavily doped layer, on OED was explained.

REFERENCES

1. R. B. Fair, J. Electrochem. Soc. **128**, 1360 (1981).
2. P. M. Fahey, P. B. Griffin, and J. D. Plummer, Rev. Mod. Phys. **61**, 289 (1989).
3. S. M. Hu, J. Appl. Phys. **45**, 1567 (1974); J. Appl. Phys. **57**, 1069 (1985).
4. K. Taniguchi, K. Kurosawa, and M. Kashiwagi, J. Electrochem. Soc. **127**, 2243 (1980).
5. M. Miyake, J. Appl. Phys. **57**, 1861 (1985).
6. M. Miyake, J. Appl. Phys. **58**, 711 (1985).
7. J. P. John and M. Law, J. Electrochem. Soc. **140**, 1489 (1993).
8. D. J. Roth and J. D. Plummer, J. Electrochem. Soc. **141**, 1074 (1994).
9. M. D. Giles, IEEE Trans. Comput. Aided Des. **8**, 460 (1989).
10. *Process and Device Simulation for MOS–VLSI Circuits*, Ed. by P. Antognetti, D. Antoniadis, R. W. Dutton, and W. G. Oldham (Nijhoft, Boston, 1983; Radio i Svyaz', Moscow, 1988).
11. C. P. Ho, S. E. Plummer, and R. W. Dutton, IEEE Trans. Electron Devices **30**, 1438 (1983).
12. A. Ural, P. B. Griffin, and J. D. Plummer, Appl. Phys. Lett. **73**, 1706 (1998).
13. W. Wijaranakula, J. Appl. Phys. **67**, 7624 (1990).
14. A. Leroy, J. Appl. Phys. **50**, 7996 (1979).
15. E. Rorris, R. R. O'Brien, F. F. Morehead, *et al.*, IEEE Trans. Comput. Aided Des. **9**, 1113 (1990).
16. S. W. Crowder, C. J. Hsieh, P. B. Griffin, and J. D. Plummer, J. Appl. Phys. **76**, 2756 (1994).
17. A. A. Samarskiĭ, *The Theory of Difference Schemes*, 2nd ed. (Nauka, Moscow, 1983; Marcel Dekker, New York, 2001), Chap. 3.
18. R. Sh. Malkovich, *Mathematics of Diffusion in Semiconductors* (Nauka, St. Petersburg, 1999), p. 134.
19. B. J. Masters and E. F. Gorey, J. Appl. Phys. **49**, 2717 (1978).

Translated by N. Korovin

Semiconductors, Vol. 37, No. 6, 2003, pp. 632–635. From Fizika i Tekhnika Poluprovodnikov, Vol. 37, No. 6, 2003, pp. 657–660.

ATOMIC STRUCTURE AND NONELECTRONIC PROPERTIES OF SEMICONDUCTORS

Defect Profiling in Semiconductor Layers by the Electrochemical Method*

Á. Nemcsics and J. P. Makai

Hungarian Academy of Sciences, Research Institute for Technical Physics and Materials Science, H-1525 Budapest, Hungary
e-mail: nemcsics@mfa.kfki.hu

Submitted September 18, 2002; accepted for publication December 4, 2002

Abstract—Special based equipment for selective electrochemical etching is presented which is appropriate for in situ observation of the defect structure. The operation of the setup is demonstrated on InGaAs/GaAs (001) heteroepitaxial systems in which the epitaxial layer thickness is above the critical layer thickness. Through incremental layer removal, the depth profile of the dislocation density is mapped. The measured defect density is inversely proportional to the layer thickness and corresponds to the theoretical model. © *2003 MAIK "Nauka/Interperiodica".*

1. INTRODUCTION

It is of considerable interest to understand the behavior of the defects induced by lattice mismatch in heteroepitaxial systems [1]. Defects in the layers can be investigated using various methods. A common method for defect distribution is X-ray topography. Its main advantage is that different kinds of defects can be investigated in a nondestructive way. The disadvantages are that the investigation is confined only to the lateral direction and the measurement is very time consuming. Another commonly used method is transmission electron microscopy. The defect distribution in the cross-sectional direction can be investigated with high resolution using this method. Investigation based on this method is also limited to only one direction, and sample preparation is a cumbersome and time consuming procedure. In this work, we present equipment based on the electrochemical method, which is appropriate for the simple and rapid investigation of crystal defects both in the lateral and vertical directions.

Using an electrolyte on the semiconductor surface, the controlled removal of the electrochemical layer can be carried out. Selective electrochemical etching is a widely used method for the investigation of defects in epitaxial layers and substrate material. One of the advantages of this method is that it enables one to determine defect distribution both in lateral [2] and vertical [3] directions. It has none of the disadvantages of the other methods: it is a rapid method with good resolution and the setup is simple.

In this study, we use selective electrochemical etching to examine the threading defects in $In_xGa_{1-x}As/GaAs$ heterostructures grown by molecular beam epitaxy (MBE). Electrochemical defect profiling is carried out with the help of a novel electrochemical defect profiler. By incremental etching, we map the depth distribution of the defects. The results obtained are compared with a theoretical model.

*This article was submitted by the authors in English.

2. THE EQUIPMENT

2.1. General Description

The electrochemical defect profilometer consists of two principal parts. One of them is the electrochemical part, the other is the optical one. A block scheme of the whole setup is shown in Fig. 1. The electrochemical part consists of a specially constructed electrochemical cell. The electrochemical cell is connected to an Elektroflex EF451 potentiostat [4]. The potentiostat is controlled by a computer, in which the connection is realized by a special interface card (EF3506) through a parallel port. The highest output voltage is ±20 V. The current can be measured in eight ranges from 2 A to 25 pA. The potentiostat is entirely digitally controlled, and the status of the equipment is displayed by light-emitting diodes on the front panel. The control program, written in Turbo Pascal, makes different working modes possible, e.g., cyclic voltammetry, impedance analysis, and integration of current. The program automatically makes a measurement report and attaches it to the measured data and the setting parameters of the setup. A printer is used to print the measured diagrams. The electrolyte in the specially designed electrochemical cell is circulated by a pump.

The optical part consists of a lens system collecting most of the light emitted by the lamp, a microscope objective, and a beam splitter, which are components of both the illuminating and viewing parts and an attached CCD camera (Sony). The case of the optical system was manufactured from an aluminum block. Adjustment of the optical system can be carried out using screws. The attached camera is connected to a computer with two monitors (one of them serves as the menu of the image processing program and the other one, for the visualization of the investigated surface). The picture can be saved as a bmp file.

1063-7826/03/3706-0632$24.00 © 2003 MAIK "Nauka/Interperiodica"

2.2. The Electrochemical Unit

One of the most important parts of the setup is the specially designed electrochemical cell, shown in Fig. 2. The cell must have a shallow depth, as the sample has to be close to the window because of the limited working distance for optical observation. The construction is also special with respect to the small cross section. The cell is cut from a Plexiglas block.

The layout of our electrochemical measuring setup is often used in electrochemical investigations. The working electrode is the semiconductor sample, the counter electrode is made of carbon and platinum wire, and the reference electrode is a saturated calomel electrode [5]. The sample is held close to a rubber ring seal 3 mm in diameter.

The narrow cell requires a special method for the removal of bubbles and for cleaning the chamber of the electrolyte. Because the size of the cell is small, the fresh electrolyte which is needed for the reaction is circulated using an attached pump. The pump also serves in the removal of bubbles, which might stick in the sealing ring, and for the cleaning of the cell with distilled water.

The removal of the electrochemical layer is carried out under two different conditions. The first is the so-called polishing or nonselective condition, where the bias is chosen on the low-slope part of the polarization curve with optical stimulation. The second condition is selective etching that can be carried out by very low polarization with illuminated surface or with high polarization in the dark. The charges crossing the electrode spacing are integrated during the etching, thus, the thickness of the removed layer was calculated by Faraday's law [6], where the actual parameters are the physical (material density, valence number, etc.) and geometrical data of the system. The etched depth is controlled by an alpha-step profiler.

2.3. The Optical Unit

The optical layout of the illuminating and viewing system is shown in Fig. 3. For simplicity, Fig. 3 does not include the etching chamber, but only the wafer. A 250-W tungsten halogen lamp is used as the light source. It can be considered a Planckian radiator of approximately 3200 K in the wavelength range of 0.3 to 2.5 μm, if used at nominal values, and can be tested by special probes [7, 8]. Either broad- or narrow-band illumination can be applied to the wafer. The spectral limiting media of the broadband illumination is the liquid in the etching chamber; if it is water based, the transmission is between 0.3 and 1.4 μm, which is much stricter than the limitation of the glass material of the lenses or the light source. Even ~10-mm-thick water-based liquid absorbs radiation above 1.4 μm; the transmissivity is only a fraction of a percent. This spectral range is only slightly wider than the sensitive range of the Si CCD camera; within this spectral range a narrow band can be selected by inserting interference filters (*F*)

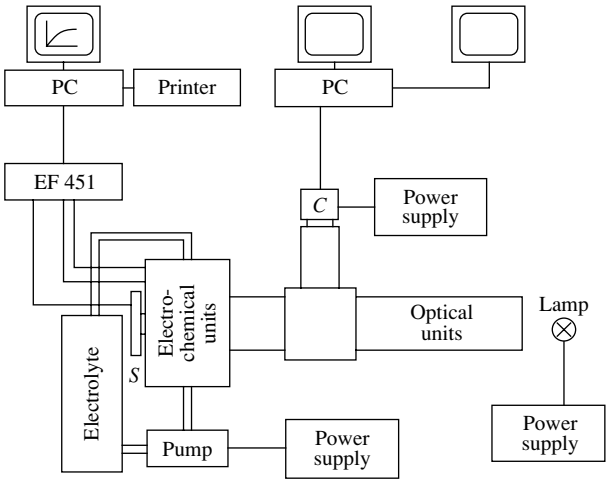

C stands for the camera; and *S*, for the sample

Fig. 1. A block scheme of the electrochemical defect profiler.

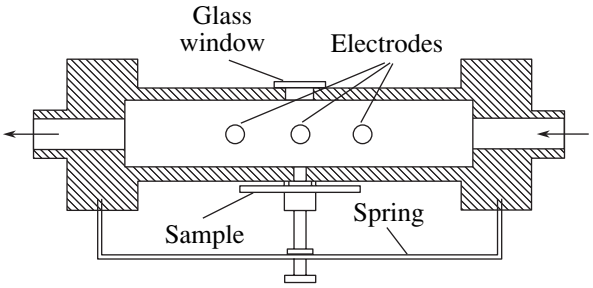

Fig. 2. Cross section of the specially designed electrochemical cell.

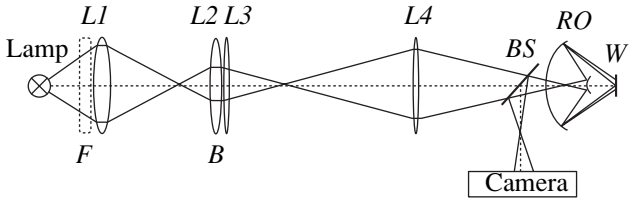

Fig. 3. Schematic representation of the optical system where *L1–L4* are lenses, *RO* is the microscope objective, and *BS* is the beam splitter.

to investigate the effect of etching as a function of the wavelength of illumination.

A magnified image of the lamp is produced by the lens *L1* on the lens *L2*. The lens pair *L2* and *L3* images, also magnified, *L1* onto the lens *L4*, which is further imaged by the reflective microscope objective *RO* onto the wafer *W*. Lens *L4* images *L3* onto the convex mirror of the objective. An image of the wafer is produced on the camera by the microscope objective through the beam splitter *BS*. A reflective microscope objective was chosen because it has a high working distance of about 15 mm, which provides room for the etching chamber.

The magnification of the objective is 15; since the usable diameter of the lenses is 20 mm, this means a light-spot diameter of 1.33 mm on the wafer. About half of this area is imaged onto the active surface of the detector. The uniformity of the light spot on the wafer is ensured by imaging the uniformly illuminated *L1* onto the wafer. The numerical aperture of the objective is 0.28, which provides an optical resolution, according to the Rayleigh criteria, of 0.65 μm at a wavelength of 300 nm, 1.42 μm at 650 nm, and 2.18 μm at 1000 nm. This suggests that the etching should be performed at the desired wavelength or wavelength band and that a picture should be taken at the shortest wavelength appropriate for the spectral emittance of the source and the sensitivity of the Si CCD camera. The pixel size of the camera used is about 10×10 μm^2; this means that the optical resolution of the objective multiplied by the magnification (0.65×15 μm^2), at the short-wavelength edge, corresponds to the size of a single pixel. The disadvantage of the reflective objective is that axial quasi-parallel rays reaching the middle portion of the convex mirror of the objective would reflect straight back to the camera through the beam splitter (*BS*), which would blind the camera. To inhibit this, a small opaque disc *B* is mounted in between *L2* and *L3*, thus blocking these rays. The beam splitter is of the pellicle type and ensures a single image of the wafer on the camera window using the objective.

Since the camera has no objective, there is no automatic iris adjustment; it is replaced either by the proper selection of the lamp current or by the translation of the lamp. Changing the current will change the so-called distribution temperature of the lamp, but if narrowband illumination is used, this will not cause any deviation from the ideal etching conditions. If broadband illumination is used, changing the lamp current also changes the spectral composition of the illumination; therefore, the translation method must be used. This ensures that no overflow of the CCD camera occurs. The lamp is mounted on an *XYZ* translation stage; the etching chamber, on an *XY* one. Vertical *Z* motion is provided by the adjustment of the entire optical system placed in the tube.

The camera is of the black-and-white type and has 512×512 pixels. It is connected to a frame grabber that allows further manipulation, for example, comparison of images, convolution, etc. It permits the simultaneous display of the buffer frame and an overlayable plane of colour graphics, as well as management of programmer access. It has online preprocessing units in combination with its look-up tables, located at the input and output of the video channels. Real-time conversion is provided by a flash converter with a resolution of eight bits.

3. EXPERIMENT AND DISCUSSION

3.1. Selective Electrochemical Etching

The GaAs (001) oriented wafers used in the experiment are Zn doped ($p = 4 \times 10^{18}$ cm^{-3}) with an etch pit density (EPD) $< 5 \times 10^{14}$ cm^{-2}. The In content in the MBE grown layer was 30% and the layer thickness was 1.2 μm. The sample preparation is described in detail in [9]. By using electrochemical etching we found that the undoped layers were slightly of the *p*-type. The Matthews–Blakeslee (equilibrium) critical layer thickness for a misfit generating dislocation [1] is about 8 nm for the sample ($In_{0.3}Ga_{0.7}As/GaAs$, lattice mismatch $f = 0.024$); i.e., our layer is much thicker that the critical layer thickness.

The morphology of the etched surface was examined using our own optical system. The thickness of the removed layer was calculated by Faraday's law and measured by a surface stylus profiler. The EPD values were determined with the defect counter on the screen, which corresponds to an area of about 586×440 μm^2 on the surface.

The etching parameters (e.g., bias voltage) were optimized by using a free GaAs substrate. According to our previous experiments, 10% NH_4OH is a suitable aqueous electrolyte for defect etching [8, 11]. Not only the type of electrolyte, but also the surface morphology depend on the bias voltage. After etching, the surface is well-structured when an anodic bias larger than 0.5 V (defect etch conditions) is applied. At lower bias voltages, the surface remains mirrorlike (polish-etch conditions). When the bias ranges between 0.5 and 0.8 V, the etching current, is stable; i.e., it increases only slowly with depth or time. The etching current is high when the doping level is high in this bias range and when the etching rate is low. In this range, we can remove thick layers and detect the location of the etched surface relative to the interface or substrate. Under an anodic bias larger than 1 V, the etching current becomes unstable and increases strongly with time or depth. In this etching current range, it is larger for the undoped layer than for the bare substrate. The slope of the I–V characteristics of the epitaxial layer above a bias of 0.5 V, is larger than the corresponding slope of the substrate. This can be attributed to the presence of defects. At higher EPD, the current versus time/depth is steeper, since, under a higher bias voltage current, filaments are formed at the imperfections [2].

Based on these results, we carried out defect etching under a bias of about 0.6 V, where the current density was lower than 2 mA/cm^2. Prior to studying the substrate, the damaged surface layer was removed by nonselective etching. The position of the interface is indicated by the current vs. depth function. The current density has an abrupt increment at the interface, because the substrate has a higher charge-carrier concentration than the epilayer (see Fig. 2 in [3]).

3.2. Comparison with the Model

A typical picture of the surface morphology for the sample after selective etching is shown in Fig. 4. The measured EPD of the substrate was about half the value

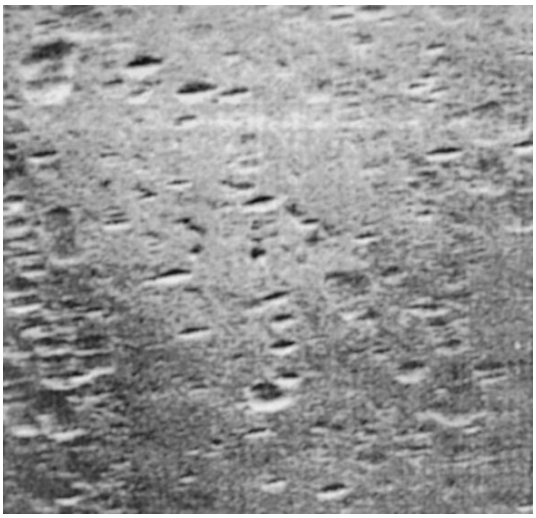

Fig. 4. View of the etched surface at 0.7 μm from the interface, where the EPD is about 2×10^8 cm^{-2}.

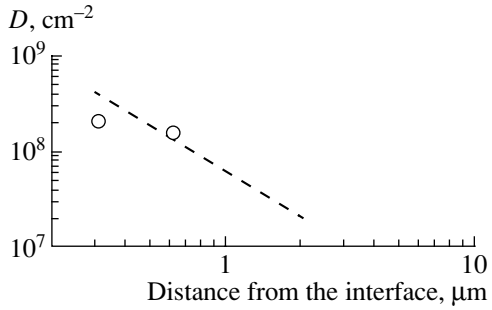

Fig. 5. The threading dislocation density D (circles) as a function of the etched depth for the measured sample in comparison with model calculation (dashed line).

specified by the supplier. The substrate defect density was found to be nonuniform. This indicates that the epilayer dislocations originate even from sources other then the grown-indislocations of the substrate. We further note that the nonuniform distribution of the threading dislocation is inherent to the mismatched systems. The average measured EPD vs. depth data are depicted on Fig. 5. The size of the etch pits are different; larger pits indicate dislocations propagating further away from the interface. This is indirect evidence for the depth inhomogeniety of the defect density. The elongated shape of the pits is due to the higher etch rate along one of the [011] axes.

Several theoretical models have been suggested to predict the threading dislocation density D in mismatched heteroepitaxial systems [1]. The threading dislocation densities determined by defect development are generally lower than the theoretically predicted values [3, 12]. Wehmann *et al.* have introduced another model for the determination of the threading dislocation density [13]. The values predicted by this model agree very well with the measured EPD on thick, highly mismatched heteroepitaxial structures [12]. In our case, the calculated curve is shown by dashed line in Fig. 5, which fits the experimental data.

4. CONCLUSIONS

Novel electrochemical equipment for the investigation of defects was presented. The setup is suitable for observing defect distribution in both lateral and vertical directions. The specially constructed electrochemical cell and optical system were described in detailed. The investigated material system was a thick InGaAs/GaAs heterostructure. It was shown that the presented setup for selective electrochemical etching is suitable for the depth-dependent study of the defect density in lattice-mismatched heteroepitaxial systems. The results agree with general physical concept of heteroepitaxial growth and processes.

ACKNOWLEDGMENTS

The authors are grateful to L. Dobos (Elektroflex), T. Pajkossy, Zs. Kerner, and M. Rácz for helpful discussions and for providing hardware and software used in the design of the equipment presented here. This study and the development of the equipment was supported by the Hungarian National Scientific Foundation (OTKA) (grants T 030426 and E 039453).

REFERENCES

1. E. A. Fitzgerald, Mater. Sci. Rep. **7**, 87 (1991).
2. Á. Nemcsics, L. Petrás, and K. Somogyi, Vacuum **41**, 1015 (1990).
3. Á. Nemcsics, F. Riesz, and L. Dobos, Thin Solid Films **343–344**, 520 (1999).
4. www.elektroflex.hu (elektroflex@deltav.hu).
5. M. M. Faktor and J. L. Stevenson, J. Electrochem. Soc. **125**, 621 (1978).
6. T. Ambridge and M. M. Fakrot, J. Appl. Electrochem. **5**, 319 (1975).
7. M. Rácz, I. Réti, and S. Ferenczi, Opt. Eng. **32**, 2517 (1993).
8. M. Rácz, I. Réti, and S. Ferenczi, in *Proceedings of International Conference on Photodetectors and Power Meters, San Diego, California, 1993* (SPIE, Belingham, Wash., 1993), Vol. 2022, p. 192.
9. Á. Nemcsics, J. Olde, M. Geyer, *et al.*, Phys. Status Solidi A **155**, 427 (1996).
10. Á. Nemcsics and K. Somogyi, Acta Phys. Hung. **70**, 259 (1991).
11. Á. Nemcsics, M. Schuszter, L. Dobos, and Gy. Ballai, Mater. Sci. Eng. B **90**, 67 (2002).
12. H. H. Wehmann, *Hablitationschrift* (TU Carolo-Wilhemina, Braunschweig, 2000).
13. H. H. Wehmann, G. P. Tang, and A. Schlachetzki, Solid State Phenom. **32–33**, 445 (1993).

Semiconductors, Vol. 37, No. 6, 2003, pp. 636–640. Translated from Fizika i Tekhnika Poluprovodnikov, Vol. 37, No. 6, 2003, pp. 661–665.

ELECTRONIC AND OPTICAL PROPERTIES OF SEMICONDUCTORS

X-ray Photoelectron Spectroscopy and X-ray Electron-Microprobe Analysis of Single Crystals Based on Bismuth Telluride

I. V. Gasenkova*, V. A. Chubarenko†, E. A. Tyavlovskaya*, and T. E. Svechnikova*****

**Institute of Electronics, Belarussian Academy of Sciences, Minsk, 220090 Belarus*
e-mail: gasenkova@inel.bas-net.by
***Shubnikov Institute of Crystallography, Russian Academy of Sciences, Leninskiĭ pr. 59, Moscow, 117333 Russia*
****Baĭkov Institute of Metallurgy and Materials Science, Russian Academy of Sciences, Leninskiĭ pr. 49, Moscow, 117911 Russia*

Submitted August 13, 2002; accepted for publication October 30, 2002

Abstract—Experimental data on the distribution and atomic fractions of elements in $Bi_2Te_{2.94}Se_{0.06}$, $Bi_2Te_{2.88}Se_{0.12}$, $Bi_{1.99}Sn_{0.01}Te_{2.94}Se_{0.06}$, and $Bi_{1.99}Sn_{0.01}Te_{2.88}Se_{0.12}$ are discussed; these data were obtained using X-ray electron-microprobe analysis and X-ray photoelectron spectroscopy. It is ascertained that Sn impurity introduced with a concentration amounting to $x = 0.01$ increases the uniformity of the Bi and Te distributions in solid solutions, whereas an increase in the Se content from $y = 0.06$ to 0.12 gives rise to fluctuations in the composition; the fluctuations range from 0.5 at. % in undoped solid solutions based on Bi_2Te_3 to 0.3 at. % in these solutions doped with Sn. The binding energies of the core electrons in the single crystals under consideration were determined; variation in the total density of electronic states in the valence band in the vicinity of the Fermi level was observed. © *2003 MAIK "Nauka/Interperiodica".*

1. INTRODUCTION

The widespread use of solid solutions based on Bi_2Te_3 in thermoelectric devices, which operate in the temperature range of 200–350 K, the need for the further improvement of the parameters of these devices, and for extending of their functional capabilities necessitate studies on the doping processes in these materials. Interest in the behavior of Sn atoms in solid solutions based on Bi_2Te_3 is due to the observed special features in the distribution of the density of states in the valence band of the solutions under consideration doped with Sn; these features are different for doped and undoped Bi_2Te_3 [1] and give rise to new electrical properties. Previously [2–4], it was shown that Bi_2Te_3 doped with Sn exhibits a number of special features which can be explained in the context of the resonance-state model. Similar behavior of kinetic coefficients can also be observed in solid solutions based on Bi_2Te_3. At the same time, inhomogeneity of composition may give rise to exactly the same electrical properties; i.e., it can reproduce the behavior of a homogeneous semiconductor with impurity levels in the band gap. In this context, it is important to know the distribution of the doping impurity and the possible composition of inhomogeneities which arise owing to crystallization of solid solutions based on bismuth telluride with significant deviations from stoichiometry; it is also important to know the electronic structure of the material under consideration.

In this paper, we discuss experimental data on the effect of Sn atoms on the composition homogeneity and the X-ray photoelectron spectra measured in single crystals of solid solutions based on Bi_2Te_3.

2. EXPERIMENTAL

Uniformity of the elements' distribution and atomic fractions of elements in the $Bi_2Te_{2.94}Se_{0.06}$, $Bi_2Te_{2.88}Se_{0.12}$, $Bi_{1.99}Sn_{0.01}Te_{2.94}Se_{0.06}$, and $Bi_{1.99}Sn_{0.01}Te_{2.88}Se_{0.12}$ single crystals and the binding energy of core electrons were determined using electron-microprobe X-ray analysis (EMXA) and X-ray photoelectron spectroscopy (XPS). The samples were examined in a JXA-8600S scanning electron-probe X-ray microanalyzer using the triple correction method and Bi, Sn, Se, and PbTe primary standards. Measurements were performed in five arbitrarily chosen zones with areas of about 5×5 μm^2 at the sample surface. The spectra of the valent and core states were measured with an ÉS-2401 electron spectrometer using MgK_α radiation with a photon energy $h\nu = 1253.6$ eV. The binding energies of core electrons were determined in reference to the 1*s* carbon level with an energy of 284.6 eV. Single crystals of the solid solutions were grown by the Czochralski method with additional feeding of the melt from a floating crucible [5]. The single crystals were grown in the [1010] direction,

†Deceased.

Table 1. Composition of $Bi_2Te_{2.94}Se_{0.06}$ and $Bi_{1.99}Sn_{0.01}Te_{2.94}Se_{0.06}$ single crystals

Compound, measurement-zone no.	Content of elements							
	Bi		Te		Se		[Bi]/([Te] + [Se])	
	[Bi], at. %	Δ, at. %	[Te], at. %	Δ, at. %	[Se], at. %	Δ, at. %	XEMA	XPS
$Bi_2Te_{2.94}Se_{0.06}$								
1	39.82	0.02	58.96	0.14	1.22	0.12	0.66	
2	39.64	0.16	59.46	0.36	0.90	0.20	0.66	
3	39.90	0.10	59.15	0.05	0.95	0.15	0.66	
4	39.89	0.09	59.03	0.07	1.08	0.02	0.66	
5	39.77	0.03	58.89	0.21	1.34	0.24	0.66	
N	39.80		59.10		1.10		0.66	0.66
$Bi_{1.99}Sn_{0.01}Te_{2.94}Se_{0.06}$								
1	39.76	0.14	59.26	0.25	0.98	0.11	0.66	
2	39.84	0.06	59.12	0.11	1.04	0.05	0.66	
3	39.88	0.02	58.90	0.11	1.22	0.13	0.66	
4	40.04	0.14	58.92	0.09	1.04	0.05	0.67	
5	40.01	0.11	58.84	0.17	1.15	0.06	0.67	
N	39.90		59.01		1.09		0.66	0.64

Note: *N* is the average value and Δ is the deviation from this value.

which was perpendicular to the principal crystallographic axis *C*. The crystals were plate-shaped with a length of about 100 mm, a width of ~30 mm, and a thickness of ~16–20 mm. The growth rate and velocities of the seed and crucible rotations were identical during the growth of the solid-solution crystals of all compositions and satisfied the conditions for obtaining high-quality single crystals; i.e., the effects of growth conditions on the equilibrium between the liquid and solid phases at the crystallization front, on the structure quality, and on the electrical properties of solid solutions were eliminated.

3. RESULTS AND DISCUSSION

Experimental data on the composition of the solid solutions under investigation are listed in Tables 1 and 2. The atomic ratios of the elements are also listed for comparison. The XPS method yielded atomic fractions which are close to those obtained by XEMA. As can be seen from Tables 1 and 2, the atomic fractions obtained by both methods coincide for selenium-containing single crystals. The difference between atomic fractions listed in Tables 1 and 2 and obtained by the XEMA and XPS methods for solid solutions doped simultaneously with tin and selenium is caused by a lower accuracy of calculations from the XPS method; these calculations were based not only on the intensity of the broad Se peak, but also on that of the Te peak, which is much broader than a similar peak in crystals without Sn impurity (see Fig. 1 and the values of the FWHM in Table 3). However, consistent data were obtained even in this case.

On the basis of the results of X-ray microanalysis, we may assume that the composition and ratio ([Bi]/([Te] + [Se])) for various regions of the crystal under consideration are virtually constant. An increase in the amount of Se introduced into the solid solution from 6 to 12 at. % gives rise to a large spread in the obtained absolute values of the atomic fractions of elements. For example, the largest deviation from the mean atomic fraction amounts to 0.42 at. % for Bi and 0.49 at. % for Te in $Bi_2Te_{2.88}Se_{0.12}$ solid solution, compared with 0.14 at. % for Bi and 0.36 at. % for Te in $Bi_2Te_{2.94}Se_{0.06}$. A similar increase in the spread of atomic fractions is characteristic of the Sn-containing crystals of solid solutions based on Bi_2Te_3. Single crystals that are doped with Sn and have a high concentration of Se also feature a larger spread in composition. For example, the data on atomic fractions deviate from the mean values by 0.30 at. % for Bi and by 0.35 at. % for Te in $Bi_{1.99}Sn_{0.01}Te_{2.88}Se_{0.12}$, compared with deviations of 0.16 at. % for Bi and 0.24 at. % for Te in $Bi_{1.99}Sn_{0.01}Te_{2.94}Se_{0.06}$. In addition, in the former solid solution, a somewhat higher content of bismuth is also observed, which is more pronounced in the samples with an Se content of 12 at. %. The difference in the Bi content between the Sn-doped doped and undoped $Bi_2Te_{2.94}Se_{0.06}$ and $Bi_2Te_{2.88}Se_{0.12}$ samples amounts to 0.1 and 0.6 at. %, respectively. The observed deviation from stoichiometry, corresponding to excess Bi, is characteristic of the compounds under consideration and is consistent both with the published data and the Bi–Te phase diagram [6]. These data indicate that, com-

Table 2. Composition of $Bi_2Te_{2.88}Se_{0.12}$ and $Bi_{1.99}Sn_{0.01}Te_{2.88}Se_{0.12}$ single crystals

Compound, measurement-zone no.	Content of elements							
	Bi		Te		Se		[Bi]/([Te] + [Se])	
	[Bi], at. %	Δ, at. %	[Te], at. %	Δ, at. %	[Se], at. %	Δ, at. %	XEMA	XPS
$Bi_2Te_{2.88}Se_{0.12}$								
1	39.59	0.08	57.85	0.07	2.56	0.01	0.66	
2	39.93	0.42	57.56	0.36	2.51	0.06	0.66	
3	39.15	0.36	58.41	0.49	2.44	0.13	0.64	
4	39.64	0.13	57.69	0.23	2.67	0.10	0.66	
5	39.24	0.27	58.10	0.18	2.66	0.09	0.65	
N	39.51		57.92		2.57		0.65	0.65
$Bi_{1.99}Sn_{0.01}Te_{2.88}Se_{0.12}$								
1	40.36	0.30	57.15	0.21	2.49	0.09	0.68	
2	40.11	0.05	57.38	0.02	2.51	0.07	0.67	
3	40.17	0.11	57.21	0.15	2.62	0.04	0.67	
4	39.76	0.30	57.71	0.35	2.53	0.05	0.66	
5	39.91	0.15	57.36	0.00	2.73	0.15	0.66	
N	40.06		57.36		2.58		0.67	0.66

Note: *N* is the average value and Δ is the deviation from this value.

Table 3. Data on X-ray photoelectron spectra in reference to the C 1*s* level (284.6 eV)

Compound	Binding energy, eV FWHM, eV					
	Bi $4f_{7/2}$	Bi $4f_{5/2}$	Te $3d_{5/2}$	Te $3d_{3/2}$	Te $4d_{5/2}$	Te $4d_{3/2}$
$Bi_2Te_{2.88}Se_{0.06}$	158.1	163.5	572.9	583.3	39.9	41.6
	1.34	1.42	1.8	2.21	2.95	
$Bi_{1.99}Sn_{0.01}Te_{2.94}Se_{0.06}$	158.2	163.5	572.8	583.2	39.9	41.5
	1.32	1.30	1.89	1.46	3.11	
$Bi_2Te_{2.88}Se_{0.12}$	158.2	163.5	572.8	582.2	40.4	41.7
	1.34	1.32	1.3	1.42	2.88	
$Bi_{1.99}Sn_{0.01}Te_{2.88}Se_{0.12}$	158.2	163.5	572.9	582.2	40.4	41.7
	1.38	1.42	1.49	1.63	3.03	

Note: FWHM stands for the full width at half-maximum of a peak.

pared to stoichiometric composition, the bismuth telluride crystals grown from a stoichiometric melt have an excess of Bi; the composition of these crystals corresponds to 40.065 at. % Bi and 59.939 at. % Te, so that [Bi]/[Te] = 0.67.

Doping typically leads to compositional fluctuations; however, the uniformity in the distribution of main elements (Bi and Te) becomes higher (see Tables 1, 2) after the introduction of Sn in an amount corresponding to $y = 0.01$ (the $Bi_{1.99}Sn_{0.01}Te_{2.94}Se_{0.06}$ and $Bi_{1.99}Sn_{0.01}Te_{2.88}Se_{0.12}$ solid solutions). Deviations from the mean values of the atomic fractions of main elements are much less in $Bi_{1.99}Sn_{0.01}Te_{2.88}Se_{0.12}$ than in $Bi_2Te_{2.88}Se_{0.12}$; in the former compound, these deviations amount to 0.30 at. % for Bi and 0.35 at. % for Te, compared with 0.42 at. % for Bi and 0.49 at. % for Te in the latter compound. In $Bi_2Te_{2.94}Se_{0.06}$, a large spread in atomic fractions is observed (0.36 at. % for Te and 14 at. % for Bi, compared with 0.17 at. % for Te and 0.16 at. % in $Bi_{1.99}Sn_{0.01}Te_{2.94}Se_{0.06}$). Thus, the Sn doping impurity not only does not give rise to significant nonuniformity in the distribution of elements but also reduces the compositional fluctuations in main elements. In this context, we may expect that the distribution of the charge-carrier concentration is more uniform and that the thermoelectric power is higher in tin-doped compounds.

The results of XPS studies of $Bi_2Te_{2.94}Se_{0.06}$, $Bi_2Te_{2.88}Se_{0.12}$, $Bi_{1.99}Sn_{0.01}Te_{2.94}Se_{0.06}$, and $Bi_{1.99}Sn_{0.01}Te_{2.88}Se_{0.12}$ single crystals are shown in Fig. 1 and listed in Table 3. We ascertained from an analysis of the XPS spectra obtained both for the freshly cleaved surface and after slight etching with argon ions that, without exception, the chemical composition of all crystals changed as a result of ion etching; the surface became enriched with bismuth.

The spectra of the Bi 4*f* core states in the single crystals under consideration are represented by narrow peaks and correspond to virtually the same binding energies (see Table 3). A comparison of the Te spectra in crystals either doped or undoped with Sn shows that the Te $3d_{5/2}$ spectra are broadened by 0.1–0.2 eV in the $Bi_{1.99}Sn_{0.01}Te_{2.94}Se_{0.06}$ and $Bi_{1.99}Sn_{0.01}Te_{2.88}Se_{0.12}$ crystals. Broadening of the spectra indicates that the surroundings of the Te ions are somewhat disordered after the introduction of Sn atoms.

We do not observe any significant shifts in the Te 3*d* and Bi 4*f* core levels after introducing Sn atoms; the Se levels are represented by a broad peak, which is poorly discernible against the background, and are located in the binding-energy range of 56.0 to 59.0 eV (see Fig. 1).

The spectrum of the Te 4*d* level contains overlapping peaks; we used double differentiation in order to determine the exact positions of these peaks. As follows from the results of decomposition, a shift of the Te $4d_{5/2}$ level to higher binding energies is observed in the solid-solution single crystals that have an increased content of Se and are either undoped or doped with Sn. Simultaneously, the energy spacing between the Te $4d_{5/2}$ and Te $4d_{3/2}$ levels increases by 0.5 eV; this spacing corresponds to spin–orbit splitting. Substitution of Te atoms for Se atoms (with sizes smaller than those of the host-crystal atoms) leads to a decrease in the interatomic spacing and, as a consequence, to stronger interatomic interaction and an increase in overlap of electron regions. It can be seen from the analysis of the spectra shown in Fig. 1 that the electronic density of the Te 4*d* levels changes; the intensity of bands corresponding to these levels decreases with respect to the intensity of the Te 3*d* band as the amount of Se introduced into the crystal increases and in the case of doping with Sn impurity. The ratio between the intensities of the bands corresponding to the Te 3*d* and Te 4*d* levels (Te 3*d*/Te 4*d*) is equal to 5.8, 7.8, 6.6, and 7.9 for the $Bi_2Te_{2.94}Se_{0.06}$, $Bi_2Te_{2.88}Se_{0.12}$, $Bi_{1.99}Sn_{0.01}Te_{2.94}Se_{0.06}$, and $Bi_{1.99}Sn_{0.01}Te_{2.88}Se_{0.12}$ crystals, respectively. The above data indicate that Se atoms exert the most pronounced effect on the electron density. The effect of Sn atoms in single crystals with an increased Se concentration is less profound. Simultaneously, a redistribution of the density of states in the energy range corresponding to the Te $4d_{5/2}$ and Te $4d_{3/2}$ states is also observed. Introduction of Sn atoms into the solid solutions brings about an increase in the relative intensity of the peak related to the Te $4d_{5/2}$ level. A change in the density of states was not observed with increasing Se content. Unfortunately, we failed to detect possible changes in the electron densities and energy positions of the Se 3*d* and Sn 3*d* levels because broad low-intensity peaks (just above the background for Se) are observed owing to the low concentration of Se and Sn impurities; in addition, only a slight increase in the background is observed in the region of the Sn 3*d* energy. This circumstance makes reliable interpretation difficult.

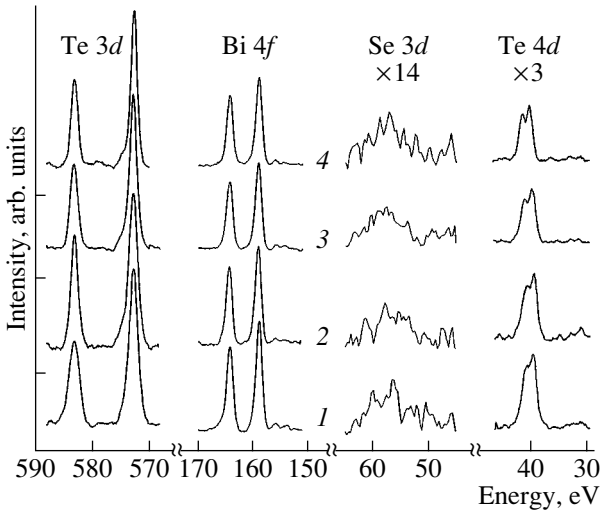

Fig. 1. X-ray Te 3*d*, Bi 4*f*, Se 3*d*, and Te 4*d* photoelectron spectra for (*1*) $Bi_2Te_{2.94}Se_{0.06}$, (*2*) $Bi_{1.99}Sn_{0.01}Te_{2.94}Se_{0.06}$, (*3*) $Bi_{1.99}Sn_{0.01}Te_{2.88}Se_{0.12}$, and (*4*) $Bi_2Te_{2.88}Se_{0.12}$ single crystals.

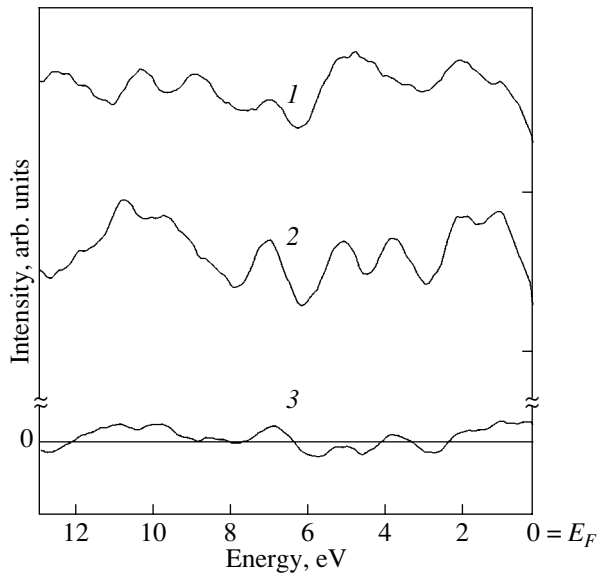

Fig. 2. Spectra of the valence band in (*1*) $Bi_2Te_{2.94}Se_{0.06}$ and (*2*) $Bi_2Sn_{0.01}Te_{2.94}Se_{0.06}$; curve *3* corresponds to the difference spectrum for the valence bands of $Bi_2Sn_{0.01}Te_{2.94}Se_{0.06}$ and $Bi_2Te_{2.94}Se_{0.06}$. The difference spectrum was normalized using the Bi 6*s* peak.

The main contribution to the formation of the valence-band top in the $Bi_2Te_{3-x}Se_x$ compounds is made by 6*p* states of Bi, 5*p* states of Te, and 4*p* states of Se (Fig. 2). These states are represented by a broad band with two poorly pronounced peaks and are located below the Fermi level (E_F) in the energy range up to about 6 eV. The first peak ($6p_{3/2}$Bi + $5p_{3/2}$Te + $4p_{3/2}$Se) in $Bi_2Te_{2.94}Se_{0.06}$ is located at about 2.5 eV and features a shoulder in the region of 1.4 eV; the XPS intensity at this shoulder amounts to 0.86 fraction of the peak intensity. The second (diffuse) peak ($6p_{1/2}$Bi + $5p_{1/2}$Te + $4p_{1/2}$Se) has the highest intensity in the valence band and is located ~5.1 eV lower than E_F. The ratio between the intensities of the first and second peaks is equal to 0.95. The 5*p* states of Sn are also involved in the formation of the valence-band top in the crystals doped with Sn. In these crystals, a redistribution of the density of states is observed. For example, the intensity of the shoulder region in the first peak increases significantly and the peak itself shifts closer to the Fermi level (the new position of the peak is equal to 1.1 eV; see Fig. 2, curve *2*). As a result, the ratio of the shoulder and peak intensities becomes equal to 1.07 instead of 0.86. The ratio between the intensities of the first and second peaks also changes to 1.4, so that the first peak now has a higher intensity. In this situation, the second peak is located at an energy of about 4.0 eV and the width of this peak decreases compared to that of the sample which was not doped with Sn. Similar changes for the $Bi_2Te_{2.88}Se_{0.12}$ and $Bi_{1.99}Sn_{0.01}Te_{2.88}Se_{0.12}$ crystals are also clearly seen. Specifically, the intensity of the second peak is approximately equal to and lower than the intensity of the first peak before and after doping with Sn, respectively; in addition, the ratio between the intensities of the first and second peaks is consistent with the value obtained for the samples with a lower Sn content and is equal to 1.6. The valence-band bottom in the compounds under consideration is predominantly formed of 5*s* Te, 6*s* Bi, and 4*s* Se states distributed in the energy range from 9 to 11 eV. The 5*s* states of Sn also contribute to the distribution of atomic states in compounds doped with Sn. The shape of the distribution of the electronic density of all of the atoms over the valence band in the single crystals doped with tin is illustrated by the difference spectrum shown in Fig. 2 (curve *3*). An increase in the electronic density in the vicinity of the Fermi level is observed up to an energy of about 2 eV; in the region of the second peak and in the middle of the valence band, the density of states is somewhat lower than the corresponding density in the crystals without Sn impurity. In addition, a higher intensity of the spectra in the region corresponding to localization of the 5*s* states of Te and 4*s* states of Se (~10–11 eV) indicates that there is a higher density of these states in the $Bi_{1.99}Sn_{0.01}Te_{2.94}Se_{0.06}$ and $Bi_{1.99}Sn_{0.01}Te_{2.88}Se_{0.12}$ crystals. An increase in the electronic density in the vicinity of the Fermi level was observed by Gasenkova *et al.* [1] when bismuth telluride crystals were doped with tin; in this context, we may assume that there also exist resonance states of Sn in the energy-band structure of solid solutions based on Bi_2Te_3 and that these states affect the electrical properties of the solid solutions under consideration. The behavior of kinetic coefficients in the $Bi_{1.99}Sn_{0.01}Te_{2.94}Se_{0.06}$ and $Bi_{1.99}Sn_{0.01}Te_{2.88}Se_{0.12}$ crystals is expected to be similar to that in Bi_2Te_3:Sn crystals.

4. CONCLUSIONS

Introducing 1 at. % of tin into solid solutions based on bismuth telluride improves the uniformity of the bismuth and tellurium distributions, which manifests itself in a decrease in the deviation of the content of these elements from the mean value, and leads to an increase in the content of bismuth in the solid solution. It is ascertained that the electronic density of 4*d* Te levels is redistributed in the valence band as Se impurity is introduced into crystals. An increase in the density of states in the vicinity of the Fermi level can be caused by the states of tin impurity.

REFERENCES

1. I. V. Gasenkova, M. K. Zhitinskaya, S. A. Nemov, and T. E. Svechnikova, Fiz. Tverd. Tela (St. Petersburg) **41**, 1969 (1999) [Phys. Solid State **41**, 1805 (1999)].
2. M. K. Zhitinskaya, S. A. Nemov, and T. E. Svechnikova, Fiz. Tverd. Tela (St. Petersburg) **40**, 1428 (1998) [Phys. Solid State **40**, 1297 (1998)].
3. V. A. Kulbachinski, V. Inoue, V. Sasaki, *et al.*, Phys. Rev. B **50**, 16921 (1994).
4. G. T. Alekseeva, P. P. Konstantinov, V. A. Kutasov, *et al.*, Fiz. Tverd. Tela (St. Petersburg) **38**, 2998 (1996) [Phys. Solid State **38**, 1639 (1996)].
5. T. E. Svechnikova, S. N. Chizhevskaya, N. M. Maksimova, *et al.*, Neorg. Mater. **30** (2), 168 (1994).
6. B. M. Gol'tsman, V. A. Kudinov, and I. A. Smirnov, *Semiconducting Thermoelectric Materials Based on Bi_2Te_3* (Nauka, Moscow, 1972).

Translated by A. Spitsyn

Semiconductors, Vol. 37, No. 6, 2003, pp. 641–645. Translated from Fizika i Tekhnika Poluprovodnikov, Vol. 37, No. 6, 2003, pp. 666–670.

ELECTRONIC AND OPTICAL PROPERTIES OF SEMICONDUCTORS

Photovoltaic Effects in CdV_2S_4 Single Crystals and Structures Based on Them

A. A. Vaĭpolin*, Yu. A. Nikolaev*, I. K. Polushina*, V. Yu. Rud', Yu. V. Rud'*, E. I. Terukov*, and N. Fernelius*****

**Ioffe Physicotechnical Institute, Russian Academy of Sciences, St. Petersburg, 194021 Russia*
e-mail: yuryrud@mail.ioffe.ru
***St. Petersburg State Polytechnic University, St. Petersburg, 195251 Russia*
****Wright Air Force Laboratory, Patterson Wright Air Force Base, OH, USA*
Submitted December 2, 2002; accepted for publication December 3, 2002

Abstract—Single crystals of the CdV_2S_4 ternary compound are grown, and their crystal structure, electrical properties, and optical absorption are studied. The substitution of vanadium for Group III element in $A^{II}B_2^{III}C_4^{VI}$ compounds results in the formation of crystals of *n*-type conduction with an electron density of ~10^{18} cm^{-3} and a Hall mobility $U_n \approx 150$ $cm^2/(V\,s)$ at $T = 300$ K, which is limited by scattering on lattice vibrations. Rectifying photosensitive structures based on CdV_2S_4 single crystals are fabricated for the first time, their photoelectric properties are studied, and a conclusion is made on their applicability in the design of wide-spectral-range photodetectors of unpolarized light. © *2003 MAIK "Nauka/Interperiodica".*

Ternary semiconductor compounds and their binary analogues make the adjustment of fundamental properties in diamond-like semiconductors possible by varying, within the same period, the types of atoms constituting these materials [1]. It has been established for several position-ordered semiconductors that the inclusion of elements from other periods allows control of material properties in an even wider range [2–4]. For example, the substitution of Group VIII for Group II atoms in $A^{II}B_2^{III}C_4^{VI}$ compounds opens the way for the fabrication of a new class of magnetic semiconductors [2–4]. The present communication presents the results obtained in studying the substitution of Group VIII for Group III atoms in $A^{II}B_2^{III}C_4^{VI}$ compounds using vanadium atom substitution for Ga as an example. CdV_2S_4 single crystals and two types of photosensitive structures were fabricated, several of the optoelectronic parameters of the compound were determined for the first time, and the prospects of applying the material in semiconductor electronics were considered.

Single-crystal CdV_2S_4 was crystallized from nonstoichiometric melts [5]. According to X-ray diffraction data, the single crystals have a face-centered cubic lattice with a lattice constant $a = 5.6577 \pm 0.0005$ Å at $T = 300$ K. Usually, these single crystals are prisms or needles elongated in the [112] crystal direction and bounded by two (111) and two (110) native mirror faceting planes. It is necessary to stress that such a faceting does not correspond to the point symmetry group of this crystal, $F43m$. The average size of the obtained single crystals was ~(6–12) × (0.4–0.6) × (0.08–0.155) mm^3. The maximum growth rate for these crystals was observed along the [112] axis, as they are elongated in this direction and often shaped as pointed needles. The minimum growth rate corresponds to the [111] direction. CdV_2S_4 crystals are opaque in transmitted white light and show metallic luster and light-gray coloration in reflected light. The sign of the thermoelectric power at $T = 300$ K shows that the crystals have *n*-type conduction. The Hall coefficient R and conductivity σ were measured using fragments of single crystals shaped as rectangular parallelepipeds with native faceting, ~$0.15 \times 0.5 \times 4$ mm in size. Point contacts of silver wire were fabricated in the necessary configuration by welding-in an electric discharge under a microscope [6]. In this manner, a sample was provided with four potential and two current probes. The contacts were ohmic and neutral with respect to illumination. The conductivity and Hall coefficient were measured in weak electrical and magnetic fields.

Figure 1 shows typical temperature dependences of the kinetic coefficients σ and R in the temperature range of 140–300 K. As seen in curves *1* and *2*, CdV_2S_4 crystals have considerable room-temperature conductivity, $\sigma \approx 50$–60 Ω^{-1} cm^{-1}, which increases steadily as the temperature decreases. The Hall coefficient demonstrates a similar temperature dependence; it increases from 6–7 to 8.5–9 cm^3/C as the temperature decreases from 300 to 140 K. The calculated density of free electrons in our single crystals is ~10^{18} cm^3 at $T = 300$ K. A slight increase in the kinetic coefficients σ and R with decreasing temperature suggests the existence of rather shallow levels that have not yet been observed in

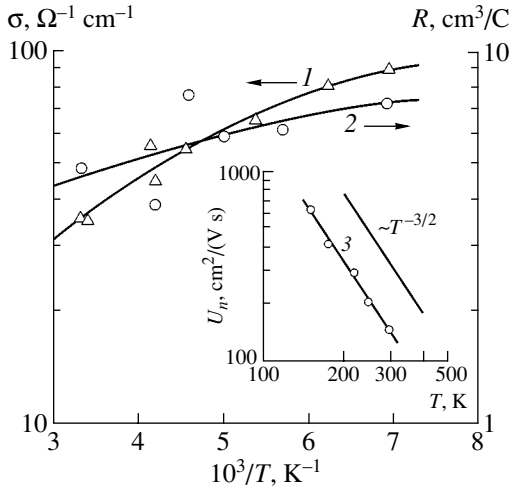

Fig. 1. Temperature dependences of (*1*) conductivity, (*2*) Hall coefficient, and (*3*) Hall mobility of electrons in CdV_2S_4 single crystal.

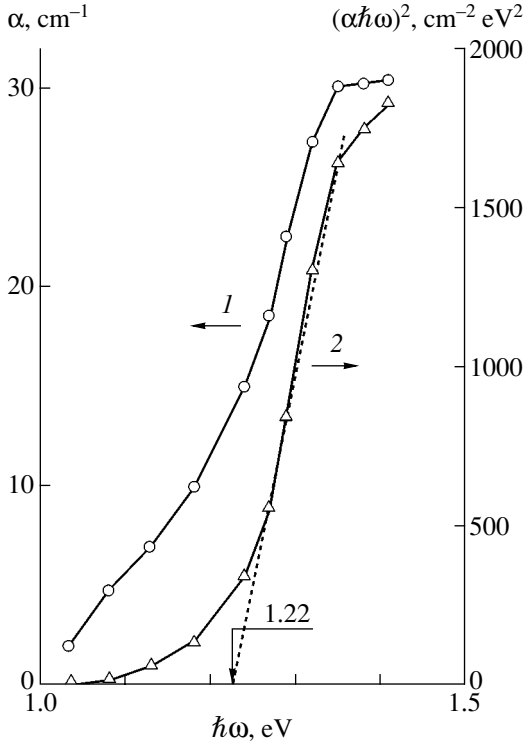

Fig. 2. The optical absorption spectrum of CdV_2S_4 single crystal at T = 300 K in the coordinates (*1*) α–$\hbar\omega$ and (*2*) $(\alpha\hbar\omega)^2$–$\hbar\omega$.

$A^{II}B_2^{III}C_4^{VI}$ compounds [7]. Thus, the replacement of Group III atoms (Cd, Zn) with vanadium induces a drastic increase in conductivity by 10–12 orders of magnitude, e.g., with respect to CdV_2S_4–$CdGa_2S_4$ [7], an analogue of CdV_2S_4. We believe that the introduction of vanadium-type atoms into $A^{II}B_2^{III}C_4^{VI}$ compounds can resolve the problem of doping for these materials [7]. Other important specific electrical properties of CdV_2S_4 single crystals are as follows:

(i) rather high Hall mobility of electrons at T = 300 K, $U_n \approx 150$ cm^2/(V s) at T = 300 K, and high electron density $n \approx 10^{18}$ cm^{-3};

(ii) increasing Hall mobility with decreasing temperature $T < 300$ K by the law $U_n \propto T^{-3/2}$, which leads to the conclusion that electron scattering by the lattice vibrations is predominant [8].

As seen in Fig. 1 (curve *3*), the Hall mobility of electrons increases to $\mu_n \approx 620$ cm^2/(V s) at T = 140 K, which indicates that CdV_2S_4 single crystals of higher perfection can, in principle, be obtained. The extrapolation of the obtained dependence to the liquid nitrogen temperature shows that $U_n \approx 2300$ cm^2/(V s) can be obtained in this ternary compound at T = 77 K if the lattice mechanism of mobility is retained. Thus, ternary compounds of the new class $A^{II}B_2^{III}C_4^{VI}$ are semiconductors and can be obtained with a rather high electron mobility (for compound semiconductors). It is necessary to note that crystals with a considerable electron mobility have still not been obtained in the ternary analogues of CdV_2S_4, i.e., the long-explored $A^{II}B_2^{III}C_4^{VI}$ compounds [4, 7], and the problem of the scattering mechanisms in these compounds has not yet been analyzed.

The optical transmission T_0 at T = 300 K was measured in very small CdV_2S_4 single crystals using absorption spectroscopy, and the absorption coefficient was calculated using the relation [9]

$$\alpha = \frac{1}{d}\ln\left\{\frac{(1-R_0)^2}{2T_0} + \sqrt{\left[\frac{(1-R_0)^2}{2T_0}\right]^2 + R_0^2}\right\}, \qquad (1)$$

where the reflectance $R_0 \approx 0.3$. Figure 2 (curve *1*) shows a typical $\alpha(\hbar\omega)$ spectrum for a CdV_2S_4 single crystal. As seen, a substantial rise in α is observed at $\hbar\omega > 1$ eV. At the photon energies above 1.24 eV this rise becomes steeper and ceases near $\hbar\omega \approx 1.34$ eV. A linear portion in the α spectrum can be selected in the coordinates $(\alpha\hbar\omega)^2$–$\hbar\omega$ (Fig. 2, curve *2*), and its extrapolation $(\alpha\hbar\omega)^2 \longrightarrow 0$ yields a band gap $E_g' \approx 1.22$ eV at T = 300 K. Taking into account the low optical absorption near E_g' ($\alpha \approx 30$ cm^{-1}), the observed band-to-band transitions can be classified as pseudo-direct by analogy with $A^{II}B^{IV}C_2^{V}$ compounds [10, 11]. It is evident, however, that, to make a final conclusion about the nature of the absorption edge in CdV_2S_4, it is necessary to pass to the range of strong optical absorption ($\alpha > 10^3$ cm^{-1}), which could not be done by conventional absorption spectroscopy with the given sample dimensions.

To apply photoelectric spectroscopy to the study of our crystals, we attempted to fabricate photosensitive structures based on *n*-CdV_2S_4 single crystals. For this

Photoelectric properties of structures based on single-crystal *n*-CdV_2S_4 at $T = 300$ K

Structure type	K	U_0, V	R_0, Ω	n	S_U^m, V W^{-1}	$\Delta\hbar\omega$, eV
In/*n*-CdV_2S_4	50	0.6	330	~1.9	50	2.7–3.3
H_2O/*n*-CdV_2S_4	20		~10^5		10	2.9–3.4

Note: K and n are, respectively, the rectification and ideality factors of the *I–V* characteristic.

purpose, we have tested the contacts between the crystals under study and metals or liquid electrolytes. The study of contacts between metals (In, Cu, Mo, Au) and the [111] plane of CdV_2S_4 single crystals led to the conclusion that thin ($d \approx 0.1$ mm) indium films deposited by vacuum evaporation exhibit definite rectification. Figure 3 shows a typical current–voltage (*I–V*) characteristic of an In/*n*-CdV_2S_4 structure. The average size of CdV_2S_4 crystals was ~$0.5 \times 0.5 \times 0.1$ mm^3. Rectification by a factor of ~50 at $|U| \approx 0.7$ V bias was obtained in the best structures (see table), with the forward bias always corresponding to positive voltage applied to the barrier contact. At $U > 0.8$ V, the *I–V* characteristics follow the relation

$$I = \frac{U - U_0}{R_0}, \tag{2}$$

where $U_0 \approx 0.6$ V is the cutoff voltage, and the residual resistance of the obtained In/CdV_2S_4 structures at $T = 300$ K $R_0 \approx 330$–350 Ω. In the coordinates $\log I$–U (Fig. 3, curve *2*), the forward *I–V* curve at $U_0 \leq 0.3$ V follows the exponential law

$$I_f = I_0 \exp\left(\frac{eU}{nkT} - 1\right) \tag{3}$$

with the nonideality factor $n \approx 1.7$–1.9, which implies a recombination character of the forward current [12] in our In/CdV_2S_4 structures. The reverse current increases gradually with increasing bias following the power law $I \propto U^\gamma$, with $\gamma = 1$ at $U < 0.35$ V, whereas at $U > 0.7$ V the current steeply increases and $\gamma \approx 10$, thus indicating the onset of a "soft" breakdown.

Similarly to [13], photoelectrochemical cells (PECC) were fabricated using CdV_2S_4 single crystals. Rectification by a factor $K \approx 20$ was observed at the voltage $|U| \approx 10$ V in H_2O/CdV_2S_4 PECC, with the R_0 values considerably higher than those for the solid-state In/CdV_2S_4 structures (see table). Such high values of R_0 are typical of PECC in general [13]; they are determined mainly by the electrolyte conductance. As a rule, the forward bias in H_2O/CdV_2S_4 PECCs corresponds to a negative voltage applied to CdV_2S_4 crystal.

Under exposure to unpolarized light, both structure types demonstrate the photovoltaic effect. The photovoltage sign in In/CdV_2S_4 and H_2O/CdV_2S_4 structures is the same, irrespective of the geometric characteristics of structure illumination and the photon energy. The negative photovoltage corresponds to CdV_2S_4 crystal, which correlates with the sign of rectification in our structures. The maximum voltage responsiveness is usually observed under illumination from the side of the barrier contact (In or H_2O), reaching $S_U^m = 50$ V/W at $T = 300$ K in In/CdV_2S_4 structures (see table). The absence of clearly pronounced degradation of photosensitivity in the obtained structures should be noted.

Figure 4 shows typical spectra of the relative quantum efficiency of photoconversion, $\eta(\hbar\omega)$, in In/CdV_2S_4 and H_2O/CdV_2S_4 structures. As is seen, the photosensitivity is observed in a wide spectral range in both structure types and the spectral profiles of $\eta(\hbar\omega)$ are similar for the structures of different nature. In all studied structures, the rise in photosensitivity begins at the photon energies $\hbar\omega \gtrsim 0.8$ eV and its maximum value is observed in the range $\Delta\hbar\omega$ between 2.7 and 3.4 eV, with no sharp short-wavelength falloff observed. Therefore, an estimate of the FWHM, $\delta \geq$

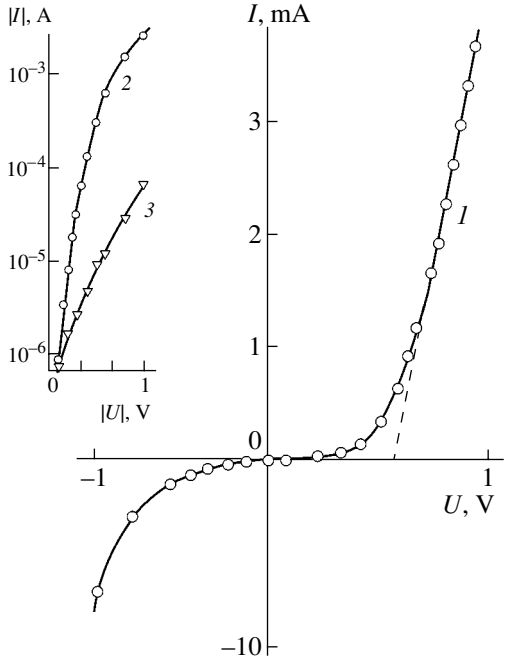

Fig. 3. *I–V* characteristic of In/*n*-CdV_2S_4 structure at $T = 300$K in the coordinates (*1*) *I–U* and $\log I$–U in the insert: (*2*) forward and (*3*) reverse curves. The forward bias corresponds to a negative voltage applied to CdV_2S_4 crystal.

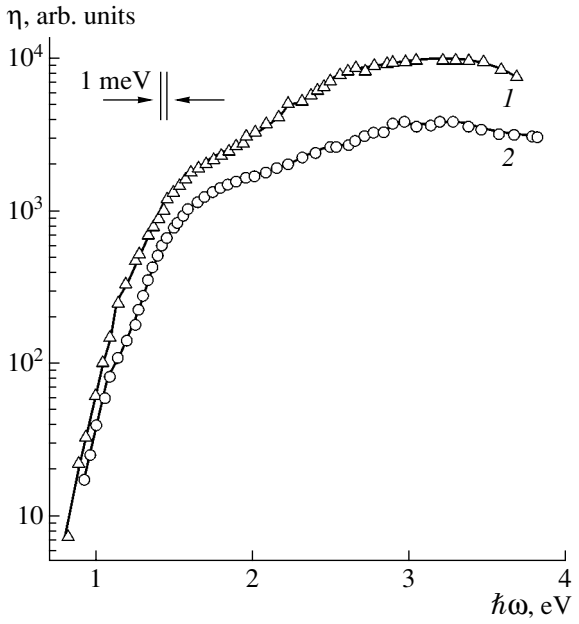

Fig. 4. Spectra of the relative quantum efficiency of photoconversion of structures based on *n*-CdV_2S_4 single crystals at T = 300 K [(*1*) In/CdV_2S_4 and (*2*) H_2O/CdV_2S_4]. The spectral resolution is no worse than 1 meV. Illumination from the side of the barrier contacts.

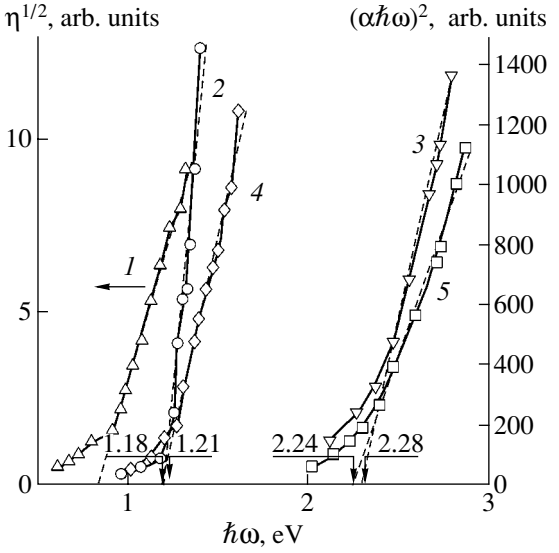

Fig. 5. Spectra of the relative quantum efficiency of photoconversion of structures based on *n*-CdV_2S_4 single crystals at T = 300 K in the coordinates (*1*) $\eta^{1/2}$–$\hbar\omega$ and (*2–5*) $(\alpha\hbar\omega)^2$–$\hbar\omega$. The structures under study: (*1–3*) In/CdV_2S_4 and (*4*, *5*) H_2O/CdV_2S_{44}. Unpolarized illumination from the side of the barrier contact.

2 eV, can be used as a quantitative characteristic of the broadness of $\eta(\hbar\omega)$ spectra. This suggests a rather high efficiency of the collection of photogenerated pairs in the structures based on CdV_2S_4 single crystals.

Figure 5 shows several examples from an analysis of $\eta(\hbar\omega)$ spectra for typical structures. As follows from Fig. 5 (curve *1*), the long-wavelength portion of the photosensitivity spectra of the surface-barrier In/CdV_2S_4 structures is well described by the Fowler law [14], which suggests the emission of photogenerated carriers above the barrier. Extrapolating the linear portion of $\eta^{1/2} \longrightarrow 0$, we can estimate the height of the energy barrier in these structures as $\varphi_B \approx 0.6$–0.9 eV for different samples, which correlates with the cutoff voltage U_0 in *I–V* characteristics (Fig. 3). The long-wavelength rise in the photoconversion efficiency is described by the law

$$\eta\hbar\omega = A(E_g - \hbar\omega)^{1/2}, \qquad (4)$$

which, according to [15], gives reason to consider that the transitions are direct and allows determining $E_g' \approx$ 1.18–1.21 eV for different structures by extrapolation $(\eta\hbar\omega)^2 \longrightarrow 0$ (curves *2* and *4* in Fig. 5). It is necessary to stress that this analysis correlates well with a similar analysis of the $\alpha(\hbar\omega)$ spectra of single crystals used in the fabrication of photosensitive structures (Fig. 2).

It also follows from Fig. 5 that the linear portion of the $(\eta\hbar\omega)^2$–$\hbar\omega$ dependence for both barrier types also exists in the short-wavelength spectral range of photosensitivity and its extrapolation $(\eta\hbar\omega)^2 \longrightarrow 0$ yields $E_g \approx 2.22$–2.28 eV. This energy of band-to-band transitions lies in the range of high optical absorption; thus, it can be related to direct band-to-band transitions in CdV_2S_4. It is necessary to stress that E_g' and E_g are virtually independent of the types of energy barriers produced on the same semiconductor compound. This fact serves as an additional indication that the obtained E_g' and E_g values are fundamental parameters of CdV_2S_4 single crystals.

Thus, our study has shown that the ternary compound CdV_2S_4 is a promising semiconductor material in the design of unpolarized-light photodetectors for the spectral range from IR to UV.

ACKNOWLEDGMENTS

This study was supported by ISTC (International Science & Technology Center) (grant no. 2008).

REFERENCES

1. N. A. Goryunova, *Compound Diamond-Like Semiconductors* (Sovetskoe Radio, Moscow, 1968).
2. M. Eibshuts, H. Herman, and S. Shtrikman, Solid State Commun. **5**, 529 (1967).
3. T. Kanomatra, H. Ido, and T. Kaneko, J. Phys. Soc. Jpn. **34**, 564 (1973).
4. R. N. Bekimbetov, N. N. Konstantinova, Yu. V. Rud', and M. A. Tairov, Izv. Akad. Nauk SSSR, Neorg. Mater. **24**, 1969 (1988).

5. V. D. Prochukhan and Yu. V. Rud', Fiz. Tekh. Poluprovodn. (Leningrad) **12**, 208 (1978) [Sov. Phys. Semicond. **12**, 121 (1978)].
6. N. A. Goryunova, F. P. Kesamanly, D. N. Nasledov, *et al.*, Dokl. Akad. Nauk SSSR **160**, 633 (1965).
7. A. N. Georgobiani, S. N. Radautsan, and I. M. Tiginyagu, Fiz. Tekh. Poluprovodn. (Leningrad) **19**, 193 (1985) [Sov. Phys. Semicond. **19**, 121 (1985)].
8. F. J. Blatt, *Theory of Mobility of Electrons in Solids* (Academic, New York, 1957); Solid State Phys. **4**, 1999 (1957).
9. H. Y. Fan and M. O. Becker, in *Proceedings of Conference on Semiconducting Materials* (Academic, New York, 1951), p. 132.
10. Yu. A. Valov, A. A. Lebedev, K. Ovezov, *et al.*, Pis'ma Zh. Tekh. Fiz. **2**, 1042 (1976) [Sov. Tech. Phys. Lett. **2**, 410 (1976)].
11. A. Yu. Shileĭka, in *Multivalley Semiconductors*, Ed. by Yu. K. Pozhela (Mokslas, Vilnius, 1978), p. 143.
12. S. M. Sze, *Physics of Semiconductor Devices* (Wiley, New York, 1969; Mir, Moscow, 1973).
13. Yu. V. Rud' and M. A. Tairov, Fiz. Tekh. Poluprovodn. (Leningrad) **21**, 615 (1987) [Sov. Phys. Semicond. **21**, 377 (1987)].
14. J. I. Pankove, *Optical Processes in Semiconductors* (Prentice Hall, Englewood Cliffs, N.J., 1971; Mir, Moscow, 1973).
15. Yu. I. Ukhanov, *Optical Properties of Semiconductors* (Nauka, Moscow, 1977).

Translated by D. Mashovets

Semiconductors, Vol. 37, No. 6, 2003, pp. 646–648. Translated from Fizika i Tekhnika Poluprovodnikov, Vol. 37, No. 6, 2003, pp. 671–673.

ELECTRONIC AND OPTICAL PROPERTIES OF SEMICONDUCTORS

Electrical Properties of Cadmium Telluride Films Synthesized in a Thermal Field with a Temperature Gradient

A. P. Belyaev, V. P. Rubets, and M. Yu. Nuzhdin

St. Petersburg Institute of Technology, Zagorodnyi pr. 49, St. Petersburg, 198013 Russia

e-mail: belyaev@tu.spb.ru

Submitted November 10, 2002; accepted for publication December 4, 2002

Abstract—The correlation between the electrical properties of CdTe films synthesized in a thermal field with a temperature gradient and their crystal structure, the ambient pressure, and the film thickness was investigated. Films of different structure, from polycrystalline to block, were studied. The conductivity of the films increases with improving their crystal structure, increasing the ambient pressure, and decreasing the film thickness. The experimental results can be satisfactorily explained in the context of a model of an inhomogeneous semiconductor with intercrystalline barriers. *© 2003 MAIK "Nauka/Interperiodica".*

1. INTRODUCTION

The electrical properties of films strongly depend on the method and conditions of their synthesis. Cadmium telluride films are no exception. The specific features of their synthesis and structure were discussed in [1, 2]. In this connection and in view of the special interest in applying such films in optoelectronics and microelectronics, in this article, we present the results of studies of electrical properties of CdTe films synthesized in a thermal field with a temperature gradient.

2. EXPERIMENTAL

All samples under study were synthesized on muscovite mica substrates in a thermal field with a temperature gradient using the method described in [2]. Depending on the synthesis conditions, the crystal structure of the films varied from polycrystalline to epitaxial. The films consisted of separate blocks (crystallites) of columnar form, whose sizes and mutual orientation determined the quantity of the crystal structure of a specimen. The near-polycrystalline specimens consisted of crystallites with characteristic sizes of about 0.3 μm; the epitaxial films consisted of crystal blocks about 1.0 μm in size and misorientated by 2–15' with respect to each other.

According to the sign of the thermopower, the specimens had *n*-type conductivity.

The electrical properties were measured in planar geometry and current mode with the aid of a V7-30 electrometer. Indium contacts were used. The ohmic behavior of contacts was controlled by the initial parts of the current–voltage characteristics.

The structure was studied using an ÉMR-100 electron diffractometer and a PÉM-100 transmission electron microscope. The thickness of the films was measured by an MII-4 microinterferometer with an accuracy to ±0.03 μm.

3. RESULTS

Experiments included measurements of the resistivity of the films in planar geometry and studies of the effect of crystal structure, ambient pressure, and film thickness on film conductivity.

The conductivity of the films increased from $\sim 10^{-8}\ \Omega^{-1}\ \text{cm}^{-1}$ for near-polycrystalline films (Fig. 1a) to $\sim 10^{-7}\ \Omega^{-1}\ \text{cm}^{-1}$ for epitaxial films (Fig. 1d). The conductivity also depended on the ambient atmosphere. In vacuum with a residual pressure of $\sim 10^{-3}$ Pa, the conductivity decreased by approximately an order of magnitude in comparison with the magnitudes given above.

The conductivity of specimens depended on their thickness. The results shown in Fig. 1 correspond to a film thickness $d \approx 0.5$ μm. The influence of the film thickness on the conductivity was investigated in detail with polycrystalline specimens (Fig. 1a). The results are shown in Fig. 2. The increase in thickness lowered the conductivity from $\sim 2 \times 10^{-8}$ to $\sim 5 \times 10^{-9}\ \Omega^{-1}\ \text{cm}^{-1}$.

The attainment of the equilibrium magnitude of conductivity in all specimens was associated with long-time relaxation. The characteristic relaxation time τ was as long as ~100 s.

The temperature dependence of conductivity obeyed a simple exponential law with an activation energy of ~(0.7–0.72) eV.

All samples exhibited weak photosensitivity. Under exposure to an incandescent 50 W lamp, the conductivity increased by no more than a factor of 2.

1063-7826/03/3706-0646$24.00

4. DISCUSSION

As a rule, condensed films are considered as disordered systems [3]. The experimental data indicate that cadmium telluride films synthesized in a thermal field with a temperature gradient are no exception. The low conductivity ($\sigma \approx 10^{-8}\ \Omega^{-1}\ \mathrm{cm}^{-1}$), high activation energy of conductivity (~0.7 eV), long conductivity-relaxation times ($\tau \approx 100$ s), and a small increase in conductivity under exposure to light (low ratio of the photoconductivity to the total conductivity) unambiguously suggest that all CdTe films studied are inhomogeneous semiconductors [4–6].

Charge transport in inhomogeneous semiconductors proceeds through the percolation level, and the conductivity at relatively high temperatures is described by the expression

$$\sigma = \sigma_0 \exp(-E/kT), \qquad (1)$$

which is qualitatively in accordance with the obtained data for CdTe. The quantity E in (1) is the energy spacing to the percolation level measured from the Fermi level, σ_0 is the pre-exponential factor, k is the Boltzmann constant, and T is the absolute temperature.

The position of the percolation level depends on the nature and the amplitude of the random potential in a specimen. For a structure similar to that of the films under study, the random field is formed predominantly at the intercrystalline boundaries [6, 7]. Repeated verification showed that such boundaries in covalent crystals $A^{II}B^{VI}$ [8] act as acceptors. They accumulate negative charge at the surface states and thus create intercrystalline barriers. The averaged effect of the intercrystalline barriers on the conductivity is taken into account by the introduction of a percolation level which characterizes the lowest energy of charge carriers necessary for the motion of carriers through the sample along classical trajectories. The higher the intercrystalline barriers, the higher the energy of the percolation level and, consequently, the lower the concentration of charge carriers at this level.

The occurrence of charge transport through the percolation level in our specimens, among other things, is confirmed by the dependence of conductivity on the quality of the crystal structure (Fig. 1). A strong mutual disorientation of crystallites in films favors an increase in the height of intercrystalline barriers and lowers the conductivity.

The effect of ambient air on the conductivity of films also supports the concept of an inhomogeneous semiconductor. This follows from the fact that any single-phase film studied represents a quasiheterogeneous three-layer system. The first layer, a comparatively thin one, is a transition (damaged) layer. The second layer (obviously, the thickest one) is the bulk of the film. Its structural quality is a criterion for the quality of the structure of the entire film. The third layer is the surface layer. The properties of this layer are governed mainly by the atmosphere.

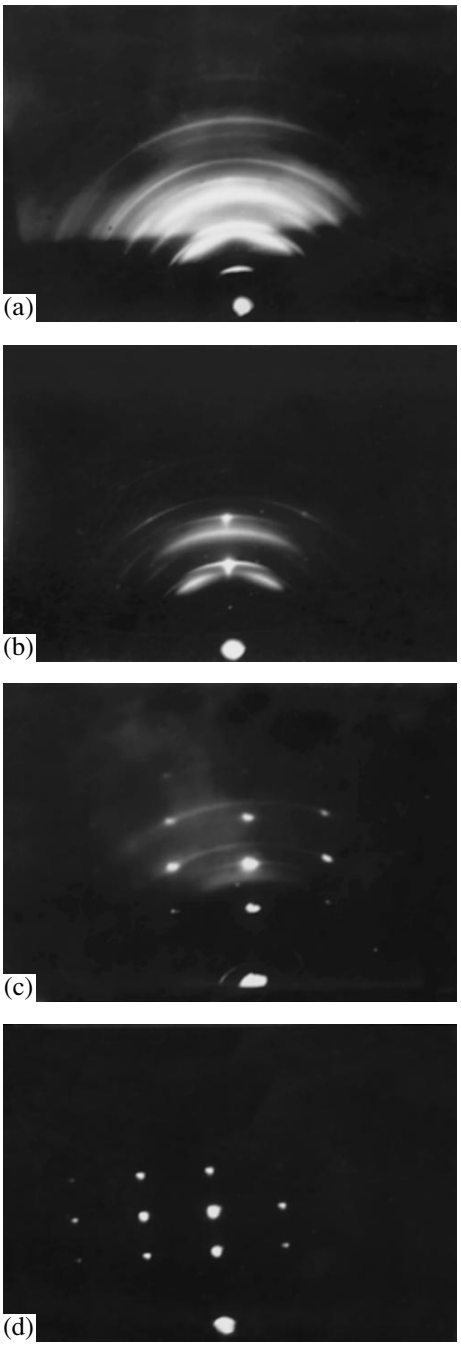

Fig. 1. Electron diffraction patterns of CdTe films synthesized in a thermal field with a temperature gradient and having the conductivity $\sigma \times 10^{-8}$ = (a) 1.2, (b) 1.4, (c) 2.0, and (d) 16 $\Omega^{-1}\ \mathrm{cm}^{-1}$.

Thus, the conductivity σ of the film can be represented as the sum

$$\sigma = \frac{1}{d}(d_1\sigma_1 + d_2\sigma_2 + d_3\sigma_3), \qquad (2)$$

where σ_i and d_i are the conductivity and the thickness of the ith layer, respectively. The conductivity σ_3 should

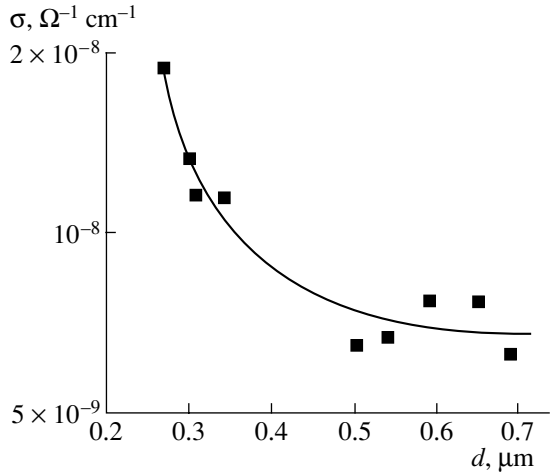

Fig. 2. Conductivity of CdTe films synthesized in a thermal field with a temperature gradient as a function of the film thickness.

decrease in air, since we know that oxygen, being adsorbed on the surface, also forms acceptor levels. However, multiply repeated experiments show [8] that prolonged contact with air may result in such a large amount of adsorbed oxygen that the inversion of the type of conductivity of the surface layer of a film becomes possible. Naturally, in this case, the conductivity of a surface layer, as well as the total conductivity of a specimen, will increase along with the increase in the amount of adsorbed oxygen. Such behavior correlates not only with the revealed effect of an ambient atmosphere but also with the influence of the thickness of a film on its conductivity (Fig. 2). The conductivity decreases with increasing the thickness due to a decrease in the contribution of $\sigma_3 d_3/\sigma d$ to the total conductivity of the low-resistivity surface layer (see formula (2)).

Experimentally revealed long-time relaxation of the conductivity in the context of the model of an inhomogeneous semiconductor with intercrystalline barriers is explained by inertia in attaining equilibrium between carriers separated by potential barriers [7]. The low ratio of the photoconductivity to the total conductivity is explained by a poor structural quality which reduces the lifetime of minority carriers.

5. CONCLUSION

Summarizing the results of this study, we can make the following conclusions.

(1) The conductivity of CdTe films synthesized in a thermal field with a temperature gradient depends on the crystal quality, as well as on the film thickness and the ambient atmosphere. The improvement of crystal quality, diminishing of the film thickness, and an increase in the atmospheric pressure favor an increase in the conductivity.

(2) The conductivity of CdTe films when there is charge transport in planar geometry can be satisfactorily explained by the model of an inhomogeneous semiconductor with intercrystalline barriers at the boundaries of blocks constituting the films.

ACKNOWLEDGMENTS

This study was supported by the Russian Foundation For Basic Research, project no. 02-03-32405.

REFERENCES

1. A. P. Belyaev, V. P. Rubets, M. Yu. Nuzhdin, and I. P. Kalinkin, Fiz. Tverd. Tela (St. Petersburg) **43**, 745 (2001) [Phys. Solid State **43**, 778 (2001)].
2. A. P. Belyaev, V. P. Rubets, M. Yu. Nuzhdin, and I. P. Kalinkin, Zh. Tekh. Fiz. **72** (4), 120 (2002) [Tech. Phys. **47**, 491 (2002)].
3. N. F. Mott and E. A. Davis, *Electronic Processes in Non-Crystalline Materials*, 2nd ed. (Clarendon Press, Oxford, 1979; Mir, Moscow, 1982).
4. V. I. Shklovskiĭ and A. L. Éfros, *Electronic Properties of Doped Semiconductors* (Nauka, Moscow, 1979; Springer, New York, 1984).
5. A. Ya. Shik, Zh. Éksp. Teor. Fiz. **71**, 1159 (1976) [Sov. Phys. JETP **44**, 606 (1976)].
6. A. P. Belyaev and I. P. Kalinkin, Thin Solid Films **158**, 25 (1988).
7. A. P. Belyaev, I. P. Kalinkin, and V. A. Sanitarov, Fiz. Tekh. Poluprovodn. (Leningrad) **18**, 1975 (1984) [Sov. Phys. Semicond. **18**, 1234 (1984)].
8. Yu. A. Ossipyan, V. F. Petrenko, and A. V. Zaretskii, Adv. Phys. **35**, 115 (1986).

Translated by A. Zalesskiĭ

Semiconductors, Vol. 37, No. 6, 2003, pp. 649–655. Translated from Fizika i Tekhnika Poluprovodnikov, Vol. 37, No. 6, 2003, pp. 674–680.

SEMICONDUCTORS STRUCTURES, INTERFACES, AND SURFACES

The Effects of Monovacancies on the Terrace Width during Sublimation from the (111) Surface of a Diamond-Like Crystal

A. V. Zverev, I. G. Neizvestny, N. L. Shvartz, and Z. Sh. Yanovitskaja

Institute of Semiconductor Physics, Siberian Division, Russian Academy of Sciences, pr. Akademika Lavrent'eva 13, Novosibirsk, 630090 Russia

e-mail: natasha@spy.isp.nsc.ru

Submitted September 26, 2002; accepted for publication October 4, 2002

Abstract—Using the three-dimensional Monte Carlo model, the effect of monovacancies on the diffusion exchange between the steps on the (111) surface of a diamond-like crystal during sublimation was investigated. The critical terrace width L_{cr} (the distance from the step edge to the nearest stable vacancy islands) was determined as a function of the relationship between the energy of adatom formation at the smooth terrace E_n and the energy of adatom desorption from the terrace E_d with retention of the sum of these energies $E_{sub} = E_n + E_d$, which characterizes the sublimation of a substance. A well-pronounced maximum exists in the dependences $L_{cr}(E_n)$ obtained. The formula is suggested which well describes the dependences $L_{cr}(E_n)$ for various values of E_{sub}. The extrapolation of the dependence $L_{cr}(E_n)$ to the value $E_{sub} = 4.2$ eV, which is characteristic of Si, permits us to compare the model results with the experimental data of other authors. The explanation of a threefold increase in the terrace width, which is observed experimentally at about 1500 K, is suggested. © *2003 MAIK "Nauka/Interperiodica".*

1. INTRODUCTION

Interest in the special features of diffusion and sublimation at atomically smooth Si surfaces is associated with the necessity of obtaining nanodimensional structures. Sublimation at the Si(111) and Si(001) surfaces has been investigated in detail [1–11]. It turns out that the activation energy of this process is nearly independent of the surface orientation and is equal to 4.2 ± 0.2 eV [3]. The issue concerning anomalously large terraces at the singular Si(111) surface has also been discussed [1, 2]. It is known that terrace sizes at singular Si(111) surfaces are an order of magnitude larger Zhan those of the Si(001) surface. Above 1420 K, vacancy islands are formed between parallel steps at the Si(001) surface; these islands grow over time [2, 3]. The sublimation rate increases sharply, since these islands act as an additional source of adatoms at the surface, along with the steps. No nucleation of vacancy islands is observed at the Si(111) surface at 1273–1537 K [2]. The nucleation of vacancy islands at the Si(111) surface was originally experimentally observed at the bottom of a specially prepared craterlike surface with deep walls in the temperature range of 1290–1595 K [4]. Due to high-temperature heating runs, circular steps one bilayer in height were formed at the bottom of the crater. Upon sublimation, the steps moved from the center to the outer edge of the crater, and the diameter of the lowest terrace at the crater bottom increased. When this diameter became equal the doubled critical width of the terrace, a vacancy island emerged at the center. The critical terrace width was determined from the distance between the steps at the crater bottom.

To date, there are no data on the experimental observation of adatom–monovacancy interaction at high temperatures at nonreconstructed Si surfaces due to insufficient temporal or spatial resolution of scanning electron microscopy. Only the observation of sufficiently large polyvacancy islands is possible [4–6]. Experimentally, the formation of polyvacancy islands using ultrahigh-vacuum reflection electron microscopy and atomic force microscopy was observed in the experiments with thermal etching of the Si(111) surface by oxygen [7]. However, the results of these experiments, which include more complex physicochemical processes occurring at the surface, could not be directly used for correlation with high-temperature sublimation.

It was assumed that an adatom's effective path length can increase due to its interaction with a monovacancy [8]. An analytical solution for the set of equations with allowance made for adatom–monovacancy interaction was derived for near-equilibrium conditions [8].

During the last decade, numerous experimental studies of sublimation at the Si(111) surface have been performed [1–6, 9–13]. However, in these studies, the specific features of surface vacancies, such as mobility, temperature dependence of concentration, and energy of formation, were not discussed. Such important parameters of the surface processes of Si as the energy of step tension, the energy of adatom formation at the terrace, and the energy of its desorption from the terrace were obtained from approximated estimations. The issue concerning the possible exchange of surface monovacancies with bulk vacancies, which are very mobile, is unclear [14]. The critical size of the polyva-

cancy island (this size should exist similarly to the critical size of an atomic island) was not determined [15]. All these questions about the Si(111) surface remain only partially understood. Recently, the diffusion of surface vacancies and the interaction of two monovacancies at the Ge(111) surface was investigated [16]. Using a series of metallic surfaces as an example, it was shown that the formation of an adatom–vacancy pair is energetically more favorable than the formation of a single vacancy [17]. It was noted [17] that the formation of surface vacancies differs considerably from the emergence of bulk vacancies.

In this study, using numerical simulation, the influence of a monovacancy on the width of stable terraces during sublimation at the (111) surface of a diamond-like crystal is investigated.

2. MODEL

In order to investigate the formation of vacancy islands during sublimation, we used a three-dimensional Monte Carlo model which allows simulation of the epitaxial growth and sublimation at the (111) surface of a diamond-like crystal [18].

Adatoms arrive at wide terraces from the steps. The diffusion and desorption of adatoms occurs with the activation energies E_{dif} and E_d. In the model, a monovacancy is equivalent to the absence of a single atom in the upper monolayer of the bilayer. The adatoms at the real (111) surface occupy bulk sites that differ from those in the model; however, this turns out to be unimportant if the energy of adatom formation and the energy of its desorption are specified independently. The structure of the (111)Si surface at high temperatures is somewhat more complex than in our model [19, 20]. However, the main processes during sublimation are accounted for in the model, and the concepts developed in [8] are applicable to the model.

It is believed that the sublimation from the (111) surface occurs in two stages: (i) the escape of an atom from the step onto the smooth terrace and (ii) subsequent evaporation. With the formation of a monovacancy, an additional adatom also emerges at the terrace. We assumed that the atom, that left the step is not necessary evaporated, but can arrive at the vacancy, temporarily decreasing the vacancy concentration at the surface. Since vacancies are formed at a constant rate at the surface, a newly formed vacancy will serve as the source of a new adatom. As the distance from the step increases, the adatom concentration decreases, whereas the vacancy concentration increases. Upon reaching a certain critical vacancy concentration, the formation of vacancy islands (polyvacancies) begins. Due to the concentration gradient, adatoms can pass relaylike over the terrace, which may led to a larger effective path length for adatoms.

Simulation was carried out under the assumption of additivity of interaction between atoms and their neighbors. In this case, the relation between the energy of adatom formation at the terrace and the energy of formation of a monovacancy, bivacancy, etc., is obvious. The energy of adatom desorption was assumed to be independent of the bonding energy in the crystal. It is also assumed that an adatom and a vacancy recombine with unitary probability when they are in close encounter. Under these assumptions, we investigate how the critical terrace width changes upon varying the relationship between the energy of adatom formation E_n and the energy of its evaporation E_d with the conservation of the sum of these energies. The latter characterizes the enthalpy of evaporation.

The numerical simulation which we carried out is equivalent to the solution of diffusion equations which describe the behavior of monovacancies and adatoms at the (111) surface of a diamond-like crystal:

$$\frac{\partial \sigma}{\partial t} = \Lambda \nabla^2 \sigma - \Lambda \nabla^2 \sigma - K\rho\sigma - \sigma\nu e^{\frac{-3E_n}{k_B T}} + [1 - N_{\text{step}}(r, t)]\nu e^{\frac{-3E_n}{k_B T}}, \tag{1a}$$

$$\frac{\partial \rho}{\partial t} = D\nabla^2 \rho - K\rho\sigma - \rho\nu e^{\frac{-E_d}{k_B T}} + [1 - N_{\text{step}}(r, t)]\nu e^{\frac{-3E_n}{k_B T}} + \sigma\nu e^{\frac{-3E_n}{k_B T}} + N_{\text{step}}(r, t)\nu e^{\frac{-2E_n}{k_B T}} - KN_{\text{step}}(r, t)\rho, \tag{1b}$$

where σ is the monovacancy concentration, Λ is the monovacancy diffusivity, ρ is the adatom concentration, D is the adatom diffusivity, K is the adatom–vacancy recombination rate, ν is the Debye frequency, and $N_{\text{step}}(r, t)$ is the number of atomic sites at the steps related to the surface area.

In Eq. (1a), the first term corresponds to monovacancy diffusion over the surface, the second term corresponds to monovacancy diffusion into the crystal bulk, the third term corresponds to the adatom–monovacancy recombination, the fourth term corresponds to formation of polyvacancies, and the fifth term corresponds to generation of monovacancies. In Eq. (1b), the first term accounts for the surface diffusion of adatoms; the second term, for recombination of adatoms with monovacancies; the third term, for desorption of adatoms fro a terrace. The fourth term corresponds to adatom generation due to the formation of monovacancies, the fifth term corresponds to the adatom generation due to the formation of polyvacancies or varying their size, the sixth term corresponds to the generation of adatoms due to the escape of atoms from the steps, and the seventh term corresponds to the incorporation of adatoms into the step.

In contrast with [8], in the set of equations which are solved using the Monte Carlo method, the formation of polyvacancies, adatom incorporation into the step, and monovacancy diffusion into the crystal bulk are taken into account; and the condition for the closeless of concentrations of adatoms and monovacancies to equilibrium values is absent.

3. RESULTS OF COMPUTATIONAL EXPERIMENT

To investigate the nucleation of vacancy islands, we selected the surface which comprises a strip which seems as though it were cut from the central part of the circular crater formed at the Si(111) surface [4, 5]. The surface constituted a strip from 10 to 300 atomic sites in width and as may as 3000 atomic sites in length. The model results were obtained in the temperature range from T = 1350 to 1550 K.

The profiles of the model surface, in which the critical terrace width L_{cr} was measured as the distance between the steps in the second atomic layer during formation of the stable vacancy island at the lowest continuous terrace, are schematically shown in Figs. 1a and 1b. The critical width was determined as the width of terraces which are bounded by the lowest steps after the emergence of a vacancy island at the lowest continuous terrace. The terrace widths in higher atomic layers were specified narrower than L_{cr} in order to prevent vacancy islands from forming on them. The error in the model data on L_{cr} was ±10%.

The E_n dependences of the critical terrace width for various $E_{sub} = E_n + E_d$ are shown in Fig. 1c. It can be seen that all curves are bell-shaped, and the peak value increases with increasing E_{sub} and shifts to larger E_n. If L_{cr} were determined by the adatom free path length until evaporation, the critical terrace width should decrease monotonically with increasing E_n, since the E_d quantity decreases in this case. However, a range of E_n values does exist in which L_{cr} rises despite a decrease in the free path length of an adatom until its evaporation L_d. In the range of a rising dependence, $L_{cr}(E_n)$ is also independent of E_{sub}, i.e., of E_d. Such behavior of L_{cr} can be attributed to the influence of vacancies.

To determine the free path length of an adatom L_d before its evaporation without thermal generation of monovacancies, a special computational experiment was carried out. The procedure for determining L_d is illustrated in Figs. 2a and 2b, and dependences $L_d(E_d)$ are shown in Fig. 2c. The parameter E_n was chosen so that no thermal generation of monovacancies occurred. At the surface of the starting model, monovacancies were uniformly distributed with a concentration amounting to about a quarter of that of the monolayer (ML) and the adatom concentration was equal to zero. At high temperature, the adatoms which were supplied by the step diffused over the surface and recombined with the previously generated monovacancies. In the course of time, a monovacancy-depletion region of constant width was formed in the step neighborhood. The width of this depletion region coincides with the adatom free path length before evaporation. As might be expected, L_d exponentially increases proportionally to $\exp(E_d/2kT)$. The L_d values obtained for model surfaces of various widths are shown in Fig. 2c. It can be seen that the result is independent of the surface width for the values of d from ten atomic sites or more. This permitted us to carry out computations for narrow surfaces, which greatly shortened computing time. A comparison of the values of L_d (Fig. 2c) with thise of L_{cr} (Fig. 1c) in the region of energies to the right of the peaks of the $L_{cr}(E_n)$ dependences showed that for the descending portions, L_{cr} coincides with the adatom free path length before evaporation L_d.

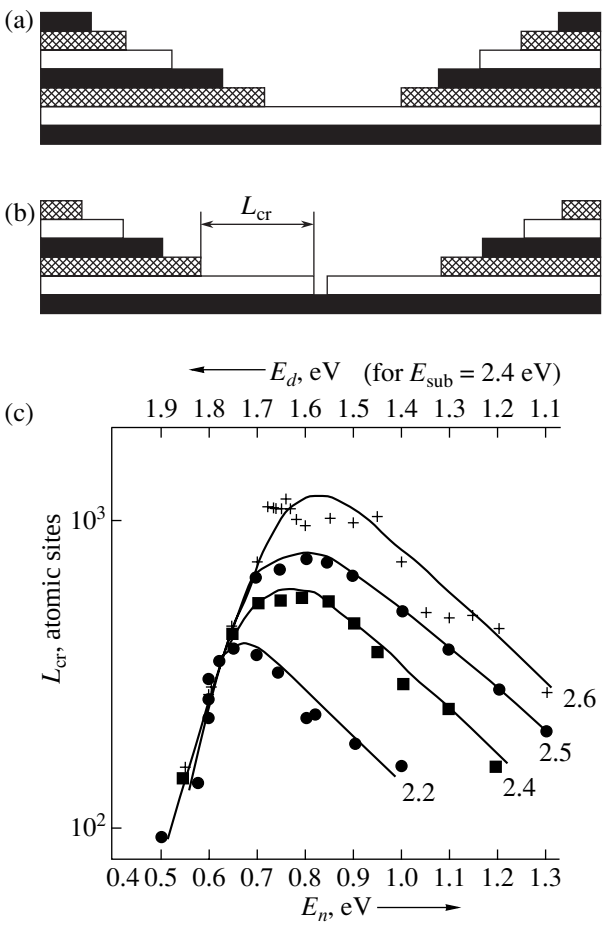

Fig. 1. (a, b) Profiles of model surfaces: (a) initial surface, (b) surface after formation of a vacancy island in the lowest terrace during sublimation; (c) dependences of the critical terrace width L_{cr} (expressed in atomic sites) on the energy of escape of an atom from the step E_n for various sublimation energies $E_{sub} = E_n + E_d$, which were calculated using the Monte Carlo model. The E_{sub} (eV) is indicated near curves.

In the region of the lowest values of E_n (E_n = 0.4 eV), the value of E_d is large, and the evaporation rate of ada-

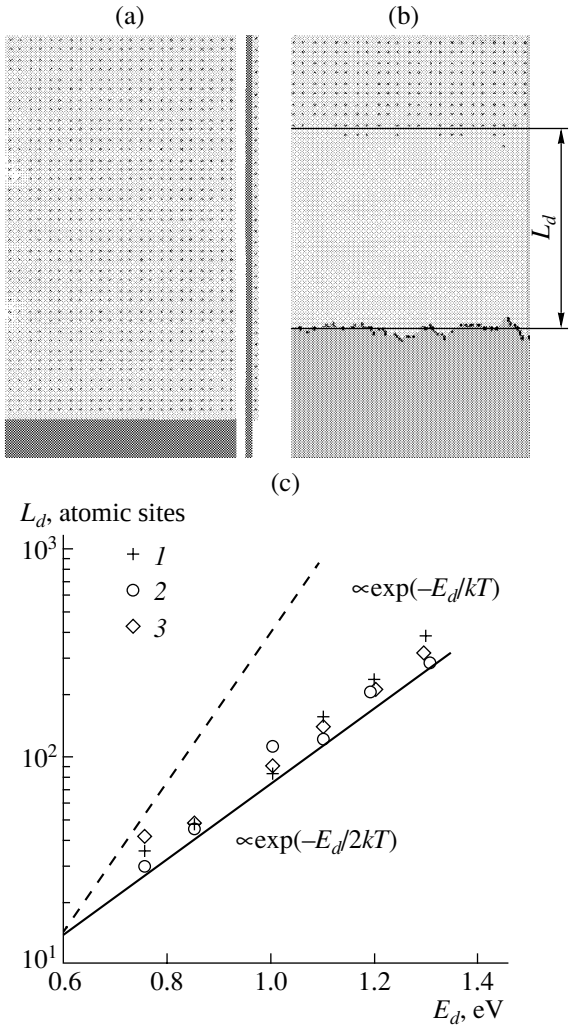

Fig. 2. (a) Initial model surface with specified vacancies (the plan view and the section); (b) vacancy-depletion steady-state region ahead of the moving step for the determination of the adatom free path length before evaporation (L_d); (c) $L_d(E_d)$ for the model surfaces of various width d (length L = 1500 atomic sites for all cases): (*1*) 10, (*2*) 50, and (*3*) 300 atomic sites.

toms is much lower than the rate of their generation from the steps and terraces. In this case, the concentrations of vacancies and adatoms at the terrace are high and the concentration gradients are absent. The critical size of vacancy islands is very large and amounts to more than ten atomic sites. The density of stably growing vacancy islands and the distance between them, as well as between islands and steps, are determined only by the generation rate of vacancies and by the critical size of a vacancy island, similarly to the two-dimensional nucleation of atomic islands according to widely accepted nucleation theory [15].

With increasing E_n, the generation rate of vacancies at the terrace decreases, their density decreases, and the flux of adatoms from the steps starts to exceed the flux from the terrace. Close to the steps, concentration gradients of adatoms and vacancies are formed. A decrease in the vacancy concentration close to the steps shifts the site of nucleation of vacancy islands from the step, and L_{cr} increases. The largest adatom path length L_d, which corresponds to the specified desorption energy E_d, is established when the flux of adatoms from the terrace to a step becomes negligibly small compared with the flux of adatoms from a step.

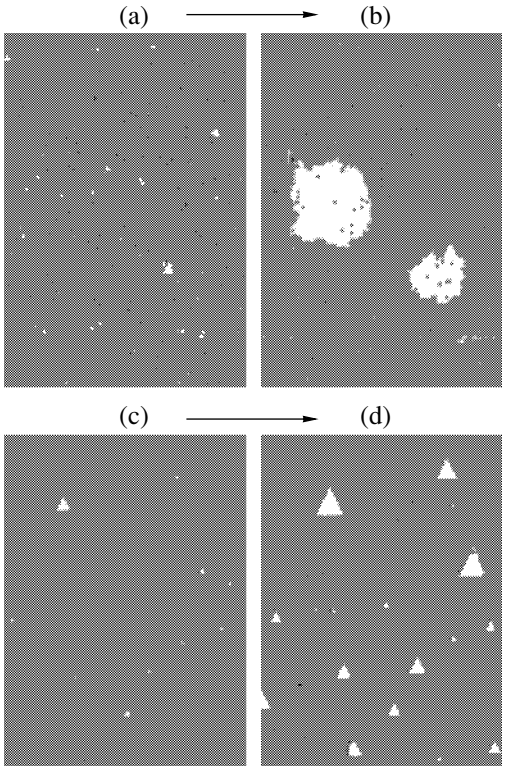

Fig. 3. Development of polyvacancy islands at distances from the step greater than L_{cr} (E_{sub} = 2.2 eV): (a, b) small values of E_n, (c, d) large values of E_n.

As follows from Fig. 1c, the same value of the critical terrace width for the specified sublimation energy corresponds to two sets of values for E_n and E_d. The images of the areas of the model surface for distances larger than L_{cr} for two energy values to the left and to the right of the $L_{cr}(E_n)$ peak, which correspond to L_{cr} = 150 atomic sites, are shown in Fig. 3. For small values of E_n (Fig. 3a), numerous adatoms and vacancies are observed at the surface. In this case, along with monovacancies, a multitude of adatoms and small vacancy islands of subcritical size are observed. Stable vacancy islands are roundish. For the smallest values E_n = 0.4 eV used by us, the stable vacancy islands form very slowly (after numerous evaporation events) and their sizes are small, although their density is high. This is associated with the simultaneous emergence of small vacancy islands, which are formed at a high adatom concentration and with the active exchange of atoms between the vacancy and atomic islands. This situation resembles premelting, which has been assumed in experimental studies [4, 5, 21, 22].

An area of the model surface with a distance from the steps greater than L_{cr} for large values of E_n is shown in Figs. 3c and 3d. Here, numerous, stable growing vacancy islands nucleate simultaneously, since the critical size of a vacancy island is approximately equal to the bilayer vacancy, which consists of a vacancy in the lower monolayer of the bilayer and three neighboring vacancies in the upper monolayer. Polyvacancy islands which are formed at the terraces have a triangular shape, which is characteristic of the (111) surface.

The E_n-dependences of area-mean concentrations of adatoms and monovacancies in steady-state conditions of constancy of these concentrations in time are shown in Fig. 4. The steady-state conditions are practically realized immediately before the formation of vacancy islands. The concentrations of adatoms and vacancies are close to each other and decrease with increasing E_n at low values of E_n according to the same law. The discrepancies between these concentrations begin for values of E_n which correspond to the descending portions of dependences $L_{cr}(E_n)$.

A simplified system of kinetic equations which describes area-concentrations of adatoms (ρ_{av}) and monovacancies (σ_{av}) at the crystal surface is written as

$$\frac{\partial \rho_{av}(t)}{\partial t} = N_{step} e^{\frac{-E_n}{k_B T}} + e^{\frac{-2E_n}{k_B T}} - K_1 \rho_{av}\sigma_{av} - K_2 \rho_{av} N_{step} - C\rho_{av} e^{\frac{-E_d}{k_B T}}, \quad (2a)$$

$$\frac{\partial \rho_{av}(t)}{\partial t} = e^{\frac{-2E_n}{k_B T}} - K_1 \rho_{av}\sigma_{av}. \quad (2b)$$

Here, the first term on the right-hand side of Eq. (2a) corresponds to adatom generation from a step, the second term corresponds to adatom generation from the terrace upon formation of monovacancies, the third term corresponds to adatom–monovacancy recombination, the fourth term corresponds to the incorporation of adatoms into a step, and the fifth term corresponds to adatom evaporation. In Eq. (2b), the first term determines the monovacancy generation and the second term determines the vacancy–adatom recombination. All coefficients in Eqs. (2a) and (2b) are normalized by dividnig by ν.

The analytical solution of this set of equations for the steady state, where the left-hand parts of the equations are equal to zero and $K_2 = K_1 = 1$ (probabilities of incorporation of an adatom into the steps and vacancies are equal to 1), is given by

$$\rho_{av}(t) = \frac{N_{step} e^{\frac{-E_n}{k_B T}}}{N_{step} + Ce^{\frac{-E_d}{k_B T}}}, \quad (3)$$

$$\sigma_{av}(t) = (N_{step})^{-1} e^{\frac{-E_n}{k_B T}} \left(N_{step} + Ce^{\frac{-E_d}{k_B T}} \right).$$

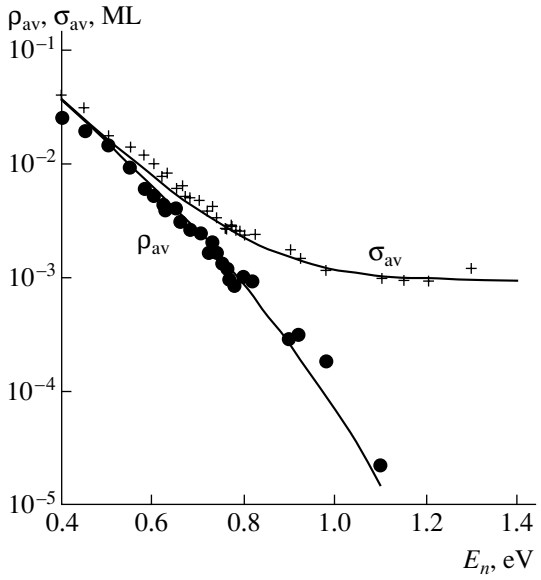

Fig. 4. Energy dependences of area-mean equilibrium concentrations of adatoms ρ_{av} and monovacancies σ_{av}: pointscorrespond to simulation; curves correspond to calculation from formulas (3). Concentrations ρ_{av} and σ_{av} are given in monolayers (ML).

In Fig. 4, along with the results of simulation, the results of calculations from formulas (3) for specified values of N_{step} and E_{sub} are shown. For large values of E_d (low E_n), the exponential term in the denominator can be disregarded, and the concentrations of adatoms and monovacancies are equal to each other and havean identical exponential dependence. For small values of E_d (high E_n), the curves deviate. The theoretical curves coincide with the model computations for $C = 1200$.

The $L_{cr}(E_n)$ dependences, which are shown in Fig. 1c, were calculated for sublimation energies substantially lower than those for Si. Calculating such dependences when $E_{sub} = 4.2$–4.4 eV would require an impractically long computation timer, due to the excessively low probabilities of adatom evaporation. Therefore, we approximated the calculated curves using the empirical analytical function *f*:

$$f = \alpha \left(\frac{1}{\beta} e^{\frac{-E_d}{2k_B T}} + e^{\frac{-3E_n}{2k_B T}} \right)^{-1}. \quad (4)$$

The function *f* approximates well the model dependences $L_{cr}(E_n, E_d)$ for parameters $\alpha = 0.2$ and $\beta = 5$. An analytical expression for the critical terrace width can be written as

$$L_{cr} = \alpha(W_1 + W_2),$$

where $W_1 = \exp(-3E_n/2kT)$ is the probability of adatom evaporation from the surface, and $W_2 = \beta^{-1}\exp(-E_d/2kT)$ is the probability of adatom–vacancy recombination. Thus, the adatom lifetime at the surface τ is determined

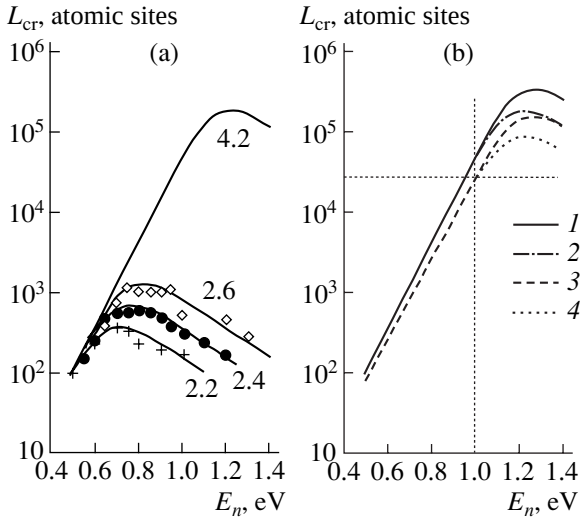

Fig. 5. (a) Dependences of the critical terrace width L_{cr} on the energy E_n for various values E_{sub}, which are denoted by digits near curves. Points represent simulation; curves represent calculation from formula (4) at $T = 1400$ K in Fig. 5a. Parameters of calculations in Fig. 5b: (*1*) $E_{sub} = 4.4$ eV, $T = 1400$ K; (*2*) $E_{sub} = 4.2$ eV, $T = 1400$ K; (*3*) $E_{sub} = 4.4$ eV, $T = 1463$ K; and (*4*) $E_{sub} = 4.2$ eV, $T = 1463$ K.

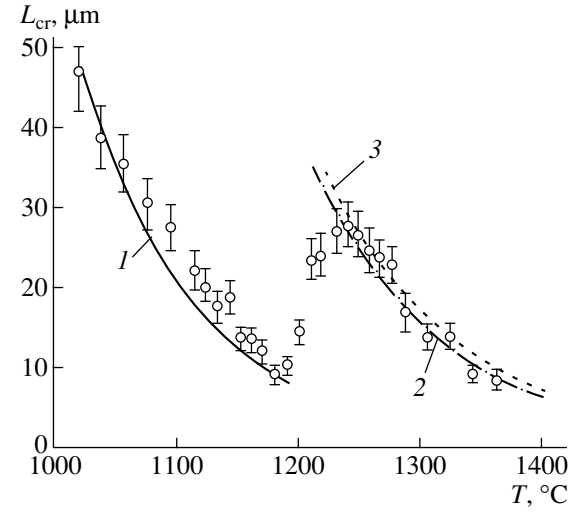

Fig. 6. Experimental dependences of L_{cr} on temperature at the Si(111) surface (circles from [5]) and theoretical dependences (4). Parameters of calculations: (*1*) $E_{sub} = 4.3$ and 4.4 eV, $E_n = 1.0$ eV; (*2*) $E_{sub} = 4.4$ eV, $E_n = 1.15$ eV; and (*3*) $E_{sub} = 4.3$ eV, $E_n = 1.2$ eV.

by its lifetime until evaporation τ_1 and its lifetime until recombination with monovacancies τ_2:

$$\tau = \alpha(1/\tau_1 + 1/\tau_2)^{-1},$$

where $\tau_1 = \beta\exp(E_d/2kT)$ and $\tau_2 = \exp(3E_n/2kT)$.

Using the fitted function, the dependence $L_{cr}(E_n)$ for the sublimation energy which corresponds to Si was plotted. The dependences $L_{cr}(E_n)$, which were obtained from calculations according to the Monte Carlo method and from formula (4), are shown in Fig. 5a. In Fig. 5b, the theoretical curves $L_{cr}(E_n)$ obtained for $E_{sub} = 4.2$–4.4 eV correspond to Si. The dotted horizontal line indicates the experimental value for the critical terrace width at 1190°C (1463 K) $L_{cr} = 2.8 \times 10^4$ atomic sites (10 μm) [5]. The intersection of this straight line with the theoretical curve, which was plotted for this temperature, yields the value $E_n = 1.0$ eV. This value corresponds to the ascending portion of the $L_{cr}(E_n)$ dependence.

Using this value of E_n, the temperature dependence of the critical terrace width was plotted from formula (4). The experimental temperature dependence $L_{cr}(T)$ taken from [6] is shown in Fig. 6 (points). The smallest value $L_{cr}(1190°C) = 10$ μm served as the reference point for determining the preexponential factor in the $L_{cr}(T)$ dependence for $E_n = 1.0$ eV. In Fig. 6, the curves calculated that we calculated for two temperature ranges are also shown by lines. Below 1190°C, the value $E_n = 1.0$ eV yields good agreement between the theory and experimental data. Some uncertainty in the values of E_{sub} is unimportant in this temperature range. For agreement between theory and experiment for the high-temperature region of $L_{cr}(T)$, variation in E_n by 0.1–0.2 eV is required and the position of the theoretical curves depends on E_{sub}. For good agreement between the theoretical curve and experimental points, the following values of E_n were chosen: $E_n = 1.15$ eV for $E_{sub} = 4.4$ eV, and $E_n = 1.2$ eV for $E_{sub} = 4.3$ eV.

4. DISCUSSION

There are experimental data which point to the structural transition of the Si(111) surface at about 1200°C. These data are as follows: (i) to obtain smooth steps at vicinal surfaces, heating above 1200°C is required [4]; (ii) an increase in the dynamic coefficient of the step tension is obtained upon increasing the temperature in the region $T > 1300$ K [11]; (iii) an increase in scattering of medium-energy ions from the Si(111) surface was observed at 1470 K [23]; (iv) in the same temperature range, a change in the current direction, which leads to step stacking, is obtained [9]; and (v) at about 1500 K, a new surface phase is found from rocking curves [21–23]. The $L_{cr}(E_n, E_d)$ dependences, which were obtained from simulation, permit us to suggests an explanation for the jumplike increase in the critical terrace width at about $T = 1200$°C, which was observed in experimental studies [4, 5].

The agreement between experimental data and model calculations, which was demonstrated in Fig. 6, allows us to assume that surface reconstruction at about 1200°C is accompanied by variation in the ratio between E_n and E_d, so that E_n becomes higher, whereas E_d becomes lower. The model calculations show that an increase in E_n by 0.1–0.2 eV is sufficient to account for

the threefold increase in the terrace width, which is observed experimentally. The ensuing decrease in the terrace width at a temperature above 1200°C may be indicative of a newly established E_n-to-E_d ratio. The cause of the variation in E_n and E_d may be a weakening of the bonding of adatoms with the surface in a partly molten layer and a decrease in E_d. This will lead to an increase in E_n so as to retain the magnitude of $E_n + E_d$, as no variation in the magnitude $E_{sub} = 4.2 \pm 0.2$ eV is experimentally observed.

5. CONCLUSION

Our investigations of the dependence of the terrace width on the E_n-to-E_d ratio with the constancy of their sum E_{sub} show that this dependence is nonmonotonic and is peaked at a certain value of E_n which depends on the value of E_{sub}. The tentative assumptions that an increase in the critical terrace width is caused by adatom–monovacancy interaction proved to be incorrect. Although the displacement of atoms over long distances due to this interaction occurs, this displacement alone does not determine the critical terrace width.

The adatom–monovacancy interaction accounts for an ascending portion of the dependence of the critical terrace width on the bonding energy of adatoms. An analytical formula for the dependence of the critical terrace width on the desorption energy and the interatomic bonding energy for a specified sublimation energy of the substance is derived. From the comparison of existing experimental data with the results of calculation, the atomic bonding energy and the desorption energy from the Si(111) surface at temperatures 1000–1200°C $E_n = 1$ eV are estimated. Above 1270°C, the value of E_n increases by 0.1–0.2 eV. The numerical experiment carried out in this study allowed us to put forward an explanation for the experimental behavior of the critical terrace width at temperatures above 1200°C.

ACKNOWLEDGMENTS

This study was supported by the Russian Foundation for Basic Research, project no. 02-02-17726; the Program of the Federal Center of Science and Technology "Research and Development Priorities in Science and Technology for Civil Application's," project no. 2-MPN-02; and the program "Surface Atomic Structures," project no. 40.012.1.1.1153.

REFERENCES

1. C. Alfonso, J. C. Heyraud, and J. J. Metois, Surf. Sci. Lett. **291**, L745 (1993).
2. J. M. Bermond, J. J. Metois, J. C. Heyraud, and C. Alfonso, Surf. Sci. **331–333**, 855 (1995).
3. J. J. Metois and D. E. Wolf, Surf. Sci. **298**, 71 (1993).
4. Y. Homma, H. Hibino, T. Ogino, and N. Aizava, Phys. Rev. B **55**, R10237 (1997).
5. Y. Homma, H. Hibino, T. Ogino, and N. Aizava, Phys. Rev. B **58**, 13146 (1998).
6. P. Finnie and Y. Homma, Phys. Rev. Lett. **82**, 2737 (1999).
7. S. S. Kosolobov, A. V. Prozorov, A. V. Latyshev, and A. L. Aseev, in *Abstracts of Meeting on Growth of Crystals and Films and on Structural Defects of Silicon* (Novosibirsk, 2002), p. 132.
8. A. Pimpinelli and J. Villain, Physica A (Amsterdam) **204**, 521 (1994).
9. A. V. Latyshev, A. B. Krasilnikov, and A. L. Aseev, Surf. Sci. **311**, 395 (1994).
10. A. V. Latyshev, A. B. Krasilnikov, and A. L. Aseev, Appl. Surf. Sci. **60–61**, 397 (1994).
11. A. V. Latyshev, H. Minoda, Y. Tanishiro, and K. Yagi, Phys. Rev. Lett. **76**, 94 (1996).
12. K. Thurmer, D.-J. Liu, E. D. Williams, and J. D. Weeks, Phys. Rev. Lett. **83**, 5531 (1999).
13. J. J. Metois, J. C. Heyraud, and S. Stoyanov, Surf. Sci. **486**, 95 (2001).
14. T. Sinno, R. A. Brown, W. Ammon, and E. Dornberger, J. Electrochem. Soc. **145**, 302 (1998).
15. J. A. Venables, G. D. T. Spiller, and M. Handbucken, Rep. Prog. Phys. **47**, 399 (1984).
16. A. J. Mayne, F. Rose, C. Bolis, and G. Dujardin, Surf. Sci. **486**, 226 (2001).
17. Yu. N. Devyatko, S. V. Rogozhkin, and A. V. Fadeev, Phys. Rev. B **64**, 193401 (2001).
18. I. G. Neizvestny, N. L. Shwartz, Z. Sh. Yanovitskaja, and A. V. Zverev, Thin Solid Films **380**, 61 (2000).
19. W. S. Verwoed, V. Nolting, and P. Badziag, Surf. Sci. **241**, 135 (1991).
20. W. Shimada, H. Tochihara, T. Sato, and M. Iwatsuki, Jpn. J. Appl. Phys. **39**, 4408 (2000).
21. Y. Fukaya and Y. Shigeta, Phys. Rev. Lett. **85**, 5150 (2000).
22. Y. Fukaya and Y. Shigeta, Phys. Rev. B **65**, 195415 (2002).
23. K. Sumitomo, H. Hibino, Y. Homma, and T. Ogino, Jpn. J. Appl. Phys. **39**, 4421 (2000).

Translated by N. Korovin

Semiconductors, Vol. 37, No. 6, 2003, pp. 656–660. Translated from Fizika i Tekhnika Poluprovodnikov, Vol. 37, No. 6, 2003, pp. 681–685.

SEMICONDUCTORS STRUCTURES, INTERFACES, AND SURFACES

Fabrication and Properties of $ZnFe_2S_4$ Single Crystals and Structures Based on Them

A. A. Vaĭpolin*, Yu. A. Nikolaev*, I. K. Polushina*, V. Yu. Rud', Yu. V. Rud'*, E. I. Terukov*, and N. Fernelius*****

**Ioffe Physicotechnical Institute, Russian Academy of Sciences, St. Petersburg, 194021 Russia*

***St. Petersburg State Polytechnic University, St. Petersburg, 195251 Russia*

****Wright Air Force Laboratory, Wright Patterson Air Force Base, OH, USA*

Submitted October 14, 2002; accepted for publication October 28, 2002

Abstract—A new class of ternary semiconductor compounds has been proposed and synthesized. $ZnFe_2S_4$ single crystals, which belong to this class, have been grown for the first time; and their structural, electrical, and optical properties have been investigated. The first photosensitive structures have been fabricated, and their photoelectric characteristics have been studied. A conclusion was made that heterostructures and surface-barrier structures based on $ZnFe_2S_4$ single crystals are promising for practical applications. © *2003 MAIK "Nauka/Interperiodica".*

Making the atomic composition of diamond-like phases more complex on the basis of the rules of their formation, developed by N.A. Goryunova, has resulted in the synthesis of multiple classes of compound semiconductor substances that form the basis of modern semiconductor materials science and which are promising for the formation of a periodic table of semiconductor materials in the future [1]. Among ternary semiconductor compounds, the $A^{II}B^{IV}C_2^V$, $A^IB^{III}C_2^{IV}$ and $A^{II}B_2^{III}C_4^{VI}$ classes are best understood [2–6]; these are crystal-chemical analogues of binary $A^{III}B^V$ and $A^{II}B^{IV}$ semiconductors and, therefore, "inherit" the numerous practically valuable properties of their simpler analogues. However, they not only "inherit" the properties of their analogues, but also exhibit entirely new physical properties, which is continuously arousing interest in developing techniques for their synthesis and initiating comprehensive studies of the physical properties of new materials.

The present study, which belongs to this topical direction, is concerned with the possibility of obtaining a new class of semiconductors formed by substituting a Group VIII atom with an unfilled *d*-shell for a Group III atom in ternary compounds with a stoichiometric vacancy $A^{II}B_2^{III}C_4^{VI}$ (where II stands for Cd or Zn; III, for Ga or In; and VI, for S, Se, or Te). As a result, the existence of such phases was confirmed for the example of $ZnFe_2S_4$, some parameters were determined experimentally, and several types of photosensitive structures based on this compound have been fabricated.

1. $ZnFe_2S_4$ single crystals were grown in a closed volume by the method of gas-transport reactions, with vapor of crystalline iodine as the transport agent. This yielded opaque black $ZnFe_2S_4$ plates with an average size of $\sim 2 \times 3 \times 0.2$ mm^3. An X-ray study of the single crystals showed that the obtained single-phase material has a face-centered cubic lattice with the lattice constant $a = (5.4257 \pm 0.0004)$ Å (at $T = 300$ K). Usually, the best developed and smoothest face of the plates has the (111) crystallographic orientation. According to X-ray diffraction data, our $ZnFe_2S_4$ single crystals exhibit microtwinning, with the twin components turned 180° with respect to one another in the (111) plane.

2. Among crystals of the same batch, the room-temperature resistivity of $ZnFe_2S_4$ plates varies in the range 10^5–10^7 Ω cm. The sign of the thermoelectric power shows that all of the obtained $ZnFe_2S_4$ single crystals have *p*-type conduction, which is untypical of $A^{II}B_2^{III}C_4^{VI}$ crystals [3]. The density of holes defined from the Hall data is $p \approx 10^{12}$–10^{14} cm^{-3}, and the Hall mobility $\mu = 10$ cm^2/V s at $T = 300$ K. Figure 1 shows the resistivity of *p*-$ZnFe_2S_4$ single crystals as a function of temperature in the range $T = 300$–380 K. An exponential temperature dependence of resistivity, typical of semiconducting materials, is observed in this temperature range:

$$\rho = \rho_0 \exp\left(\frac{E_a}{kT}\right) \quad (1)$$

where k is the Boltzmann constant. From this dependence, the activation energy of the impurity centers can be estimated as $E_A = 0.29$ eV assuming an extrinsic conduction mechanism under conditions of strong compensation.

3. Figure 2 shows a typical spectral dependence of the optical absorption coefficient α, which was obtained in the study of the optical transmission $\tilde{T}$ of $ZnFe_2S_4$ single-crystal plates. Assuming that the optical reflection $\tilde{R} = 0.3$, we determined the optical absorption coefficient α using the relation [7]:

$$\alpha = \frac{1}{d}\ln\left(\frac{(1-\tilde{R})^2}{2\tilde{T}} + \sqrt{\left[\frac{(1-R)^2}{2\tilde{T}}\right]^2 + \tilde{R}^2}\right), \qquad (2)$$

where d is the plate thickness. As seen in Fig. 2 (curve *1*), our crystals demonstrate a high optical absorption in the range of photon energies $\hbar\omega = 0.65$–1.8 eV. The rise in α near the photon energy $\hbar\omega > 0.65$ eV ceases at about $\hbar\omega \gtrsim 0.9$ eV, and the absorption levels off at $\alpha \approx 130$ cm^{-1} in the energy range 0.9–1.15 eV. Further, a significant rise of the optical absorption begins at $\hbar\omega \gtrsim 1.2$ eV. As seen in Fig. 2 (curve *1*), this rise ceases at $\hbar\omega \gtrsim 1.6$ eV and the dependence tends to level off at $\alpha \approx 460$–470 cm^{-1}. At the same time, this rise is linear in the $(\alpha\hbar\omega)^{1/2}$–$\hbar\omega$ coordinates in a rather wide range of photon energies (Fig. 2, curve *2*); thus, the extrapolation $(\alpha\hbar\omega)^{1/2} \longrightarrow 0$ yields a characteristic energy $E_0 \approx 0.84$ eV. In terms of the theory of optical absorption in semiconductors [7–9], this energy (E_0) can be related to indirect band-to-band transitions in $ZnFe_2S_4$ single crystals. In this case, the long-wavelength shoulder of the $\alpha(\hbar\omega)$ spectrum at $\hbar\omega < 1.2$ eV can be assigned to the absorption involving the lattice defect levels in $ZnFe_2S_4$ semiconductor crystals. A strong absorption, $\alpha \approx 130$ cm^{-1}, in the range $\hbar\omega = 0.8$–1.2 eV indicates a high density of these defects, which can be due to position-disordering of Zn and Fe atoms in the anion sublattice of $ZnFe_2S_4$, as in $ZnSnAs_2$ ternary compound in the chalcopyrite $\longrightarrow$ zinc blende phase transition [2].

4. The study of effects arising at the contacts between single-crystal *p*-$ZnFe_2S_4$ and metals (In, Au, Cu) or layered $A^{III}B^{VI}$ semiconductors (*n*-InSe, *p*-GaSe) has demonstrated the possibility of fabricating photosensitive structures based on the new class of semiconductors.

A metal layer of 0.1 mm thickness was deposited by thermal evaporation in vacuum onto the postgrowth (111) $ZnFe_2S_4$ surface. In addition to surface-barrier structures, heterostructures were fabricated by bringing natural cleavages of $A^{III}B^{VI}$ crystals and the postgrowth mirror surface of *p*-$ZnFe_2S_4$ single crystals into direct optical contact. A specific feature of the latter method is that the heterostructure components are not subjected to any external actions, which is especially important in the investigation of compound materials that may change their composition in the course of technological processes [10].

The study of static current–voltage $I(U)$ characteristics has demonstrated rectification at the contacts of

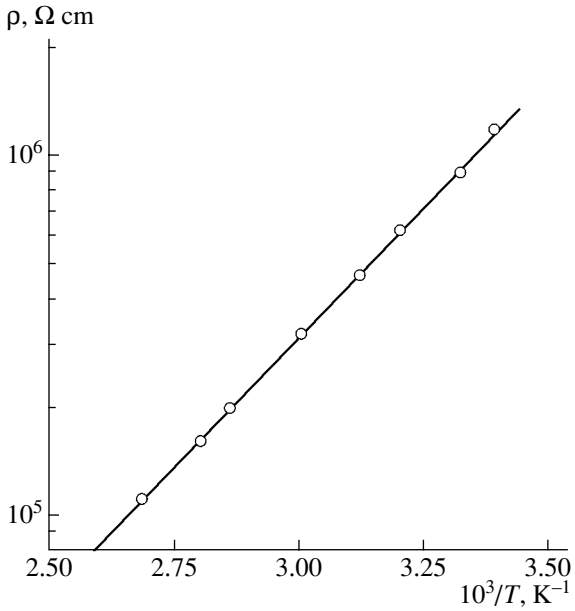

Fig. 1. Temperature dependence of the resistivity of *p*-$ZnFe_2S_4$ single crystal (sample no. 9*p*).

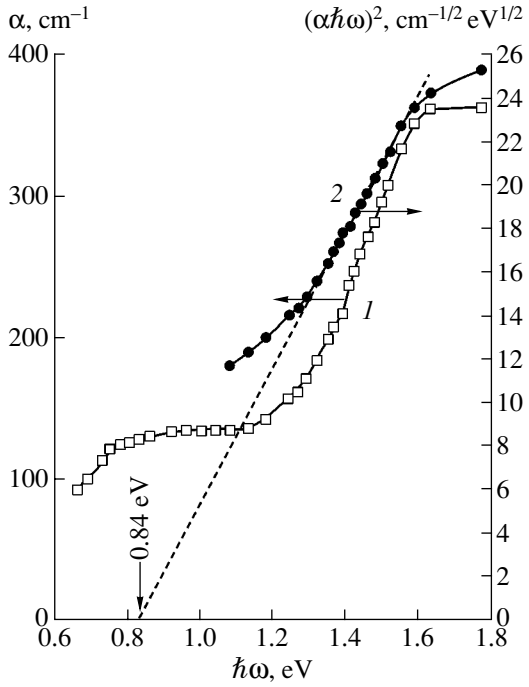

Fig. 2. Spectral dependence of the optical absorption coefficient of a *p*-$ZnFe_2S_4$ single crystal (sample 7*p*) at $T = 300$ K in the coordinates (*1*) α–$\hbar\omega$ and (*2*) $(\alpha\hbar\omega)^{1/2}$–$\hbar\omega$.

p-$ZnFe_2S_4$ single crystals with metallic indium and with $A^{III}B^{VI}$ semiconductors. Curves *1–3* in Fig. 3 show *I–V* characteristics typical of rectifying structures. The forward bias corresponds to a positive external voltage U applied to *p*-$ZnFe_2S_4$ crystal in In/*p*-$ZnFe_2S_4$ surface-

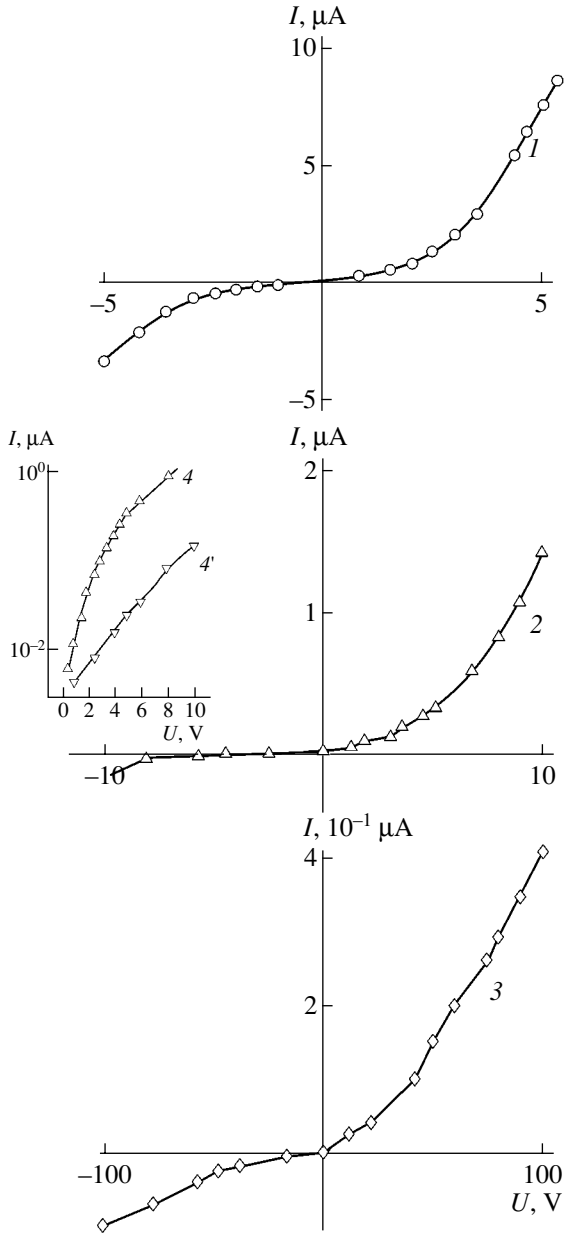

Fig. 3. Static *I–V* characteristics of photosensitive structures based on *p*-$ZnFe_2S_4$ single crystals, $T = 300$ K, for (*1*) In/*p*-$ZnFe_2S_4$ (sample no. 17), (*2*, *4*, *4'*) *n*-InSe/*p*-$ZnFe_2S_4$ (sample 11), and (*3*) *p*-GaSe/*p*-$ZnFe_2S_4$ (sample 3).

barrier structures and *n*-InSe/*p*-$ZnFe_2S_4$ heterostructures, while in *p*-GaSe/*p*-$ZnFe_2S_4$ heterostructures the forward bias corresponds to a negative voltage applied to *p*-$ZnFe_2S_4$. We believe that this difference is due to specific features of the band diagram of the fabricated contacts, but its parameters have not been determined yet. In the range of bias $U > U_0$, the *I–V* characteristics obey the law

$$I = \frac{U - U_0}{R_0}, \tag{3}$$

where U_0 is the cutoff voltage, and R_0 is the residual resistance, the values of which are listed in the table. Greater attention must be given to the increase of R_0 in heterostructures as compared with the surface-barrier In/$ZnFe_2S_4$ structures, which is presumably related to the properties of $A^{III}B^{VI}$ crystals and to the method for fabricating the optical heterocontact. As seen in the table, the highest rectification among our structures was demonstrated by InSe/$ZnFe_2S_4$ contacts. Only in these structures does the forward *I–V* characteristic follow, at $U > 3$ V (Fig. 3, curve *4*), the exponential law typical of a photodiode [9]

$$I = I_0 \exp\left(\frac{eU}{nkT} - 1\right), \tag{4}$$

where the diode factor $n \approx 25$–30 in different structures, which can be attributed to their high series resistance. The reverse *I–V* characteristics in all of the structures follow the power law $I \propto U^\gamma$, where the factor $\gamma > 1$ at $U < 5$ V and increases with increasing bias voltage, which can be related to the defective structure of the periphery in the first structures based on *p*-$ZnFe_2S_4$ single crystals.

5. The obtained structures demonstrate photosensitivity. In the surface-barrier structures exposed to unpolarized light, the photovoltaic effect is stronger when the structure is illuminated from the side of the barrier contact. The metallic contact is charged negatively with respect to *p*-$ZnFe_2S_4$, which corresponds to rectification polarity. In the case of InSe/$ZnFe_2S_4$ and GaSe/$ZnFe_2S_4$ structures, the effect is stronger under illumination from the side of $ZnFe_2S_4$. In these cases, InSe is charged negatively, and GaSe, positively, with respect to the $ZnFe_2S_4$ plate, which also correlates with the direction of rectification in the heterostructures.

Figure 4 shows typical spectra of the relative quantum efficiency of photoconversion η for all structure types and for two configurations of structure illumination. The sign of the photovoltage is independent of the incident photon energy and the location of the incident beam (focused onto a spot ~0.2 mm in diameter) on the sample. This leads to the conclusion that the photovoltaic effect in our structures is defined by the separation of photoexcited pairs by the electric field of the barriers between $ZnFe_2S_4$ and the metal or $A^{III}B^{VI}$ compound. The maximum voltage responsivity S_U^m obtained in the best structures of different types and the corresponding photon energies $\hbar\omega^m$ are listed in the table. It is necessary to stress that the $\hbar\omega^m$ values in our structures are significantly higher than the characteristic energy $E_0 \approx 0.84$ eV obtained from the $\alpha(\hbar\omega)$ spectra. Unfortunately, the size and quality of the plates obtained have given no way, as yet, of fabricating samples with the thickness and area necessary for determining the opti-

Photoelectric characteristics of structures based on *p*-$ZnFe_2S_4$ single crystals. $T = 300$ K

Structure type	R_0, Ω	K*	S_U^m, V W^{-1}	$\hbar\omega^m$, eV	δ, eV
In/*p*-$ZnFe_2S_4$	6.7×10^5	2.5(3)	200	3.7	0.3
n-InSe/*p*-$ZnFe_2S_4$	7.1×10^6	16(5)	500	2.8–3.2	1.0**
p-GaSe/*p*-$ZnFe_2S_4$	2.8×10^8	6(40)	10	2.9	0.5**

* K is the ratio of forward to reverse current.

** Because of the absence of a clearly defined short-wavelength falloff in the η($\hbar\omega$) spectra, only the FWHM of the long-wavelength portion is indicated.

cal absorption coefficient in $ZnFe_2S_4$ by conventional spectroscopy up to high energies (~4 eV). Therefore, presently, the specific features of the photoactive absorption in $ZnFe_2S_4$ can be considered only with account of the photosensitivity spectra η($\hbar\omega$) obtained for the first time for the structures under consideration (Fig. 4). As seen in this figure, the η($\hbar\omega$) spectra of InSe/$ZnFe_2S_4$ and GaSe/$ZnFe_2S_4$ illuminated from the side of $A^{III}B^{VI}$ crystal (curves *1* and *2*) have the form of rather narrow bands peaked near the energy gap of $A^{III}B^{VI}$ crystals ($E_G = 1.2$ eV in InSe and 2.0 eV in GaSe [11]). In this case, the short-wavelength falloff of η is due to the fact that, as the photon energy approaches the E_G value of a $A^{III}B^{VI}$ semiconductor, the distance between the layer in which photoexcited carriers are generated and the active region of a heterostructure exceeds the diffusion length of photoexcited carriers. When the heterostructures are illuminated from the side of $ZnFe_2S_4$, the η spectra are broadened (Fig. 4, curves *3* and *4*), so their FWHM δ strongly increases (see table) and the energy position of the photosensitivity peak $\hbar\omega^m$ is considerably shifted to $\hbar\omega \gg E_0$. As seen in Fig. 4, the short-wavelength falloff of η at $\hbar\omega >$ 3 eV is weak. As a result, the short-wavelength portion of δ could not be determined, so we restricted our consideration to the long-wavelength component (see table). It is also worth noting that, under different geometric characteristics of structure illumination, the positions of the long-wavelength edges of photosensitivity are close ($\hbar\omega \approx 1$ eV) only in InSe/$ZnFe_2S_4$ structures (Fig. 4, curves *1* and *3*), while the position of the long-wavelength edge of photoactive absorption in GaSe/$ZnFe_2S_4$ structures illuminated from the side of $ZnFe_2S_4$ (Fig. 4, curve *4*) is nearly the same as in the case of InSe/$ZnFe_2S_4$.

This leads to the suggestion that the position of the long-wavelength edge of photosensitivity in both structures is defined by high photoactive absorption in $ZnFe_2S_4$ plates. For this reason, the position of the long-wavelength edge of photosensitivity η($\hbar\omega$) is largely determined by the onset of band-to-band absorption only in the case of GaSe/$ZnFe_2S_4$ structures illuminated from the side of the GaSe plate (Fig. 4, curve *2*).

On the whole, the specific features of the η($\hbar\omega$) spectra of our heterostructures suggest that their wide-bandgap component is indeed $ZnFe_2S_4$ crystal, and, on the basis of this fact, a tentative estimation of the energy of direct transitions in $ZnFe_2S_4$ can be made, $E_G > 2$ eV. As seen in Fig. 4 (curve *5*), the photosensitivity peak in In/$ZnFe_2S_4$ surface-barrier structures is considerably blue-shifted with respect to the peak in heterostructures. This fact indicates the high efficiency of collection of photogenerated pairs in In/$ZnFe_2S_4$ barriers. The η falloff at $\hbar\omega > 3$ eV in the heterostructures (Fig. 4, curves *2* and *4*) can be attributed to a rise in optical absorption in the bulk of $ZnFe_2S_4$. As follows from

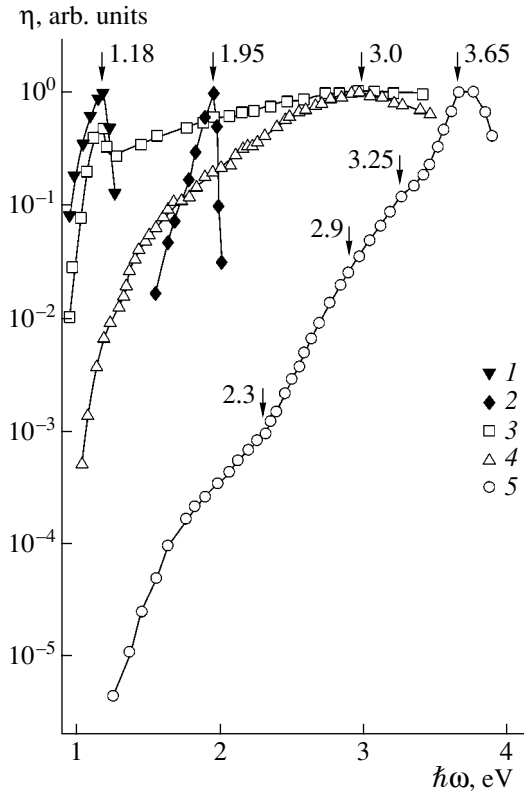

Fig. 4. Spectral dependences of the relative quantum efficiency of photoconversion, η, of structures based on *p*-$ZnFe_2S_4$ single crystals at $T = 300$ K: (*1*, *3*) InSe/$ZnFe_2S_4$, (*2*, *4*) GaSe/$ZnFe_2S_4$, and (*5*) In/$ZnFe_2S_4$. Illumination from the side of (*1*) InSe, (*2*) GaSe, (*3*, *4*) $ZnFe_2S_4$, and (*5*) the barrier contact. The spectra are reduced to the absolute maximum of η. Arrows indicate the breaks in the spectra, with the corresponding energies given in electronvolts.

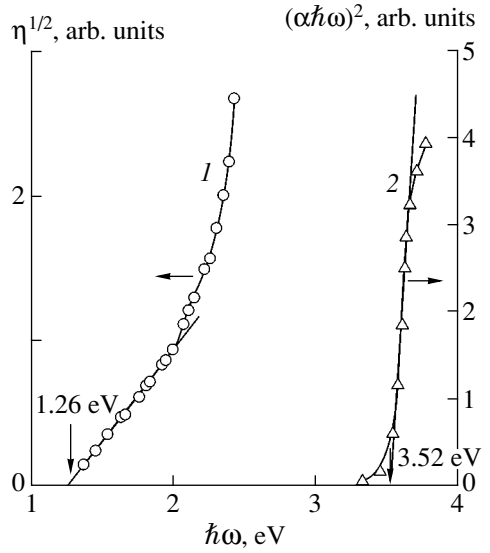

Fig. 5. (*1*) $\eta^{1/2}$–$\hbar\omega$ and (*2*) $(\eta\hbar\omega)^2$–$\hbar\omega$ dependences for the In/$ZnFe_2S_4$ structure at $T = 300$ K. Illumination from the side of the barrier contact. The spectral resolution was no worse than 10^{-3} eV.

Fig. 4, the photosensitivity gradually increases in the spectral range from 1 to 3.6 eV, with breaks (indicated by arrows) reproducibly observed in different structures. The analysis of the $\eta(\hbar\omega)$ spectra of In/$ZnFe_2S_4$ (Fig. 5, curve *1*) has shown that their long-wavelength ($\hbar\omega < 2$ eV) portion follows the Fowler law $\sqrt{\eta} \propto \hbar\omega$, which is characteristic of carrier photoemission, whence the extrapolation of a linear portion at $\sqrt{\eta} \longrightarrow 0$ yields a barrier height $\zeta_B \approx 1.26$ eV, which is close to that obtained earlier for $A^{II}B^{IV}C_2^V$ ternary semiconductors [2]. Further analysis of the experimental $\eta(\hbar\omega)$ spectra based on known theoretical relations of the type

$$\eta\hbar\omega = A(\hbar\omega - E_G)^m \qquad (5)$$

yields very ambiguous results for the range of 2–3.3 eV. The breaks at 2.9 and 3.25 eV and the low slope of $\eta(\hbar\omega)$ spectra, $S = d(\ln\eta)/d(\hbar\omega)$, estimated to be 4–6 eV^{-1} in the spectral range 2.4–3.3 eV, allow us to attribute this absorption to indirect optical transitions in $ZnFe_2S_4$ [12]. Finally, a sharp rise in the photosensitivity of In/$ZnFe_2S_4$ structures illuminated from the side of the barrier contact in the range $\hbar\omega > 3.5$ eV (Fig. 5, curve *2*) follows the relation (5) with $m = 1/2$, which, according to [7–9], makes it possible to consider the optical transitions in $ZnFe_2S_4$ as direct and to determine E_G as 3.5 eV at $T = 300$ K by the extrapolation $(\eta\hbar\omega)^2 \longrightarrow 0$.

Polarization measurements of the photosensitivity of the obtained structures exposed to light incident along the normal to the surface did not reveal any natural photopleochroism. This conclusion correlates with the structure of $ZnFe_2S_4$ crystals [13].

Thus, the spectral dependences of two types of photosensitive structures based on the first fabricated single crystals of a new class demonstrate for the example of $ZnFe_2S_4$ the possibility of using $A^{III}B^{VI}/ZnFe_2S_4$ heterostructures as wide-spectral-range photodetectors and In/$ZnFe_2S_4$ surface-barrier structures as short-wavelength detectors which have a peak photosensitivity at about $\hbar\omega \approx 3.65$–3.75 eV and are insensitive in the energy range $\hbar\omega \lesssim 3.3$.eV.

REFERENCES

1. N. A. Goryunova, *Compound Diamond-Like Semiconductors* (Sovetskoe Radio, Moscow, 1968).
2. V. D. Prochukhan and Yu. V. Rud', Fiz. Tekh. Poluprovodn. (Leningrad) **12**, 209 (1978) [Sov. Phys. Semicond. **12**, 121 (1978)].
3. A. N. Georgobiani, S. I. Radautsan, and I. M. Tiginyanu, Fiz. Tekh. Poluprovodn. (Leningrad) **19**, 193 (1985) [Sov. Phys. Semicond. **19**, 121 (1985)].
4. F. P. Kesamanly and Yu. V. Rud', Fiz. Tekh. Poluprovodn. (St. Petersburg) **27**, 1761 (1993) [Semiconductors **27**, 969 (1993)].
5. Yu. V. Rud', Fiz. Tekh. Poluprovodn. (St. Petersburg) **28**, 1105 (1994) [Semiconductors **28**, 633 (1994)].
6. B. H. Bairamov, V. Yu. Rud', and Yu. V. Rud', MRS Bull. **23**, 41 (1998).
7. Yu. I. Ukhanov, *Optical Properties of Semiconductors* (Nauka, Moscow, 1977).
8. J. I. Pankove, *Optical Processes in Semiconductors* (Prentice Hall, Englewood Cliffs, N.J., 1971; Mir, Moscow, 1973).
9. S. M. Sze, *Physics of Semiconductor Devices* (Wiley, New York, 1969; Mir, Moscow, 1973).
10. Yu. V. Rud' and M. Serginov, Fiz. Tekh. Poluprovodn. (Leningrad) **19**, 1718 (1985) [Sov. Phys. Semicond. **19**, 1057 (1985)].
11. *Physicochemical Properties of Semiconductors*, Ed. by A. V. Novoselova, V. B. Lazarev, Z. S. Medvedeva, N. P. Luzhina, and A. A. Levin (Nauka, Moscow, 1979).
12. A. Shileika, Surf. Sci. **37**, 730 (1973).
13. F. P. Kesamanly, V. Yu. Rud', and Yu. V. Rud', Fiz. Tekh. Poluprovodn. (St. Petersburg) **30**, 1921 (1996) [Semiconductors **30**, 1001 (1996)].

Translated by D. Mashovets

Semiconductors, Vol. 37, No. 6, 2003, pp. 661–666. Translated from Fizika i Tekhnika Poluprovodnikov, Vol. 37, No. 6, 2003, pp. 686–691.

SEMICONDUCTORS STRUCTURES, INTERFACES, AND SURFACES

Determination of the Absolute Value of the Semiconductor Surface Potential by the Quasi-Static Capacitance–Voltage Characteristics of an MIS Structure

A. G. Zhdan, N. F. Kukharskaya, and G. V. Chucheva

Institute of Radio Engineering and Electronics, Russian Academy of Sciences (Fryazino Branch), pl. Vvedenskogo 1, Fryazino, Moscow oblast, 141190 Russia

Submitted August 5, 2002; accepted for publication November 3, 2002

Abstract—A simultaneous analysis of the derivatives $C'_V V_g$ of the experimental and ideal quasi-static capacitance–voltage characteristics (plotted as a function of the normalized differential capacitance of a metal–insulator–semiconductor (MIS) structure) allows identification of regions within the semiconductor band gap E_g, in which interface states are virtually aTSent and the relation between the surface potential ψ_S of the real semiconductor and the voltage V_g applied to the MIS structure may be readily ascertained. This allows an accurate enough determination of the additive constants $\psi_{S0}(V_{g0})$ necessary to calculate the dependence $\psi_S(V_g)$ in the entire range of V_g by numerical integration of the experimental quasi-static *C–V* characteristic. The comparison of this dependence with the ideal one characterizes in detail the integral electronic properties of the semiconductor–insulator heterojunction: the E_g-averaged density of interface states, the qualitative pattern of their distribution over the band gap, and the flat-band voltage V_{FB} and its components caused by a charge fixed in the undergate insulator and a charge localized at boundary states. A high accuracy of the V_{FB} measurements allows detection of even a weak physical response of MIS structures to external factors or to variations in the heterojunction technology. Results of such an analysis for a typical SiO_2/Si interface of an *n*-Si-MOS (metal–oxide–semiconductor) structure are considered. The application of C'_V–C_V diagrams for analyzing the high-frequency *C–V* characteristics is considered. © *2003 MAIK "Nauka/Interperiodica".*

All the major factors controlling the electronic properties of the semiconductor–insulator heterojunction (HJ) region manifest themselves in the dependence of the semiconductor surface potential ψ_S on the voltage V_g applied to the metal–insulator–semiconductor (MIS) structure: localized electron states, fixed and mobile charges in insulator, the contact potential difference between the field electrode and semiconductor, fluctuation effects, and the semiconductor doping profile [1, 2]. The dependences $\psi_S(V_g)$ allow estimation of changes in these properties after thermal–field and radiation stresses which enhance, in particular, defect generation and charge accumulation or annihilation in the undergate insulator. Such data are of particular significance with respect to the degradation phenomena in the ultrathin (~2 nm) undergate oxides of submicrometer field-effect transistors [3, 4]. At the same time, the determination of the function $\psi_S(V_g)$ is a limiting stage for almost all of the methods of *C–V* spectroscopy (CVS), which is a basic instrument of HJ diagnostics [1, 2, 5].

One of the most commonly accepted algorithms for determining the dependence $\psi_S(V_g)$ is based on the relations (see [1, 2, 6])

$$\psi'_S(V_g) = d\psi_S(V_g)/dV_g = 1 - C_V(V_g), \quad (1)$$

$$\psi_S(V_g) = \psi_{S0} - \int_{V_{g0}}^{V_g} [1 - C_V(V_g)]dV_g, \quad (2)$$

where $C_V(V)_g = C(V_g)/C_i$ is the normalized quasi-static *C–V* characteristic (QS CVC) of the MIS structures, C_i is the insulator capacitance,

$$\psi_{S0} = \psi_S|_{V_g = V_{g0}},$$

and V_{g0} is the voltage corresponding to a certain characteristic point of the QS CVC. The function $\psi_S(V_g)$ is determined by numerical integration of Eq. (2) to an accuracy up to the additive constant ψ_{S0}. Even small deviations $\Delta\psi_{S0}$ of the quantity ψ_{S0} from the actual value ψ^*_{S0} cause significant deviations of the observed HJ characteristics from the actual ones. Figure 1 illus-

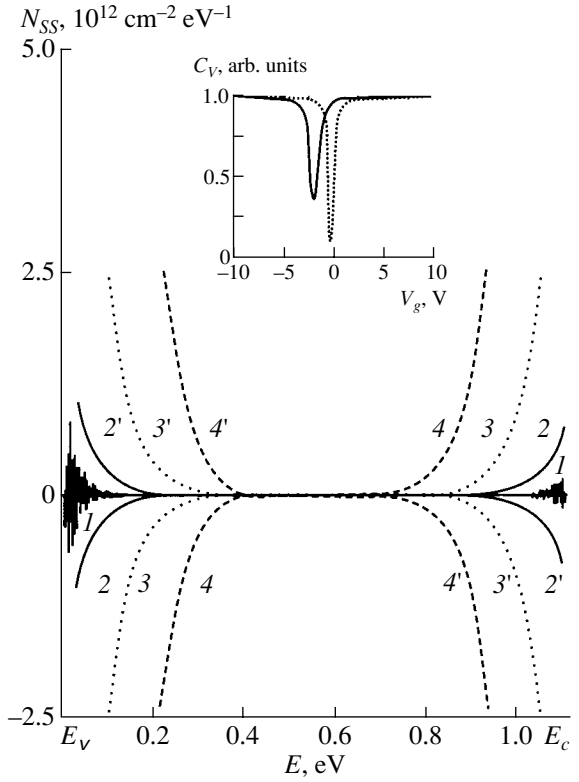

Fig. 1. Calculated density of states caused by the statistical error in calculations (*1*) and the systematic errors of ψ_{S0} "determination" (*2–4*, *2'–4'*). The values of ψ_{S0} were taken to be equal to ψ^*_{S0} (*1*), ($\psi^*_{S0} - \Delta\psi_{S0}$) (*2–4*), and ($\psi^*_{S0} + \Delta\psi_{S0}$) (*2'–4'*); ψ^*_{S0} = 0.35307 eV (V_g = 20 V). The values of $\Delta\psi_{S0}$ were 0.1 (*2*, *2'*), 1 (*3*, *3'*), and 10 meV (*4*, *4'*). The inset shows the experimental (solid line) and ideal (dashed line) dependences $C_V(V_g)$ for the structure under study.

trates this situation through the example of the quasi-equilibrium CVS (QE CVS) method [1, 2]. Figure 1 displays the spectra of interface states (IS) $N_{SS}(E) = N_{SS}(\psi_{S0})$, derived from interface from an ideal equilibrium CVC calculated to an accuracy of $\pm 5 \times 10^{-8}$ with the parameters of the *n*-Si–MOS structure under study. The conventional notation, $E = \psi_S + E_g - E_F$, $E_g = E_c - E_v$ is the semiconductor band gap, E_g(Si) = 1.12 eV, E_F is the Fermi energy, E_v is the valence band top, and E_c is the conduction band bottom is used in Fig. 1; the value of ψ_S is measured from the level E_c in the semiconductor bulk: $\psi_S > 0$ in the enhancement state and $\psi_S < 0$ in the depletion and inversion states.

We studied an Al–(SiO_2 thermal oxide)–Si:P structure with the (100) substrate orientation, a phosphorus concentration $N_d = 1.58 \times 10^{13}$ cm^{-3}, and an oxide thickness h_{SiO_2} = 1700 Å; the field-electrode area $S = 2.4 \times 10^{-2}$ cm^2, C_i = 489.1 pF, and T = 293 K. The same values of the parameters h_{SiO_2}, N_d, C_i, and T were used to calculate the ideal equilibrium CVC. The relatively low doping level of silicon allowed us to ignore a probable nonuniformity in the impurity distribution, which is insignificant at $N_d < 10^{15}$ cm^{-3} (see [1]).

A rigorous realization of the QE-CVS method algorithm using the CVC measured at $\psi_{S0} = \psi^*_{S0}$ should obviously result in a zero density of states (DoS) over the entire Si band gap. In fact, this does take place (see Fig. 1, curve *1*). As ψ_{S0} deviates from ψ^*_{S0}, the function $N_{SS}(E)$ drastically changes its shape (Fig. 1, curves *2–4*, *2'–4'*): the confidence region in the TS spectrum abruptly narrows down, and fictitious "tails" in the DoS, gradually increasing to the band gap edges, arise in the dependences $N_{SS}(E)$. In particular, in the case of enhancement, when $\psi_{S0} = \psi^*_{S0} - \Delta\psi_{S0}$ (ψ^*_{S0} = 0.35307 eV, V_g = 20 V), the DoS is high and positive near $E = E_c$, while the DoS is high and negative near $E = E^*_v$; the opposite case occurs when $\psi_{S0} = \psi^*_{S0} + \Delta\psi_{S0}$. It is noteworthy that the perturbation $\Delta\psi_{S0}$ introduced into ψ^*_{S0}, e.g., in the enhancement region, is translated into the inversion region with no change in the value and sign.

These facts are easily understood if we take into account the basic QE CVS equation (see [1, 2, 6])

$$C_{SS}(\psi_S) = qN_{SS}(\psi_S) = \frac{C_i}{S}\left[\frac{C_V[\psi_S(V_g)]}{1 - C_V[\psi_S(V_g)]} - \frac{C_S(\psi_S)}{C_i}\right], \quad (3)$$

where $C_{SS}(\psi_S)$ is the specific IS capacitance, $C_S(\psi_S)$ is the capacitance of the space-charge layer of semiconductor [1, 2], q is the elementary charge, and S is the MIS structure area. As follows from Eq. (3), near the edges of the semiconductor band gap (in the case $|\psi_S| \gg kT$), we have $C(V_g) \longrightarrow C_i$, $C_V(V_g)/[1 - C_V(V_g)] \longrightarrow \infty$, and $C_S/C_i \propto \exp|\psi_S|/2kT \longrightarrow \infty$ as $|V_g|$ increases. The first and second terms in Eq. (3) are exactly equal at any ψ_S and nearly equal at zero and small IS density, respectively. In other words, in the case of high enhancement or deep inversion, the IS density $N_{SS}(\psi_S)$ is defined by a difference of two large numbers, and even small systematic errors in ψ_{S0} (hence, ψ_S) significantly distort the function $N_{SS}(E)$. This causes nonphysical "tails" in the DoS, which are positive and negative due to underestimation and overestimation of the second term in Eq. (3), respectively. For the same cause, random errors in calculations or measurements manifest themselves as statistical noise, whose amplitude increases as the semiconductor band-gap edges are approached (see Fig. 1, curve *1*).

Meanwhile, there are no reliable quantitative techniques for identifying ψ_{S0} that are adequate for determing $\psi_{S0}(V_g)$ and for QE CVS problems. The conventional approaches for estimating ψ_{S0} [1, 6, 7] postulate that the inequality $C_S/S \gg C_{SS}$ should be valid near the band-gap edges of the semiconductor adjacent to the

insulator. Thus, it is assumed a priori that the ideal $[C_{Vid}(\psi_S)]$ and experimental $[C_{Vex}(\psi_S)]$ QS CVCs plotted versus ψ_S may be brought into coincidence.

To transform the experimental QS CVC $C_{Vex}(V_g) \longrightarrow C_{Vex}(\psi_S)$, we used Eq. (2). The value of ψ_{S0} is quite arbitrarily selected near the V_g range boundaries ($|\psi_S| \gg kT$), where the dependence $\psi_S(V_g)$ is rather weak [1]. Then, this value of ψ_{S0} is corrected for the shift $\pm\Delta\psi_{S0}$ required to bring similar $C_{Vid}(\psi_S)$ and $C_{Vex}(\psi_S)$ portions into coincidence. One then varies ψ_{S0} and finds the $N_{SS}(E)$ spectral region, which is stable to such variations and is explained by the CVS result [8]. The qualitative character of this algorithm for estimating ψ_{S0} manifests itself in a significant narrowing of the energy range ΔT of the observed IS density, as well as in the $N_{SS}(E)$ errors, even within this range ΔE [8]. In the case of Si, $\Delta E \simeq \pm E_g/4$ with respect to the Si mid gap at $N_{SS}(E) \simeq 10^{11}$ cm^{-2} eV^{-1}.

This suggests the necessity of seeking a sufficiently accurate method for identifying ψ_{S0} in the enhancement and inversion regions. In what follows, one of the approaches to the solution of this problem is employed.

Taking the voltage V_g as a parameter, we represent the experimental and ideal QS CVCs in the coordinates

$$C'_{V\,ex}(V_g^{ex})\text{–}C_{V\,ex}(V_g^{ex}), \quad (C'_{V\,id}(V_g^{id})\text{–}C_{V\,id}(V_g^{id}),)$$

where

$$C'_{V\,ex}(V_g^{ex}) = dC_{V\,ex}/dV_g^{ex}, \quad C'_{V\,id}(V_g^{id}) = dC_{V\,id}/dV_g^{id}.$$

The coincidence of these curves in any range of the common argument of the functions $C_V(V_g) = C_{Vex}(V_g^{ex})$ and $C_V(V_g) = C_{Vid}(V_g^{id})$, determined within the same interval (0, 1), indicates the equality of the functions themselves and their derivatives. This also suggests that both CVCs can be brought into exact coincidence by translating one of them along the voltage axis by a certain constant ΔV_g = const. In other words, if

$$C'_{V\,ex}[C_{V\,ex}(V_g^{ex})] = C'_{V\,id}[C_{V\,id}(V_g^{id})]$$

and

$$C_{V\,ex}(V_g^{ex}) = C_{V\,id}(V_g^{id}),$$

we have

$$\psi_S^{ex}(V_g^{ex}) \equiv \psi_S^{id}(V_g^{id});$$

i.e., the surface potential ψ_S^{ex} of a real semiconductor at the voltage V_g^{ex} is equal to the surface potential ψ_S^{id} of an ideal semiconductor at the voltage V_g^{id}. In this case, $V_g^{ex} - V_g^{id} = \Delta V_g$ = const; $\Delta V_g > 0$ at $V_g^{ex} > V_g^{id}$ and $\Delta V_g < 0$ at $V_g^{ex} < V_g^{id}$. Hence, selecting any value of $C_{Vex}(V_g^{ex})$ from the range of agreement between the

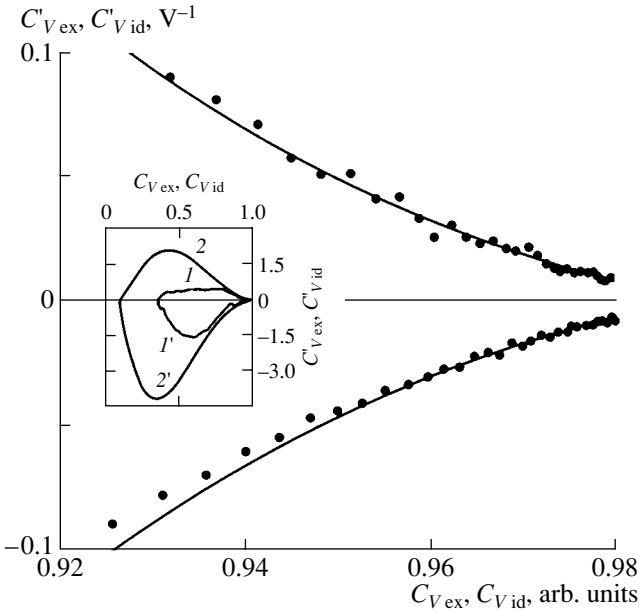

Fig. 2. Regions where the experimental (dots) and ideal (solid lines) curves are brought into coincidence in the cases of enrichment (top) and inversion (bottom). The inset shows the general form of the voltage (V_g) derivatives of the experimental $C'_{V\,ex}$ (*1*, *1*') and ideal $C'_{V\,id}$ (*2*, *2*') QS CVCs versus the normalized capacitances C_{Vex} and C_{Vid} of a MOS structure.

experimental and ideal C'_V–C_V curves, we find the voltage V_g^{ex} and take it to be V_{g0}. Using the equal values of $C_{Vex}(V_{g0})$ and $C_{Vid}(V_g^{id})$, we find the voltage V_g^{id}, as well as the corresponding. exactly known surface potential $\psi_S^{id} = \psi_{S0}$ of an ideal semiconductor, i.e., the sought-for integration constant $\psi_{S0}(V_{g0})$ (see Eq. (2)).

Thus, the exact relation between the surface potential ψ_{S0} of a real semiconductor and the voltage V_{g0} applied to the MIS structure under study is determined purely analytically with no geometrical manipulations. As a result, self-consistent identification of the experimental and ideal QS CVC regions with the functionally identical dependences $\psi_S^{ex}(V_g^{ex}) = \psi_S^{id}(V_g^{id})$ is attained, which does not require any assumptions about the shape of the IS spectrum. Such regions can appear in various QS CVC portions, which immediately indicate a very low density of ISs or their absence. Therefore, this method may be applied to identify a number of potentials $\psi_{S0}(V_{g0})$ (rather than a single one) required to calculate the functions $\psi_S(V_g)$ and $N_{SS}(E)$, as well as for the independent verificotion of data obtained.

The QS CVCs $C(V_g) = I(V_g)/\beta_V$ of the MOS structure were measured in the mode of linear field sweep,

$$V_g = V_g^0 + \beta_V t, \quad V_g^0 = V_g|_{t=0},$$

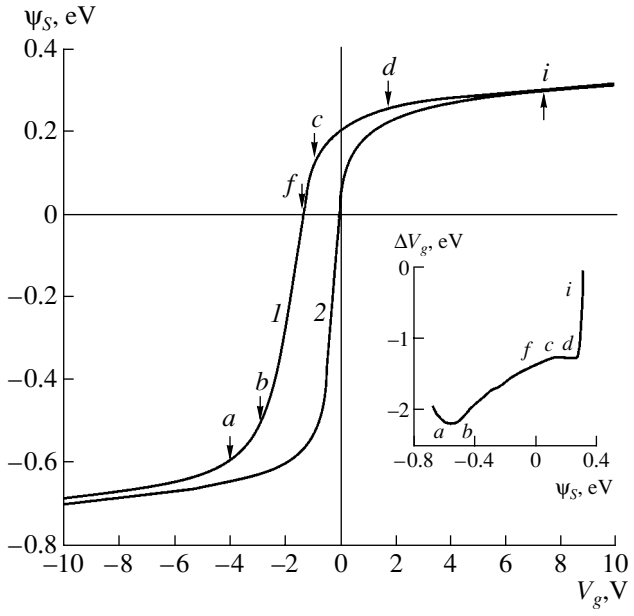

Fig. 3. Experimental (*1*) and ideal (*2*) dependences of the silicon surface potential ψ_S on the voltage V_g for the structure under study. Arrows *a*, *b* (inversion) and *c*, *d* (enhancement) indicate the region were the curves of Fig. 2 are brought into coincidence. The inset illustrates the effect of ψ_S on the shift ΔV_g between curves *1* and *2* along the voltage axis.

where β_V = const = ±40 mV/s is the sweep rate, *t* is the time, $C(V_g)$ is the differential capacitance of the MOS capacitor, and $I(V_g)$ is the current. Two QS CVCs were measured using a digital system [9] in the range $-10 \le V_g \le 10$ V: at $V_g^0 = -10$ V ($\beta_V > 0$) and at $V_g^0 = 10$ V ($\beta_V < 0$). The curves $C(V_g)/C_i$ measured at $\beta_V > 0$ and $\beta_V < 0$ were averaged, which allowed elimination of systematic errors caused by the contribution of noncapacitive current components to the QS CVC [10]. The normalizing factor

$$C_i = (|I_{a1}| + |I_{a2}|)/2|\beta_V| = 489.1 \text{ pF}$$

was determined by the averaged QS CVC; I_{a1} and I_{a2} are the currents corresponding to the states of high enhancement of the Si surface at $\beta_V > 0$ and $\beta_V < 0$, respectively.

The experimental data and the results on the numerical calculations of the experimental and ideal QS CVCs (see Fig. 1, inset)

$$C'_{V\,\mathrm{ex}}(V_g^{\mathrm{ex}}) = f[C_{V\,\mathrm{ex}}(V_g^{\mathrm{ex}})] \text{ and}$$
$$C'_{V\,\mathrm{id}}(V_g^{\mathrm{id}}) = f[C_{V\,\mathrm{id}}(V_g^{\mathrm{id}})]$$

for the MOS structure under study are shown in Fig. 2 (curves *1*, *1'* and *2*, *2*'). The upper and lower portions correspond to the Si surface enrichment ($C'_{V\,\mathrm{ex}}(V_g^{\mathrm{ex}})$, $C'_{V\,\mathrm{id}}(V_g^{\mathrm{id}}) > 0$) and inversion ($C'_{V\,\mathrm{ex}}(V_g^{\mathrm{ex}})$, $C'_{V\,\mathrm{id}}(V_g^{\mathrm{id}}) < 0$), respectively. In both regions, curves *1*, *2* and *1'*, *2'* coincide at $C_V(V_g) > 0.95$ (high $|V_g|$) within experimental error. The sign of the derivatives changes only at the transition from the enrichment mode to the depletion and inversion mode, remaining unchanged in the corresponding V_g ranges. In the entire range of arguments, we have $\left|C'_{V\,\mathrm{ex}}(V_g^{\mathrm{ex}})\right| \le \left|C'_{V\,\mathrm{id}}(V_g^{\mathrm{id}})\right|$, which reasonably represents the experimental QS CVC "extension" caused by the ISs. Violation of this pattern can point to one of the following factors: (i) the QS CVCs measured are nonequilibrium ($|\beta_V|$ is too large); (ii) discrete or quasi-discrete ISs exist at the HJ (i.e., the "smooth spectrum" condition, requiring weak variation of the DoS in the energy region ~*kT*, is violated [1]); and (iii) a certain interaction takes place in the electron system of the surface [11, 12]. Thus, the correlation between the functions $C'_{V\,\mathrm{ex}}(V_g^{\mathrm{ex}})$ and $C'_{V\,\mathrm{id}}(V_g^{\mathrm{id}})$ is a sensitive indicator of both the correctness of the QE CVS technique and manifestations of unexpected physical factors.

Figure 3 (curve *1*) shows the aTSolute surface potential of Si versus V_g. The potential was calculated by numerical integration of Eq. (2) using the values of $\psi_{S0}(V_{g0})$ obtained by the procedure described above for both the enhancement $[\psi_{S0}^{\mathrm{as}}(V_{g0}^{\mathrm{as}})]$ and inversion $[\psi_{S0}^{\mathrm{in}}(V_{g0}^{\mathrm{in}})]$ modes. The inset in Fig. 3 illustrates the effect of ψ_S on the shift of curve *1* ΔV_g along the voltage axis with respect to ideal curve *2*. Arrows *a*, *b* (inversion) and *c*, *d* (enhancement) indicate the regions where the experimental and ideal curves are brought into coincidence in Fig. 2. We can see that ΔV_g = const in the regions where the curves in Fig. 2 coincide; i.e., curve *1* is equidistant from ideal curve *2* in these ranges to a high accuracy. This confirms the reliability and correctness of the technique suggested for calculating the additive constants $\psi_{S0}(V_{g0})$ and the actual dependence $\psi_S(V_g)$. We used the following parameters for calculating the dependences in Fig. 3: $\psi_{S0}^{\mathrm{as}} = 0.2840$ eV, $V_{g0}^{\mathrm{as}} = 4.25$ V, $\psi_{S0}^{\mathrm{in}} = -0.5736$ eV, and $V_{g0}^{\mathrm{in}} = -3.5$ V. The values of $\psi_{S0}^{\mathrm{as}}(V_{g0}^{\mathrm{as}})$ and $\psi_{S0}^{\mathrm{in}}(V_{g0}^{\mathrm{in}})$ were taken at the centers of intervals (*c*, *d*) and (*a*, *b*). The steep "tails" of the function $\Delta V_g(\psi_S)$ in Fig. 3 can be caused by an increase in the systematic error in the experimental determination of the QS CVC at the measuring range edges (see Eq. (3)).

It is noteworthy that significant systematic errors accumulate in ψ_S due to the poor accuracy of the measurements and calculations at the limits of the numerical integration ranges of Eq. (2). To minimize errors, the additive constants $\psi_{S0}^{\mathrm{in}}(V_{g0}^{\mathrm{in}})$ and $\psi_{S0}^{\mathrm{as}}(V_{g0}^{\mathrm{as}})$ were selected in the central portion of the intervals (*a*, *b*) and (*c*, *d*), within which ΔV_g = const. Equation (2) was ini-

tially integrated from $V_g = V_{g0}^{in}$ to $V_g^0 = 10$ V and again from $V_g = V_{g0}^{as}$ to $V_g^0 = 10$ V, and then from $V_g = V_{g0}^{as}$ to $V_g^0 = 10$ V and again from $V_g = V_{g0}^{as}$ to $V_g^0 = -10$ V. The results of integration were joined at the Si mid gap, where calculation error is minimum [1].

We now consider the possibility of determining the electronic characteristics of the Si/SiO_2 HJ on the basis of the data in Fig. 3. In the ranges of the absence of IS (portions *a–b* and *c–d*, see the inset), a constant shift ΔV_g^{as} between curves *1* and *2* takes place, where the averaged shift $\Delta V_g^{as} = -1.254 \pm 0.002$ V in the enrichment region differs from that in the inversion region $\Delta V_g^{as} = -2.149 \pm 0.005$ V. Curve *1* is shifted with respect to curve *2* to negative V_g due to a fixed positive charge with a density Q_f in the oxide.[1] The flat-band voltage for curve *1* is

$$V_{FB} = V_g|_{\psi_S = 0} = -1.348 \text{ V}$$
$$= V_k - \text{sgn}(q)V_f - \text{sgn}(q)V_{SS},$$

where $V_k = -0.426$ V is the Al/Si contact potential difference, $V_f = SQ_f/C_i$; $V_{SS} = SQ_{SS}/C_i$; and Q_{SS} is the charge density, localized at the IS at $V_g = V_{FB}$.

$$V_k(\text{Al/Si})$$
$$= -(1/q)\{0.38 + kT\ln[N_c(T)10^4/N_c(300\text{ K})N_d]\},$$

where N_c is the effective DoS in the Si conduction band Si [2]. At $T = 293$ K and $N_d = 1.58 \times 10^{13}$ cm^{-3}, $V_k = -0.426$ V.

To determine Q_f, the density Q_{SS} of charged interface states located below the energy level $E = \psi_S = 0$ should be estimated. It is evident that

$$SQ_{SS} \simeq \delta\Delta V_g C_i = V_{SS}C_i,$$

where $\delta\Delta V_g = 0.792$ V is the increment of the voltage difference ΔV_g between curves *1* and *2* from point *f* in Fig. 3, where $\psi_S = 0$, to point *b*, $\psi_S = -0.506$ eV (see also the inset), i.e,. $V_{SS} = \delta\Delta V_g$. Then we have

$$\text{sgn}(q)V_f = -V_{FB} + V_k - \text{sgn}(q)V_{SS}$$
$$= 1.348 - 0.426 + 0.792 = 1.714 \text{ V}$$

and the density of positive charges fixed in SiO_2 is

$$N_f = Q_f/qS = V_f C_i/qS \simeq 2.2 \times 10^{11} \text{ cm}^{-2},$$

while the number of ISs filled at $V_g = V_{FB}$ is

$$N_S = Q_{SS}/qS = V_{SS}C_i/qS \simeq 1.0 \times 10^{11} \text{ cm}^{-2}.$$

A similar procedure can be used to estimate the number of ISs localized in the ψ_S ranges from point *f* to point *c* ($V_{SS} = 0.092$ V, $N_S \simeq 1.2 \times 10^{10}$ cm^{-2}) and from point *f* to the intersection point *i* of curves *1* and *2* ($V_{SS} = 1.348$ V, $N_S \simeq 1.71 \times 10^{11}$ cm^{-2}). Hence, the average density of ISs within the Si band gap $E_g = 1.12$ eV is $N_{SS} \simeq 2.42 \times 10^{11}$ cm^{-2} eV^{-1}.

The estimates of N_f, N_{SS}, and the qualitative distribution of ISs over the Si band gap are adequate for most of the problems of physical diagnostics of electronic properties of semiconductor–insulator HJs. The appreciable (up to $\Delta E \simeq 0.9$ eV) broadening of the observational energy range of the function $\psi_S(V_g)$, extending also to the density $N_{SS}(E)$ of ISs, offers not only the possibility of, but also a high (tenths of a percent) accuracy of V_{FB} measurements. Thus, the detection of even a very weak "physical" response of the MIS structure to external effects or to variations in Hj fabrication is ensured; in particular, this applicable to the silicon HJ with promising new undergate insulators, which are necessary for submicrometer MIS transistors [15, 16]. Hence, an analysis of the dependences $\psi_S(V_g)$ constructed using the C_V'–C_V diagrams allows one to abandon the conventional practice of studying semiconductor–insulator HJs on the basis of purely qualitative observations of the QS CVC shape and position evolution along the voltage axis [17, 18] in favor of direct quantitative studies of HJ electronic properties and their variations with time, operating conditions, as well as under various stresses.

The method of C_V'–C_V diagrams can be readily generalized to the case of high-frequency (HF) CVCs. The determination of the energy "gaps" containing no localized electron states in the IS spectra using such diagrams will allow the determination of the reference points $\psi_{S0}(V_g)$ and the absolute values of $\psi_S(V_g)$ independently of the measuring signal frequency f_m. Thus, it becomes possible to eliminate a certain ambiguity in the data extracted from HF CVCs, which is caused by insufficiently high values of f_m that do not meet the "high-frequency" CVC condition $f_m \gg \tau^{-1}$, where τ is the characteristic recharging time of "fast" ISs.[2] A similar problem arises in the methods for studying the MIS structures based on the stabilization of their HF capacitance at a given level by a corresponding variation in V_g [5, 20, 21]. The problem can be solved by stabilizing the MIS structure capacitance at the values of ψ_S, $C(V_g)$, and V_g determined by the C_V'–C_V diagrams and corresponding to the energy "gaps" in the density of ISs. This, in principle, will allow one to control the

[1] In the vicinity of room temperature, the mobile charge does not manifest itself in the oxide of the structures under study [13, 14].

[2] As a rule, HF CVCs are measured at the frequency $f_m = 1$ MHz [1, 2, 5]. Meanwhile, the population of "fast" ISs has time to respond to the testing signal frequency up to $f_m > 100$ MHz ([1, ch. 8, 2.4; 19]), which results in significant errors when determining the electronic characteristics of the MIS structures by the HF CVC methods ([1, ch. 8, 3.3]).

absence of the contribution of the capacitance of fast ISs to the stabilized capacitance signal.

ACKNOWLEDGMENTS

We are grateful to E.I. Gol'dman for his helpful participation in discussions and E.L. Novikova for assistance in the course of this study.

REFERENCES

1. E. H. Nicollian and J. R. Brews, *MOS (Metal Oxide Semiconductor) Physics and Technology* (Wiley, New York, 1982).
2. S. M. Sze, *Physics of Semiconductor Devices*, 2nd ed. (Wiley, New York, 1981; Mir, Moscow, 1984), Vol. 1.
3. H. Watanabe, T. Baba, and M. Ichikawa, J. Appl. Phys. **85**, 6704 (1999).
4. E. M. Vogel, M. D. Edelstein, and J. S. Suechle, J. Appl. Phys. **90**, 2338 (2001).
5. L. S. Berman and A. A. Lebedev, *Deep-Level Transient Spectroscopy of Semiconductors* (Nauka, Leningrad, 1981).
6. C. N. Berglund, IEEE Trans. Electron Devices **13**, 701 (1966).
7. V. Kuhn, Solid-State Electron. **13**, 873 (1970).
8. G. Declerk, R. van Overstraeten, and G. Broux, Solid-State Electron. **16**, 1451 (1973).
9. E. I. Gol'dman, A. G. Zhdan, and G. V. Chucheva, Prib. Tekh. Éksp., No. 6, 110 (1997).
10. A. G. Zhdan, N. F. Kukharskaya, and G. V. Chucheva, Prib. Tekh. Éksp., No. 1, 1 (2002).
11. V. G. Prikhod'ko, Candidate's Dissertation (Moscow, 1982).
12. A. G. Zhdan and V. G. Prikhod'ko, Fiz. Tekh. Poluprovodn. (Leningrad) **17**, 690 (1983) [Sov. Phys. Semicond. **17**, 430 (1983)].
13. E. I. Gol'dman, A. G. Zhdan, and G. V. Chucheva, Fiz. Tekh. Poluprovodn. (St. Petersburg) **31**, 1468 (1997) [Semiconductors **31**, 1268 (1997)].
14. E. I. Goldman, A. G. Zhdan, and G. V. Chucheva, J. Appl. Phys. **89**, 130 (2001).
15. J. Kwo, M. Hong, A. R. Kortan, *et al.*, J. Appl. Phys. **89**, 3920 (2001).
16. R. S. Johnson, J. G. Hong, and G. Lucovsky, J. Vac. Sci. Technol. B **19**, 1606 (2001).
17. R. Sharma, J. L. Fretwell, T. Ndai, and S. Banerjee, J. Vac. Sci. Technol. B **17**, 460 (1999).
18. R. Wetzler, A. Wacker, E. Schöll, *et al.*, Appl. Phys. Lett. **77**, 1671 (2000).
19. M. R. Boudry, Appl. Phys. Lett. **22**, 530 (1973).
20. V. Lang, J. Appl. Phys. **45**, 3023 (1974).
21. V. I. Antonenko, A. G. Zhdan, A. I. Minchenko, and P. S. Sul'zhenko, Fiz. Tekh. Poluprovodn. (Leningrad) **20**, 208 (1986) [Sov. Phys. Semicond. **20**, 131 (1986)].

Translated by A. Kazantsev

Semiconductors, Vol. 37, No. 6, 2003, pp. 667–674. Translated from Fizika i Tekhnika Poluprovodnikov, Vol. 37, No. 6, 2003, pp. 692–699.

SEMICONDUCTORS STRUCTURES, INTERFACES, AND SURFACES

Atomic-Force-Microscopy Visualization of GeSi Buried Nanoislands on Crystal Cleavages in Silicon Structures

M. S. Dunaevskiĭ*, Z. F. Krasil'nik, D. N. Lobanov**, A. V. Novikov**, A. N. Titkov*, and R. Laiho*****

**Ioffe Physicotechnical Institute, Russian Academy of Sciences, Politekhnicheskaya ul. 26, St. Petersburg, 194021 Russia*
***Institute for Physics of Microstructures, Russian Academy of Sciences, Nizhni Novgorod, 603600 Russia*
****Wihury Laboratory, University of Turku, Turku, Finland*
Submitted November 21, 2002; accepted for publication December 3, 2002

Abstract—The topographic characteristics of cleaved surfaces in Ge/Si structures containing buried layers of GeSi nanoislands were investigated by atomic-force microscopy in atmospheric air. The relaxation of elastic stresses in islands and in adjacent regions of the Si matrix on the free cleaved surface was shown to result in local topographic features on the cleavages of the structures. It was found that the islands can appear on the cleaved surface in the form of two types of topographic features: as hillocks, if the cleavage plane directly crosses an island elastically compressed in the Si matrix, or as a pit, if the cleavage plane crosses the Si-matrix region adjacent to the island and subjected to tensile stress. The investigations performed showed the potential of the new method of studying buried nanoislands for revealing their presence; estimating their sizes, size distribution, and interaction effects in multilayer structures; and also for revealing strains associated with them.

1. INTRODUCTION

Semiconductor layers with incorporated self-organizing nanometer islands of another semiconductor material, called quantum dots (QDs), are important structural elements in promising devices of semiconductor electronics [1]. Among the many problems in forming and describing semiconductor structures with incorporated QD layers, a crucial problem is the direct visualization of buried QDs. Solving this problem is necessary for determining the sizes and shapes of QDs, their size distribution, and the correlation of their mutual positions within a single layer, as well as in nearby layers for multilayer structures. Correlation of the mutual positions of QDs is caused by the presence of elastic strains around them, due to a mismatch in the lattice constants of materials in the QDs and in the surrounding matrix.

Presently, the visualization of buried QDs is typically realized by transmission electron microscopy (TEM) with observations made in two configurations: planar and transverse. The TEM method is reliable, highly sensitive, and informative in studying buried QDs [1]. However, its application is markedly limited by the complexity and long duration of the procedure for preparing thin samples hundreds or even tens of nanometers in size, which is necessary for TEM investigations. Furthermore, the sizes of sections of the necessary thickness turn out to be small, which additionally hampers performing comprehensive investigations of QD properties with sufficient statistics.

The current methods of scanning probe microscopy—scanning tunneling microscopy (STM) [2] and atomic-force microscopy (AFM) [3]—are opening up new opportunities for investigating the cleaved surfaces of structures when these surfaces interest the layers with QDs. In this case, it is possible to reveal QDs appearing at the cleaved surface; i.e., the QDs are observed "in profile" in their growth plane. The STM observation of QDs on a cleaved surface is based on a distinction between the electron properties of the QDs and those of the surrounding matrix, and also on the detection of local features appearing in the smooth-cleavage topography due to the relaxation of elastic stresses in the QDs. AFM is predominantly sensitive to variations in the topographic characteristics (henceforth, in the topography) of the cleavages associated with the presence of QDs.

There are several well-known works dealing with the STM investigation of structures with buried QDs [4–7]. All of these investigations were concerned with a single system, i.e., InGaAs QDs in a GaAs matrix. The InGaAs-QD sizes are characterized by mean values of the base diameters (approximately 15 nm) and heights (3–4 nm). The lattice constant for InAs is 7% larger than that for GaAs, which gives rise to elastic compressive strains in InAs QDs and elastic tensile strains in the GaAs region adjacent to the QDs. For such system parameters, the STM investigation of the cleavages of structures revealed QDs in InAs in the form of hillocks, 0.3 nm in height, on the cleaved surfaces. In the studies mentioned, detailed information was obtained on the linear dimensions, density, and

correlation in the distribution of InAs QDs. The sensitivity of the STM method to the electronic properties of QDs made it possible to obtain valuable data on the distribution of the electronic-state density in the bulk of individual InAs QDs [5].

Despite its good results, the STM investigation of buried QDs is very complicated and thus unlikely to gain wide application. Among the unavoidable difficulties, we can mention the necessity of performing STM investigations in an ultrahigh vacuum so as to avoid the oxidation of the cleaved surfaces, which must also be prepared in vacuum; the complexity of preparing the probing tips; the spontaneous modification of the tips in the process of scanning the surface; and also the general complexity of the STM method.

In this context, the use of the AFM method seems to be much simpler and more expeditions for studying buried QDs because it allows for the study of the surface topography in atmospheric air with a resolution better than 0.1 nm in height and down to several nanometers in plane. In addition, ready-made probing tips of the necessary sharpness can be obtained from commercially. Furthermore, the oxidation of surfaces does not present an obstacle to performing AFM investigations. Nevertheless, as far as we know, there have been no AFM investigations of buried QDs. The appearance of roughness on initially atomically smooth cleaved surfaces in the case of their oxidation under room-temperature conditions can hamper the observation of individually arranged nanohillocks associated with QDs. However, it is known that the roughness of oxidized cleaved surfaces does not usually impede the observation of monatomic steps, whose height is approximately 0.3 nm in many semiconductors. The general contamination of surfaces in atmospheric air seems to be a more substantial problem; all possible precautions have to be taken to reduce this contamination.

This study is aimed at revealing the potential of AFM in studying buried QDs. As the objects of investigation, we chose self-organizing nanoislands in a GeSi/Si(001) structure (henceforth, the GeSi islands) incorporated in a silicon matrix [8–11]. The mismatch between the lattice constants of Ge and Si amounts to 4.2%, which is markedly less than that for the crystal lattices of InAs and GaAs. The sizes of GeSi islands depend heavily on the growth temperature, and, at the Ge-deposition temperature $T_g \gtrsim 600$°C, the GeSi nanoislands have linear dimensions which are an order of magnitude larger than those of the InAs QDs [11]. For this reason, and taking into account that the values of strains around the QDs depend both on the difference in lattice constants and on the QD sizes [12, 13], we can expect that larger GeSi islands will markedly protrude above the cleavage plane.

The atmospheric-air AFM study of the topography of the cleaved surfaces in Si structures with buried GeSi islands actually makes it possible to reveal the presence of islands in the morphology of the cleaved surface. As it turns out, in addition to islands appearing on the cleavage plane and manifesting themselves in the form of local hillocks, there are islands that do not appear directly on the surface, but lie close to it and induce a local depression of the surface above them. The cause of this effect is the strain that also arises in the Si matrix near the islands, along with that in the GeSi islands themselves. The strain in the Si regions is tensile and manifests itself in the form of local depressions of the cleaved surface above the islands lying nearby. Investigations of cleaved surfaces in multilayer Ge/Si structures have made it possible to observe the characteristic effects of the vertical alignment of GeSi islands in neighboring layers. These investigations have also made it possible to characterize the stresses in the Si layers separating the GeSi islands.

2. EXPERIMENTAL

Structures with GeSi islands were grown on Si(001) substrates using molecular-beam epitaxy at Ge-deposition temperatures $T_g = 600$ and 700°C. Silicon and germanium were evaporated using electron-beam evaporators. The growth rate was 0.15 nm/s for Ge. We grew single-layer and multilayer (five-layer) structures with GeSi islands. The equivalent thickness of deposited Ge was between seven and nine monolayers (one monolayer ≈ 0.14 nm). As a test structure, we grew a structure consisting of five periods of $Ge_{0.3}Si_{0.7}$ quantum wells, 9 nm thick, and separated by Si layers 30 nm thick.

AFM studies of the topography of the cleaved surfaces in the structures obtained were performed with a P-47 SEMI system (NT-MDT company) in the tapping mode. As probes, we used silicon cantilevers, whose probing-pyramid tip had with a curvature radius of 15–20 nm (SCNC12, NT-MDT), as well as whiskers, whose distinctive feature was the termination of the probing pyramid by an extended, narrow, and more acute cone from a material based on carbon (NCC05, NT-MDT). The application of whiskers markedly improved the contrast of the Ge-island images, especially in the case of multilayer structures, as the spacings between layers with GeSi islands decreased. The structures were cleaved along the [111] and [110] crystal directions. For obtaining atomically smooth cleaved surfaces free of step formations, the structures were thinned by polishing from the substrate side to a thickness less than 100 μm before cleaving.

3. RESULTS AND DISCUSSION

As shown in Fig. 1a, the AFM studies of Si(001) surfaces with deposited Ge layers indicate, that, at a growth temperature of 700°C and for an effective thickness of deposited Ge monolayers of $d_{Ge} = 7$–9, GeSi islands are formed on the surface of structures; these islands have a predominantly dome shape (so-called "dome" islands). The lateral size and height of unburied

islands determined from statistical analysis of the AFM images was 100–110 and 15–20 nm, respectively (see the distributions shown in Fig. 1b). These sizes exceed the typical sizes of InAs QDs by an order of magnitude, which is associated with an initially lower mismatch in the crystal lattices of the Ge/Si heterostructure as compared with the InAs/GaAs heterostructure. In addition, at the Ge-deposition temperature $T_g \geq 600$°C, the formation of a GeSi alloy with an Si content reaching 60 at. % [11] takes place, which results in a further reduction in the mismatch between the crystal lattices of the GeSi island and the Si matrix to a level of 1–2%.

In Fig. 2, we show the AFM images of cleaved surfaces for single-layer structures with GeSi buried islands grown at 700°C and differing only in the thickness of the Si covering layer. In the images of both structures, it can be seen that the cleaved surface contains local elevations (hillocks) and lowerings (pits) aligned in parallel to the growth surface of structures and separated from it by the value of the thickness of the Si covering layer for each structure. The AFM images in Figs. 2b and 2c, which were obtained at a high magnification, make it possible to discern hillocks and pits extended along the arrangement line. The magnitude of the roughness along this line (150–200 nm) is only slightly larger than the mean value of the diameter of the base of unburied GeSi islands (110 nm). These observations make it possible to relate the appearance of these features in the cleaved surface with the relaxation of elastic stresses in the layer of self-organizing GeSi islands and in their neighborhood. Detailed consideration of the AFM images and the profiles on the basis of the features revealed shows that they have a complex shape: the hillocks are surrounded by pits (Fig. 2b) and the pits are surrounded by elevations in the neighboring surface (Fig. 2c).

An interpretation of the origin of the features discovered on the cleavages of structures with GeSi islands and their relation to elastic-strain relaxation in the GeSi islands and in the surrounding Si matrix is illustrated in Fig. 3. If the structure cleavage passes directly through a GeSi island, the relaxation of elastic compression strains in the island bulk leads to its local elevation above the initially smooth cleaved surface. At the same time, the relaxation of elastic extension strains in the Si-matrix regions adjacent to the island leads to the lowering of the cleaved-surface areas adjacent to the island. As a result, if the cleavage passes directly through a GeSi island, the relaxation of elastic strains induces the formation of a local elevation of the surface surrounded on both sides by a local lowering of the surface (Figs. 3a, 2b).

If a GeSi island is located close to the cleaved surface, the relaxation of elastic stresses in the Si layer compressed in the neighborhood of the island leads to the appearance of pits on the cleavage surface surrounded by local surface elevations compensating the strain (Figs. 3b, 2c). In general the same elevations

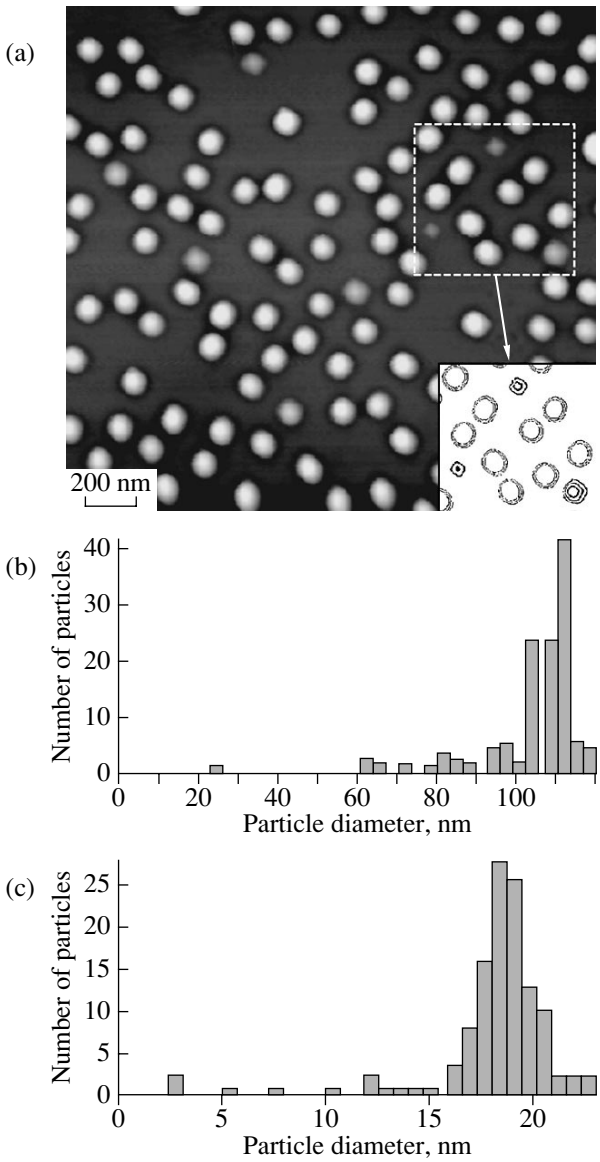

Fig. 1. (a) AFM image of a sample with unburied self-organizing GeSi islands grown at $T_g = 700$°C; (b) and (c) are histograms of the distribution in lateral size and height of the islands obtained as a result of processing the image (a).

should also accompany the lowering of the Si-matrix level when there is a direct outcrop of a GeSi island on the surface. In this study, we do not discuss these elevations because they were not reliably detected. As an estimate of the deepest lowering of a GeSi island relative to the cleaved surface, when it can still be observed in the cleavage topography, we can evidently take the value of 50–60 nm, which corresponds to the falloff distance for a strain in the Si matrix as it recedes from the GeSi island [14].

According to the model suggested for the formation of the features observed on the cleaved surface and induced by the relaxation of elastic stresses in and around GeSi islands, the sizes of the features along the

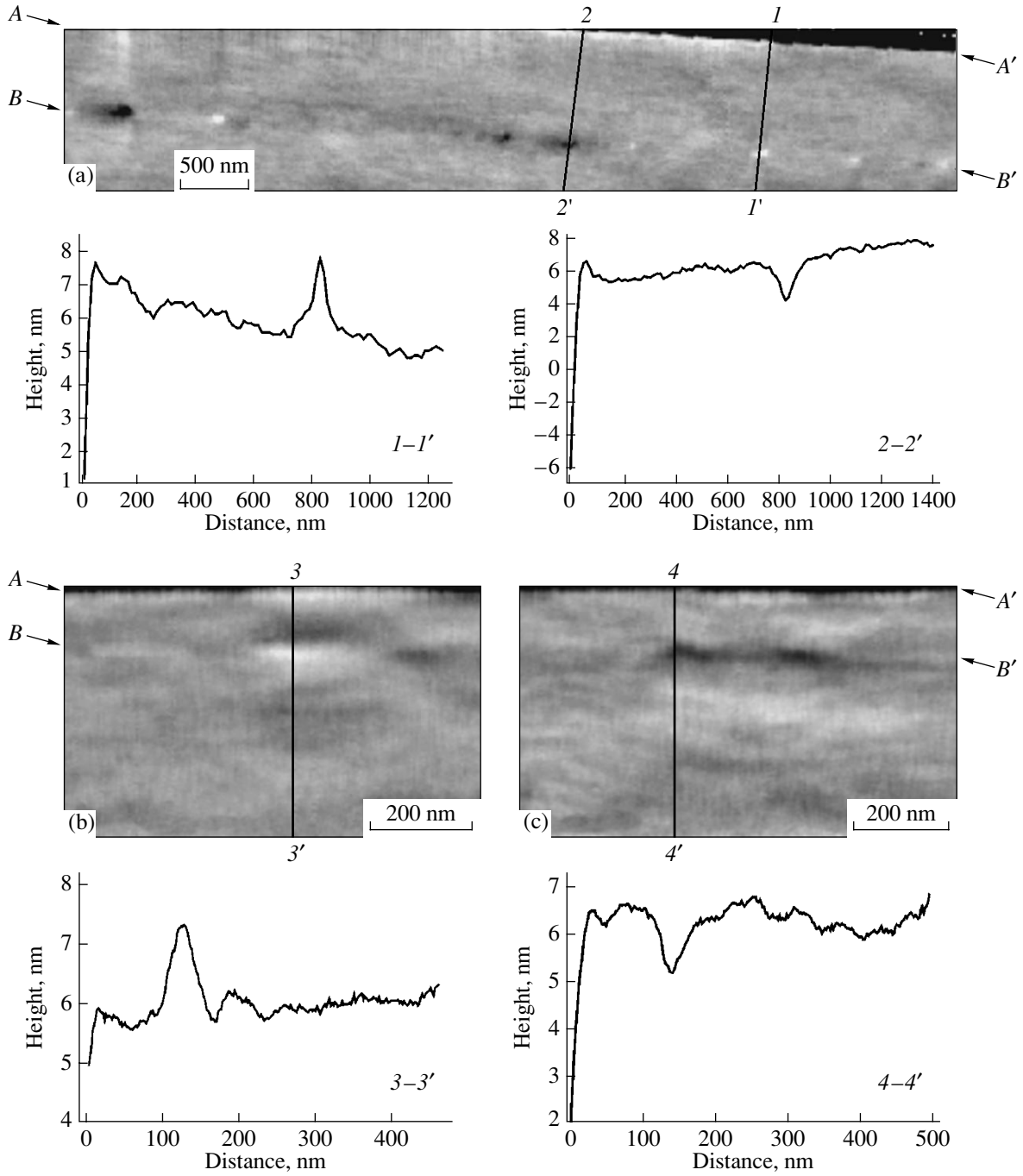

Fig. 2. AFM image and the topography of cleaved surfaces for single-layer structures with GeSi islands grown at 700°C and whose covering Si layer has a thickness (a) 760 and (b, c) 110 nm.

structure-growth direction must be associated with the heights of the buried islands, while the lengths of the features in the growth plane are related to the lateral size of the islands. Measuring the revealed features of the cleaved surfaces may enable one, in the future, to control the sizes of interest of the buried nanoislands. These observations, performed for the first time, show that the lateral sizes of the features somewhat exceed the mean values of the height and diameter of unburied GeSi islands. An increase in the lateral size of islands in the process of overgrowth was previously observed in [15] and was associated with changes in the shape of an island. According to the model [15], in the case of high-temperature overgrowth, the island height decreases. However, the AFM measurements of cleavages of structures yield an estimate of 50–60 nm for the island height, which greatly exceeds the mean height of unburied islands (20 nm). One of the natural causes of

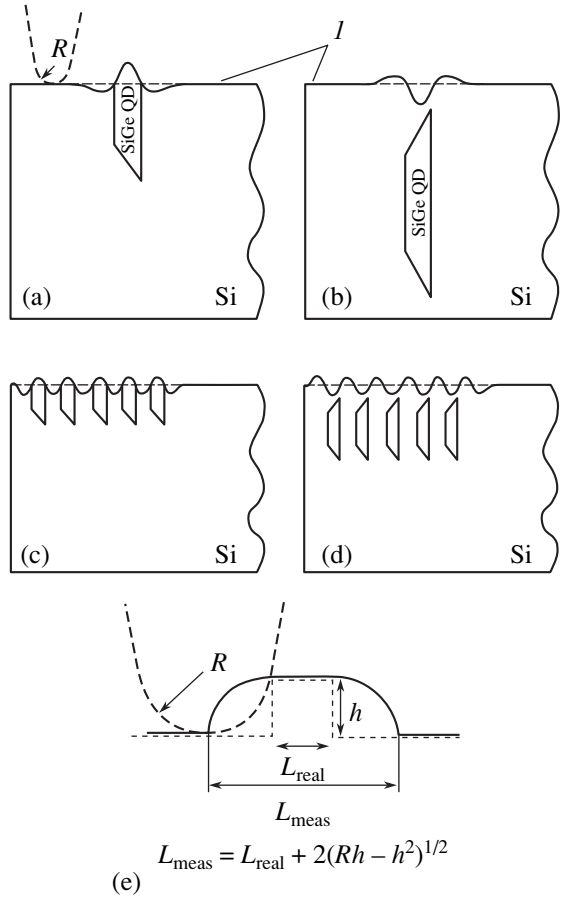

Fig. 3. Schematic representation of the origin of the topographic features observed on the cleaved surface and associated with elastic-strain relaxation in the SiGe islands and in the Si matrix: (a, b) for single-layer structures and (c, d) for multilayer structures when cleavage passes (a, c) through the islands or (b, d) close to them; (e) an estimate of the increase in the sizes of topographic features in the cleavage plane due to the finite size of the tip of the atomic-force-microscope.

the discrepancy revealed is the finite size of the microscope tip in the AFM measurements and the related increase in the sizes of features detected in the cleavage plane. This contribution to the broadening can be estimated using the expression resulting from the layout of the measurements:

$$L_{meas} = L_{real} + 2(2Rh - h^2)^{1/2},$$

where L_{meas} is the measured value, L_{real} is the true value, R is the probing-pyramid radius, and h is the height of a feature on the cleaved surface. In our case, $R = 20$ nm and $h = 1$ nm, from which we obtain an instrumental contribution to the broadening of approximately 15 nm for the island height, which is insufficient for explaining the found discrepancy. It is possible that the magnitude of the roughness on the cleaved surface along the growth direction substantially exceeds the height of the buried islands due to the fact that this is also a part of

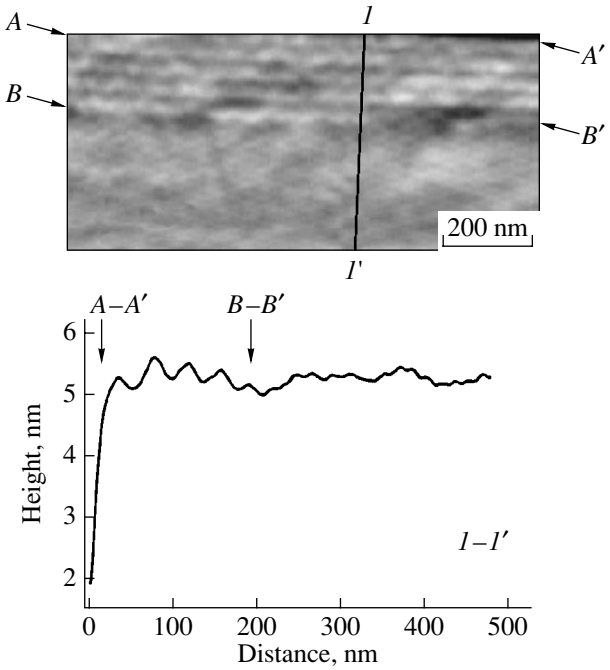

Fig. 4. AFM image and the topography of the cleaved surface of the multilayer structure with $Ge_{0.3}Si_{0.7}$ quantum wells.

the Si matrix, which is elevated in the neighborhood of the island together with it. To clarify the causes of the observed discrepancy, we think it necessary to assess the exact shape of the surface features under consideration. Such information can be obtained by considering the elastic-strain relaxation on the cleaved surfaces of structures with buried nanoislands using, for example, the method of finite-element analysis.

We now consider the topography of cleaved surfaces in the Ge/Si structures containing several layers of GeSi islands. In Fig. 4, for the sake of comparison, we show the AFM image of a multilayer test structure with island-free $Ge_{0.3}Si_{0.7}$ quantum wells. For this structure, a local elevation at the cleaved surface is observed in the form of five ridges aligned in parallel to the growth plane. The number of ridges and their repetition period coincides with the number of deposited GeSi layers and with the given period of the grown multilayer structure. These observations enable us to relate the appearance of the observed local surface elevations with the relaxation of elastic compression strains in the $Ge_{0.3}Si_{0.7}$ layers at the sites of their emergence onto the cleaved surface. Our attention is drawn to the height of the ridges (less than 0.5 nm), which is smaller than the height of features on the GeSi islands; this can be attributed to the larger content of Si in the $Ge_{0.3}Si_{0.7}$ layers, i.e., to a smaller mismatch between the lattices of the layers and the Si matrix.

For multilayer structures with islands, the cleaved-surface topography is much more complex than that of the structures with GeSi layers (Figs. 5, 6). On the

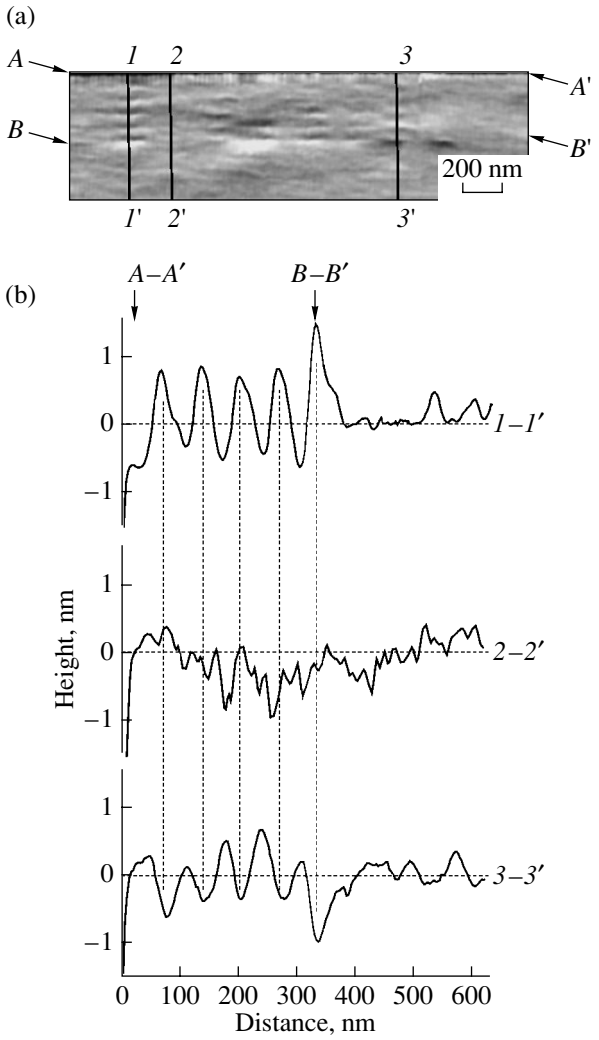

Fig. 5. (a) AFM image of the cleaved surface of the multilayer structure with self-organizing GeSi nanoislands grown at 700°C; (b) topography of the cleaved surface along the lines shown in the AFM images.

cleaved surfaces of structures with islands, we also observed the alternation of local surface elevations and depressions along the growth axis with a multilayer-structure period, whereas the number of alternations coincides with the number of deposited Ge layers. However, the modulation of the surface topography is neither continuous nor homogeneous in the growth plane and is simultaneously characterized by a substantially larger difference in heights (up to 2 nm as compared with 0.5 nm for a structure without GeSi islands) (see Fig. 4). From the analysis of the topography for the cleaved surfaces in structures with islands, we can conclude that there are two types of topographic modulation. For the first type of modulation, a local surface elevation is observed at sites corresponding to the outcrop of island layers on the cleaved surface, while, at sites of outcrop of the Si layers separating the layers with islands, a local surface depression is observed (Fig. 5, section *1–1*').

The second type of modulation features have the same period as those of the first type, but are in antiphase relative to these: we observed a surface depression at sites of the outcrop of island layers and the local elevation for the outcrop of the Si layers (Fig. 5, section *3–3*'). Similarly to the cleaved surfaces of single-layer structures with GeSi islands, the appearance of these two types of roughnesses can be related to the relaxation of elastic strains in the islands and in the Si matrix. Features of the first type are observed if the cleavage plane passes directly through the islands (Fig. 3c), while those of the second type are observed in the immediate vicinity of the islands (Fig. 3d). The periodicity in the surface topography for the cleavage along the growth axis is associated with the correlation in the vertical arrangement of islands in the neighboring layers of multilayer structures. This correlation is induced by the propagation of elastic-stress fields from the islands in lower layers of the multilayer structure to the upper layers, as well as by the related predominant nucleation of islands in the upper layers of the multilayer structure over the islands in the lower lying layers [12]. A vertical correlation in the arrangement of GeSi nanoislands in the multilayer structures was observed in the TEM investigation of structures with islands [14, 16].

Quantitative analysis of amplitudes of features observed on the cleaved surfaces and associated with GeSi islands shows that the highest amplitude both for elevations and depressions on the cleaved surface corresponds to the first grown layer of islands (Fig. 5). For the islands in upper layers of the multilayer structure, we observe an increase in the amplitudes of the features indicating to a lower initial value of elastic strains for islands in these layers. A decrease in the strain of islands can occur due to the transfer of a part of the stresses to the separating Si layers. An appreciable deviation of the Si-layer surface level from the general surface level of the Si substrate indicates considerable strain in these layers. One more reason for the dependence of feature amplitudes on the number of islands can be a difference in the composition of islands in various layers of a multilayer structure. Recently, it was shown [17] that the Si content in GeSi islands increases with the number of island layers in a structure. This fact is related to enhancement of Si diffusion into the islands from the elastically stressed separating Si layers. The islands with a higher content of Si have less mismatch between their crystal lattice and that of the Si matrix; therefore, the features appearing on the cleaved surface as a result of stress relaxation must have a lower amplitude.

Notably, there is a substantial spatial inhomogeneity in the strain in the separating Si layers; this inhomogeneity can vary both in magnitude and in type for sites differently arranged with respect to GeSi islands passing from tension to compression. The shift in the sur-

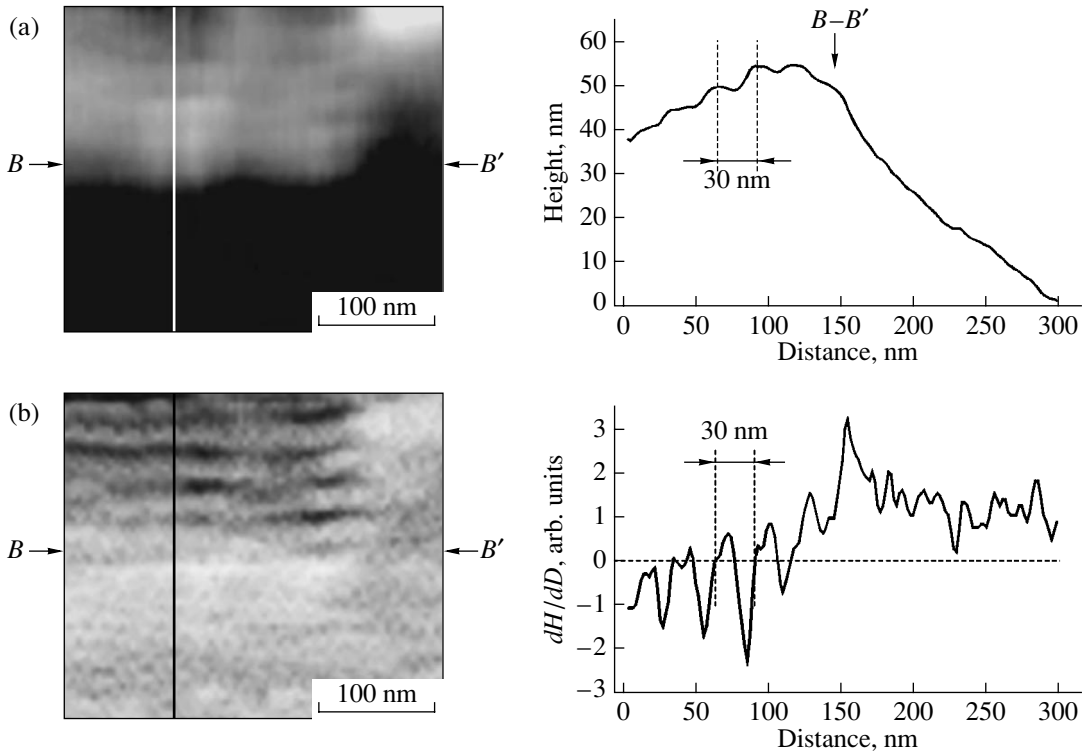

Fig. 6. AFM image and the cross section of the cleavage of the multilayer structure with self-organizing GeSi nanoislands grown at 600°C; (b) image and cross section of the cleavage obtained as a result of differentiation of the AFM image (a) with respect to the vertical coordinate *D*: *dH*/*dD* (*H* is the height, and *D* is the distance).

face level of barrier layers on the cleaved surface relative to the surface level of a relaxed Si substrate can serve as an indicator of the value and character of the initial strains (before cleaving) in various sections of these barrier layers. For example, in Fig. 5, the profile *2*–*2*' indicates the presence of a general extension of Si layers at a section of the cleaved surface, even without the observed GeSi islands.

Figure 6 shows the AFM image and topography of the cleaved surface on a multilayer structure with islands grown at a lower temperature (600°C) and with spacings of 30 nm between island layers. Unburied GeSi islands grown at this temperature were characterized by smaller mean sizes: 50–60 nm in base diameter and 10–12 nm in height. In order to obtain AFM images for the cleaved surface of a given structure, we used a whisker. In Fig. 6, it is seen that the GeSi islands and the effect of their vertical alignment were reliably detected also in the case of this considerably finer structure. A convenient possibility for enhancing the contrast of the features associated with the islands is the differentiation of the AFM images with respect to the vertical coordinate; the result of this differentiation is shown in Fig. 6b.

4. CONCLUSION

Using the example of structures with self-organizing GeSi/Si(001) islands, we have shown the possibility of revealing and studying buried nanoislands in crystalline semiconductor structures when investigating the topography of their cleaved surfaces by atomic-force microscopy with high spatial resolution. The mechanism of the appearance of nanoislands in the topography of initially smooth cleaved surfaces is associated with the relaxation of elastic strains in the islands and in the adjacent matrix regions on the free cleaved surface. In this study, we conducted a detailed consideration of the main types of topographic features corresponding to the manifestation of nanoislands both in the case of single layers and multilayer structures with nanoislands.

Since the manifestation of nanoislands in the topography of cleavages is caused by the relaxation of related elastic strain, the analysis of the shapes and sizes of the corresponding topographic features for cleaved surfaces can be used to characterize the stresses in structures with nanoislands. The development of methods for such an analysis seems to be very topical.

ACKNOWLEDGMENTS

This study was supported by the Russian Foundation for Basic Research (project nos. 00-02-16948 and 02-02-16792), INTAS (grant no. NANO-0444), and by programs of the Ministry of Industry, Science, and Technology of the Russian Federation.

REFERENCES

1. D. Bimberg, M. Grundmann, and N. N. Ledentsov, *Quantum Dot Heterostructures* (Wiley, New York, 1998).
2. *Scanning Tunneling Microscopy I: General Principles and Applications to Clean and Adsorbate-Covered Surfaces*, Ed. by H.-J. Güntherodt and R. Wiesendanger (Springer, Berlin, 1992), Springer Ser. Surf. Sci., Vol. 20.
3. *Scanning Tunneling Microscopy II: Further Applications and Related Scanning Techniques*, Ed. by H.-J. Güntherodt and R. Wiesendanger (Springer, Berlin, 1992), Springer Ser. Surf. Sci., Vol. 28.
4. W. Wu, J. R. Tucher, G. S. Solomon, and J. S. Harris, Appl. Phys. Lett. **71**, 1083 (1997).
5. B. Legrand, B. Grandidier, J. P. Nys, *et al.*, Appl. Phys. Lett. **73**, 96 (1998).
6. H. Eisele, O. Flebbe, T. Kalka, and M. Dahne-Prietsch, Surf. Interface Anal. **27**, 537 (1999).
7. B. Legrand, J. P. Nys, B. Grandidier, *et al.*, Appl. Phys. Lett. **74**, 2608 (1999).
8. G. Abstreiter, P. Schittenhelm, C. Engel, *et al.*, Semicond. Sci. Technol. **11**, 1521 (1996).
9. N. V. Vostokov, S. A. Gusev, I. V. Dolgov, *et al.*, Fiz. Tekh. Poluprovodn. (St. Petersburg) **34**, 8 (2000) [Semiconductors **34**, 6 (2000)].
10. A. I. Yakimov, A. V. Dvurechenskii, Yu. Yu. Proskuryakov, *et al.*, Appl. Phys. Lett. **75**, 1413 (1999).
11. Z. F. Krasil'nik, P. Lytvin, D. N. Lobanov, *et al.*, Nanotechnology **13**, 81 (2002).
12. J. Tersoff, C. Teichert, and M. G. Lagally, Phys. Rev. Lett. **76**, 1675 (1996).
13. A. A. Maradudin and R. F. Wallis, Surf. Sci. **91**, 423 (1980).
14. O. Kienzle, F. Ernst, M. Rühle, *et al.*, Appl. Phys. Lett. **74**, 269 (1999).
15. P. Sutter, E. Matveeva, J. S. Sullivan, and M. G. Lagally, Thin Solid Films **336**, 262 (1998).
16. C. J. Huang, D. Z. Li, B. W. Cheng, *et al.*, Appl. Phys. Lett. **77**, 2852 (2000).
17. O. G. Schmidt, U. Denker, S. Christiansen, and F. Ernst, Appl. Phys. Lett. **81**, 2614 (2002).

Translated by V. Bukhanov

Semiconductors, Vol. 37, No. 6, 2003, pp. 675–680. Translated from Fizika i Tekhnika Poluprovodnikov, Vol. 37, No. 6, 2003, pp. 700–705.

LOW-DIMENSIONAL SYSTEMS

Determination of the Parameters of Multilayer Nanostructures Using Two-Wave X-ray Reflectometry

N. L. Popov*, Yu. A. Uspenskiĭ*, A. G. Turyanskiĭ*, I. V. Pirshin*, A. V. Vinogradov*, and Yu. Ya. Platonov**

**Lebedev Physical Institute, Russian Academy of Sciences, Leninskiĭ pr. 53, Moscow, 119991 Russia*
e-mail: nlpopov@zmail.ru
***Osmic Incorporated, 1900 Tailor RD, 48326 Auburn Hills, MT, USA*
Submitted September 9, 2002; accepted for publication October 16, 2002

Abstract—A method for determining the parameters of multilayer nanostructures by measuring the angular dependence of the X-ray reflectance at two wavelengths has been considered. A calculation scheme taking into account the specificity of the method was suggested, which allows operation with samples of any size and shape. The scheme was applied to C/Ni/C, $Si_{1-x}Ge_x$, and $Al_xGa_{1-x}As$ multilayer structures. It was shown that two-wave reflectometry allows elimination of the influence of instrumental errors; hence, the thickness, density, and composition of both polycrystalline and monocrystalline nanostructure layers reliably determined. © *2003 MAIK "Nauka/Interperiodica".*

1. INTRODUCTION

X-ray reflectometry at wavelengths $\lambda \approx 0.1$ nm is widely used to determine the parameters of thin films, ultrasmooth substrates, and multilayer nanostructures. Measurements in this spectral range are especially convenient because bright laboratory sources and efficient monochromators are available and in-air measurements are possible. Routine determination of the film-structure parameters includes the measurement of the angular dependence of the reflectance R at the same wavelength (e.g., at the CuK_α line) and the calculation of the model parameters describing the structure by fitting the calculated curve to the experimental one. Since the reflection from a sample becomes appreciable only at grazing angles $\theta < 2°$–$4°$, the dependence $R(\theta)$ may be correctly measured using only rather large samples. Indeed, the probing X-ray beam begins to partially pass over the sample surface, not reflecting from it even at angles $\theta < h/L$, where h and L are the beam and sample diameters, respectively. with typical values of $\theta \leq \sim 0.5\theta_c \approx 0.2°$ (θ_c is the angle of total external reflection) and $h \geq 0.1$ mm, the minimum sample diameter is about 30 mm. Thus, it is impossible to determine the nanostructure parameters using samples with $L < 10$ mm, which is typical of laboratory practice.

A solution to this problem was suggested in [1, 2]. The essence of the solution consists in the simultaneous measurement of R at two wavelengths (e.g., at CuK_α and CuK_β lines) and in using the ratio of the intensities of the reflected signals, $\xi = I_\beta/I_\alpha$. Since the geometric parameters (sample shape and size) have an identical effect on I_α and I_β, the quantity ξ is virtually independent of the shape and size of a sample. For the same reason, fluctuations of the source strength, variations in the widths of collimating slits, and many other factors have no effect on ξ either. Thus, the use of the ratio of two reflected signals with different wavelengths allows determination of the nanostructure parameters using small and irregular-shaped samples. Moreover, the noise immunity of the procedure appreciably increases.

The use of $\xi(\theta)$ as a principal parameter for determining the structure parameters introduces a number of specific features into the calculation scheme. The conventional procedure used in reflectometry does not yield adequate results. In this paper, we analyze the causes of difficulties and suggest a method allowing correct determination of the thickness, density, and composition of layers, as well as the interface roughness in small samples. As an example, we consider the measurement data and the calculation of the parameters of several structures produced by magnetron deposition and molecular-beam epitaxy.

2. CALCULATION SCHEME USING THE RATIO OF REFLECTED SIGNALS

The calculation of the multilayer-structure parameters includes the calibration of the intensities of reflected signals and fitting the calculated curve to the experimental one. The former procedure is conventionally carried out using an $R(\theta)$ run at $\theta \longrightarrow 0$. In the wavelength range $\lambda \approx 0.1$ nm, the estimates of permittivity, $0 \leq \mathrm{Re}(1-\varepsilon) \leq 10^{-4}$ and $0 \leq \mathrm{Im}(\varepsilon)/\mathrm{Re}(1-\varepsilon) \leq 10^{-2}$, are valid for all materials. According to the Frenkel formulas (see [3]),

$$R(\theta) \approx 1 - 2\theta \mathrm{Im}\,\varepsilon/\theta_c^3 + o(\theta\theta_c^2) \quad \text{at} \quad \theta \ll \theta_c, \qquad (1)$$

$\theta_c = \sqrt{1 - \mathrm{Re}(\varepsilon)}$. It follows from (1) that $1 \geq \mathrm{Re}(\theta) \geq 0.99$ even at $\theta < 0.5\theta_c$. This yields a reasonable method for normalizing the experimental curve to unity at $\theta \longrightarrow 0$. A formula in the form of (1) is valid for multilayer structures only in the case of reflection from an infinite surface. As indicated above, a fraction of incident radiation passes beside the finite-size sample surface not reflecting from it at $\theta < h/L$; thus, $I(\theta) \approx \sin\theta$ at $\theta \longrightarrow 0$. Even if the sample shape is regular, it is impossible to reconstruct the dependence $R(\theta)$ at $\theta \ll \theta_c$, since, due to nonuniform intensity distribution over the beam cross section, $I(\theta)$ only vaguely resembles $\sin\theta$. When using the intensity ratio $\xi(\theta) = I_\beta(\theta)/I_\alpha(\theta)$, there is no problem with the calibration, since $\xi(\theta) \longrightarrow$ const at $\theta \longrightarrow 0$ and $\tilde{\xi}(\theta) \equiv R_\beta(\theta)/R_\alpha(\theta) = \mathrm{const}^{-1} I_\beta(\theta)/I_\alpha(\theta)$. Thus, the two-wave method allows us to easily determine the ratio $\tilde{\xi}$, which is a function of the sample composition and structure, rather than of the sample shape.

In practice, the structure parameters $\{X_k\}$ are determined by minimizing the residual functional

$$F\{X_k\} = \sum_i \left(f^{\mathrm{th}}(\theta_i, \{X_k\}) - F^{\mathrm{exp}}(\theta_i)\right)^2 w_i. \qquad (2)$$

As a rule, it is assumed $w_i = 1$ and $f(\theta) = \ln R(\theta)$ (the latter is due to a wide range of $R(\theta)$). When determining the parameters by $\tilde{\xi}^{\mathrm{exp}}(\theta)$, it is reasonable to set $f(\theta) = \ln(R_\beta(\theta)/R_\alpha(\theta))$. One readily sees that the function $f(\theta)$ has a maximum absolute value at points where $R_\alpha(\theta) \approx 0$ or $R_\beta(\theta) \approx 0$. Such points are noisier than others due to significant statistical error in the number n_f of photons. For example, the relative error $\delta n_f/n_f \geq 1/\sqrt{10} \approx 0.32$ at $n_f \leq 10$. When $w_i = 1$, these points make a maximum contribution to $F\{X_k\}$; thus, they have a significant effect on the parameters $\{X_k\}$. To avoid the case where the curve portions measured with the largest error control the structure parameters, we used the weight function

$$w_i = \delta f_i^2 / \left[\sqrt{\delta f_i^2 + \Delta_i^2} + \Delta_i\right]^2, \qquad (3)$$

where $\delta f_i \equiv f^{\mathrm{th}}(\theta_i) - f^{\mathrm{exp}}(\theta_i)$. The random experimental error Δ_i appearing in expression (3) may be determined as follows. As is known, $R(\theta)$ is a smooth, slowly varying function of θ on the scale $\Delta\theta \ll \lambda/4D$ (D is the least of two values: the multilayer-structure thickness or the radiation penetration depth). Introducing the experimental function $\overline{f^{\mathrm{exp}}}(\theta)$ smoothed at the scale $\Delta\theta$, we define Δ_i as

$$\Delta_i^2 = \sum_{j=i-m}^{i+m} \left(\overline{f^{\mathrm{exp}}}(\theta_j) - f^{\mathrm{exp}}(\theta_j)\right)^2/(2m+1), \qquad (4)$$

where the summation is carried out over $-\Delta\theta/2 \leq \theta_j - \theta_i \leq +\Delta\theta/2$. It is evident that the weight function introduced is small, when δf_i falls within the confidence interval $\pm\Delta_i$ (this corresponds to an intuitive concept of the equal applicability of calculated curves differing from $\overline{f^{\mathrm{exp}}}(\theta)$ by a value smaller than the experimental error) and large when δf_i is beyond this interval:

$$w_i \approx \delta f_i^2/4\Delta_i^2 \ \text{ at } \ |\delta f_i| \ll \Delta_i, \qquad w_i \approx 1 \ \text{ at } \ |\delta f_i| \gg \Delta_i. \qquad (5)$$

Thus, weight function (3) enables one to determine the parameters $\{X_k\}$ by the most reliable experimental data.

The functional $F\{X_k\}$ was minimized in two stages. First, the genetic algorithm [4] was used to determine approximately the parameter sets corresponding to the deepest residual minima. At the second stage, these sets were refined using the simplex method, after which the best solution $\{X_k^{\min}\} = \arg\min F\{X_k\}$ was selected. To estimate the possible error in the parameter set $X^{\min} = \{X_k^{\min}\}$, the set $M = \{X : F(X) - F(X^{\min}) \leq F^{\mathrm{exp}}\}$ was considered. The cross-section radius $\Delta X_k = \sup_{X \in M} \left|X_k - X_k^{\min}\right|$ was interpreted as the possible error in the parameter X_k, caused by inaccuracy in the experimental-data. The set M was constructed from points randomly selected from the parameter space X and satisfying the condition $F(X) - F(X^{\min}) \leq F^{\mathrm{exp}}$. The set M constructed in such a way contained no local minima of F for any of the samples under consideration; therefore, to speed up the procedure, the set M may be sought in a certain vicinity of the global minimum $X^{\min}$. The numerical experiments we carried out, in which the dependences $R_\alpha(\theta)$ and $R_\beta(\theta)$ were calculated, made noisy, and, used as experimental data, showed the good accuracy of the approach described above.

The calculation scheme suggested is independent of the features of the heterostructure under study and the model selected to describe it. However, the parameter set $\{X_k\}$ and the form of the function $f^{\mathrm{th}}(\theta, \{X_k\})$ should be specifies during the numerical calculations. In further examples, the thicknesses of all heterostructure layers were included in the set of varied parameters. In the cases where the exact layer density was unknown, density variation within ±5% was allowed. The diffusion-related interface spread was disregarded, since trial calculations showed this factor to be insignificant for the structures under study. The interface roughness was described by the simplest Debye–Waller model [5], which is valid for completely correlated roughnesses of all interfaces. When studying the heterostructures with thick layers, the angular divergence of the incident X-ray beam was taken into account, which was 40″ in the measurements we carried out.

3. SAMPLE PREPARATION AND REFLECTANCE MEASUREMENTS AT TWO WAVELENGTHS

The film structures under study were different in size, quality, and function. They represented the two types most commonly encountered.

(i) Multilayer X-ray mirrors. These mirrors are the most important units of optical systems operating in the soft X-ray range, which are used in X-ray lithography, astrophysics, plasma physics, biology, and materials science. We used a C/Ni/C/Si experimental structure, which was created for developing mirror technology.

(ii) Semiconductor heterostructures. The heterostructures forming quantum wells are widely used to manufacture high-frequency bipolar and field-effect transistors, optical detectors, resonant tunnel diodes, semiconductor lasers, and other quantum devices. We studied heterostructures based on $Si_{1-x}Ge_x$ and $Al_xGa_{1-x}As$.

The experimental three-layer C/Ni/C/Si structure was obtained by magnetron deposition. In the course of its fabrication, the technology of forming continuous ultrathin Ni films was developed using the ion-etching technique. The heterostructure based on Si and $Si_{1-x}Ge_x$ solid solution of varied composition was grown by molecular-beam epitaxy. The structure consisted of three Si layers, five $Si_{0.7}Ge_{0.3}$ layers, and one $Si_{0.3}Ge_{0.7}$ layer. Layers of the same composition, but of different function, differed in deposition and doping conditions. Since X-ray reflectometry does not allow detection of differences between layers of similar composition, this structure in fact may be considered as consisting of four layers of different composition, whose parameters were determined. Another heterostructure under study was designed on the basis of $Al_xGa_{1-x}As$ solid solution. This structure, consisting of eight layers and four quantum wells, was also prepared by molecular-beam epitaxy.

The angular dependences of the reflectance were measured using a two-wave reflectometer with a horizontal goniometer. An X-ray tube with a copper anode was characterized by a focus projection of 8×0.04 mm^2. The incident X-ray beam was shaped by collimating slits and a mobile absorbing screen positioned immediately in front of the sample. The beam cross section was about 4×0.04 mm^2. An X-ray beam splitter placed on a rotary arm of the detector allowed simultaneous measurements of the reflected signal at two characteristic wavelengths. The CuK_α line was separated from reflected radiation by a 46-μm-thick semitransparent monochromator made of (0001) pyrolytic graphite. The monochromator reflected 22% of the signal at the CuK_α wavelength and transmitted 85% of the CuK_β signal. The CuK_β line was separated by the second graphite monochromator. The signals were measured by two detectors and fed to a computer. The two-wave measuring system is described in [2] in more detail.

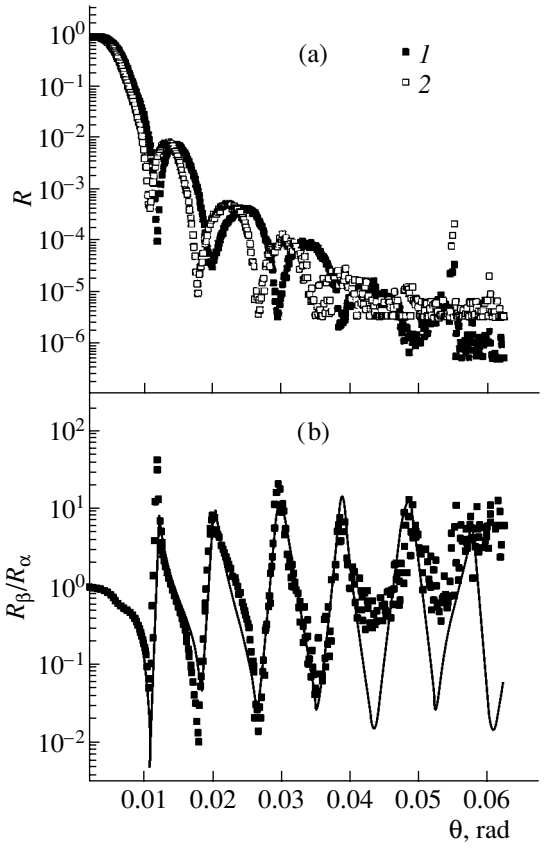

Fig. 1. Reflectance of the C/Ni/C structure versus the grazing angle of incidence (θ): (a) the reflectance at the (*1*) CuK_α and (*2*) CuK_β lines and (b) the ratio R_β/R_α; the solid curve is the calculated dependence.

4. DETERMINATION OF THE MULTILAYER STRUCTURE PARAMETERS. RESULTS AND DISCUSSION

The calculations of the parameters of three measured film structures allowed us to practically check the suggested calculation scheme and to ascertain its characteristic features. The diameter of the C/Ni/C structure on Si was 40 mm. For this structure, a steep slope of the curve $R(\theta)$ at $\theta \longrightarrow 0$ was observed only at $\theta < 0.3\theta_c$ (see Fig. 1). In this case, the calculations were carried out in two ways: using only the CuK_α line as in conventional reflectometry and with the CuK_α and CuK_β lines using the ratio $\xi(\theta)$. The calculated results agree well with each other and conform to the layer thicknesses that were preset during layer deposition (see Table 1). The calculated curves $R(\theta)$ and $\tilde{\xi}(\theta)$ approximate well the corresponding experimental dependences. This indicates the adequacy of the model of homogeneous layers with correlated roughnesses. The ratio $F^{\min}/F^{\exp} = 4.2$ (where $F^{\exp}$ is the residual between the experimental curve $\xi(\theta)$ and the smoothed experimental curve $\bar{\xi}(\theta)$) can serve as a quantitative measure of the quality of the

Table 1. Parameters of the C/Ni/C structure

Layer no.	Material	d_0, nm	d, nm	d', nm	ε, %
1	C	4.0	4.03	4.11	1
2	Ni	8.0	8.02	8.06	0.3
3	C	4.0	4.06	3.99	2

Note: d_0 is the preset layer thickness, d is the layer thickness calculated by the two-wave method, d' is the layer thickness calculated by the conventional method at $\lambda = 0.154$ nm, and ε is the relative error in the layer thickness. The roughness height σ is 0.166 nm. The minimum residual F^{min} is $4.2F^{exp}$ (for the thicknesses d_0, the residual F is $4.8F^{exp}$).

fit. Since the amorphous-carbon density ρ_C can slightly vary, depending on the deposition method, this parameter was also varied. The value determined, ρ_C = 2.12 g/cm^3, differs from the tabulated one [6] only by 2%. The small value of roughness, $\sigma = 0.17$ nm, indicates that the technology used allowed us to grow a continuous Ni film of rather high quality.

The sample of the heterostructure based on the $Si_{1-x}Ge_x$ solid solution was irregularly shaped; its average diameter was about 7 mm. In this case, the steep-slope region of $R(\theta)$ at $\theta \longrightarrow 0$ included even a critical angle (Fig. 2a); therefore, the structure parameters were determined only by the ratio $\xi(\theta)$). The calculated value $\sigma = 0.89$ nm (see Table 2) indicates a certain inaccuracy (for this sample) of the model of sharp interfaces with totally correlated roughnesses. This can probably be explained by diffusion at the interface between silicon and silicon–germanium solid solution. We note that the thickness of the last layer of the heterostructure is ~200 nm; therefore, the reflection curves exhibit oscillations with a period $\Delta\theta \approx 80''$. Such frequent oscillations are comparable to the angular divergence of the incident beam and the angular size (40″) of the entrance slit. To take into account this effect, the calculated curve was smoothed by a Gaussian curve 40″ wide. This smoothing decreased the residual from $25.5F^{exp}$ to $5.25F^{exp}$, which suggests the importance of taking angular divergence into consideration in the theoretical model. The significant error (~30%) in determining the thickness of the last layer (see Table 2) is also explained by finite angular divergence. For other layers, this factor is insignificant; therefore, their thicknesses were determined with an accuracy within a few percent. In the course of fitting, the Si density was assumed to be equal to the tabulated value (2.33 g/cm^3). The densities of the $Si_{0.7}Ge_{0.3}$ and $Si_{0.3}Ge_{0.7}$ layers were varied within 5% of the values determined by Vegard's law to take into account probable deviations from the preset composition during growth. We also note an appreciable deviation of the calculated layer thicknesses from the preset ones (7.3%). For comparison, Fig. 2c shows the calculated curve corresponding to the preset thicknesses d_0. The curve residual is much larger, $F = 33.0F^{exp}$.

Table 2. Parameters of the $Si/Si_{0.7}Ge_{0.3}/Si_{0.3}Ge_{0.7}/Si_{0.7}Ge_{0.3}/Si$ structure

Layer no.	Material	d_0, nm	d, nm	ε, %
1	Si	10.0	10.1	6
2	$Si_{0.7}Ge_{0.3}$	62.0	58.4	2
3	$Si_{0.3}Ge_{0.7}$	10.0	11.9	7
4	$Si_{0.7}Ge_{0.3}$	200	188	30

Note: The notation is same as in Table 1; $\sigma = 0.89$ nm, $F^{min} = 5.25F^{exp}$ (for thicknesses d_0, the residual F is $33.0F^{exp}$).

Table 3. Parameters of the $GaAs/Al_{0.3}Ga_{0.7}As$ structure

Layer no.	Material	d_0, nm	d, nm	ε, %
1	GaAs	10.0	8.88	3
2	$Al_{0.34}Ga_{0.66}As$	20.0	17.5	2
3	GaAs	10.0	7.93	5
4	$Al_{0.34}Ga_{0.66}As$	30.0	25.4	3
5	GaAs	20.0	16.2	6
6	$Al_{0.34}Ga_{0.66}As$	12.0	11.0	10
7	GaAs	30.0	27.6	43
8	$Al_{0.34}Ga_{0.66}As$	30.0	23.0	50

Note: The notation is the same as in Table 1; $\sigma = 0.58$ nm, $F^{min} = 6.31F^{exp}$ (for thicknesses d_0, the residual F is $33.9F^{exp}$).

Similar qualitative results were obtained for the heterostructure based on the $Al_xGa_{1-x}As$ solid solution. This sample was also small (the average diameter was about 6 nm) and irregularly shaped. An interesting feature of this structure is that the values of $Re(\varepsilon - 1)$ for GaAs and AlGaAs differ only by 10%. Therefore, the amplitudes of the extrema in the curves $R(\theta)$ are small and are comparable to noise at certain angles (Fig. 3). The curve $\tilde{\xi}(\theta)$ has a more prominent structure. The signal-to-noise ratio is appreciably higher, since the extrema $\xi(\theta)$ correspond to the extrema of both curves $R_\alpha(\theta)$ and $R_\beta(\theta)$. The structure roughness (0.58 nm) is smaller than in the case of $Si_{1-x}Ge_x$, which suggests rather sharp interlayer boundaries. However, the residual and the deviations from the preset thicknesses are significantly larger, $6.31F^{exp}$ and 11.8%, respectively (see Table 3).

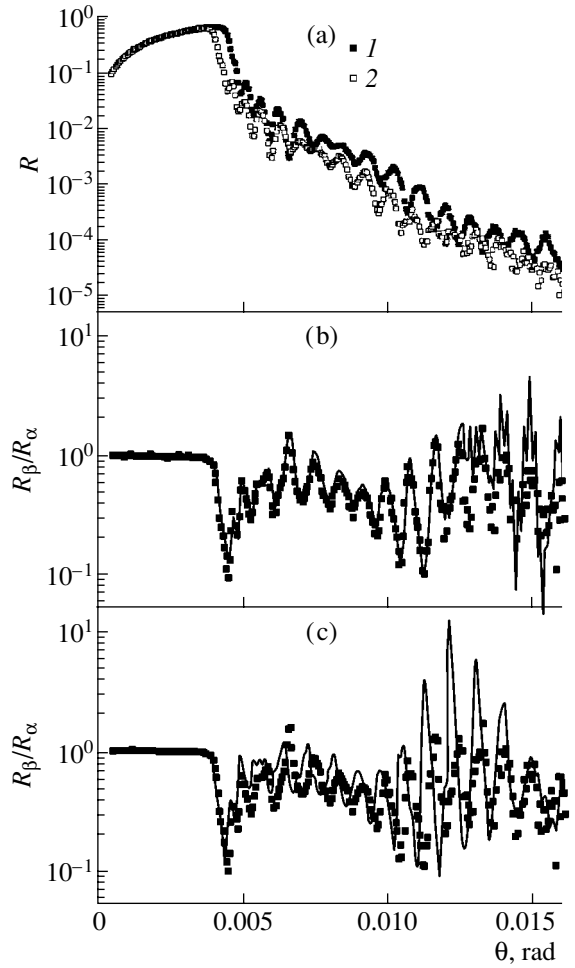

Fig. 2. Reflectance of the $Si/Si_{0.7}Ge_{0.3}/Si_{0.3}Ge_{0.7}/Si_{0.7}Ge_{0.3}/Si$ heterostructure versus the grazing angle of incidence θ: (a) the reflectances at the (*1*) CuK_α and (*2*) CuK_β lines; (b) the ratio R_β/R_α, the solid line is the calculated dependence; (c) the ratio R_β/R_α corresponding to the preset thicknesses d_0; the solid curve is the calculated dependence.

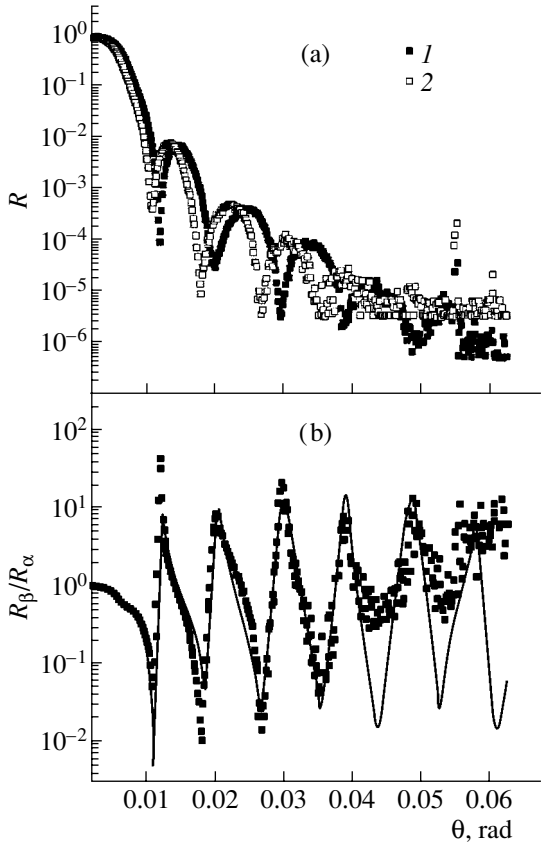

Fig. 3. Reflectance of the heterostructure $GaAs/Al_{0.3}Ga_{0.7}As$ versus the grazing angle of incidence θ: (a) the reflectances at the (*1*) CuK_α and (*2*) CuK_β lines and (b) the ratio R_β/R_α; the solid curve is the calculated dependence.

The calculated thickness errors may be interpreted as follows. It is evident that the accuracy of determining the thicknesses of thin layers is directly controlled by the range of measured angles θ_{max}, since the Bragg peak positions become undeterminable at $d \le \lambda/2\theta_{max}$. At the same time, the thickness-determination accuracy for thick layers depends on the angular divergence δθ of the incident beam, since individual Bragg peaks can not be distinguished for layers with $d \ge \lambda/2\delta\theta$. Furthermore, the accuracy of determining the deep-layer parameters is lower, since these layers have a weaker effect on the reflectance. The results of thickness determination listed in Tables 1–3 show that these factors appreciably impair the accuracy of thickness determination only for the deepest heterostructure layers, which are buffer layers. The parameters of the heterostructure regions of prime interest were determined with a sufficiently high accuracy.

5. CONCLUSION

A scheme for determining the parameters of multilayer nanostructures by the ratio of the reflectances at two wavelengths has been considered. Calculations carried out for various types of film structures showed that two-wave reflectometry in combination with the calculation scheme developed allows determination of the layer thickness, density, and roughness with the same accuracy using small samples as for large samples. Estimates of the parameter-determination errors showed that it is possible to improve the determination accuracy. To this end, the entrance-slit width should be selected individually for each structure so as to attain an optimum ratio between the measured angle range and the angular divergence of the incident beam. This technique can be readily extended to the case of the simultaneous use of three, four, or more wavelengths. Such widening of the body of information obtained by a single measurement makes it possible to appreciably improve the accuracy of parameter determination. Even more significant is that this allows the study of complex heterogeneous structures inaccessible to conventional reflectometry using individual or sequentially selected spectral lines.

ACKNOWLEDGMENTS

We are grateful to I.P. Kazakov, M.M. Rzaev, Yu.P. Pershin, and V.M. Roshchin for the multilayer structure samples placed at our disposal.

This study was supported by the Russian Foundation for Basic Research (project nos. 01-02-17432a, 02-02-17349, 02-02-06644(mas), and 00-15-96698); the federal program "Integration" (project nos. B0056 and I0859); and the CRDF (grant RP1-2267). This study was also supported in part by the International Science and Technology Center (project no. 2997).

REFERENCES

1. A. G. Touryanski and I. V. Pirshin, Instrum. Exp. Tech. **41** (5), 118 (1998).
2. A. G. Tur'yanskiĭ, A. V. Vinogradov, and I. V. Pirshin, Prib. Tekh. Éksp., No. 1, 105 (1999).
3. A. V. Vinogradov, I. A. Brytov, and A. Ya. Grudskiĭ, in *Mirror X-ray Optics*, Ed. by A. V. Vinogradov (Mashinostroenie, Leningrad, 1989), p. 47.
4. J. H. Holland, *Adaptation in Natural and Artificial Systems* (Univ. of Michigan Press, Ann Arbor, 1975).
5. E. Spiller, *Soft X-ray Optics* (SPIE, Bellingham, 1994).
6. *Physical Quantities. Handbook*, Ed. by I. S. Grigor'ev and E. Z. Meĭlikhova (Énergoatomizdat, Moscow, 1991), p. 98.

Translated by A. Kazantsev

Semiconductors, Vol. 37, No. 6, 2003, pp. 681–685. Translated from Fizika i Tekhnika Poluprovodnikov, Vol. 37, No. 6, 2003, pp. 706–710.

LOW-DIMENSIONAL SYSTEMS

Superradiance in Quantum Heterostructures

A. I. Klimovskaya, Yu. A. Driga, E. G. Gule, and O. O. Pikaruk

Institute of Semiconductor Physics, National Academy of Sciences of Ukraine, Kiev, 03028 Ukraine

e-mail: allaK@isp.kiev.ua

Submitted March 25, 2002; accepted for publication October 28, 2002

Abstract—Dependences of spectra, intensity, and relaxation time of superradiance in $GaAs/In_xGa_{1-x}As/GaAs$ quantum heterostructures on the excitation power density in the range of 1×10^{-3}–1×10^{6} W/cm^2 are investigated. It is shown for the first time that filling of the quantum well affects all spectral characteristics of superradiance.

1. INTRODUCTION

The effect of superradiance was first considered by Dicke in 1954 [1] and, since then, has been investigated in detail both theoretically and experimentally for the cases of gases and bulk solids [2, 3]. Basically, this effect lies in the fact that, in a medium where a high density of excited atoms (dipoles) is created, they can be phase-locked to each other by the electromagnetic field of their own radiation. Such synchronization becomes possible if the spacing l between the radiating dipoles is much smaller than the radiation wavelength λ but, at the same time, is sufficiently large to keep the dipole–dipole interaction negligibly weak. In addition, it is necessary that the time of excited-state spontaneous relaxation time and the scattering-induced depolarization be considerably longer than the time required for the establishment of phase locking. Under these conditions, a macrodipole forms in the excited medium and avalanche-like growth of the radiation intensity takes place. The characteristic time of superradiance τ_N is inversely proportional to the number of elementary dipoles N in the macrodipole, $\tau_N \propto 1/N$; the radiation intensity I is proportional to the square of the number of phase-locked dipoles: $I \propto N/\tau_N \propto N^2$.

In recent years, much interest has been drawn to superradiance in quantum heterostructures [4–10]. This is related to the fact that, compared with gases and bulk solids it is easier to achieve the necessary density of excited states and to reduce the contribution from the scattering processes in heterostructures. These studies showed that the creation of electromagnetic radiation sources emitting pulses of extremely short duration is a real possibility. The pulse width can be less than the period of the radiated electromagnetic wave, which is on the order of several femtoseconds for the optical spectral region.

However, interpretation of the results obtained in the studies of superradiance in quantum heterostructures brought about a number of questions that could not be answered in the context of conventional views [1]. In particular, it was impossible to explain the fact that the superradiance time does not change [6], or even increases [8], with an increase in the pump level (according to [1], τ_N should be inversely proportional to N) and also that the shape of the superradiance spectrum remained unchanged when the pump level was varied by three orders of magnitude. Another problem is that estimates for the number of dipoles N obtained from different experimental data do not agree with each other.

The purpose of this study is to reveal the origin of unusual features of superradiance in quantum heterostructures and to understand the cause of the above inconsistencies.

The samples under study are heterostructures with a single elastically strained quantum well (QW). This ensures that the rate of scattering, which limits the superradiance intensity, is low; in addition, this makes it possible to calculate the energy structure of the QW with good accuracy.

To carry out measurements in a wide range of pump power density, optical pumping of the heterostructures was used. Variations in the main characteristics of superradiance—spectral shape, intensity, and relaxation time—with pump power were investigated.

The results obtained indicate that these characteristics vary in accordance with the Dicke theory up to pump power density corresponding to the complete filling of the QW with photogenerated electron–hole pairs. When the pump power is increased above this value, the spectral shape is stabilized, the growth in the emission intensity becomes much less steep, and the relaxation time τ_N remains unchanged. Thus, the unusual features of superradiance in quantum heterostructures, which were noticed in [6, 8], are related to the quasi-discrete nature of their energy spectrum and to the finitness of the available number of states of quantum objects.

2. EXPERIMENTAL

The heterostructures under study were quantum layers of $In_xGa_{1-x}As$ embedded into a GaAs matrix. They were grown by atmospheric-pressure MOCVD tech-

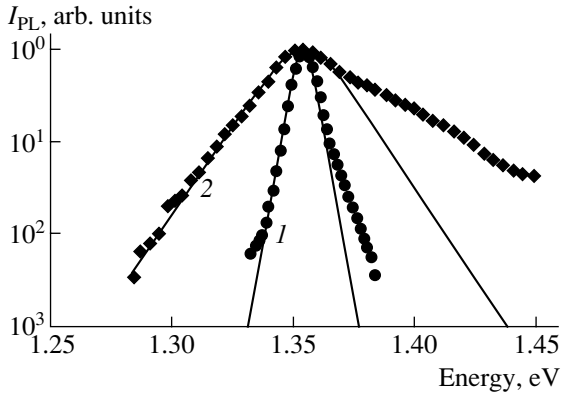

Fig. 1. Photoluminescence spectra of a GaAs/$In_{0.16}Ga_{0.84}As$/GaAs quantum heterostructure at low and high excitation levels; P_{exc} = (*1*) 0.1 and (*2*) 9×10^6 W/cm^2. Solid lines represent the spectra calculated according to (1).

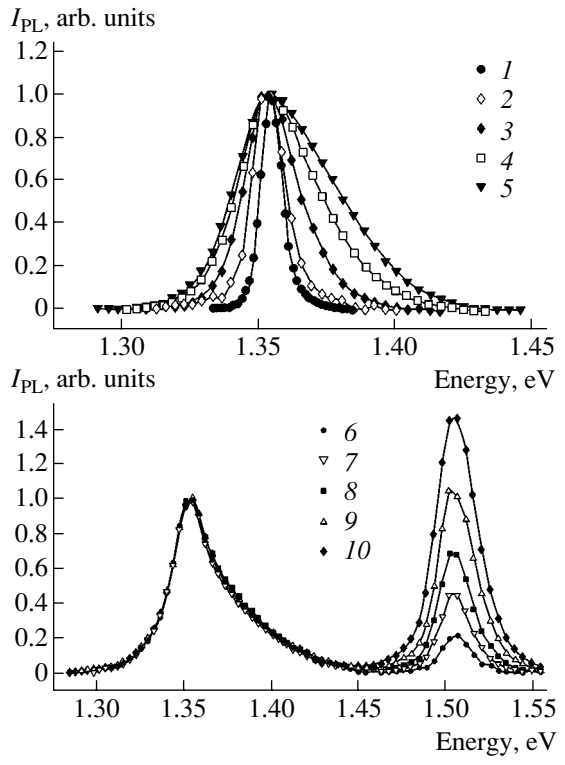

Fig. 2. Photoluminescence spectra of a GaAs/$In_{0.16}Ga_{0.84}As$/GaAs quantum heterostructure at different excitation power densities: P_{exc}/P_{exc}^{max} = (*1*) 3.3×10^{-6}, (*2*) 3.5×10^{-4}, (*3*) 2.8×10^{-3}, (*4*) 5.7×10^{-3}, (*5*) 8×10^{-3}, (*6*) 1.8×10^{-1}, (*7*) 3.5×10^{-1}, (*8*) 2.5×10^{-1}, (*9*) 7.1×10^{-1}, and (*10*) 1; here, P_{exc}^{max} = 9×10^6 W/cm^2.

nology. The thickness and the In content in the layers were kept in such limits so that they remained elastically strained and so that misfit dislocations due to the lattice mismatch between the layer and the matrix did not appear.

Two excitation sources were used: an LGI-201 continuous-wave He–Ne laser with a power of ~1.7 mW, operating at 632.8 nm, and an LGI-21 pulsed nitrogen laser with a pulse power of 1.5 kW, operating at 337.1 nm. The excitation intensity was varied by using calibrated neutral filters and by focusing the laser beam.

The emission spectra were recorded using a modified KSVU-23 optical spectrometer. To avoid distortion in the shape of the spectra, which can be introduced, e.g., upon waveguide propagation of emitted light, the radiation to be analyzed was collected from the sample surface. During the measurements, the samples were kept at a temperature $T \approx 100$ K.

3. RESULTS

The power density P_{exc} of the optical pump was varied from ~1×10^{-3} to 9×10^6 W/cm^2. This enabled us to determine the main features of superradiance in quantum heterostructures. By changing the pump level, we were able to study the variation of the shape of the emission spectrum $I_{PL}(E)$, the integrated emission intensity I_{PL}, and the superradiance relaxation time τ_N.

3.1. Spectral Shape

Two QW emission spectra, one recorded at a low and the other at a high excitation level, are plotted in Fig. 1 on a semilog scale. In Fig. 1, solid lines represent the calculated spectra of the QW emission; the spectral dependence characteristic of Dicke superradiance [6] is given by

$$I_{QW} \propto \operatorname{sech}\{2\pi^2 \tau_N (E - E_{max})/h\}, \qquad (1)$$

where E_{max} is the energy of intensity maximum. One can see that the spectra have an asymmetric shape. The low-energy tail is well described by (1) over a variation of intensity of three orders of magnitude. At the same time, the higher the excitation level, the more pronounced the deviations from this lineshape at the high-energy tail of the spectrum, although the contribution from superradiance is still dominant.

Figure 2 shows a set of photoluminescence (PL) spectra $I_{PL}(E)$ recorded at different excitation levels; the curves are normalized by their peak values. One can see that, with increasing excitation power P_{exc}, the PL band at ~1.35 eV broadens until P_{exc} approaches ~10^6 W/cm^2. At higher excitation levels, the shape of this band does not depend on P_{exc} and another band at 1.504 eV appears. The presence of a high-energy band is evidence that the QW is almost completely filled and that the relaxation of excess electron–hole pairs takes place in the matrix.

Thus, these data indicate that the contribution from Dicke superradiance is dominant in the PL spectrum at all excitation levels and that the stabilization of the shape of the QW emission band is related to the filling of the well.

3.2. Radiation Intensity

Figure 3 shows the dependence of the integrated PL intensity on the excitation-power density. Curve *1* represents the total intensity I_{PL}, including the emission from the GaAs matrix; curve *2* represents the intensity I_{QW} of the QW PL only. In the region of P_{exc} below the value ~10^6 W/cm^2 (shown by an arrow in Fig. 3), both dependences coincide. At very low excitation levels, we observe the dependence $I_{QW} \propto P_{exc}^2$ (see Fig. 3b). At high excitation levels, the dependence is sublinear: $I_{QW} \propto P_{exc}^{0.5}$. Note that the transition to sublinear variation of I_{QW} takes place in the same range of excitation power densities where the weakening of the dependence of the spectral shape of the QW emission on P_{exc} occurs, which points to the correlation between this transition and the filling of the quantum-confinement subband. Since, at all excitation levels, a major contribution to the QW emission is made by Dicke superradiance, we conclude from the shape of the experimental dependence $I_{QW}(P_{exc})$ that the relationship between the Dicke emission intensity and the excitation power is nonlinear. In addition, one can see from the shape of the dependence $I_{PL}(P_{exc})$ that the relative rate of nonradiative recombination is considerably lower in the QW than in the matrix.

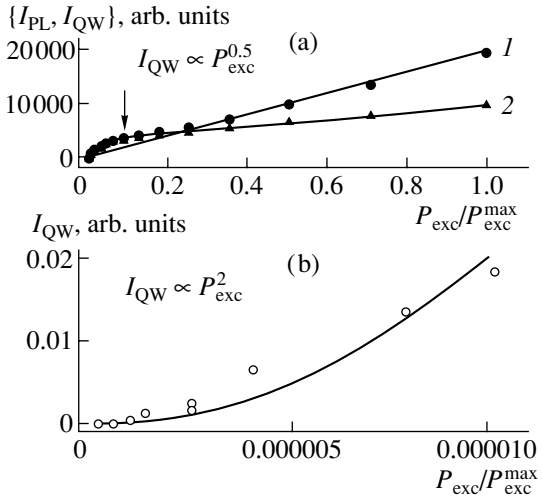

Fig. 3. Dependences of the emission intensity on the normalized excitation power density. (a) Integrated intensity of (*1*) total heterostructure emission I_{PL} and (*2*) QW emission I_{QW}; the straight line shows the dependence characteristic of usual spontaneous relaxation. (b) Integrated intensity of the QW emission I_{QW} at low excitation levels. $P_{exc}^{max} = 9 \times 10^6$ W/cm^2.

3.3. Relaxation Time

The relaxation time was determined from the slope of the low-energy tail of the spectrum. In Fig. 4, the dependence of τ_N on the excitation level is shown. With an increase of the excitation power density in the range $P_{exc} = 1 \times 10^{-3}$–$9 \times 10^6$ W/cm^2, the relaxation time is reduced from 70 to 20 fs. The most rapid variation of τ_N occurs at P_{exc} below ~10^6 W/cm^2. A further increase in the excitation level has virtually no effect on the relaxation time. A comparison of this behavior with the excitation-level dependences of the emission intensity and spectrum suggests that leveling-off of τ_N is also related to the filling of the QW.

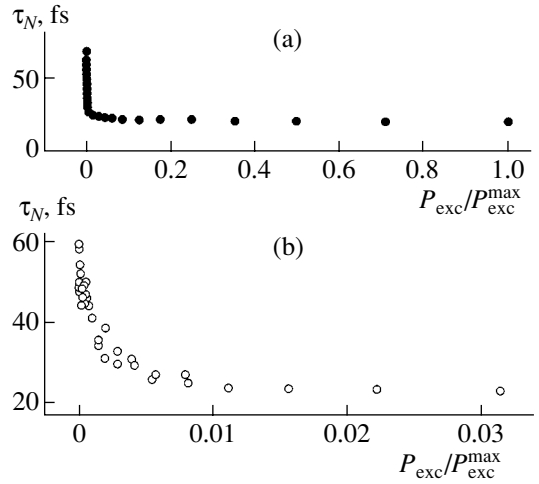

Fig. 4. (a) Dependence of the superradiance relaxation time on the normalized excitation power density. (b) The same dependence at low excitation levels. $P_{exc}^{max} = 9 \times 10^6$ W/cm^2.

4. DISCUSSION

Relying on our calculations of the energy structure of the QW, carried out in the four-band model taking into account strain effects and the energy dependence of the effective mass [11], and on the calculations of the exciton binding energy performed in [12], we may conclude that the observed QW luminescence originates from recombination of excitons associated with the first electron and first heavy-hole subbands. The excitonic nature of the emission is also confirmed by the fact that at low pump levels the FWHM of the luminescence band is smaller than *kT*, i.e., smaller than the value typical of ideal two-dimensional QWs.

The shape of the excitonic emission spectrum depends significantly on whether the excitons radiate independently or take part in the formation of a macrodipole; in other words, whether they are phase-locked with one another by the radiation field. We showed previously that at low excitation levels the shape of the PL spectra of these heterostructures is best described by the dependence typical of Dicke superradiance [10]. The results shown in Fig. 1 indicate that a dominant contribution to the PL at high excitation levels also comes from superradiance.

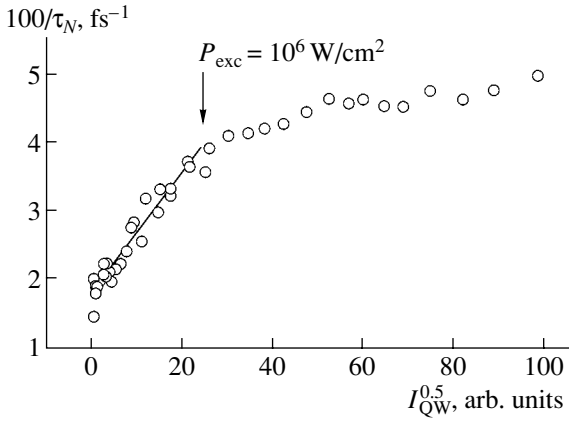

Fig. 5. Relationship between the inverse of the Dicke relaxation time τ_N^{-1} and the square root of the integrated QW $I_{QW}^{0.5}$ luminescence intensity.

The exciton binding energy in the structures under study at $T = 100$ K, estimated using the calculation results of [12], is ~6 meV, i.e., slightly lower than kT. This means that excitons, free electrons and holes are present in the QW. Since the times of thermal scattering of free charge carriers in the QW exceed 10^{-12} s, which is considerably longer than the superradiance relaxation time τ_N, it is quite plausible that the carriers occupying the quantum-confinement subbands are also involved in the superradiance process. Thus, at high excitation levels, superradiance related to the transitions between the quantum-confinement subbands is observed along with excitonic superradiance.

The nonlinear dependence of the QW luminescence intensity on the excitation power can be easily explained as follows: at low excitation levels, this nonlinearity is related to the steady-state balance between the rate of excited state generation G and the rate of their relaxation R ($G = R$), while at high excitation levels the finitness of the available number of states in the QW becomes important.

There are several relaxation channels in the heterostructures under study: nonradiative recombination, radiative recombination of independent dipoles, and radiative recombination by the Dicke mechanism. Each of them can be described by some characteristic time τ_n, τ_i, or τ_N, respectively. Then,

$$R = N_0\left(\frac{1}{\tau_n} + \frac{1}{\tau_i} + \frac{1}{\tau_N}\right),$$

where N_0 is the total number of pairs generated in the QW. If the excitation level is so low that the condition $l \ll \lambda$, which is necessary for the appearance of superradiance, is not satisfied, spontaneous emission of independent dipoles takes place and a certain dipole density is established in the steady state. Note that, if the relationship between the nonradiative and radiative recombination rates does not change, i.e., τ_n and τ_i are independent of the excitation level, the emission intensity varies linearly with the excitation power. In the experimental conditions under consideration, this is the case for the matrix emission; this can be clearly seen from the excitation dependence of the total luminescence intensity of the heterostructure (Fig. 3, curve *1*) in the region of high excitation levels, where the QW is filled completely and notable emission from the matrix is present.

The situation changes when an additional relaxation channel due to the Dicke mechanism comes into play. Its basic feature is that the Dicke time τ_N depends on the excitation level. In this case, redistribution of the relaxation over different channels occurs with variation in the excitation power. Since τ_N decreases with increasing excitation power, while τ_n and τ_i remain unchanged or vary much more weakly, the role of the Dicke relaxation channel grows at the expense of both radiative and nonradiative recombination. Thus, for a given excitation level (i.e., for a given generation rate), the integrated emission intensity from a medium with independent emitters will be lower than that from a medium where the emitters form a macrodipole.

Analyzing the variation of the shape of the spectra (Fig. 2), the emission intensity (Fig. 3), and the superradiance relaxation time (Fig. 4) with the excitation power, we conclude that, in all cases, considerable changes take place in the range of excitation power density around $P_{exc} \approx 10^6$ W/cm^2. At these excitation levels, the QW becomes almost completely filled, and a further increase in P_{exc} should not lead to a significant increase in the number of electron–hole pairs in the well. Thus, it is the nonlinear relationship between the number of the dipoles in the QW and the excitation power that causes the apparent discrepancy between the results of experimental studies of superradiance in quantum heterostructures and the theory and experiments in gases and bulk solids. It is not easy to determine this relationship. However, since $\tau_N \propto 1/N$ and $I_{PL} \propto N^2$ in any superradiance process, the quantities $1/\tau_N$ and $I_{PL}^{0.5}$ determined from experimental data should be related by a linear dependence. In Fig. 5, we plot this dependence according to our experimental data. One can see that the curve does have a linear portion corresponding to the variation of the excitation level by nine orders of magnitude, up to the power densities of 10^6 W/cm^2 (where complete filling of the QW takes place). A slight decrease in the relaxation time with a further increase in the emission intensity is, probably, related to a low occupancy of the second quantum-confinement subband; this subband is spaced by about kT from the top of the QW and can readily exchange electrons with the conduction band of the heterostructure matrix.

5. CONCLUSION

In this study, we showed for the first time the importance of QW filling for the processes of superradiance in quantum heterostructures. The dependence of the superradiance relaxation time on the excitation power density P_{exc} was determined over a range of P_{exc} variation of ten orders of magnitude. It was shown that, in the situation where the QW is almost completely filled with nonequilibrium electron–hole pairs, the shape of the emission spectrum becomes independent of the excitation level and the relaxation time also levels off. It was shown that the relationship $1/\tau_N \propto \sqrt{I_{QW}}$ between the relaxation time and the emission intensity, characteristic of superradiance processes, is valid in the QWs.

REFERENCES

1. R. H. Dicke, Phys. Rev. **93**, 99 (1954).
2. A. V. Andreev, V. I. Emel'yanov, and Yu. A. Il'inskiĭ, Usp. Fiz. Nauk **131**, 653 (1980) [Sov. Phys. Usp. **23**, 493 (1980)].
3. V. V. Zheleznikov, V. V. Kocharovskiĭ, and Vl. V. Kocharovskiĭ, Usp. Fiz. Nauk **159**, 193 (1989) [Sov. Phys. Usp. **32**, 835 (1989)].
4. S. V. Zaĭtsev and A. M. Georgievskiĭ, Fiz. Tekh. Poluprovodn. (St. Petersburg) **32**, 366 (1998) [Semiconductors **32**, 332 (1998)].
5. A. A. Belyanin, V. V. Kocharovsky, and Vl. V. Kocharovsky, Quantum Semiclassic. Opt. **10**, L13 (1998).
6. S. V. Zaĭtsev, N. Yu. Gordeev, L. A. Graham, *et al.*, Fiz. Tekh. Poluprovodn. (St. Petersburg) **33**, 1456 (1999) [Semiconductors **33**, 1309 (1999)].
7. A. A. Belyanin, V. V. Kocharovskiĭ, and Vl. V. Kocharovskiĭ, Izv. Ross. Akad. Nauk, Ser. Fiz. **62**, 372 (1998).
8. A. M. Georgievskiĭ, S. V. Zaĭtsev, N. Yu. Gordeev, *et al.*, Fiz. Tekh. Poluprovodn. (St. Petersburg) **33**, 847 (1999) [Semiconductors **33**, 779 (1999)].
9. A. A. Belyanin, V. V. Kocharovskiĭ, Vl. V. Kocharovskiĭ, and D. S. Pestov, Izv. Vyssh. Uchebn. Zaved. Radiofiz. **44** (1–2), 17 (2001).
10. A. I. Klimovskaya, E. G. Gule, and Yu. A. Driga, Fiz. Tekh. Poluprovodn. (St. Petersburg) **36**, 232 (2002) [Semiconductors **36**, 224 (2002)].
11. N. N. Grigor'ev, E. G. Gule, A. I. Klimovskaya, *et al.*, Ukr. Fiz. Zh. **45**, 853 (2000).
12. I. A. Avrutskiĭ, V. A. Sychugov, and B. A. Usievich, Fiz. Tekh. Poluprovodn. (Leningrad) **25**, 1787 (1991) [Sov. Phys. Semicond. **25**, 1074 (1991)].

Translated by M. Skorikov

Semiconductors, Vol. 37, No. 6, 2003, pp. 686–691. Translated from Fizika i Tekhnika Poluprovodnikov, Vol. 37, No. 6, 2003, pp. 711–716.

LOW-DIMENSIONAL SYSTEMS

Electron Transport in Coupled Quantum Wells with Double-Sided Doping

G. B. Galiev*, V. E. Kaminskiĭ*, V. G. Mokerov*, V. A. Kul'bachinskiĭ, R. A. Lunin**, I. S. Vasil'evskiĭ**, and A. V. Derkach****

**Institute of Radio Engineering and Electronics, Russian Academy of Sciences, Moscow, 101999 Russia*
e-mail: kamin@mail.cplire.ru
***Moscow State University, Moscow, 119899 Russia*
Submitted July 10, 2002; accepted for publication October 28, 2002

Abstract—The conductivity and Hall mobility have been measured in heterostructures with coupled quantum wells (QW) as functions of temperature and the QW width. If a tunnel-transparent barrier is inserted in the middle of a QW, the mobility increases in narrow wells and decreases in wide wells. The experimental data have been compared with the calculated dependences. It has been shown that the number of filled quantum-well subbands depends on the well width and the presence of a barrier. The magnetoresistance and Hall resistance were measured at a temperature of 4.2 K in the range of magnetic fields of 1–40 T. The filling of subbands was determined from a Fourier analysis of the Shubnikov–de Haas oscillations, and good agreement with the calculated data was obtained. © *2003 MAIK "Nauka/Interperiodica".*

1. INTRODUCTION

The electrical characteristics of AlGaAs/GaAs/AlGaAs quantum wells (QW) are of interest both for fundamental physics and commercial applications. These structures are widely used nowadays in the fabrication of photodetectors, optical modulators, high-power transistors, etc. A QW located between symmetrical AlGaAs barriers makes it possible to obtain the desired spectral characteristics of optoelectronic devices. Quite often, the parameters of these structures are improved by using coupled QWs produced by dividing a GaAs QW with a thin, about 3–4 monolayers (ML) thick, AlAs barrier [1, 2].

In field-effect transistors (FETs) for microwave applications, the double-sided doping of AlGaAs/GaAs/AlGaAs structures provides considerable enhancement of the output power [3–5]. In this type of heterostructure, the phonon spectrum is quantized similarly to the electron energy spectrum. According to calculations [6], this effect should suppress the electron–phonon scattering and thus enhance the mobility of electrons. As follows from theoretical calculations [7, 8], at a certain QW size, the insertion of a thin AlAs barrier should considerably reduce the rate of intrasubband scattering and may lead to an additional increase in mobility. This can further improve the transistor characteristics. All these facts show that the study of QWs with thin barriers is topical.

In this report, we present results concerning electron transport in AlGaAs/GaAs/AlGaAs structures with QWs of different widths. To perform a comparative analysis, similar structures were grown without a barrier and with a thin AlAs barrier in the middle of a QW. Components of the resistivity tensor were measured as functions of the magnetic field intensity at 4.2 K in a quantizing magnetic field.

2. SAMPLE PREPARATION AND MEASUREMENT PROCEDURE

The samples were grown by MBE on semi-insulating (100) GaAs substrates misoriented by 2° in the [110] direction. First, a 0.5-μm-thick GaAs buffer layer was grown. Then, an $Al_{0.2}Ga_{0.8}As$ barrier, a GaAs QW, an ~1.8-nm-thick AlAs barrier, a GaAs QW, and an $Al_{0.2}Ga_{0.8}As$ barrier were grown. Finally, an 8-nm-thick GaAs capping layer was grown. Both QWs in the structure had the same width. Several parameters of the samples under study, including the AlAs barrier thickness d and the total width of the QWs W, are listed in the table. The thickness of the AlGaAs barriers was the same (33 nm) in all the structures. One half (across the thick-

Surface densities n_H and mobilities μ_H of electrons as defined from the Hall measurements at a temperature of 4.2 K

Sample no.	W, nm	d, nm	n_H, 10^{12} cm^{-2}	μ_H, cm^2 V^{-1} s^{-1}
2	13	0	1.33	10000
3	13	1.8	1.31	12800
4	26	0	2.07	11900
5	26	1.8	2.09	12500
6	35	0	2.02	15000
7	35	1.8	2.02	13000

1063-7826/03/3706-0686$24.00

ness) of each barrier adjacent to the QW remained undoped, whereas the other half was doped with Si to ~10^{-18} cm^{-3}. The same concentration of Si was in the capping layer. GaAs and AlAs layers were grown at a temperature of 600°C, and AlGaAs, at 640°C. The ratio of As to Ga fluxes in the zone of growth was 30. For purposes of comparison similar structures were grown without a central AlAs barrier in the QW. As an example, Fig. 1 shows the band diagram calculated for sample 3.

Samples in the shape of Hall bridges were prepared for galvanomagnetic measurements. Temperature dependences of the resistance were measured in the range $4.2 < T < 300$ K, as was the Hall effect at 4.2 K and in the range $77 < T < 300$ K. The temperature dependences of the Hall density of electrons in the structure, n_H, and their mobility μ_H were determined in the temperature range $77 < T < 300$ K. The values of these parameters at 4.2 K for all of the structures are listed in the table. The resistance ρ_{xx} and Hall resistance ρ_{xy} were measured in the Hall bridges at liquid helium temperature in a magnetic field up to 40 T.

3. RESULTS AND DISCUSSION OF GALVANOMAGNETIC MEASUREMENTS

Figure 2 shows the resistance of structures versus temperature. In all samples, the resistance decreases with decreasing temperature to 60 K. At $T < 60$ K, the resistance of samples 5 and 6 slightly increases with decreasing temperature, which can be attributed to weak localization of carriers. The decreasing of the resistance with decreasing temperature in the range $T >$ 60 K is due to an increase in the electron mobility. Indeed, the measured Hall mobility μ_H increases with decreasing temperature (Fig. 3). It is easily seen that the insertion of an AlAs barrier raises the Hall mobility in a narrow QW with W = 13 nm. As the temperature decreases, the mobility ratio μ_{H3}/μ_{H2}, where μ_{H2} and μ_{H3} are, respectively, the Hall mobilities in samples 2 and 3, increases (Fig. 3). With temperature varied in the range $77 \text{ K} < T < 280$ K, the ratio of mobilities is within the range $1.21 > (\mu_{H3}/\mu_{H2}) > 1.06$. At the same time, the insertion of a barrier in both of the wide QWs reduces the mobility in comparison with samples without a barrier (Fig. 3). However, the temperature dependences of the ratio of mobilities are different in these cases. In the same temperature range, the samples with W = 26 nm demonstrate $1.05 < (\mu_{H4}/\mu_{H5}) < 1.206$; i.e. the ratio decreases with decreasing temperature. However, in the samples with W = 35 nm we have $1.176 < (\mu_{H6}/\mu_{H7}) <$ 1.1; i.e. the ratio increases with decreasing temperature. As is seen, these variations are not great; they do not exceed 15% in the entire temperature range.

In all of the samples, the Hall density decreases with decreasing temperature (Fig. 4). It can be inferred that the observed $n_H(T)$ dependence is related to the specific features of the band structure of the samples under study. As is seen from the band diagram (Fig. 1), the sample conductance consists of the conductances of the potential well on the substrate side, the doped parts of the AlGaAs barriers, and a QW. As is known, the Hall

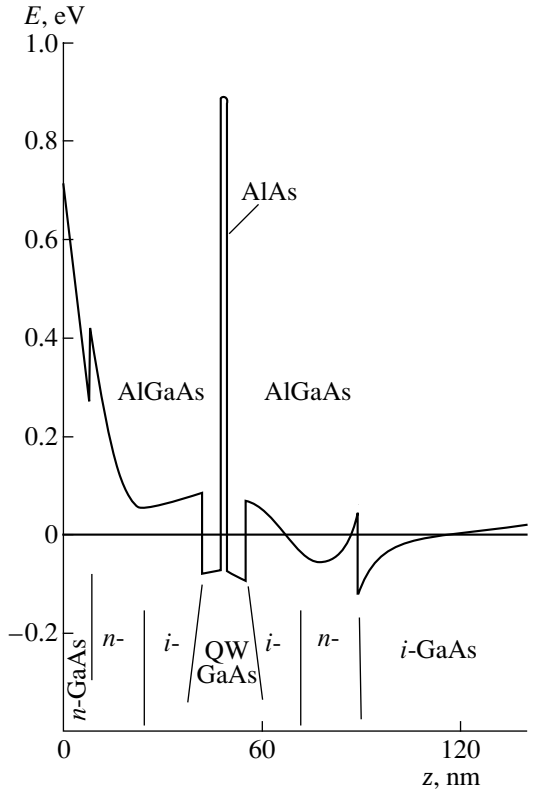

Fig. 1. The energy-band diagram of sample 3. The energy is reckoned from the Fermi level.

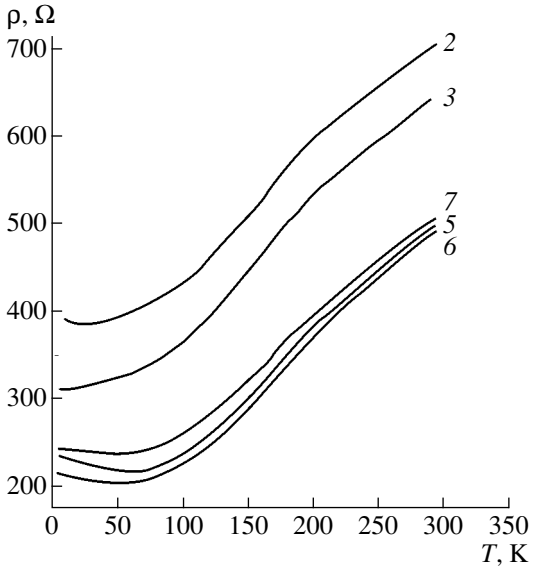

Fig. 2. Temperature dependences of the resistance of structures under study. Curve numbers correspond to sample numbers in the table.

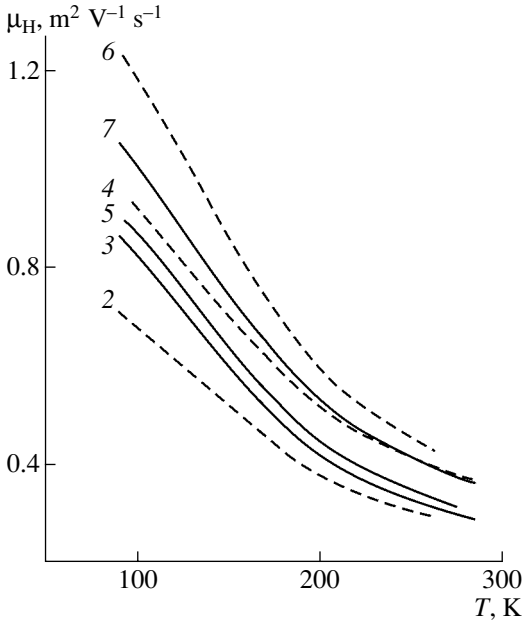

Fig. 3. Temperature dependences of the Hall mobility of electrons μ_H in different samples. Curve numbers correspond to sample numbers in the table. Solid and dashed lines: samples with and without an AlAs barrier in the QW, respectively.

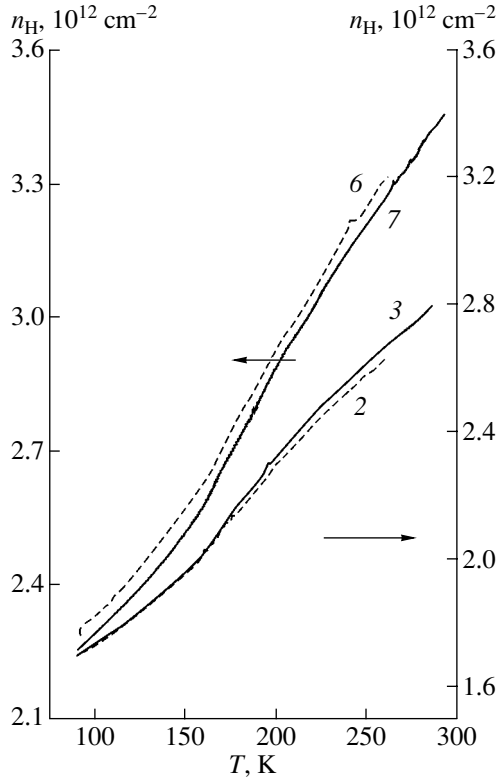

Fig. 4. Temperature dependences of the Hall density of electrons in samples 2 and 3 with a narrow (W = 13 nm) QW, and 6 and 7 with a wide (W = 35 nm) QW. Curve numbers correspond to sample numbers in the table.

mobilities and densities in layered structures are determined from the relations

$$\mu_H = \frac{\sum_i \gamma_i \mu_i^2 n_i}{\sum_i \mu_i n_i}, \quad n_H = \frac{\left(\sum_i \mu_i n_i\right)^2}{\sum_i \gamma_i \mu_i^2 n_i}, \qquad (1)$$

where μ_i, n_i are the mobility and surface density of electrons in the layers; γ_i is the Hall constant; and i is the index of summation over the layers. The solution to a system of self-consistent Kohn–Sham equations for the potential and quantum wells, similar to that obtained in [9], shows that the electron density changes only slightly with temperature. Calculations show that the electron gas is either degenerate or nearly degenerate in all the samples in the temperature range under study. Therefore, in our calculations, we assumed that $\gamma_i = 1$. In this case, it is easily shown using (1) that the decrease in the Hall density with decreasing temperature is due to a decrease in the ratio

$$\frac{\mu_3 n_3}{\mu_1 n_1 + \mu_2 n_2}, \qquad (2)$$

where the parameters with indices 1 and 2 refer to, respectively, the potential and quantum wells, and index 3, to the doped section of the AlGaAs barrier. At a temperature of 4.2 K, the mobility in the doped barrier is very small and the conduction in this layer can be disregarded. Then, (1) yields the relation $n_1 < n_H < n_1 + n_2$. The proximity of n_H to one limit or another depends on the ratio $p = \mu_2/\mu_1$.

The solution of the system of self-consistent Kohn–Sham equations for the surface densities in the wells yields $n_1 = 1.2 \times 10^{12}$ cm^{-2} and $n_2 = 1.06 \times 10^{12}$ cm^{-2}. Using (1) and the data for T = 4.2 K listed in the table, we obtain the mobility ratios: $p \approx 0.1$ for narrow QWs and $p \approx 0.6$ for wide wells. At the same time, at high temperatures, $n_1 < n_H < n_1 + n_2 + n_3$. As is seen in Fig. 4, the value of n_H in wide QWs is close to the total electron density in a structure. For narrow QWs, n_H is significantly smaller (Fig. 4). This results from a lower mobility of electrons in narrow QWs.

The samples under study were grown in approximately the same conditions. Therefore, the electron mobilities and densities in the barriers and QWs for all of the structures must be approximately the same. Then, as can easily be shown from (1), the value of μ_2 must be higher in the structure with larger $n_H\mu_H^2$. As is seen in Fig. 4, the n_H values virtually coincide in the structures with and without a barrier. Therefore, the ratio between the values of μ_H in the structures with and without a barrier qualitatively reflects the ratio between the values of μ_2 in these structures. Hence, the insertion of an AlAs barrier raises μ_2 in narrow QWs and reduces

it in wide wells. Further, as is seen in Fig. 3, μ_2 at $T >$ 77 K increases with increasing W regardless of the presence of an AlAs barrier.

A weak temperature dependence of ρ indicates that the observed dependences of μ_H and, correspondingly, μ_2 on the structure parameters are due to the quantum confinement. The influence of the width of a rectangular QW on mobility has been widely discussed in the literature (see [7] and references therein), and it was shown that $\mu_2 \propto W$ in moderately wide wells. This is not quite the case when there is a high electron density and, correspondingly, when a potential profile is present in a well. The scattering on polar optical phonons prevails in GaAs at $T > 77$ K. In this case, as is shown in [10], when there is a single filled quantum-well subband

$$\mu_2 \propto [\int \psi^4(z)dz]^{-1}, \quad (3)$$

where ψ is the wave function in the direction of quantum confinement. The dependence $\mu_2 \propto W$ is a particular case of (3) for a rectangular well. The solution of the system of self-consistent Kohn–Sham equations for the structures under study shows that the number of filled subbands in different samples is different: one in sample 3; two in samples 2, 4, and 5; and three in samples 6 and 7. A direct extension of (3) to the case of several filled subbands is the relation

$$\frac{\mu_2}{\mu_{20}} = \sum_j \alpha_j [\int \psi_j^4(z)dz]^{-1}, \quad (4)$$

where μ_{20} is the mobility in an extremely wide QW, α_j is the relative filling of a subband with electrons, and the summation is done over all of the quantum-well subbands. Figure 5 shows the dependences of the ratio μ_2/μ_{20} on the width of a QW without a barrier and with a 1.8-nm-thick AlAs barrier, calculated for $T = 100$ K using relation (4). In the calculation, the subbands with a relative filling greater than 0.03 were taken into account. The number of such subbands for each of the samples was indicated above. The calculation also shows that the dependences vary only slightly in the temperature range $77 < T < 300$ K. The results obtained in solving the system of self-consistent Kohn–Sham equations were used for the calculation. As is seen, the dependences are in qualitative agreement with the experimentally determined ratios of the Hall mobilities. Further, calculation by Eq. (4) yields $\mu_{23}/\mu_{22} = 1.11$, $\mu_{26}/\mu_{27} = 1.13$, and $\mu_{24}/\mu_{25} = 1.1$, where the second index is the sample number. As is seen, these values fall within the range of variation of the ratios between the measured Hall mobilities.

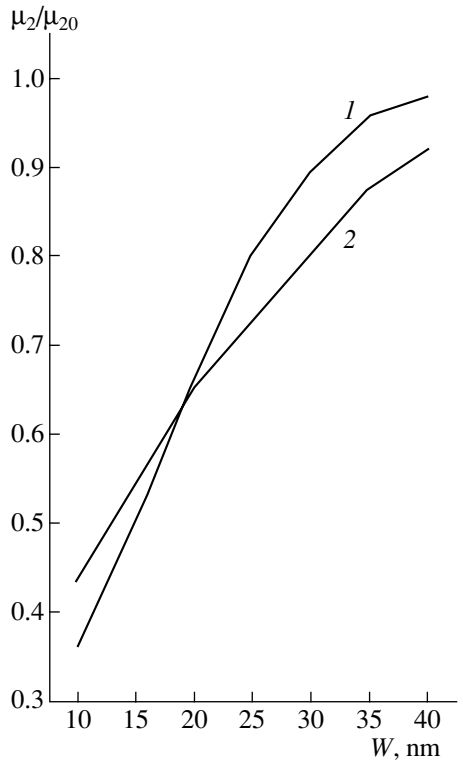

Fig. 5. Dependences of the normalized mobility μ_2/μ_{20} (see Eq. (4)) on the QW width: (*1*) without a barrier; (*2*) with a 1.8-nm-thick AlAs barrier. μ_2 is the mobility in the first subband of a GaAs QW, and μ_{20} is that in a very wide QW.

4. MAGNETOTRANSPORT IN A QUANTIZING MAGNETIC FIELD

Figure 6 shows the dependences of resistance ρ_{xx} and Hall resistance ρ_{xy} on the magnetic field intensity B for samples 6 and 7. At 4.2 K, the magnetic field with an intensity $B > 0.2$ T is a quantizing field in GaAs. Indeed, Shubnikov–de Haas oscillations were observed in all samples. However, they are not periodic in an inverse magnetic field $1/B$. This is due to the presence of two QWs in a structure with several filled quantum-well subbands. To determine the filling of these subbands, we performed a Fourier transform of the $\rho_{xx}(1/B)$ dependences for samples 6 and 7. The surface densities of electrons in the subbands were calculated from the frequencies F corresponding to the Fourier spectra peaks using the relation for the electron density

$$n = \frac{qF}{\pi\hbar}. \quad (5)$$

The insets to Fig. 6 show the Fourier spectra (for samples 6 and 7) as functions of density n, with two peaks clearly seen. The more pronounced peak corresponds to $n = 1.08 \times 10^{12}$ cm^{-2}. This value is close to the calculated filling of the potential well (see above). The second peak corresponds to $n = 4.5 \times 10^{11}$ cm^{-2} and 5.3×10^{11} cm^{-2} for samples 6 and 7, respectively. The

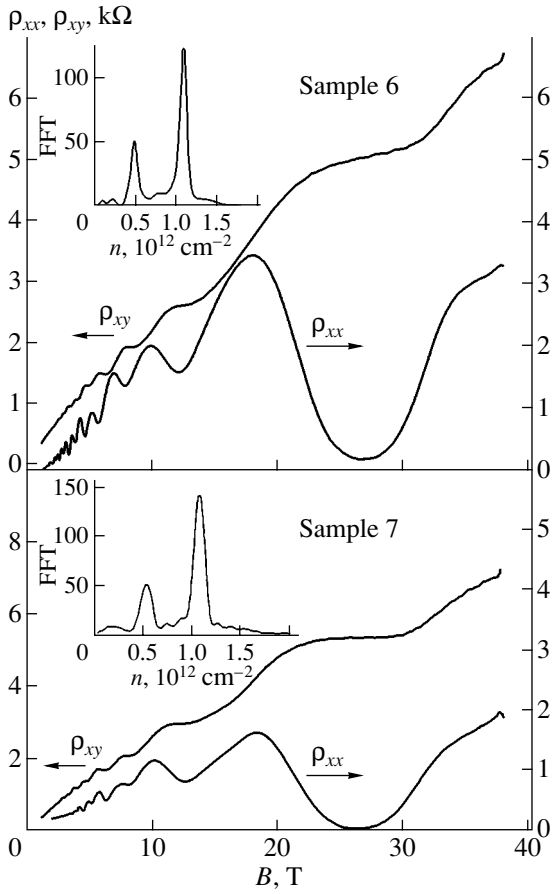

Fig. 6. The magnetoresistance and Hall resistance of samples 6 and 7 at a temperature of 4.2 K. Insets: Fourier spectra of the ρ_{xx} oscillations.

calculated fillings of three quantum-well subbands in a QW are as follows: 4.7×10^{11}, 4.4×10^{11}, and 1.5×10^{11} cm^{-2} for sample 6; and 4.6×10^{11}, 4.5×10^{11}, and 1.6×10^{11} cm^{-2} for sample 7. As is seen, the second peak for both samples corresponds to two subbands with nearly the same filling. This degeneracy of subbands is due to the QW symmetry. As is seen in Fig. 1, such a QW has two potential wells near the heterojunctions. At low temperatures, the wave functions of the lowest energy levels are weakly coupled and the energies of the levels become close. Calculations show that, with rising temperature, the levels diverge, and the higher the temperature the stronger their fillings. The total surface density of electrons in a QW remains virtually unchanged in this situation. A weak peak is observed for sample 6 in the range of small n. This peak is presumably related to the third filled subband. It may be assumed that a similar peak for sample 7 merges with the zero-frequency component of the Fourier spectrum. We believe that the presence of this feature leads to a shift of the peak corresponding to two filled subbands for sample 7 to higher n values.

As is seen in Fig. 6, the average value of $\rho_{xx}(B)$ increases almost linearly with increasing magnetic field in the range $B < 8$ T. Similar dependences were also observed in other samples. It is known that the classical magnetoresistance of degenerate 2D electron gas with one filled subband equals zero. The only known mechanism responsible for a positive magnetoresistance is the filling of several subbands with different mobilities or the presence of several layers in the system. As is shown in [11], the average values of $\rho_{xx}(B)$ and $\rho_{xy}(B)$ of 2D electrons in a quantizing magnetic field are described by the same relations. Therefore, for a structure with two conducting layers, we obtain

$$\delta = \frac{\rho_{xx}(B)}{\rho_0} - 1 = \frac{a}{p}\frac{x^2(p-1)^2}{(1+ap)^2 + x^2(1+a)^2},$$

where $a = n_2/n_1$ and $x = \mu_2 B$. This dependence is quadratic in the weak field range, when $x \ll 1$. In a high field, the magnetoresistance tends to a limiting value and

$$\delta_{\max} = \frac{a}{p}\left(\frac{p-1}{a+1}\right)^2.$$

Our calculations yield $a \approx 0.85$ and $d_{\max} \approx 0.066$ for samples 6 and 7. In contrast, almost linear $\rho_{xx}(B)$ dependences are observed in experiment. At $B = 5$ T, we obtain $\delta = 2.7$ and $\delta = 1.6$ for samples 6 and 7, respectively. The reasons for such a large magnetoresistance and the significant disagreement with theory are still unclear.

5. CONCLUSION

The temperature dependences of the conductance and mobility of electrons in coupled quantum wells of various widths have been studied. As is shown, these quantities increase as the well width increases in the entire temperature range under study. The insertion of a thin AlAs barrier reduces the electron mobility in wide QWs and raises it in narrow ones. The variation in mobility is due to the changing intensity of the electron–phonon coupling. This results from the strong reconstruction of the electron wave functions and a change in the energy spectrum upon the insertion of an AlAs barrier.

ACKNOWLEDGMENTS

This study was supported by FTNS (Fixed Telecommunications Network Services) Program of the Ministry of Industry and Science of the Russian Federation, and by the Russian Foundation for Basic Research (project no. 00-02-17493).

REFERENCES

1. W. Trzeciakowski and B. D. McCombe, Appl. Phys. Lett. **55**, 891 (1989).
2. A. Lorke, U. Merkt, F. Malcher, *et al.*, Phys. Rev. B **42**, 1321 (1990).
3. J.-L. Cazaux, N. G. Geok-Ing, D. Pavlidis, and Hin-Fai Chau, IEEE Trans. Electron Devices **35**, 1223 (1988).
4. M. Nawaz, Solid-State Electron. **43**, 687 (1999).
5. C. S. Whelan, W. E. Hoke, R. A. McTaggart, *et al.*, IEEE Electron Device Lett. **21**, 5 (2000).
6. J. Pozela, V. Jucene, and K. Pozela, Solid State Technol. **10**, 1076 (1995).
7. Yu. Pozhela, K. Pozhela, and V. Yutsene, Fiz. Tekh. Poluprovodn. (St. Petersburg) **34**, 1053 (2000) [Semiconductors **34**, 1011 (2000)].
8. T. Tsuchiya and T. Ando, Phys. Rev. B **48**, 4599 (1993).
9. V. É. Kaminskiĭ, Fiz. Tekh. Poluprovodn. (Leningrad) **23**, 662 (1989) [Sov. Phys. Semicond. **23**, 414 (1989)].
10. V. É. Kaminskiĭ, Fiz. Tekh. Poluprovodn. (Leningrad) **25**, 453 (1991) [Sov. Phys. Semicond. **25**, 274 (1991)].
11. A. Isihara and I. Smrčka, J. Phys. C: Solid State Phys. **19**, 6777 (1986).

Translated by D. Mashovets

Semiconductors, Vol. 37, No. 6, 2003, pp. 692–698. Translated from Fizika i Tekhnika Poluprovodnikov, Vol. 37, No. 6, 2003, pp. 717–723.

LOW-DIMENSIONAL SYSTEMS

Zero Bias Anomalies of Transport Characteristics of Single-Barrier GaAs/AlAs/GaAs Heterostructures as a Result of Resonance Tunneling between Parallel Two-Dimensional Electron Gases and Suppression of Resonance Tunneling in a Magnetic Field as a Manifestation of the Coulomb Gap in the Tunnel Density of States

Yu. N. Khanin, Yu. V. Dubrovskiĭ, and E. E. Vdovin

Institute of Microelectronic Technology and Ultrahigh-Purity Materials, Russian Academy of Sciences, Chernogolovka, Moscow oblast, 142432 Russia

e-mail: khanin@ipmt-hpm.ac.ru

Submitted October 9, 2002; accepted for publication October 28, 2002

Abstract—Electron tunnel transport across single-barrier GaAs/AlAs/GaAs heterostructures is investigated. It is shown that "zero bias anomalies"—extrema in differential conductivity close to the zero bias—in the structures investigated are caused by resonance tunneling between parallel two-dimensional electron gases in enriched layers, which are formed from both sides of the barriers due to the presence of Si donor impurities in barriers. The suppression of resonance tunneling between parallel two-dimensional electron gases is found in narrow ranges close to the zero bias (tunnel gap) in a strong magnetic field parallel to the current direction only when a single Landau level is occupied for each of the two-dimensional electron gases. Suppression is induced by a Coulomb gap at the Fermi level in the tunnel density of states. This experiment originally revealed the manifestation of a Coulomb gap in tunneling between parallel two-dimensional electron gases with relatively low mobilities. For these electron gases, the influence of disorder or random potential fluctuations on the mechanism of formation of the tunnel gap is noticeable. © *2003 MAIK "Nauka/Interperiodica".*

1. INTRODUCTION

The problem of "zero bias anomalies" is the problem of the century for tunnel structures. In almost all experiments with conventional (nonsuperconducting) tunnel structures, zero bias anomalies are observed. These anomalies, which comprise the resistance peak or the conductivity peak close to zero bias, often substantially distort transport characteristics, and thus complicate the solution of experimental and applied problems. A comprehensive review of earlier experiments of this kind and discussion of them can be found, for example, in the Wolf monograph [1]. In this monograph, various models are suggested for specific tunnel systems to describe the observed zero bias anomalies, although a number of experiments have still not been explained [2, 3]. Tunnel heterostructures, despite having a considerably more controllable composition compared with other types of structures, are not the exception in this sense. These structures traditionally show the presence of zero bias anomalies (see, for example, [4, 5]), the causes of which are not always clear.

Zero bias anomalies, which manifest themselves in the differential conductivity of tunnel structures in the presence of a magnetic field, can be considered as a separate class. These are, for example, tunnel gaps, i.e., specific features, which indicate the presence of a Coulomb gap in the density of states upon tunneling between two two-dimensional electron gases (2DEGs). To date, numerous theoretical models exist which predict the emergence of a Coulomb gap at the Fermi level in the electron density of states for various cases of tunneling between parallel 2DEGs which differ from each other by the degree of disorder [6–10]. However, published experimental results in which the emergence of a Coulomb gap was observed upon tunneling between two parallel 2DEGs in a magnetic field $B \parallel I$ are scarce [8, 11]. We will compare our experimental data with these results. The results reported in [8, 11] are not adequately described by any of the existing theories; the results obtained in [8] were partly interpreted in [9]. To date, these results have been explained only qualitatively in the context of concepts of the strongly correlated nature of two-dimensional electron systems (2DESs) in strong fields $B \parallel I$ when only the lower Landau level is occupied [8]. For simplicity's sake, we may assume that each 2DES in this case constitutes a strongly correlated electron liquid, whose short-range order is similar to a Wigner crystal. The gap in the tunnel density of states for tunneling between 2DESs accounts for the additional energy necessary to force

out an electron, which will be further involved in tunneling, from the strongly correlated electron liquid. The same additional energy is also required for the incorporation of the tunneling electron into the correlated electron liquid. As a result, the gap width in the tunnel density of states is governed by the order of magnitude of the energy of the Coulomb electron interaction in the 2DES $E_C = e^2/\varepsilon\langle a\rangle$. Here, $\langle a\rangle$ is the average distance between electrons and ε is the permittivity. Due to this, it becomes clear why the Coulomb barrier for tunneling is often mentioned when discussing the suppression of tunneling in a magnetic field. Finally, we note that previous experiments, in which the emergence of a Coulomb gap was observed upon tunneling between parallel 2DESs in the field $B \parallel I$, were carried out using samples whose 2DESs possess high mobilities $\mu > 2 \times 10^5$ cm^2/(V s). Therefore, the important issue concerning the role of disorder in gap formation upon tunneling between 2DESs remains open.

The content of our publication is based on a description of investigations of tunneling and magnetotunneling across single-barrier GaAs/AlAs/GaAs heterostructures.

(i) Conductivity magnetooscillations in the magnetic field $B \parallel I$ for single-barrier heterostructures with various barrier thicknesses are investigated. The analysis of magnetooscillations showed that the cause of zero bias anomalies in the differential conductivity of these structures is the resonance tunneling between parallel 2DEGs in enriched layers which are formed on both sides of the barriers due to the presence of Si donor impurity in the barriers.

(ii) The transport across single-barrier heterostructures with 2DEG layers fabricated on both sides of the barrier using δ-doping of the near-barrier regions with Si donors is investigated. The transport characteristics of such heterostructures in the low-bias range turned out to be completely identical to the characteristics of structures without Si-doped δ-layers. This fact confirmed the interpretation of zero-bias anomalies in structures without δ-layers as the manifestation of resonance tunneling between parallel 2DEGs.

(iii) The transport in the magnetic field $B \parallel I$ across the structures both with δ-doping and without it is investigated. In both cases, the data obtained showed that in strong fields (when only a single Landau level is occupied in each of the 2DEGs on both sides of the barrier), resonance tunneling is suppressed in narrow voltage ranges close to the zero bias. This suppression is caused by the formation of a Coulomb gap at the Fermi level in the tunnel density of states under conditions of an ultraquantum limit. We compared our experimental results with the results of previous experiments in which tunneling between 2DEGs with a high electron mobility was investigated. This comparison gave us grounds to assume that the manifestation of a Coulomb gap during tunneling between parallel 2DEGs with a low mobility in the ultraquantum limit was revealed in our experiments for the first time. Moreover, the behavioral similarity of the transport characteristics of the samples with and without δ-doping provided additional evidence for the interpretation of zero-bias anomalies.

2. MAGNETOOSCILLATIONS OF CONDUCTIVITY IN SINGLE-BARRIER GaAs/AlAs/GaAs HETEROSTRUCTURES AND SPECIFIC FEATURES OF THE ELECTRON TRANSPORT ACROSS THESE STRUCTURES IN THE LOW-BIAS RANGE

In this section, we will report the results of investigations of conductivity magnetooscillations in the magnetic field $B \parallel I$ for single-barrier symmetric heterostructures. Analysis of oscillations showed that the zero-bias anomalies of transport characteristics in these structures are caused by resonance tunneling between parallel 2DEGs in enriched layers formed on both sides of the barriers due to the presence of Si donor impurities in the barriers. In addition, we report results of investigating the transport in the field $B \parallel I$ which are indicative of the suppression of tunneling between 2DEGs; this suppression is caused by the emergence of a Coulomb gap in the tunnel density of states.

We investigated samples which comprised single-barrier heterodiodes grown by molecular-beam epitaxy on heavily doped N^+-GaAs(100) substrates at 570°C. Si was used as the doping impurity; its concentration in the substrates was 2×10^{18} cm^{-3}.

Symmetric heterostructures included the following sequence of layers:

(i) an N^+-GaAs layer 0.4 μm thick, $N = 2 \times 10^{18}$ cm^{-3};

(ii) an N^--GaAs spacer 50 nm thick, $N = 2 \times 10^{16}$ cm^{-3};

(iii) an undoped GaAs spacer 10 nm thick;

(iv) an undoped AlAs barrier 2.5, 3.5, or 5 nm thick;

(v) an undoped GaAs spacer 10 nm thick;

(vi) an N^--GaAs spacer 50 nm thick, $N = 2 \times 10^{16}$ cm^{-3}; and

(vii) an N^+-GaAs contact layer 0.4 μm thick, $N = 2 \times 10^{18}$ cm^{-3}.

Nonrectifying contacts were formed by sequential deposition of the AuGe/Ni/Au layers and heat treatment at $T = 400$°C. To fabricate mesas with a diameter of 100 μm, the standard chemical etching procedure was used. The differential conductivity $G = dI/dV = f(V)$ and $G = dI/dV = f(B)$ was measured using the conventional modulation procedure.

The dependences $dI/dV = f(V)$ for the sample with a 5-nm-thick barrier, which were measured at $T = 4.2$ K in the field range $B \parallel I$ from 0 to 15 T, are shown in Fig. 1. As can be seen from Fig. 1, for low voltages, the dependences show the presence of a zero-bias anomaly of the "conductivity-peak" type. As will be seen from what follows, this anomaly is associated with resonance tunneling between 2DEGs on different sides of the barrier. The behavioral details of tunnel characteris-

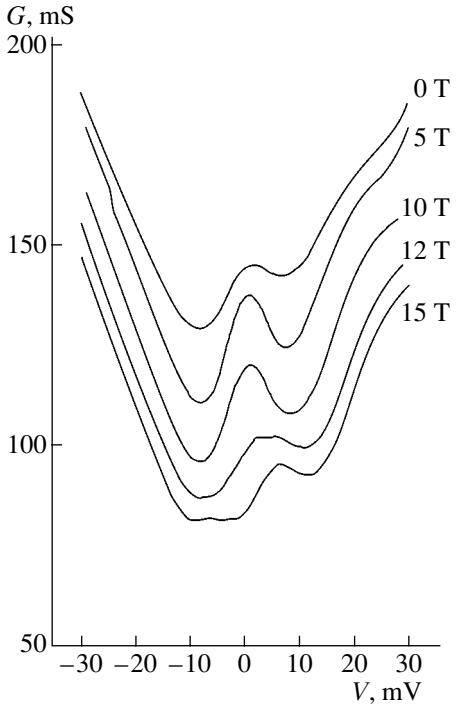

Fig. 1. Experimental dependences $dI/dV = G(V)$ for the sample with a 5-nm-thick barrier at $T = 4.2$ K in the magnetic field from 0 to 15 T parallel to the current.

tics with B increasing will be also clarified below. However, even now, the conductivity suppression by the magnetic field starting at 12 T should be pointed out. This suppression is supposedly the manifestation of the Coulomb gap.

Similar characteristics were typical of samples with other barrier thicknesses. However, the sample with a barrier 2.5 nm thick (Fig. 2) showed the most striking measurement results from the point of view of the magnitude of the zero-bias anomaly and emergence of the Coulomb gap in the magnetic field. It is possible that the reason for the somewhat larger amplitude of zero resonance (anomaly) for this sample is the smallest thickness of the tunnel barrier. As can be seen from Fig. 2, the conductivity suppression of $V \longrightarrow 0$ for $B >$ 8 T (tunnel gap) is clearly pronounced in the characteristics of the sample with a 2.5-nm-thick barrier. The dependence of the parameter of the tunnel gap, which is chosen as the difference between the voltages of maxima in $dI/dV = G = f(V)$, on the magnetic field B is almost linear (similarly to [8, 11]) and described by the expression $\Delta \approx 0.3\omega_c$, where ω_c is the cyclotron frequency.

However, let us return to the problem of zero-bias anomalies. To reveal their nature, the $G(B)$ dependences were measured for all sample types at various voltages V. The conductivity magnetooscillations with increasing B for high voltages V reflect the formation and shift of Landau levels relative to the Fermi level in the emitter accumulation layer [12]. Processing these

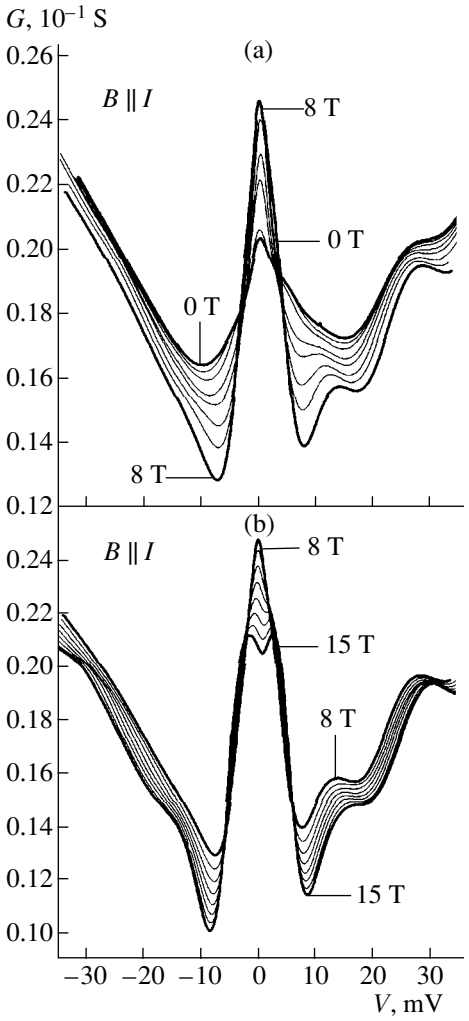

Fig. 2. Experimental dependences $dI/dV = G(V)$ for the sample with a 2.5-nm-thick barrier at $T = 4.2$ K in the magnetic field from 0 to 15 T parallel to the current. The ranges of the magnetic field B: (a) 0–8, (b) 8–15 T.

oscillations according to the standard procedure allows one to determine the Fermi energy and electron density in the accumulation layer for a specified voltage. A typical form of the $G(B)$ dependence obtained by us is shown in Fig. 3. All sample types showed the presence of clearly distinguishable oscillations at high voltages, with the only difference being that oscillations for samples with 2.5-nm-thick barriers were considerably more broadened compared with those for samples with 5.0- and 3.5-nm-thick barriers. This is evidently associated with a shorter electron lifetime in the emitter accumulation layer confined by the 2.5-nm-thick barrier. The dependence of the Fermi energy on the voltage $E_F(V)$, which was obtained from processing the oscillations for the sample with the 5-nm-thick barrier, is shown in Fig. 4. Similar dependences were also observed for other samples. The extrapolation of this dependence to zero voltage points to a considerable electron density ($\sim 2.5 \times 10^{11}$ cm^{-2}) in the 2DEG layer in the absence of

voltage. This is probably caused by the existence of a residual enriched electron layer in the emitter near-barrier region for $V = 0$. Similar voltage dependences of the Fermi energy and electron density were also obtained for $V < 0$. Therefore, due to the symmetry of our structures, it should be assumed that, for $V = 0$, enriched layers with almost identical electron densities exist in the near-barrier regions on both sides of the barrier. However, the real electron densities in enriched layers in the absence of voltage will probably be substantially lower than those obtained from the extrapolation of the $E_F(V)$ dependences to $V = 0$ for a certain broadening of Landau levels, which was obtained from the processing of magnetooscillations for high *V*. Here, the inapplicability of the concepts of a linear variation in parameters of the emitter accumulation layer in the range of low positive voltages, where the enriched collector layer vanishes, should be taken into account.

Thus, the analysis carried out indicates that, in the samples under consideration, enriched electron layers can exist on different sides of the barrier for $V = 0$. The coincidence of the energies of two-dimensional subbands in these layers, which occurs for $V \approx 0$, leads, according to [11], to the presence of a local maximum in the $G(V)$ dependences (a conductivity peak). The most probable reason for the formation of such layers is the presence of positively charged Si donors in the barrier, which are there due to residual doping and diffusion from the contact layer.

3. MANIFESTATION OF THE COULOMB GAP AT TUNNELING BETWEEN PARALLEL 2DEGS FOR SINGLE-BARRIER δ-DOPED $GaAs/Al_{0.4}Ga_{0.6}As/GaAs$ HETEROSTRUCTURES

In this section, the results of investigating electron transport across single-barrier $GaAs/Al_{0.4}Ga_{0.6}As/GaAs$ heterostructures will be reported. In these heterostructures, parallel layers of low-mobility 2DEG on both sides of the barrier were formed using Si-doped δ-layers. Measurements in the absence of a magnetic field showed the presence of a conductivity peak $G(V)$ for $V \longrightarrow 0$, which is caused by resonance tunneling between these parallel 2DEGs in the near-barrier regions. This fact provided additional confirmation of the interpretation of zero-bias anomalies given in the previous section. The main result of investigations described in this section consists in the observation of the Coulomb gap in the tunnel density of states during tunneling between 2DEGs with low electron mobility, which manifests itself in the suppression and splitting (tunnel gap) of the conductivity peak for $V \longrightarrow 0$ in a strong magnetic field $B \parallel I$. The similarity of manifestations of the Coulomb gap for the structures with δ doping and without it provides one more independent confirmation of the validity of interpreting the nature of zero bias anomalies for the structures without δ doping.

The single-barrier $GaAs/Al_{0.4}Ga_{0.6}As/GaAs$ structures investigated here differ from those used in the experiments described in the previous section by the presence of 2DEG layers, which were fabricated on both sides of the barrier using δ-doping with Si. The Si concentration in the δ-layers was 3×10^{11} cm^{-2}; these layers were spaced by 5 nm from the barrier. Measurements of the Shubnikov–de Haas oscillations for these structures showed that the electron density in the 2DEG

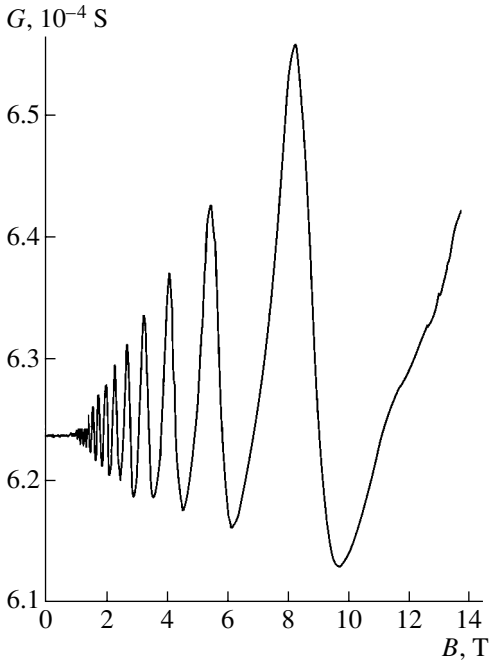

Fig. 3. Dependence $dI/dV = G(V)$ for the sample with a 5-nm-thick barrier at a bias voltage $V = 900$ mV and $T = 4.2$ K.

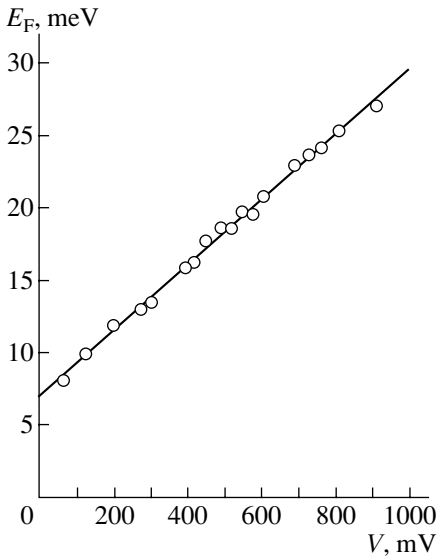

Fig. 4. Dependence of the Fermi energy E_F on the voltage V in the accumulation layer of the sample with a barrier 5 nm thick; this dependence was obtained from an analysis of magnetooscillations. A linear approximation of the dependence is shown by the solid line.

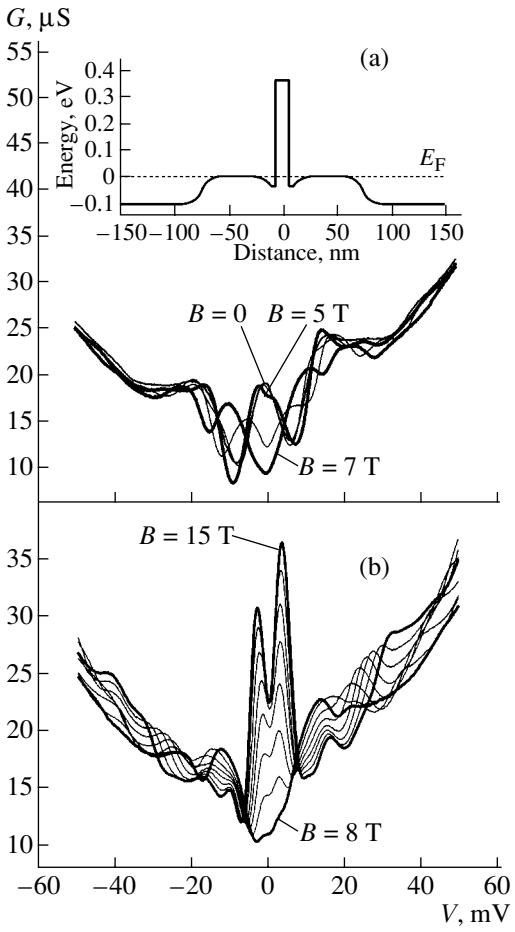

Fig. 5. Dependences $dI/dV = G(V)$ for the sample with Si-doped δ-layers measured at $T = 4.2$ K in the range $B \parallel I$ from 0 to 15 T. The ranges of the magnetic field B: (a) 0–7, (b) 8–15 T. The energy-band diagram of the investigated structure is shown in the inset.

coincides with the nominal Si concentration in δ-layers. Moreover, these structures differed from the previous ones by the barrier thickness, which was equal to 12 nm, and, obviously, by the composition of the barrier layer. The profile of the conduction band bottom of the structures investigated for $V \longrightarrow 0$ is shown in the inset to Fig. 5.

The dependences $dI/dV = G(V)$ for these structures, which were measured at $T = 4.2$ K in the range of current-parallel magnetic fields from 0 to 15 T, are shown in Fig. 5. As can be seen from Fig. 5a, the dependence $G(V)$ for $B = 0$ features a noticeable conductivity peak close to the zero bias. This peak is caused by resonance tunneling between parallel 2DEGs, which are located on different sides of the barrier [11]. The nature of conductivity peaks for high voltages will not be discussed. The conductivity peak at $V \longrightarrow 0$ for these structures, which differ from the structures considered in the previous section only in the intentionally fabricated 2DEG layers, confirms the interpretation of zero-bias anomalies which we suggested. The variations in conductivity with increasing $B \parallel I$ during tunneling between parallel 2DEGs reflect, according to [12], the formation and shift of Landau levels relative to the Fermi level. From this point of view, the conductivity oscillations for $V \longrightarrow 0$ with B increasing from 0 to 7 T can be easily related to variations in the density of states at the Fermi level in the 2DEG in a magnetic field. Substantially weaker oscillations dI/dV ($V \longrightarrow 0$) for the samples without δ doping in this B range are probably caused by the lower electron density in 2DEG for comparable values of broadening of the Landau levels. An evident structure of specific features, which manifest themselves for nonzero voltages beginning from $B \approx 5$ T, is associated with transitions between the Landau levels with various indices. Upon reaching $B = 8$ T, when only one Landau level remains below the Fermi level for each of the 2DEGs, the conductivity for $V \longrightarrow 0$ again starts to increase according to the increase in the density of states at the Fermi level in each 2DEG as the last Landau level approaches the Fermi level. Simultaneously with an increase in the conductivity peak, a dip in the $G(V)$ dependence for $V \longrightarrow 0$ emerges and becomes more profound. This dip indicates that the Coulomb gap is formed in the tunnel density of states under conditions of an ultraquantum limit.

Let us now compare our experimental data, which concern the observation of a Coulomb gap, with the data [8, 11], where a Coulomb gap was observed during tunneling between 2DEGs with high electron mobility. The B dependence of the gap parameter Δ was determined by analogy with [8, 11] as the voltage difference V for the peaks of the $G(V)$ dependence for $V \longrightarrow 0$. In our case, this dependence turned out to be virtually linear; it is described by the expression $\Delta = 0.3\omega_c$. In [8, 11], these dependences were also linear, and described by expressions $\Delta = 0.44\omega_c$ and $\Delta = 0.2\omega_c$, respectively. Note that an attempt was made [8] to approximate the experimental data by the expression $\Delta = 2\pi e^2/\varepsilon l_0$, where $l_0 = (\hbar/eB)^{1/2}$ is the magnetic length. This expression was obtained theoretically [9]. However, the approximation of the data by the functions $\Delta = Ae^2/\varepsilon l_0$, where A is a coefficient, led to the result $\Delta = 0.9e^2/\varepsilon l_0$, which differs by an order of magnitude from that predicted in [9]. Moreover, it should be noted that the magnitude $\Delta = 0.3\omega_c$ coincides with that obtained in the previous section for the samples without δ doping.

The investigation of the temperature dependence of G for $B = 15$ T in the range from 2.5 to 15 K (Fig. 6) showed that the gap is almost completely suppressed at $T \approx 11$ K. A similar result, despite a difference in electron densities in 2DEGs, was also reported in [8]. In the latter case, when the density was equal to 1.6×10^{11} cm^{-2}, gap suppression in the field $B = 14$ T occurred at $T = 10$ K. The data [11] concern the results from investigating the temperature dependence only for $B \leq 8$ T. For $B = 8$ T, the gap was suppressed at $T = 6$ K. Based on a comparison of our data with the data [8], we assume that the concentration of 2DEG weakly affects the gap width (in [11], the concentration was 10^{11} cm^{-2}). Since

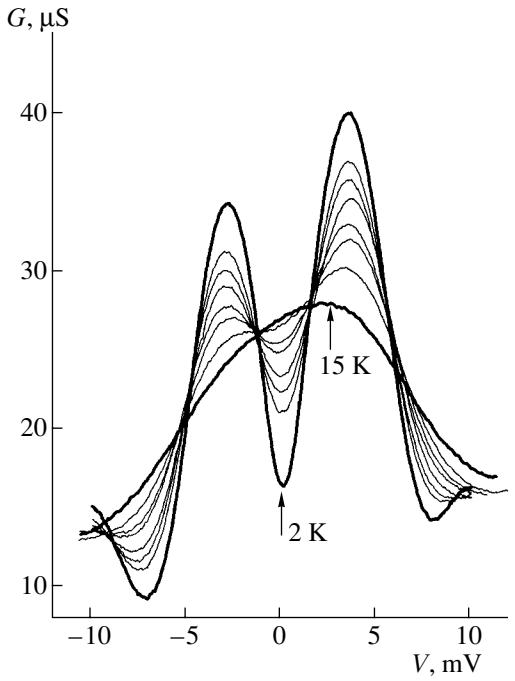

Fig. 6. Dependences $G(V)$ for the sample with Si-doped δ-layers measured at $B = 15$ T in the temperature range from 2 to 15 K (at $T = 2.0$, 4.2, 5.2, 6.1, 7.2, 8.3, 10.3, and 15 K).

the dependence of Δ on the magnetic field is linear, $\Delta = 0.44\omega_c$, we may assume that the gap suppression for the field $B \approx 14$ T should occur under experimental conditions [11] at $T \approx 10$ K and consider this result to be in coincidence both with our result and with the data [8]. The gap parameters Δ almost coincide for identical B. For example, for $B = 10$ T, we observed $\Delta \approx 5$ mV, whereas in [11] and [8] $\Delta \approx 7$ mV and $\Delta \approx 10$ mV, respectively.

Our samples differed from those investigated in [8, 11] by a substantially lower electron mobility. According to estimations, it was no higher than 10^4 cm^2/(V s) at $T = 4.2$ K, which is an order of magnitude lower than the lowest mobility of the samples in [8, 11]. Therefore, in our case, the substantial influence of disorder (random potential) on the mechanism of formation of the Coulomb gap could not be excluded. The width of the conductivity peak for $V \longrightarrow 0$ which we observed for $B = 0$ and which was considerably larger compared with that in [8, 11] also points to the noticeable role of disorder under our experimental conditions. The theories which make allowance for the influence of disorder on the correlation Coulomb interaction of electrons predict various singular tunnel gaps at the Fermi level (see, for example, [6, 7]). To reveal the role of disorder in our samples, it is necessary to carry out additional experiments at $T < 1$ K. These experiments may provide the possibility for a correct quantitative comparison of the $G(V)$ dependences in the gap region both with theoretical predictions and with previous experimental results [8, 11], which were obtained predominantly at $T < 1$ K. Irrespective of the specific form of the theoretical model which predicts a tunnel gap at the Fermi level, the principal cause for the emergence of this gap is the correlation Coulomb interaction with 2DES. Therefore, despite uncertainty with respect to the specific mechanism for the formation of the Coulomb gap, we have all the reasons to assume that a Coulomb gap during tunneling between parallel 2DESs with a low electron mobility—in the ultraquantum limit by the magnetic field—was detected for the first time in our experiment.

4. CONCLUSION

In this publication, we report the results of investigations of conductivity magnetooscillations in the magnetic field parallel to the current ($B \parallel I$) for single-barrier GaAs/AlAs/GaAs heterostructures with spacers and various barrier thicknesses. The data obtained allowed us to show that the cause of anomalies in the differential conductivity G of these structures for $V \longrightarrow 0$ is the resonance tunneling between parallel two-dimensional electron gases (2DEGs) in enriched layers formed on both sides of the barrier due to the presence of Si donor impurity in the barrier. The results of investigating the transport across the heterostructures (both with δ doping and without it) in the magnetic field $B \parallel I$ are reported. These data showed that in strong fields, when only one Landau level is occupied in each 2DEG on both sides of the barrier, an anomaly emerges in the $G(V)$ dependence in narrow bias ranges close to the voltage $V \longrightarrow 0$ (tunnel gap), which is caused by the effect of the correlation Coulomb interaction of electrons in 2DEG. It is generally assumed that the interaction leads to the formation of a Coulomb barrier or Coulomb gap at the Fermi level in the electron density of states. Our experiment for the first time revealed the manifestation of a Coulomb gap during tunneling between parallel 2DEGs with relatively low mobilities. In such structures, the influence of disorder, i.e., random potential fluctuations, on the mechanism for the formation of a tunnel gap is significant. Analysis of the obtained data additionally confirmed the interpretation of the zero-bias anomaly for the samples without δ doping. Moreover, it was found that the magnetic-field and temperature dependences of the main energy parameter of the tunnel gap (gap "width" or energy gap) obtained by us are similar to those observed in experiments in which tunneling between parallel 2DEGs with high mobilities was investigated and where the effect of disorder was conventionally assumed to be negligible.

ACKNOWLEDGMENTS

We thank T.G. Andersson and M. Henini for the heterostructures placed at our disposal, and J.-K. Portal and D.K. Mod for their helpful participation in discussions.

This study was supported in part by the Russian Foundation for Basic Research program "Physics of Solid-State Nanostructures," and INTAS (project no. 01-2362).

REFERENCES

1. E. L. Wolf, *Principles of Electron Tunneling Spectroscopy* (Oxford Univ. Press, New York, 1985; Naukova Dumka, Kiev, 1990).
2. J. M. Rowell and L. Y. L. Shen, Phys. Rev. Lett. **17**, 15 (1966).
3. R. N. Hall, J. H. Racette, and H. Ehrereich, Phys. Rev. Lett. **4**, 456 (1960).
4. R. T. Collins, J. Lambe, T. C. McGrill, and R. D. Burnham, Appl. Phys. Lett. **44**, 532 (1984).
5. K. Hirakava, Phys. Rev. B **40**, 3451 (1989).
6. A. L. Efros and B. I. Shklovskii, in *Electron–Electron Interactions in Disordered Systems*, Ed. by A. L. Efros and M. A. Pollak (North-Holland, Amsterdam, 1985), p. 109.
7. B. L. Altshuler, A. G. Aronov, and K. W. Lee, Phys. Rev. Lett. **44**, 1288 (1980).
8. J. P. Eisenshtein, L. N. Pfeiffer, and K. W. West, Phys. Rev. Lett. **69**, 3804 (1992).
9. Song He, P. M. Platzman, and B. I. Halperin, Phys. Rev. Lett. **71**, 777 (1993).
10. P. Johannson and J. M. Kinaret, Phys. Rev. Lett. **71**, 1435 (1993); Phys. Rev. B **50**, 4671 (1994).
11. N. Turner, J. T. Nicholls, E. H. Linfield, *et al.*, Phys. Rev. B **54**, 10614 (1996).
12. E. Bockenhoff, K. von Klitzing, and K. Ploog, Phys. Rev. B **38**, 10120 (1988).

Translated by N. Korovin

Semiconductors, Vol. 37, No. 6, 2003, pp. 699–704. Translated from Fizika i Tekhnika Poluprovodnikov, Vol. 37, No. 6, 2003, pp. 724–729.

LOW-DIMENSIONAL SYSTEMS

Low-Temperature Anti-Stokes Photoluminescence in CdSe/ZnSe Nanostructures

M. Ya. Valakh*, N. V. Vuychik*, V. V. Strelchuk*, S. V. Sorokin, T. V. Shubina**, S. V. Ivanov**, and P. S. Kop'ev****

**Institute of Semiconductor Physics, National Academy of Sciences of Ukraine, Kiev, 252028 Ukraine*
e-mail: valakh@isp.kiev.ua

***Ioffe Physicotechnical Institute, Russian Academy of Sciences, Politekhnicheskaya ul. 26, St. Petersburg, 194021 Russia*

Submitted October 16, 2002; accepted for publication October 28, 2002

Abstract—Intense anti-Stokes photoluminescence was observed at low temperatures in CdSe/ZnSe nanostructures with separate CdSe inserts in a ZnSe matrix; the nominal thickness of these inserts amounted to 1.5 and 0.6 monolayers. It is shown that the intensity of an anti-Stokes band excited by the photons of energies considerably lower than the band's peak is quadratic in the excitation power; in the case of resonance excitation, a weaker dependence is obtained. A mechanism behind the excitation of anti-Stokes photoluminescence is suggested on the basis of nonlinear two-step two-photon absorption via the deep states of the defect centers including cation vacancies localized at the barrier–nanoisland interface. *© 2003 MAIK "Nauka/Interperiodica".*

1. INTRODUCTION

Semiconductor quantum dots (QDs) on the basis of II–VI and III–V compounds in semiconductor matrices hold promise for modern optoelectronic applications, in particular, for the development of highly efficient light-emitting diodes and lasers with a high quantum efficiency and extremely low pump intensity. A considerable number of investigations in this field are concerned with the self-organized growth of QDs. For example, TEM studies of CdSe/ZnSe heterosystems [1] showed that the deposition of CdSe layers with a nominal thickness of 0.5–3.0 monolayers (MLs) at a temperature ≤280°C results in the formation of a two-dimensional (2D) $Zn_{1-x}Cd_xSe$ layer with mixed composition and a thickness of ~10–11 ML (one ML corresponds to 0.283 nm). This 2D layer contains two prevailing types of coherently stressed islands: cadmium-enriched small islands (≤10 nm) with a high density (~10^{11} cm^{-2}) and large islands (30–130 nm) with a comparably lower density (~10^{10} cm^{-2}). These intralayer 2D islands may be considered as forerunners of three-dimensional (3D) islands. Therefore, the realization of a 2D–3D morphological transition can be assumed as smooth in contrast to the Stranski–Krastanov mechanism, which has a pronounced threshold and is typical of most III–V systems, where the 2D wetting layer abruptly transforms into 3D islands.[1] An appreciable thickening of the 2D layer in comparison with the nominal thickness of the deposited CdSe layer may be due to the interdiffusion and segregation of Cd/Zn at the heterointerface [1]. Highly efficient mixing of the barrier and quantum-well materials in the CdSe/ZnSe heterostructure was previously observed both for an individual quantum well and for superlattices [3–5]. An increase in the diffusion length of Cd atoms in this system is attributed to nonequilibrium growth conditions during molecular-beam epitaxy, which leads to the formation of cation vacancies with a high density. The lifetime of carriers captured by defects may be fairly long. In the presence of such defects and sufficiently fast radiative-recombination centers in the steady-state condition, the excitation by photons with a lower energy may cause the emission of photons with a higher energy (anti-Stokes emission).

Anti-Stokes photoluminescence (APL) was observed in crystalline semiconductors [6, 7], porous silicon [8], colloidal semiconductor QDs [9], semiconductor heterojunctions and quantum wells (QWs) [10–13], as well as in InAs QDs [14] and InP QDs [15]. In most of these studies, interpreting the physical mechanism behind the ALP process involved the Auger recombination of carriers [12, 13] and nonlinear two-step two-photon absorption via the real intermediate states [6–11, 14, 15]. For bulk GaAs [6], epitaxial GaAs and GaAlAs layers [7], and InP QDs [15], APL was interpreted as the process of a two-step optical excitation of an electron–hole pair via the intermediate deep levels of defects. Note that, in the case of semiconductor heterojunctions and nanostructures with QWs and QDs, the two-step photoexcitation of highly efficient APL both via the deep levels of defects and via the size quantization levels was observed in the region of wide gap material. In this study, we investigate the phenomenon of anti-Stokes luminescence in CdSe/ZnSe nanostructures emitting from the region of CdSe insert, which is a narrower (in comparison to ZnSe) energy-gap component

[1] According to [2], the formation of 3D islands in II–VI nanostructures can be stimulated in a special mode of thermal activation.

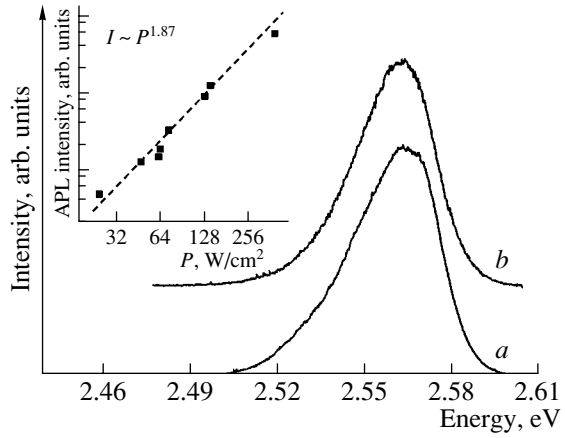

Fig. 1. PL spectra of a CdSe/ZnSe nanostructure containing a CdSe insert with a nominal thickness of 1.5 ML under excitation by an Ar^+-laser with E_{exc} = (*a*) 2.602 and (*b*) 2.41 eV at T = 90 K. The inset shows anti-Stokes PL (APL) intensity I vs. the pump power density at E_{exc} = 2.41 eV on the log–log scale.

of the heterostructure. The dependences of APL on the wavelength and the intensity of excitation were analyzed.

2. EXPERIMENTAL

The pseudomorphic growth of CdSe/ZnSe epitaxial structures was carried out by molecular-beam epitaxy (MBE) at a temperature of 280–300°C on a GaAs (001) buffer epilayer grown in a $A^{III}B^{V}$ MBE chamber, which was vacuum-coupled to a $A^{II}B^{VI}$ MBE chamber. The conventionally initiated epitaxial growth of ZnSe on GaAs with enhanced migration of atoms was followed by the deposition of an 80-nm-thick ZnSe buffer layer. CdSe layers with nominal thicknesses of 0.6 and 1.5 ML were grown by the submonolayer cyclic MBE technique [16, 17]. The nominal thickness of the CdSe layers was determined by the number of deposition cycles (0.3 ML per cycle), with the growth being interrupted for 10 s after each cycle. At the last stage, the deposition of a 20-nm-thick protective bounding ZnSe layer completed the growth of a sample.

For the excitation of PL and Raman scattering (RS), various lines of Ar^+-laser radiation were used. Some of the PL spectra were excited by Xe lamp. RS and PL spectra were measured using a DFS-24-type double spectrometer with detection based on the photon-counting system. The spectral position of lines was determined at a precision no worse than 0.3 cm^{-1}, which was ensured by the simultaneous detection of laser lines.

3. RESULTS AND DISCUSSION

Figure 1 shows the PL spectra measured at T = 90 K in CdSe/ZnSe nanostructures containing the CdSe individual insert with a nominal thickness of 1.5 ML. The PL spectrum obtained under conventional high-energy excitation (photon energy E_{exc} = 2.602 eV, Fig. 1, curve *a*) exhibits a well-pronounced band corresponding to the emission from CdSe islands with a peak at ~2.564 eV and a half-width $\Delta E \approx 35$ meV. The asymmetry of the band and the spectral position of its peak are in agreement with recently published results [16, 18] and can be caused by the simultaneous contribution to the PL spectrum of radiation from 2D excitons localized in the $Zn_{1-x}Cd_xSe$ wetting layer (high-energy wing) and of that of the excitons localized in small intralayer islands with local peaks of Cd concentration (low-energy wing).

When PL is excited by photons with energies below the peak of the PL exciton band (photon energy E_{exc} = 2.41 eV, Fig. 1, curve *b*), anti-Stokes radiation is observed. The position of the peak and the shape of the PL band are retained, while the half-width of the band slightly decreases ($\Delta E \approx 5$ meV). In this case, the excitation of anti-Stokes luminescence may be interpreted on the basis of the two-step electron–hole pair excitation via deep levels including singly and doubly charged cation vacancies localized mainly at the barrier–nanoisland boundary. For a sufficiently dense array of nanoislands, where the distance between them is comparable to the size of a single island (for a CdSe insert with a nominal thickness of 1.5 ML, the density of small islands is ~10^{11} cm^{-2} and the average distance between them is between 15 and 20 nm [1]), one should take into account their elastic interaction that stems from the penetration of a nonuniform stress field, which is produced by the islands, into the substrate. This may lead to the gettering of point defects from the ZnSe barrier layers and CdSe nanoislands at their heteroboundaries.

In ZnSe, defect centers containing cation vacancies are known to be responsible for an absorption band at ~500 nm (~2.48 eV) associated with the doubly charged Zn vacancy (V_{Zn}^{-2}), as well as bands at ~885 nm (~1.4 eV) and ~468 nm (~2.65 eV) attributed to a singly charged Zn vacancy (V_{Zn}^{-1}) [19]. A broad band observed in the PL spectra of ZnSe at ~620 nm (~2.01 eV) corresponds to self-activated emission from the complex consisting of a donor and doubly charged Zn vacancy (D–V_{Zn}^{-2}), and the band at ~720 nm (1.72 eV) should be ascribed to the emission from a defect center containing an isolated Zn vacancy [19]. The lifetime of carriers captured by these centers amounts to ~10^{-3} s. Unfortunately, no evidence of emission from such centers was found in the PL spectra of single-layer structures considered in this study. However, this emission was reliably detected in the experiments with multilayer CdSe/ZnSe structures; these results will be reported in detail in a future paper.

In order to ascertain the dominant mechanism for the excitation of the anti-Stokes radiation, we investigated the dependence of the APL intensity (I) on the

excitation power (P). Since the experiments were performed at low temperatures, the thermal excitation of carriers may be disregarded.[2] In addition, we also disregarded the possible contribution of the direct two-photon absorption in view of the low excitation power ($P < 400$ W/cm^2) used in the experiment. Note also that, because of the Fermi level position near the midgap in ZnSe, as is typical of $A^{II}B^{VI}$ compounds, the defect centers containing cation vacancies are expected to be initially filled with electrons. Therefore, the absorption of a photon by such a long-lived impurity center with the following excitation of nonequilibrium electrons to the conduction band at the ZnSe (and/or ZnCdSe wetting layer) barrier may be regarded as the first stage of APL excitation. During the eventual thermalization, these electrons may be captured by the lower levels of size quantization of the islands. As the next stage, we consider the photoinduced transition of electrons from the valence band of the ZnSe barrier layer (and/or wetting layer) to the defect centers. The resulting holes are captured by the levels in the potential well of nanoislands, and the radiative recombination of a pair of carriers occurs. Taking into consideration the fact that, at low temperature, the band gap of the ZnSe barrier amounts to ~2.8 eV, the energy level involved in the two-step excitation by photons with an energy of 2.41 eV lies at least 0.4 eV below (above) the conduction (valence) band edge of the ZnSe barrier. The efficiency of two-step two-photon absorption can increase with increasing density of these intermediate states. A quadratic dependence of the resulting APL intensity on the excitation intensity should be expected at sufficiently small values of the latter (see, e.g., [10]). This dependence was obtained for a sample containing a CdSe insert with a 1.5-ML nominal thickness and is shown in the inset in Fig. 1 on a log–log scale, and it is actually close to a straight line with a slope of 2. It should be noted that the intensity of PL obtained by conventional high-energy excitation depended almost linearly on the excitation power. The efficiency of APL excited by 2.41 eV photons amounts to several percent of that from direct excitation with 2.707 eV photons of comparable intensity ($P \approx 10$ W/cm^2).

As an alternative to the APL excitation mechanism considered above, we also analyzed the mechanism that implies electron transitions at the GaAs/ZnSe boundary. We recognize that the energy positions of the conduction bands in GaAs and ZnSe are close to each other (the valence band top in GaAs lies approximately 1 eV higher than that in ZnSe); as a result, an electron excited from the GaAs valence band may enter the ZnSe conduction band and, after diffusion, a CdSe too. A hole may appear in the well as a result of a transition from the ZnSe valence band where this hole can be produced due to the photoexcitation of the electron to the GaAs valence band. However, this scenario encounters the following inconsistencies.

(1) In direct-gap GaAs, the lifetime of photoexcited electrons is fairly short; therefore, a comparatively high power would be required for the two-step excitation in order to exceed the efficiency of the competing recombination channel in the GaAs bulk material. In our case, APL was observed at $P < 10$ W/cm^2.

(2) We failed to observe even weak APL from the ZnSe barrier, which should have been possible during the above alternative process.

(3) Even after the photoexcitation power was increased by one to two orders of magnitude, no indication of expected plasmon–phonon interactions was detected in the phonon RS spectrum from the GaAs substrate.

We also studied the PL spectra of samples subjected to resonance excitation in a low-energy wing of the emission band ($E_{exc} = 2.54$ eV, Fig. 2). We detected PL in both the Stokes and anti-Stokes spectral regions. In the Stokes region, a band with a peak at ~2.522 eV and a half-width of ~5 eV appears. We attributed this band to the exciton recombination of the resonantly excited ensemble of nanoislands of a certain size and composition. The excitonic origin of this band is evidenced by its small half-width and its constant energy position with increasing excitation power.

Using a well-known dependence obtained within the context of the quantum-disk model [20] and relating the spectral position of peaks in cathodoluminescence spectra to the size of islands and the Cd content, we estimated the content of Cd corresponding to the band under consideration. The calculation yielded $x \approx 0.4$, which appreciably exceeds the value for samples with the same nominal thickness of the insert [1] but which were grown in by conventional MBE deposition conditions farther from equilibrium. The fact that this band does not manifest itself under high-energy nonresonance excitation (Fig. 1, spectrum *a*) may be due to an insufficient density of nonequilibrium carriers or some special features of their relaxation in the system of islands with a spatially nonuniform potential.

It should be noted that, under resonance excitation, the APL efficiency is about one order of magnitude higher than that in the case of nonresonance excitation (Fig. 1, spectrum *b*). This enhancement of APL may be caused by an additional contribution of the size-quantization levels of nanoislands acting as intermediate states. Another possible mechanism of APL enhancement under resonance excitation of nanoislands is the Auger recombination process. However, this mechanism implies a cubic dependence of the APL intensity on the excitation intensity, which contradicts the experimental data ($\sim I^{1.3}$). Thus, we conclude that, in our case, the Auger process is not the dominant mechanism of anti-Stokes radiation.

Three curves in Fig. 2 illustrate changes in the PL spectrum with an increase in the power density of exci-

[2] We failed to detect anti-Stokes PL at room temperature. It is evidently the thermal activation of carriers and their nonradiative recombination that is dominant in this case.

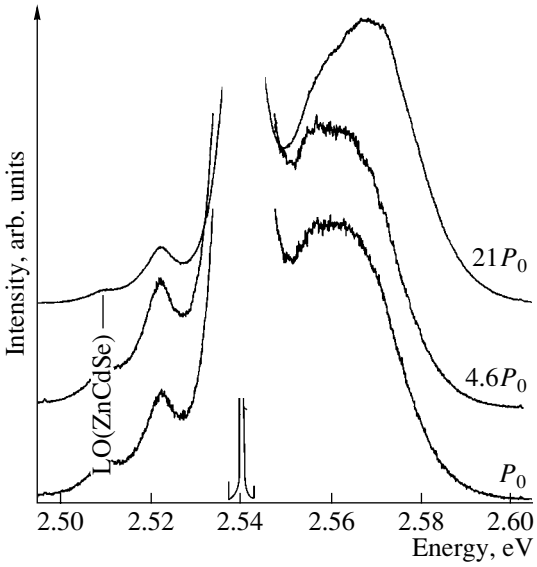

Fig. 2. PL spectra under resonant excitation of the CdSe/ZnSe nanostructure containing a CdSe insert with a nominal thickness of 1.5 ML for different pump power density. E_{exc} = 2.54 eV, P_0 = 30 W/cm^2. T = 90 K.

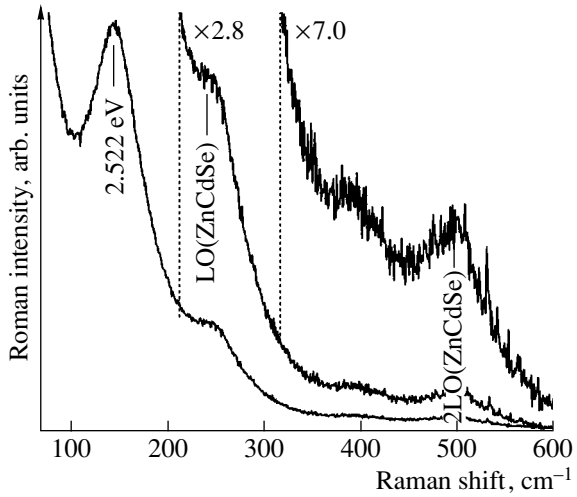

Fig. 3. Resonance RS spectra of a CdSe/ZnSe nanostructure containing a CdSe insert with a nominal thickness of 1.5 ML. E_{exc} = 2.54 eV. T = 90 K.

tation from 30 to 630 W/cm^2. It is seen that, along with an increase in the APL intensity, an additional peak appears on the high-energy side, so that, at P = 630 W/cm^2, the spectrum features two bands peaked at ~2.56 and ~2.57 eV. In study [21], this higher energy component in a resonantly excited PL band was attributed to the recombination via the first excited state of nanoislands. We believe that this issue deserves further investigation, since a number of other variants are possible: for example, the recombination with transitions from the ground state to the light-hole level (*e–lh*) or

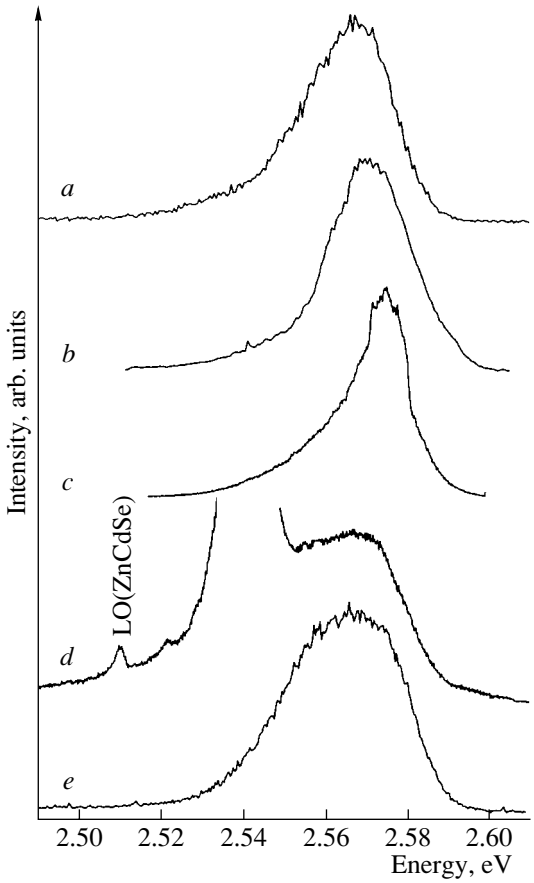

Fig. 4. PL spectra of a CdSe/ZnSe nanostructure containing a CdSe insert with a nominal thickness of 1.5 ML under excitation with photons with energies E_{exc} = (*a*) 2.882, (*b*) 2.707, (*c*) 2.602, (*d*) 2.54, and (*e*) 2.41 eV. T = 5 K.

the emission from an average-composition ZnCdSe well surrounding the islands.

The excitation by photons with an energy of 2.54 eV also gives rise to lines of Raman scattering, which are clearly seen in Fig. 3. The resonance RS spectrum contains LO and 2LO lines corresponding to scattering by longitudinal optical phonons in the $Zn_{1-x}Cd_xSe$ insert at frequencies $\nu_{LO} \approx 248$ cm^{-1} and $\nu_{2LO} \approx 500$ cm^{-1}. The frequencies of the LO and 2LO bands indicate that an RS signal forms in the region of the CdSe insert and corresponds to the mixed solid solution $Zn_{1-x}Cd_xSe$ with $x \approx$ 20–25% [22, 23]. The comparatively large half-widths of the detected lines ($\Gamma_{LO} \approx 32$ cm^{-1} and $\Gamma_{2LO} \approx 43$ cm^{-1}) can be due to the inhomogeneous composition of the insert, as well as to the effect of elastic strain in the probed regions.

Figure 4 shows the PL spectra of the studied sample at T = 5 K. As a result of excitation in the range of the ZnSe barrier absorption (Fig. 4, spectrum *a*), we observed an inhomogeneously broadened band with a peak at ~2.568 eV. Comparing this spectrum with that of the PL obtained at T = 90 K (Fig. 1, spectrum *a*), we notice a decrease in the band half-width from 35 to

24 meV, a higher symmetry of the curve, and a shift of its peak to higher energies by ~4 eV. The latter circumstance is attributed to both the temperature shift and a more pronounced (as compared to the case of nanoislands) growth of the high-energy wing, which is formed by the radiation of 2D excitons in the ZnCdSe wetting layer. The position and shape of the PL band from CdSe islands remains nearly constant if the excitation-photon energy is less than the band-gap width of the ZnSe barrier (Fig. 4, spectrum *b*). This situation changes radically when the photon energy is close to the energy of the excitonic transition of a light hole[3] (Fig. 4, spectrum *c*). The PL band peak shifts to higher energies by $\Delta E \approx 6$ meV, and its half-width decreases from ~35 to ~13 meV. This effect stems from the selectively resonant excitation of localized exciton states below the Mott–Anderson mobility edge [24] with the involvement of LO and TO phonons. A similar effect was observed in [25] for CdS_xSe_{1-x} solid solutions and CdSe/ZnSe superlattices with CdSe layers having a submonolayer thickness [26, 27]. A mobility edge appearing in such systems is due to the nonuniform distribution of internal strain and the inhomogeneous composition of the insert.

When the photon energy corresponds to the low-energy wing of the PL band (Fig. 4, spectrum *d*), a PL signal is detected in both the Stokes and anti-Stokes spectral regions (similar to the case illustrated in Fig. 2). In the Stokes region, a weak band appears at 2.522 eV; this band was related above (Fig. 2) to the radiation from nanoislands of certain size and composition. The spectrum also contains an RS line, which corresponds to scattering by $Zn_{1-x}Cd_xSe$ LO phonons ($\nu_{LO} \approx 249.5$ cm^{-1}). When the photon energy was considerably lower than the nanoisland band peak, we again observed an APL band (Fig. 4, spectrum *e*). It should be noted that no APL radiation from the ZnSe barrier was detected; this fact points to the dominant role of carrier capture by the energy levels of the size quantization of islands.

APL radiation was also observed for the sample containing a single CdSe insert with a nominal thickness of 0.6 ML. The resulting PL spectrum ($T = 5$ K) obtained under excitation by photons with an energy of 2.707 eV is shown in Fig. 5. An intense band with a half-width of ~5 meV is observed at ~2.751 eV. In [23], the Cd content in $Zn_{1-x}Cd_xSe$ solid solution was estimated from the energy position of the PL peak to be $x \approx 0.03$–0.04; with the quantum-confinement effect taken into consideration, $x \approx 0.07$ [20]. Similarly to the previous case, no APL from ZnSe barrier was detected. The physical nature of the two weak peaks arising in the spectrum at ~2.760 and ~2.732 eV has yet to be clarified.

[3] The energy of this transition (*e*–*lh*) for the sample considered was determined from the PL excitation spectrum.

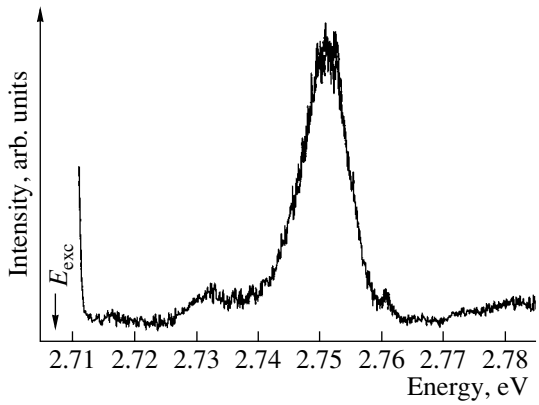

Fig. 5. APL spectrum of a CdSe/ZnSe nanostructure containing a CdSe insert with a nominal thickness of 0.6 ML under excitation with $E_{exc} = 2.707$ eV. $T = 5$ K. The arrow indicates the spectral position of the excitation energy.

4. CONCLUSION

Thus, we reported the results of the experimental study of efficient low-temperature APL in CdSe/ZnSe heterostructures containing individual CdSe inserts with nominal thicknesses of 1.5 and 0.6 ML under excitation by photons with energies smaller than the energy of the lower size-quantization levels. This phenomenon indicates that deep defect levels are located at the barrier–nanoisland boundary and act as intermediate states in the anti-Stokes process. Two-step two-photon absorption is found to be the dominant mechanism of APL excitation, which is indicated by a nearly quadratic dependence of the APL intensity on the power density of excitation. The anomalously high APL intensity is due to the high density of nanoislands, the efficient capture of carriers by size-quantization levels, and the considerable concentration of the deep states of defects containing cation vacancies at the barrier–nanoisland boundary.

REFERENCES

1. N. Peranio, A. Rosenauer, D. Gerthsen, *et al.*, Phys. Rev. B **61**, 16015 (2000); D. Litvinov, A. Rosenauer, D. Gerthsen, and N. N. Ledentsov, Phys. Rev. B **61**, 16819 (2000).
2. D. Litvinov, A. Rosenauer, D. Gerthsen, *et al.*, in *Proceedings of 10th International Symposium on Nanostructures: Physics and Technology* (St. Petersburg, 2002), p. 49.
3. A. Rosenauer, T. Reisinger, E. Steinkirchner, *et al.*, J. Cryst. Growth **152**, 580 (1995).
4. G. Bacher, D. Tönnies, D. Eisert, *et al.*, J. Appl. Phys. **79**, 4368 (1996).
5. R. N. Kyutt, A. A. Toropov, S. V. Sorokin, *et al.*, Appl. Phys. Lett. **75**, 373 (1999).
6. E. J. Johnson, J. Kafalos, R. W. Davies, and W. A. Dyes, Appl. Phys. Lett. **40**, 993 (1982).
7. L. G. Quagliano and H. Nather, Appl. Phys. Lett. **45**, 555 (1984).

8. N. Künzner, D. Kovalev, H. Heckler, *et al.*, Phys. Status Solidi B **224**, 21 (2001).
9. Yu. P. Rakovich, S. A. Filonovich, M. J. M. Gomes, *et al.*, Phys. Status Solidi B **229**, 449 (2002).
10. R. Hellman, A. Euteneuer, S. G. Hense, *et al.*, Phys. Rev. B **51**, 18053 (1995).
11. M. Satake, Y. Masumoto, T. Miyajima, *et al.*, Phys. Rev. B **61**, 12654 (2000).
12. S. Kalem, A. Gurtis, Q. Hartmann, *et al.*, Phys. Status Solidi B **221**, 517 (2000).
13. W. Seidel, A. Titkov, J. P. Andree, *et al.*, Phys. Rev. Lett. **73**, 2356 (1994).
14. P. P. Paskov, P.-O. Holtz, B. Monemar, *et al.*, Jpn. J. Appl. Phys. **40**, 2080 (2001).
15. I. V. Ignatiev, I. E. Kozin, H. W. Ren, *et al.*, Phys. Rev. B **60**, R14001 (1999).
16. S. V. Ivanov, A. A. Toropov, T. V. Shubina, *et al.*, J. Appl. Phys. **83**, 3168 (1998).
17. S. Sorokin, T. Shubina, A. Toropov, *et al.*, J. Cryst. Growth **200–201**, 461 (1999).
18. C. S. Kim, M. Kim, S. Lee, *et al.*, J. Cryst. Growth **214–215**, 761 (2000).
19. K. M. Lee, Le Si Dang, and G. D. Watkins, Solid State Commun. **35**, 527 (1980).
20. I. Yamakawa, S. Sorokin, A. Toropov, *et al.*, Jpn. J. Appl. Phys. **39**, L851 (2000).
21. E. Kurtz, T. Sekigushi, Z. Zhu, and T. Yao, Superlattices Microstruct. **25** (1/2), 119 (1999).
22. M. Ya. Valakh, M. P. Lisitsa, G. S. Pekar, *et al.*, Phys. Status Solidi B **113**, 635 (1982).
23. R. G. Alonso, E.-K. Suh, A. K. Ramdas, *et al.*, Phys. Rev. B **40**, 3720 (1989).
24. N. F. Mott and E. A. Davis, *Electronic Processes in Non-Crystalline Materials*, 2nd ed. (Oxford Univ. Press, Oxford, 1979; Mir, Moscow, 1982).
25. E. Cohen and M. D. Sturge, Phys. Rev. B **25**, 3828 (1982).
26. A. A. Toropov, T. V. Shubina, S. V. Sorokin, *et al.*, Phys. Rev. B **59**, 2510 (1999).
27. A. A. Toropov, T. V. Shubina, S. V. Sorokin, *et al.*, J. Cryst. Growth **201–202**, 1231 (1999).

Translated by A. Sidorova

Semiconductors, Vol. 37, No. 6, 2003, pp. 705–709. Translated from Fizika i Tekhnika Poluprovodnikov, Vol. 37, No. 6, 2003, pp. 730–734.

LOW-DIMENSIONAL SYSTEMS

Nonohmic Conductivity under Transition From Weak to Strong Localization in GaAs/InGaAs Structures with a Two-Dimensional Electron Gas

A. A. Sherstobitov*, G. M. Minkov*, O. É. Rut*, A. V. Germanenko*, B. N. Zvonkov, E. A. Uskova**, and A. A. Biryukov****

**Research Institute of Physics and Applied Mathematics at the Ural State University, pr. Lenina 51, Yekaterinburg, 620083 Russia*

e-mail: grigori.minkov@usu.ru

***Physicotechnical Research Institute at Lobachevskiĭ State University, pr. Gagarina 23/5, Nizhni Novgorod, 603600 Russia*

Submitted September 18, 2002; accepted for publication October 30, 2002

Abstract—Dependences of electrical conductivity σ on temperature and electric-field strength were studied in a wide range of conductivities (from $\sigma \ll e^2/\hbar$ to $\sigma \gg e^2/\hbar$) in GaAs/InGaAs/GaAs structures with a two-dimensional electron gas. It is shown that one cannot reliably determine the mechanism of conductivity from the temperature dependence of ohmic conductivity. Studies of nonohmic conductivity make it possible to determine the range of values of low-temperature conductivity that correspond to the transition from the diffusion mechanism of conductivity to the hopping mechanism. It is shown that, in the structures under investigation, the conductivity is still controlled by diffusion as the degree of disorder increases even when the low-temperature conductivity is much lower than $e^2/\hbar$. *© 2003 MAIK "Nauka/Interperiodica".*

1. INTRODUCTION

An increase in the degree of disorder (δ) or a lowering of the Fermi energy (E_F) leads to a change of the conductivity mechanism at low temperatures: the diffusion-controlled electron conductivity at $E_F/\delta > 1$ is replaced by hopping conductivity at $E_F/\delta < 1$. This transition can be readily ascertained in three-dimensional systems [1]. The situation in two-dimensional (2D) systems is substantially more complex since, in the 2D case of diffusion-controlled conductivity, the relative magnitudes of quantum-mechanical corrections to the conductivity are much larger; these corrections are negative, and an increrase in their magnitude with decreasing temperature can result in a decrease in the conductivity $\sigma(T)$ to values that are much lower than the Drude conductivity $\sigma_0 = \pi G_0 k_F l$, where $G_0 = e^2/(\pi\hbar) = 1.23 \times 10^{-5}\ \Omega^{-1}$, k_F is the quasi-momentum at the Fermi level, and l is the free-path length. Under these conditions, a strong temperature dependence $\sigma(T)$ is observed even if the electrical conductivity is diffusion-controlled. We will refer to this mode of conductivity as the weak-localization mode, despite the fact that the magnitudes of corrections are comparable to the Drude conductivity. It is clear that an increase in the degree of disorder should eventually lead to a change in the conductivity mechanism, i.e., to a transition to the hopping conductivity (to strong localization); however, the values of the parameters corresponding to this transition are not reliably known.

Under the conditions of weak localization at low temperatures, the major contribution to the temperature and field dependences is made by the quantum-mechanical corrections to the electrical conductivity. If the value of $k_F l$ is not too large, these corrections can be comparable to the value of conductivity itself at a sufficiently low temperature; as a result, a strong dependence $\sigma(T)$ arises [2]. In this case, according to the self-consistent theory of weak localization [3], the temperature dependence of conductivity in the 2D case is expected to be described by the following expression:

$$\begin{aligned}\Delta\Sigma(T) &= \sigma_0/G_0 + \ln(\sigma_0/G_0)\\ -[\sigma(T)/G_0 + \ln(\sigma(T)/G_0)] &= K\ln(T).\end{aligned} \quad (1)$$

Here, $G_0 = e^2/\hbar$ and K is a coefficient. For large values of conductivity ($\sigma \gg G_0$), dependence (1) transforms into conventional logarithmic dependence σ_0, i.e., $\sigma(T) \propto \ln(T)$ [4].

It is generally believed that the transition to hopping conductivity occurs when the conductivity becomes lower than G_0; as a result, a rather strong temperature dependence of the resistivity ρ emerges in the form of

$$\rho = \rho_0 (T)^m \exp(T_0/T)^\gamma, \quad (2)$$

where ρ_0 is a constant which depends on the sample parameters; m = 0–1; and the exponent γ is equal to either 0.3 or 0.5, depending on the relationship between the Coulomb gap and $k_B T$. As far as we know, the above

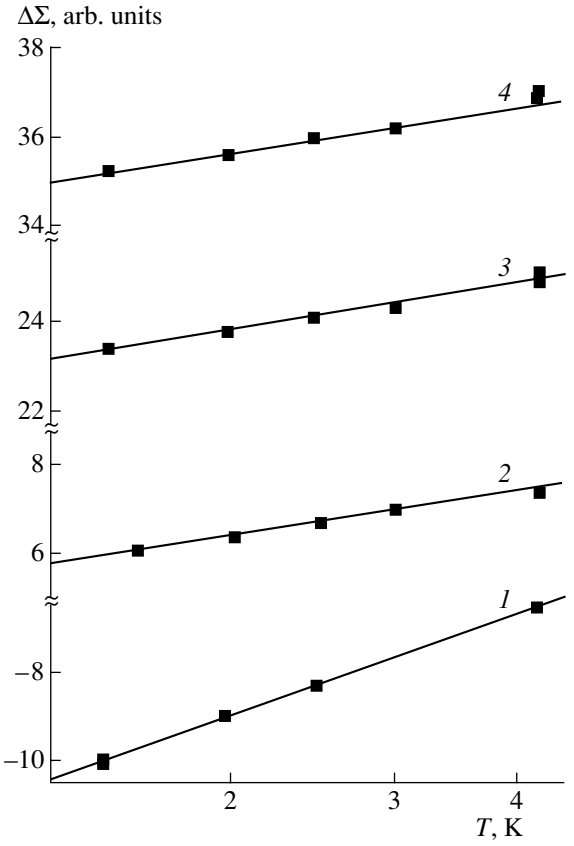

Fig. 1. Temperature dependences of electrical conductivity for several values of illumination intensity; these dependences were calculated using formula (1). The values of relative conductivity σ/G_0 at $T = 1.5$ K are equal to (*1*) 4×10^{-5}, (*2*) 4.5, (*3*) 20.5, and (*4*) 30.

criteria were used in all previous publications as indicators of the hopping mechanism of conductivity [5, 6].

In this paper, it is shown that an analysis of the temperature dependence of electrical conductivity by itself does not allow for the unambiguous determination of the conditions for the transition from the diffusion-controlled conductivity to hopping conductivity. However, additional information can be obtained by studying the nonlinear effects in a strong electric field. In particular, we show that the conductivity remains controlled by diffusion if the conductivity values are as small as about $0.1G_0$.

2. EXPERIMENTAL

In this paper, we report the results of studying the electrical conductivity of GaAs/InGaAs/GaAs structures with a 2D electron gas at temperatures of 1.5–10 K in electric fields E with a strength as high as 10 V/cm. The samples were grown by the method of metal-organic gas-phase epitaxy on semi-insulating GaAs substrate and had the following structure: a 200-nm-thick GaAs buffer layer, an 8-nm-wide InGaAs quantum well with indium content of 20 at. %, and a 200-nm-thick GaAs top layer. The δ-doped silicon layers were located at a distance of 9 nm from both sides of the quantum well. We considered three samples with different doping levels. The values of dark conductivity at a temperature of 1.5 K and electron concentration n were equal to $\sigma = 10^{-4}G_0$ and $n \approx 10^{11}$ cm^{-2}; $\sigma = 2G_0$ and $n = 1.4 \times 10^{11}$ cm^{-2}; and $\sigma = 20G_0$ and $n = 3 \times 10^{11}$ cm^{-2}, respectively. Measurements were performed at a constant current using the Hall bridges with a width $b = 0.5$ mm and with the distance between potential contacts equal to $L = 1$ mm. Resistance of the samples was changed by varying the illumination intensity. In addition, the effect of persistent conductivity made it possible to gradually vary the conductivity within the ranges of $(10^{-4}–20)G_0$, $(2–30)G_0$, and $(20–100)G_0$ at 1.5 K for the three samples under investigation, respectively. Estimations show that the electric field E does not lead to heating of the crystal lattice within the entire range under investigation.

3. RESULTS AND DISCUSSION

The temperature dependence $\Delta\Sigma(T)$ in accordance with expression (1) is shown in Fig. 1. It can be seen that, in the situation where $\sigma > 10G_0$ (when the conductivity is undeniably diffusion-controlled), the slope K of the dependence $\Delta\Sigma(T)$ as a function of $\ln T$ is close to 1.5. This slope corresponds to the total contribution of interference correction and the correction for electron–electron interaction [2, 4]. However, the dependence $\sigma(T)$ and the slope of this dependence are retained for a conductivity as low as $\sigma \approx 0.01G_0$; the value of K starts to increase only if the conductivity decreases further (see below). The conductivity at a temperature of 1.5 K will hereafter be taken as the parameter that characterizes the state of the sample. Undoubtedly, it is better to use a parameter with a clearer physical meaning (e.g., $k_F l$); however, a large error in the determination of conductivity arises if the conductivity is low. The qualitatitive agreement between experimental data and theoretical dependence (1) would suggest that the conductivity mechanism always remains related to diffusion and only at the lowest values of conductivity where the slope K increases does the transition to the hopping mechanism set in.

However, if the aforementioned data are considered from the standpoint of hopping conductivity, it can be seen that it is not easy to differentiate between the conductivity types. Let us now plot the temperature dependences of conductivity σ for $\sigma < 10G_0$ as a logarithm of resistivity versus T^γ in accordance with expression (2). It is impossible to reliably determine the value of γ in a moderately wide temperature range; we set $\gamma = 0.33$, as in the majority of publications concerned with hopping conductivity in the 2D case. As can be seen from Fig. 2, the experimental data are completely rectified in the chosen coordinates; i.e., these data are consistent with the hopping mechanism of conductivity. As far as we know [5, 6], the possibility of the above lineariza-

tion has been invariably considered as the sole criterion for the hopping mechanism of conductivity; as we showed above, this criterion is inherently ambiguous. It is worth noting that, as in the majority of previous publications, the extrapolated point of ρ for $T = \infty$, i.e., the quantity ρ_0 in formula (2), is independent of the parameters of the sample in a wide range of conductivities. Such universality of the value of ρ_0 contradicts the commonly accepted theory of hopping conductivity [1]. In order to qualitatively explain the universality of ρ_0, a phononless mechanism of hopping conductivity (electron–electron-interaction-assisted hopping conductivity) has been suggested [6, 7]. The value of ρ_0 starts to increase only at the lowest conductivity $\sigma < 10^{-3}G_0$, in accordance with the generally accepted theory of hopping conductivity.

Thus, the aforementioned results show that, in the range of low-temperature conductivity of $\sim(4–10^{-4})G_0$, the temperature dependence of conductivity is adequately described in the context of both the hopping and diffusion-related mechanisms of conductivity; as a result, it is impossible to unambiguously identify the conductivity mechanism from the dependences $\sigma(T)$.

We now consider the dependence of conductivity on the electric-field strength E. In the conditions under consideration, the electron–phonon interaction represents a bottleneck in the process of energy transfer from the electronic subsystem to a thermostat. Furthermore, if the energy-transfer rate within the electronic subsystem is higher than the rate of energy transfer from the electronic subsystem to the thermostat, a new distribution function with an effective electron temperature T_e is established in the electronic subsystem. Estimations show that, in the conditions under consideration, the time for the establishment of equilibrium in the electronic subsystem is several orders of magnitude shorter than the characteristic time of electron–phonon interaction. At low temperatures, the conductivity in the diffusion mode depends only on the temperature of the electronic system T_e; therefore, by comparing the dependences of conductivity on temperature and electric-field strength, we can determine the dependence of T_e on an applied electric field or on the power per unit area of the sample $P = UI/S$, where U is the voltage drop across potential contacts, I is the current flowing through the sample, and $S = Lb$. Under steady-state conditions, the power P is equal to the rate of electron-energy relaxation; this rate was previously calculated for various mechanisms of electron–phonon interaction [8, 9]. In the region of hopping conductivity, σ depends not only on T_e but also on the lattice temperature T. Moreover, a new mechanism of variation in conductivity with increasing electric-field strength arises; this new mechanism is related to impact ionization. Therefore, if we process the experimental dependences $\sigma(T)$ and $\sigma(E)$ in the same way in the region of diffusion-controlled conductivity, the dependence $P(T_e)$ is bound to change radically at the point of transition to hopping conductivity.

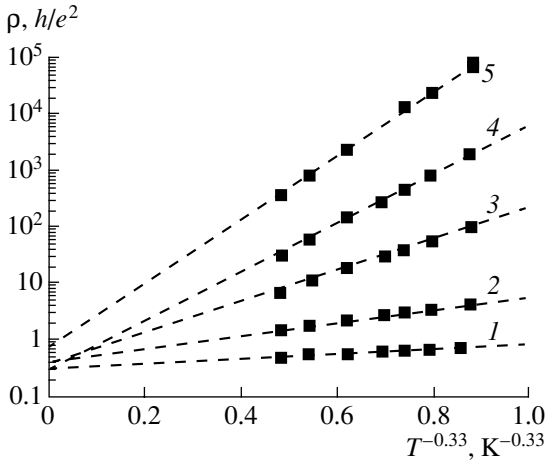

Fig. 2. Temperature dependences of resistivity (plotted versus $T^{-0.33}$) for several values of illumination intensity. The values of relative conductivity at 1.5 K σ/G_0 are equal to (*1*) 4.5, (*2*) 0.7, (*3*) 3×10^{-2}, (*4*) 1.5×10^{-3}, and (*5*) 4×10^{-5}.

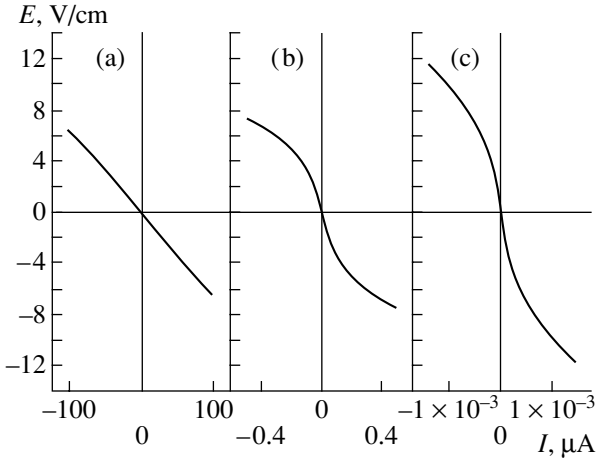

Fig. 3. Dependences of current on electric-field strength (T = 1.5 K) for the samples with relative conductivity σ/G_0 = (a) 20.5, (b) 3×10^{-2}, and (c) 4×10^{-5}.

The initial current–voltage characteristics for three different values of conductivity are shown in Fig. 3. It can be seen that nonlinearity is higher for lower conductivity. Let us first consider the state with a high conductivity ($\sigma > 10G_0$). Detailed studies of quantum-mechanical corrections show that the conductivity in this case is undoubtedly controlled by diffusion [2]. If $k_B T \ll E_F$ (this inequality is satisfied for all structures under investigation), the temperature dependence of conductivity is governed by quantum-mechanical corrections; i.e., the conductivity depends only on T_e and is independent of the lattice temperature T. Then, as illustrated in Fig. 4, we can compare the dependence of conductivity on temperature with that on applied power P and determine the temperature dependence of the power required for heating the electron subsystem to

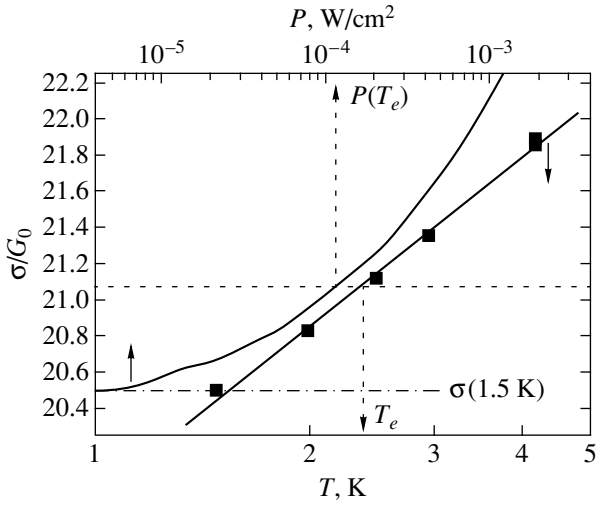

Fig. 4. Comparison of the dependence of conductivity on the temperature T_e with that on the power applied to the sample P at T = 1.5 K. Solid arrows indicate the horizontal axes to which the curves are referred to. Dotted lines indicate the method for the determination of T_e. The dash-and-dot line corresponds to the value of conductivity in a weak electric field at T = 1.5 K.

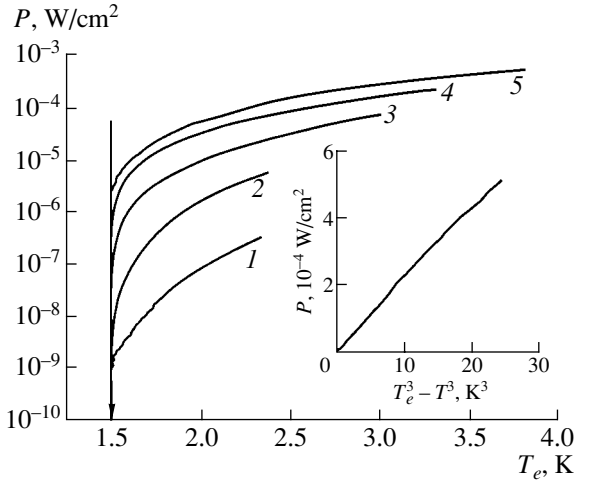

Fig. 5. Dependences of the power required for heating the electronic subsystem to the temperature T_e for several values of illumination intensity. The relative conductivity σ/G_0 at T = 1.5 K is equal to (*1*) 4×10^{-5}, (*2*) 1.5×10^{-3}, (*3*) 3.1×10^{-2}, (*4*) 0.73, and (*5*) 20.5. The dependence of P on $T_e^3 - T^3$ for a sample with relative conductivity $\sigma(1.5\text{ K})/G_0$ = 20.5 is shown in the inset.

the temperature T_e at a fixed lattice temperature T. This method is widely used to determine the dependence $P(T, T_e)$ (see, for example, [6]).

Dependences of the power P required for heating the charge carriers to a temperature T_e on T_e at the lattice temperature T = 1.5 K are shown in Fig. 5. It can be seen that, at low power levels P, the value of T_e is virtually independent of the applied power; at higher power levels, the dependence $T_e(P)$ obeys a power law. In structures based on III–V semiconductors, the dominant mechanism of electron-energy relaxation at low temperatures (T, T_e < 20 K) is related to interaction of electrons with the piezoelectric potential of acoustical phonons. Theory predicts the following dependence of P for this mechanism: $P \propto A(T_e^\alpha - T^\alpha)$, where A is a coefficient which depends on the material's parameters; and α = 3 or 5 depending on the ratio between the wavevector magnitude of thermal transverse phonons and the screening length [8, 9]. The power required for heating electrons to a temperature T_e as a function of $T_e^3 - T^3$ is shown in the inset to Fig. 5. It can be seen that the experimental data are adequately approximated for α = 3. The same value of α was obtained by Savel'ev *et al.* [10] in studies of GaAs/AlGaAs heterostructures. It is worth noting that the experimental value of α is smaller than the theoretical value. This discrepancy is possibly related to special features of the phonon spectrum in a stressed lattice due to mismatch between lattice parameters of GaAs and InGaAs. In this paper, we do not intend to discuss quantitatively the rate of electron-energy relaxation in the region of diffusion-controlled conductivity; we restrict ourselves to a consideration of the dependence of P on the value of the low-temperature conductivity (i.e., on the degree of disorder).

Let us consider the effect of a strong electric field for smaller values of conductivity. The dependences of T_e on P for all values of conductivity were determined by the method described above. We will now analyze the dependence of power $P(\Delta T_e, \sigma)$ required for heating the electrons by a certain fixed value, $\Delta T_e = T_e - T$ = 0.5 K, in relation to the value of conductivity (Fig. 6). It can be seen that, in the range of conductivities from $100G_0$ to ~$10G_0$, in which case conductivity is undoubtedly controlled by diffusion [2], the dependence $P(0.5, \sigma)$ changes only slightly as the conductivity varies. It is noteworthy that the value of P(0.5 K, σ) also varies only slightly when σ/G_0 decreases to ~0.1.

As can be seen from Fig. 6, a drastic decrease in P(0.5 K, σ) is observed for $\sigma/G_0 < 0.01$. A similar kink in the dependence $P(\sigma)$ at $\sigma = (0.1–0.01)G_0$ is also observed for other values of ΔT_e and T. A decrease in P(0.5 K, σ) can be related to the transition to hopping conductivity. In this case, a strong electric field leads not only to changes in T_e but also to an increase in the free-carrier concentration due to the excitation of localized electrons as a result of impact ionization, which should in fact be the reason for the decrease in $P(\sigma)$ determined by the above method. The emergence of macroscopic inhomogeneities at small values of conductivity can be another cause of a decrease in $P(\sigma)$. In this case, the effective area of the sample becomes smaller (most of the power is dissipated in the regions

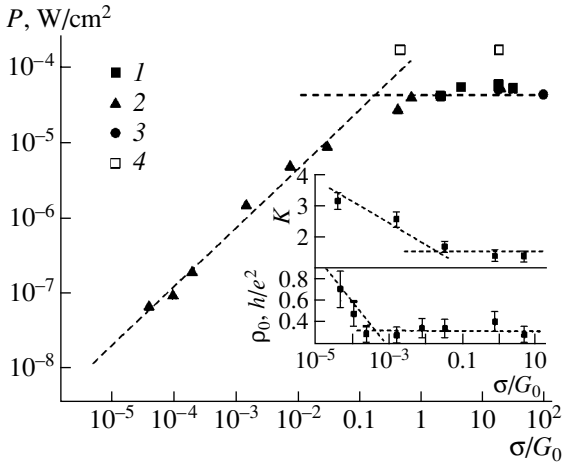

Fig. 6. The power required for heating the electronic subsystem by $\Delta T_e = 0.5$ K at a temperature $T = 1.5$ K as a function of σ ($T = 1.5$ K). Experimental data *1–3* are obtained in this study; the data *4* were reported by Gershenson *et al.* [6]. Dependences of ρ_0 and K on σ ($T = 1.5$ K) are shown in the inset.

with highest resistivity), which brings about an apparent decrease in $P(\sigma)$. The independence of P from σ as $\sigma(1.5\ \text{K})$ decreased to $0.3G_0$ was also observed by Gershenson *et al.* [6]. However, it was believed [6] that the transition to hopping conductivity occurs at $\sigma(1.5\ \text{K}) < (2–3)G_0$; therefore, in order to explain the constancy of P in the diffusion-controlled and hopping regions, it was assumed [6] that electron–electron-interaction-assisted hopping conductivity (rather than the conventional mechanism of hopping conductivity) is realized in the structures under investigation [6, 7].

In our opinion, the independence of P from σ for $\sigma(1.5\ \text{K}) > 0.1G_0$ and the drastic decrease in $P(\sigma)$ for $\sigma < 0.01G_0$ unambiguously indicate that the conductivity remains controlled by diffusion even for values of low-temperature conductivity on the order of $0.1G_0$. This inference is consistent with the data shown in the inset to Fig. 6: a deviation of the coefficient K in expression (1) from the value of 1.5, corresponding to the contribution of quantum-mechanical corrections, is also observed for $\sigma(1.5\ \text{K})/G_0 < 0.01$. It is noteworthy that an increase in the value of ρ_0 in formula (2) as σ decreases, which corresponds to the conventional mechanism of hopping conductivity, occurs at even smaller values of $\sigma(1.5\ \text{K})/G_0$, as can be seen from the data shown in the inset to Fig. 6.

4. CONCLUSION

Thus, the main results of our studies of the dependences of electrical conductivity on temperature and electric-field strength in a wide range of conductivities can be summarized as follows. The temperature dependence of ohmic conductivity is not a sufficient criterion for identifying the mechanism of conductivity; studies of nonohmic conductivity make it possible to determine the range of values of low-temperature conductivity where the diffusion-related mechanism of conductivity is replaced by the hopping mechanism. We showed that the conductivity remained controlled by diffusion as the degree of disorder increased in GaAs/InGaAs/GaAs structures with a two-dimensional electron gas; this transport mechanism was preserved down to values of low-temperature conductivity much lower than $e^2/\hbar$.

ACKNOWLEDGMENTS

This study was supported by the Russian Foundation for Basic Research (project nos. 0-02-16215, 01-02-06471, and 01-02-17003), the programs "Physics of Solid-State Nanostructures" and "Russian Universities—Basic Research" (grant no. UR.06.01.002), and grant REC-005 from the US Civil Research and Development Foundation (CRDF).

REFERENCES

1. B. I. Shklovskiĭ and A. L. Éfros, *Electronic Properties of Doped Semiconductors* (Nauka, Moscow, 1979; Springer, New York, 1984).
2. G. M. Minkov, O. E. Rut, A. V. Germanenko, *et al.*, Phys. Rev. B **65**, 235322 (2002).
3. D. Vollhardt and P. Woelfle, Phys. Rev. Lett. **45**, 842 (1980); Phys. Rev. B **22**, 4666 (1980).
4. B. L. Altshuler and A. G. Aronov, in *Electron–Electron Interactions in Disordered Systems*, Ed. by A. L. Efros and M. A. Pollak (North-Holland, Amsterdam, 1985), p. 1.
5. H. W. Jiang, C. E. Jonson, and K. L. Wang, Phys. Rev. B **46**, 12830 (1992); T. Wang, K. P. Clark, G. F. Spenser, *et al.*, Phys. Rev. Lett. **72**, 709 (1994); C. H. Lee, Y. H. Chang, Y. W. Suen, and H. H. Lin, Phys. Rev. B **58**, 10629 (1998); F. V. van Keuls, X. L. Hu, H. W. Jiang, and A. J. Dahm, Phys. Rev. B **56**, 1161 (1997); H. W. Jiang, C. E. Johnson, K. L. Wang, and S. T. Hannahs, Phys. Rev. Lett. **71**, 1439 (1993).
6. M. E. Gershenson, Yu. B. Khavin, D. Reuter, *et al.*, Phys. Rev. Lett. **85**, 1718 (2000).
7. S. Marnieros, L. Bergè, A. Juillard, and L. Dumoulin, Phys. Rev. Lett. **84**, 2469 (2000).
8. P. J. Price, J. Appl. Phys. **53**, 6863 (1982).
9. E. Chow, H. P. Wei, S. M. Girvin, and M. Shayegan, Phys. Rev. Lett. **77**, 1143 (1996); D. V. Khveshchenko and M. Reizer, Phys. Rev. B **56**, 15822 (1997).
10. I. G. Savel'ev, T. A. Polyanskaya, and Yu. V. Shmartsev, Fiz. Tekh. Poluprovodn. (Leningrad) **21**, 2096 (1987) [Sov. Phys. Semicond. **21**, 1271 (1987)].

Translated by A. Spitsyn

Semiconductors, Vol. 37, No. 6, 2003, pp. 710–712. Translated from Fizika i Tekhnika Poluprovodnikov, Vol. 37, No. 6, 2003, pp. 735–737.

LOW-DIMENSIONAL SYSTEMS

On the Temperature Dependence of the dc Conductivity of a Semiconductor Quantum Wire in an Insulator

N. A. Poklonskiĭ, E. F. Kislyakov, and S. A. Vyrko

Belarussian State University, F. Skorina av. 4, Minsk, 220050 Belarus

e-mail: poklonski@bsu.by

Submitted November 14, 2002; accepted for publication November 18, 2002

Abstract—The dc resistivity of a semiconductor quantum wire in an insulator host matrix, caused by the interaction between charge carriers and longitudinal acoustic phonons of the host, is considered. Based on an approximation of the relaxation time, simple analytical expressions for calculating the conductivity were derived for the case of a nondegenerate gas of carriers in a quantum wire. If the carrier concentration is independent of temperature, the wire resistivity increases with temperature as $T^{5/2}$, i.e., more steeply than in a bulk covalent semiconductor. *© 2003 MAIK "Nauka/Interperiodica".*

1. INTRODUCTION

The problem of calculating the temperature dependence of quantum-well wire (QWW) conductivity (taking into account the quantum-confinement restrictions of the transverse motion of conduction electrons and holes) appears in many fields of condensed-matter physics (see, e.g., [1–3]) and is important for applications in nanoelectronics. In this case, QWWs are, as a rule, in a three-dimensional (3D) insulator host; i.e., their conductivity depends, among other factors, on the interaction between the conduction electrons and acoustic phonons of the host. It would be practical to have formulas for estimating the effects related to this interaction. The purpose of this study is to derive an analytical expression for the QWW conductivity in the case of scattering of nondegenerate conduction electrons by longitudinal acoustic (LA) phonons of the host.

We derive a formula for the resistivity caused by the interaction between conduction electrons and LA phonons of the host on the basis of the kinetic Boltzmann equation within the relaxation-time approximation. We also intend to ascertain the changes in the conventional [4–7] relations for the temperature dependence of the conductivity of 3D semiconductor materials in the case of quantum-mechanical restriction on carrier motion in two directions transverse to the line of motion.

2. DERIVATION OF THE EQUATIONS

Let us consider the case of an extremely narrow QWW, where we can restrict ourselves to the contribution of only the lowest quantum-size energy level to the electron conductivity. We characterize the conduction electron in the QWW by the longitudinal quasi-momentum $p_z = \hbar k_z$ and the wave function $|k_z\rangle = L^{-1/2}\exp(ik_z z)$ at $x, y = 0$, where L is the rectilinear QWW length along the OZ axis, and $k_z = p_z/\hbar$ is the quasi-wave vector of an electron moving along the QWW. In this case, we totally disregard the variance of the electron wave function in the lateral direction, which is valid when the wavelength of phonons efficiently interacting with conduction electrons is longer than the QWW diameter. The approximation of strict transverse localization of electrons in the QWW implies complete uncertainty of their transverse momentum; i.e., the law of conservation of momentum is invalid for transverse components. This increases the phase-space volume that is accessible during electron–phonon scattering; hence, the scattering probability is also higher than in the 3D case (see also [7]).

The magnitude of the matrix element of the Hamiltonian of the interaction between a QWW conduction electron and a longitudinal acoustic phonon of the insulator host in the deformation-potential approximation is given by (see [4])

$$\begin{aligned}\left|V^{q}_{k_z,\,k_z\pm q_z}\right| &= \frac{Cq}{3}\sqrt{\frac{2\hbar}{V_1\omega_q\rho_l}\left(N_q+\frac{1}{2}\mp\frac{1}{2}\right)}\\ &\equiv w(q)\sqrt{N_q+\frac{1}{2}\mp\frac{1}{2}},\end{aligned} \tag{1}$$

where k_z and $k_z' = k_z \pm q_z$ are the electron quasi-wave vectors before and after interaction with a phonon (the upper and lower signs correspond, respectively, to the absorption and emission of a phonon with the wave-vector component q_z along the QWW axis), q is the modulus of the phonon quasi-wave vector, ω_q is the circular frequency, ρ_l is the density of the host material, V_1 is the normalizing volume, C is the deformation potential constant, and $N_q = [\exp(\hbar\omega_q/k_BT) - 1]^{-1}$ is the average number of LA phonons with an energy $\hbar\omega_q$ at a thermal energy k_BT.

1063-7826/03/3706-0710$24.00

According to [4–7], the dc conductivity of a rectilinear QWW oriented along the *OZ* axis may be reduced to the form

$$\sigma_z = \frac{-2e^2}{\pi\hbar m^2 A}\int_0^{+\infty} p_z^2 \frac{\partial f}{\partial \varepsilon_z}\tau_z dp_z, \tag{2}$$

where A is the QWW cross section, e is the modulus of the elementary charge, $\varepsilon_z \equiv \varepsilon_{k_z} = (\hbar k_z)^2/2m$ is the kinetic energy of motion of an electron with an effective mass m along the QWW, $f = [\exp((\varepsilon_{k_z} - E_F)/k_BT) + 1]^{-1}$ is the Fermi–Dirac function, E_F is the Fermi level measured from the first quantum-confinement level of electron motion across the QWW, and $\tau_z \equiv \tau(k_z)$ is the relaxation time of the conduction electron quasi-momentum along the QWW.

The probability of an electron transition from the state k_z to the state k_z' in unit time due to interactions with acoustic phonons of the host in the first order of the perturbation theory is given by (see [4, 7])

$$W_{k_z, k_z'} = \frac{2\pi}{\hbar} w^2(q)[(1 + N_q)\delta(\varepsilon_{k_z, k_z - q_z} + \hbar\omega_q) + N_q\delta(\varepsilon_{k_z, k_z + q_z} - \hbar\omega_q)], \tag{3}$$

where $w(q)$ is defined by relation (1), $\delta(\varepsilon_{k_z, k_z \mp q_z} \pm \hbar\omega_q)$ is the Dirac delta function, and $\varepsilon_{k_z, k_z'} = (p_z'^2 - p_z^2)/2m$.

The longitudinal relaxation time τ_z is determined [8] by summing Eq. (3) over all the final states k_z' allowed by the laws of the conservation of energy, which were taken into account by the Dirac delta functions, as well as by averaging over the LA phonons not involved in electron scattering and characterized by wave vectors $\mathbf{q}_\perp$ normal to the QWW axis. This yields

$$\frac{1}{\tau_z} = \frac{V_1}{(2\pi)^3}\int_{-\infty}^{+\infty}\left(1 - \frac{k_z'}{k_z}\right)dk_z' \int W_{k_z, k_z'} d^2\mathbf{q}_\perp, \tag{4}$$

where $q_\perp = |\mathbf{q}_\perp|$ is the modulus of the transverse component of the quasi-wave vector $\mathbf{q}$ of the host acoustic phonon and $d^2\mathbf{q}_\perp = 2\pi q_\perp dq_\perp$.

In the case of nondegenerate electron gas, $q_z = |k_z - k_z'| \ll q$, so that $q \approx q_\perp$, and Eq. (4) can be written as

$$\frac{1}{\tau_z} \approx \frac{C^2}{9\pi\hbar\rho_l v_l}\int_{-\infty}^{+\infty} dp_z'\left(1 - \frac{p_z'}{p_z}\right)\int_0^\infty dq q^2 \times [(1 + N_q)\delta(\varepsilon_{p_z, p_z'} + \hbar\omega_q) + N_q\delta(\varepsilon_{p_z, p_z'} - \hbar\omega_q)], \tag{5}$$

where $v_l = \omega_q/q$ is the longitudinal velocity of sound in the host; the delta function $\delta(\varepsilon_{p_z, p_z'} \pm \hbar\omega_q) \equiv \delta(\varepsilon_{k_z, k_z \mp q_z} \pm \hbar\omega_q)$ represents the law of energy conservation in the cases of phonon emission (upper sign) and absorption (lower sign), respectively.

Taking into account the relations $\delta(\varepsilon_{p_z, p_z'} \pm \hbar\omega_q) = (v_l\hbar)^{-1}\delta(\varepsilon_{p_z, p_z'}/v_l\hbar \pm q)$, we can rewrite Eq. (5) as

$$\frac{1}{\tau_z} \approx \frac{C^2}{9\pi\rho_l(v_l\hbar)^2}\left[\int_{-p_z}^{+p_z} dp_z'\left(1 - \frac{p_z'}{p_z}\right)\left(\frac{p_z'^2 - p_z^2}{2m\hbar v_l}\right)^2 \times\left(1 - \exp\left(\frac{p_z'^2 - p_z^2}{2mk_BT}\right)\right)^{-1} + \int_{|p_z'| > |p_z|} dp_z'\left(1 - \frac{p_z'}{p_z}\right) \times\left(\frac{p_z'^2 - p_z^2}{2m\hbar v_l}\right)^2\left(\exp\left(\frac{p_z'^2 - p_z^2}{2mk_BT}\right) - 1\right)^{-1}\right] = \frac{C^2 p_z^5}{18\pi\rho_l m^2(v_l\hbar)^4}\Phi\left(\frac{p_z^2}{2mk_BT}\right), \tag{6}$$

where

$$\Phi(\beta) = \int_0^1 \frac{(\alpha^2 - 1)^2 d\alpha}{1 - \exp(\beta(\alpha^2 - 1))} + \int_1^\infty \frac{(\alpha^2 - 1)^2 d\alpha}{\exp(\beta(\alpha^2 - 1)) - 1};$$

$$\alpha = p_z'/p_z; \quad \beta = p_z^2/mk_BT.$$

In the extreme cases of high and low temperatures, the function $\Phi(\beta)$ is expressed in terms of the Euler gamma function Γ and Riemann zeta function ζ (see, e.g., [9]);

$$\Phi\left(\frac{p_z^2}{2mk_BT}\right) = \Phi(\beta) \approx \begin{cases}\Gamma(5/2)\zeta(5/2)\beta^{-5/2}/2 \approx 0.89\beta^{-5/2} & \text{at } \beta < 2\\ 8/15 \text{ at } \beta > 5.\end{cases} \tag{7}$$

In the nondegenerate QWW, the energy distribution function for electrons with kinetic energies ε_z is given by $f \approx \exp((E_F - \varepsilon_z)/k_BT)$; thus, formulas (2) and (6), yield the QWW conductivity

$$\sigma_z = \frac{e^2 36\rho_l(v_l\hbar)^4}{\hbar A C^2 k_BT} \times \exp\left(\frac{E_F}{k_BT}\right)\int_0^{+\infty}\frac{\exp(-p_z^2/2mk_BT)}{p_z^3\Phi(p_z^2/2mk_BT)}dp_z. \tag{8}$$

Taking into account the fact that the parameter β for an electron with an average thermal energy $k_BT/2$ in a one-dimensional (1D) nondegenerate gas is approximately equal to 0.5 and, according to formula (7),

the approximation $\Phi(\beta) \approx 0.89\beta^{-5/2}$ is valid, integration in formula (8) yields

$$\sigma_z \approx 8.95\frac{\rho_l e^2 \hbar^3 v_l^4}{mA(Ck_BT)^2}\exp\left(\frac{E_F}{k_BT}\right). \quad (9)$$

The 1D concentration of nondegenerate conduction electrons is given by (see [1])

$$n = \frac{2}{2\pi\hbar}\int_{-\infty}^{+\infty} f\,dp_z \approx \frac{1}{\pi\hbar}\sqrt{2\pi m k_B T}\exp\left(\frac{E_F}{k_BT}\right); \quad (10)$$

at a temperature $T < \pi(\hbar n)^2/2k_B m$, degeneracy of the electron gas sets in (the Fermi level E_F is shifted to the band of allowed energies).

Eliminating the Fermi level E_F from formulas (9) and (10), one finds that the conductivity of the nondegenerate gas of QWW electrons, where the former is limited by scattering at LA phonons of the host, is written as

$$\sigma_z \approx 11.21\left(\frac{e}{C}\right)^2 \frac{\rho_l(\hbar v_l)^4 n}{Am^{3/2}(k_BT)^{5/2}}, \quad (11)$$

where n/A is the 3D concentration of conduction electrons.

3. APPLICATIONS

Undoped diamond crystal is a promising host material for semiconductor QWWs. According to [2, 10], the *p*-type QWW may be patterned by boron ion implantation into diamond using an ultrathin beam (tens of nanometers in diameter). It is important that subsequent annealing does not broaden the doping profile, since boron atoms substituting for carbon atoms in the diamond lattice are almost immobile [11].

Let the 1D concentration of hydrogen-like acceptors in charge states (0) and (–1) be $N = N_0 + N_{-1}$, and the concentration of positively charged donors be KN; thus, the concentration of holes delocalized along the QWW is $p = N_{-1} - KN$. The concentration of negative acceptors, disregarding their excited states, is given by (see [5, 6])

$$N_{-1} = N\left(1 + \gamma_a \exp\left(\frac{E_F + E_a}{k_BT}\right)\right)^{-1}, \quad (12)$$

where γ_a is the degeneracy factor of the hydrogen-like acceptor with the ionization energy E_a in the QWW; E_F and E_a are measured from the first quantum-confinement level of the valence band.

At low temperatures, when $p \ll K(1-K)N$, the electroneutrality equation $N_{-1} \approx KN$, taking into account formulas (12) and (10), yields $E_F = -E_a + k_BT\ln[(1-K)/K\gamma_a]$; hence, it follows from formula (9) that

$$\sigma_z \approx 8.95\left(\frac{e}{C}\right)^2 \frac{\rho_l \hbar^3 v_l^4 (1-K)}{Am(k_BT)^2 K\gamma_a}\exp\left(-\frac{E_a}{k_BT}\right); \quad (13)$$

i.e., measuring the temperature dependence $\sigma_z T^2$ allows for the determination of the energy E_a of hole (with an effective mass m) detachment from an acceptor in the QWW.

According to formula (11), at high temperatures, when $p \approx (1-K)N$, the QWW conductivity in the case of hole scattering only at LA phonons of the host decreases with temperature: $\sigma_z \propto 1/T^{5/2}$. Under the same conditions in a 3D nondegenerate covalent semiconductor, $\sigma \propto 1/T^{3/2}$ [4–7]. This difference in the temperature dependences of σ_z and σ is consistent with the above qualitative discussion on the strict localization of conduction electrons across a QWW.

ACKNOWLEDGMENTS

This study was supported by the Belarussian Foundation for Basic Research, project no. F01-199.

REFERENCES

1. S. Kagoshima, H. Nagasawa, and T. Sambongi, *One-Dimensional Conductors* (Springer, Berlin, 1988).
2. *Nanotechnology*, Ed. by G. Timp (Springer, New York, 1999).
3. *Electronic Properties of Dislocation in Semiconductors*, Ed. by Yu. A. Osip'yan (Éditorial URSS, Moscow, 2000).
4. A. I. Ansel'm, *Introduction to the Theory of Semiconductors* (Nauka, Moscow, 1978).
5. V. L. Bonch-Bruevich and S. G. Kalashnikov, *Physics of Semiconductors*, 2nd ed. (Nauka, Moscow, 1990).
6. K. Seeger, *Semiconductor Physics: An Introduction*, 7th ed. (Springer, Berlin, 1999).
7. B. K. Ridley, *Quantum Processes in Semiconductors*, 4th ed. (Clarendon Press, Oxford, 1999; Mir, Moscow, 1986), Chaps. 3, 10.
8. É. L. Nagaev, Zh. Éksp. Teor. Fiz. **100**, 1297 (1991) [Sov. Phys. JETP **73**, 717 (1991)].
9. *Handbook of Mathematical Functions*, Ed. by M. Abramowitz and I. A. Stegun, 2nd ed. (Dover, New York, 1971; Nauka, Moscow, 1979).
10. L. A. Dobrinets, A. M. Zaitsev, T. Etzel, *et al.*, J. Wide Bandgap Mater. **9** (1/2), 7 (2001).
11. V. S. Vavilov, Usp. Fiz. Nauk **167**, 17 (1997) [Phys. Usp. **40**, 15 (1997)].

Translated by A. Kazantsev

Semiconductors, Vol. 37, No. 6, 2003, pp. 713–717. Translated from Fizika i Tekhnika Poluprovodnikov, Vol. 37, No. 6, 2003, pp. 738–742.

LOW-DIMENSIONAL SYSTEMS

The Effect of Implantation of P Ions on the Photoluminescence of Si Nanocrystals in SiO_2 Layers

G. A. Kachurin*, S. G. Yanovskaya*, D. I. Tetelbaum, and A. N. Mikhaĭlov****

**Institute of Semiconductor Physics, Siberian Division, Russian Academy of Sciences, pr. Akademika Lavrent'eva 13, Novosibirsk, 630090 Russia*

***Physicotechnical Research Institute at Nizhni Novgorod State University, pr. Gagarina 23/5, Nizhni Novgorod, 603950 Russia*

Submitted November 11, 2002; accepted for publication November 20, 2002

Abstract—The effects of implanting 10^{13}–10^{16} cm^{-2} P ions and subsequent annealing at 600–1100°C on the photoluminescence of Si nanocrystals formed preliminarily in SiO_2 layers were studied. Quenching of the 780-nm luminescence band related to nanocrystals was observed immediately after the implantation of 10^{13} cm^{-2} P ions. The recovery of emission from partially damaged nanocrystals was noticeable even after annealing at 600°C; however, heat treatments at 1000–1100°C were needed when the amorphization-threshold dose was exceeded. Intensification of luminescence was observed as a result of heat treatments of SiO_2 layers implanted with low doses of P ions; if the P content was higher than ~0.1 at. %, the recovery of luminescence was promoted. The former effect is attributed to impact crystallization of nanoprecipitates. The latter effect is attributed to the promotion of crystallization by an impurity and (along with the dose dependence of postannealing luminescence) is considered an indication that P atoms penetrate into the Si nanocrystals. Contrary to a number of estimations, introducing P does not result in the quenching of luminescence due to Auger recombination. This discrepancy is attributed to the interaction of charge carriers with the nuclei of donors. *© 2003 MAIK "Nauka/Interperiodica".*

1. INTRODUCTION

The sizes of microelectronic components are already in the nanometer region, where classical concepts of charge-carrier behavior no longer hold. The wave properties of electrons and quantum-mechanical size effects start to play a decisive role. In particular, in silicon (the most important semiconductor), the quantum-mechanical size effects in nanocrystals give rise to intense visible luminescence of these crystals. This circumstance indicates that the advent of optoelectronics based solely on silicon can be expected and arouses additional interest in the properties of silicon nanocrystals (nc-Si) and in methods for modifying these properties. Doping (at present, ion-implantation doping is used predominantly) is a key operation in fabricating semiconductor devices; therefore, it is important to study the effects of ion implantation as applied to nc-Si. These effects have been investigated inadequately and the obtained results are contradictory. In studies [1–5], attempts were made to dope nc-Si with B or P; nanocrystals were formed by the cosputtering of Si and borosilicate or phosphosilicate glasses with subsequent annealing at 1100°C. The content of impurities in nc-Si was not measured; however, according to indirect data, this content was on the order of 1 mol %. Introduction of B with a concentration amounting to 0.5–1.5 mol % reduced the intensity of photoluminescence (PL) [2]. Doping with phosphorus to a level of 0.4–1.7 mol % increased the PL intensity [3, 4]; however, phosphorus at concentrations exceeding 0.6 mol % suppressed the emission [5]. It was reported that PL is quenched if Ga atoms accidentally make their way into nc-Si [6]. At the same time, the PL intensity of nc-Si nanocrystals formed by implantation of Si and P ions into SiO_2 with subsequent annealing at 1000°C was higher than that without P implantation [7]. It is believed that the most probable mechanism of the PL intensification is related to the removal of nonradiative-recombination centers [3–5, 7], whereas PL quenching is typically attributed to the Auger recombination of excess charge carriers in nc-Si [2, 5, 6]. A common factor for all the above-cited publications [1–7] was that the level of doping was invariably high. In addition, the impurity was not introduced into preliminarily formed nc-Si; rather, it was assumed that the impurity was introduced into nc-Si during the formation of nanostructures.

The aim of this study is to gain insight into the effects of implantation of P ions and subsequent annealing on the PL of nc-Si formed preliminarily in SiO_2 layers.

2. EXPERIMENTAL

The nc-Si structure was formed by implanting 140-keV Si ions at a dose of 10^{17} cm^{-2} into 0.6-μm-thick SiO_2 layers thermally grown on Si. The ion-current density was no higher than 2 $\mu A/cm^2$. After heat treatments for 2 h at 1100°C, the layers featured an

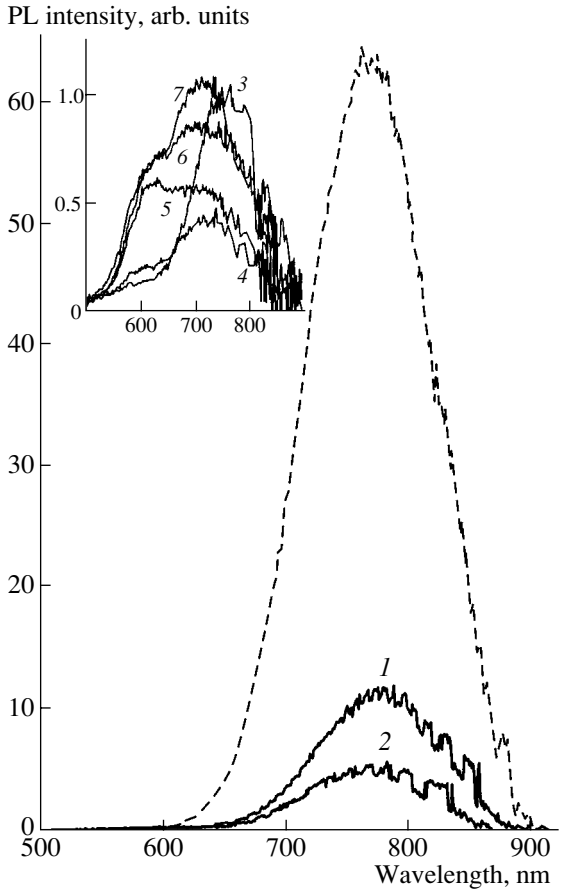

Fig. 1. Photoluminescence spectra (dashed line) before and after implantation of P ions at doses of (*1*) 1×10^{13}, (*2*) 3×10^{13}, (*3*) 1×10^{14}, (*4*) 3×10^{14}, (*5*) 1×10^{15}, (*6*) 3×10^{15}, and (*7*) 1×10^{16} cm^{-2}. Spectra *3*–*7* are shown in the inset on the expanded scale.

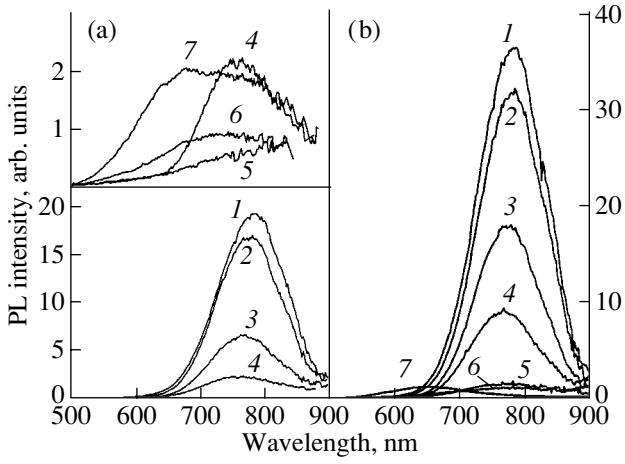

Fig. 2. Photoluminescence spectra after implantation of P ions and subsequent heat treatments for 30 min at (a) 600 and (b) 800°C. Numeration of the curves corresponds to that in Fig. 1. Spectra *4*–*7* are shown on the expanded scale in the upper part of panel *a*.

intense PL with a peak at about 780 nm, which is characteristic of quantum-mechanical size effects in Si nanocrystals. The 150-keV P ions were then implanted into the layers at doses ranging from 1×10^{13} to 1×10^{16} cm^{-2}. The chosen relation between the energies of Si and P ions ensured that the Si and P ion ranges were virtually the same. The samples were then annealed for 30 min in an N_2 atmosphere at temperatures of 600, 800, 1000, and 1100°C. We measured the changes in the PL spectra excited by the 488-nm line of an argon laser at 20°C. The spectrum of a reference (unimplanted) sample was measured as well; the PL intensities in all figures listed below are normalized to the same level.

3. RESULTS

Immediately after the implantation of P ions, the PL intensity decreased drastically even for the lowest doses of ions (Fig. 1). This could be expected since each P ion produced about 1000 displacements of Si atoms during slowing down. At the same time, as can be seen from the inset in Fig. 2, an increase in the dose of P ions is accompanied by successive changes in the PL spectra. Starting with the dose of 10^{14}–3×10^{14} cm^{-2}, a decrease in the intensity of the main band at 780 nm was accompanied at first with an increase in the PL intensity in the orange spectral region; for higher doses, the PL in the vicinity of the borderline between the visible and infrared regions became dominant again.

The heat-treatment temperatures of 600 and 800°C were found to be insufficiently high for the recovery of the initial PL (Fig. 2), although the PL intensity increased with increasing heat-treatment temperature. It is noteworthy that the PL is intensified not only in the red–infrared spectral region (where the emission from nc-Si is typically observed) but also in the region with shorter wavelengths ($\lambda < 700$ nm); the latter emission is often attributed to noncrystalline Si nanoprecipitates in SiO_2. Intensification of this emission can be caused either by an increase in the number of noncrystalline nanoprecipitates or by a decrease in the number of nonradiative-recombination centers. The lower the dose of P ions, the greater was the recovery of the 780-nm band. This situation took place in the dose range from 1×10^{13} to 1×10^{15} cm^{-2}. However, if the dose exceeded 10^{15} cm^{-2}, the PL recovery became more complete (Fig. 2). The spectra for high doses are shown on an expanded scale in the upper part of Fig. 2a. It can be seen that an increase in the P concentration is conducive to the intensification of PL in the samples subjected to heat treatment at a comparatively low temperature.

A rather considerable increase in the PL intensity is observed after heat treatments at 1000 and 1100°C (Fig. 3). Two special features are noteworthy after annealing at 1000°C: (i) the orange-emission band completely disappears and (ii) the intensity of the main PL band for the sample implanted with the lowest dose of P ions exceeds the intensity of this band before

implantation. As the dose of P ions increases, the intensity of the 780-nm band decreases, except for the sample implanted with the highest dose of ions (10^{16} cm^{-2}, see Fig. 3a). In this case, the emission intensity was higher than it was after implantation at a dose of 3×10^{15} cm^{-2}. It is also noticeable that, as a result of annealing at 1000°C, the PL peak shifts somewhat to longer wavelengths for the samples implanted with high doses of P ions. An increase in the heat-treatment temperature to 1100°C gives rise to a pronounced dependence of the PL intensity on the dose of P ions. For the lowest dose, the intensity of PL at 780 nm still exceeds the intensity before implantation (Fig. 3b). As the dose of P ions is increased, the intensity of emission decreases but remains relatively high. An increase in the dose of P ions by three orders of magnitude (from 1×10^{13} to 1×10^{16} cm^{-2}) reduces the emission merely by a factor of ~2. It is also noteworthy that an increase in the dose does not induce any significant shift of the main PL peak after annealing at 1100°C. This peak is located in the vicinity of 780 nm, which coincides with the position of the peak in the PL spectrum of the initial undoped nc-Si. A slight shoulder in the region of 820–830 nm appears on the long-wavelength side of the main peak in the PL spectrum of the sample implanted with 1×10^{16} cm^{-2} of P ions and annealed at 1100°C.

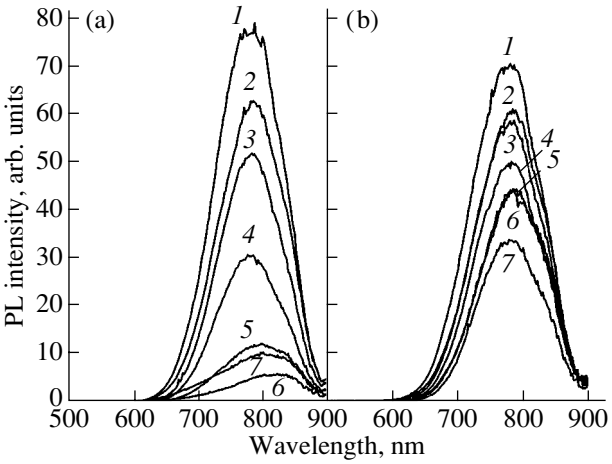

Fig. 3. Photoluminescence spectra after implantation of P ions and subsequent heat treatment for 30 min at (a) 1000 and (b) 1100°C. Numeration of the curves corresponds to that in Fig. 1.

4. DISCUSSION

In order to analyze the aforementioned results, first of all we have to estimate the number of P atoms and the number of displacements in a single Si nanocrystal under our experimental conditions. The corresponding concentration profiles for P atoms and displacements (vacancies) were calculated using the TRIM-95 software package (Fig. 4). The volume of a single Si nanocrystal is approximately equal to 10^{-19} cm^{-3}; thus, on average, we had ~0.05 P atoms and ~50 displacements per Si nanocrystal after implantation with 10^{13} cm^{-2} of P ions and ~50 P atoms and 5×10^4 displacements per Si nanocrystal after implantation with 10^{16} cm^{-2} of P ions. These estimates make it possible to recognize which of the observed effects are caused by defects and which are caused by P impurity.

Quenching of PL as a result of irradiation even with the lowest dose of P ions (Fig. 1) is consistent with theoretical estimates [8] and experimental data [9], according to which even a single defect in an Si nanocrystal can suppress radiative recombination. This suppression can be explained if we assume that the indirect structure of energy bands is retained in nc-Si, which hampers the radiative recombination in an excited electron–hole pair; as a result, the lifetime of this pair can reach ~10–100 μs. For the sake of comparison, recombination of closely spaced electrons and holes in direct-gap semiconductors occurs within ~1 ns. The long lifetime of an electron–hole pair in *nc*-Si makes the capture of a charge-carrier by a single defect very likely since the capture rate is estimated at 10^{10}–10^{11} s^{-1} [8]. The

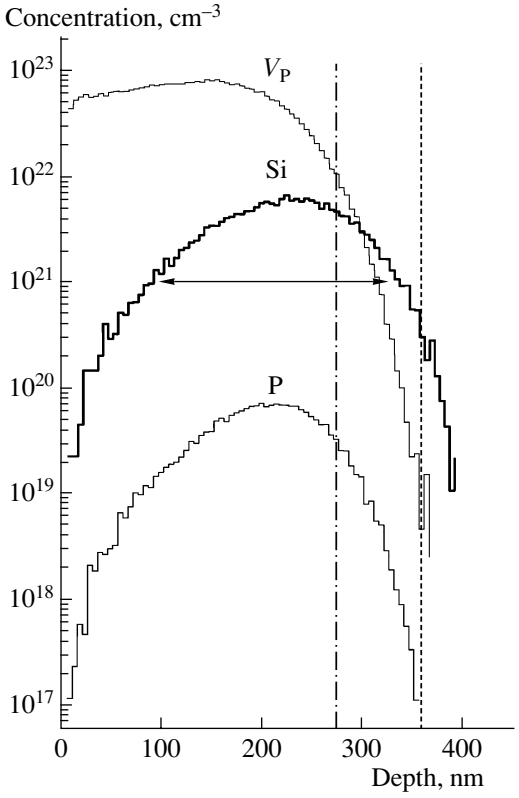

Fig. 4. Depth distributions of 140-keV Si ions (10^{17} cm^{-2}), 150-keV P ions (10^{15} cm^{-2}), and vacancies (V_p) produced by P ions according to calculations using the TRIM-95 software package (the displacement threshold energy was set to 15 eV). Arrows indicate the depth range where Si nanocrystals can form. For a dose of P ions equal to 10^{15} cm^{-2}, we show the depth where there is no less than one displacement per volume of an Si nanocrystal on average (dotted line) and the depth that corresponds to the internal boundary of complete amorphization of nc-Si (the dash-and-dot line).

partial retention of PL after implantation of low doses of P ions is related to the nonuniformity of depth distributions of ions and displacements and by the incomplete overlap of these distributions (Fig. 4).

The increase in the PL intensity after irradiation with low doses of P ions and subsequent annealing at 1000 and 1100°C (Fig. 3) is also unrelated to P impurity. Previously, a similar effect was observed after irradiation with He ions [9]. This effect was attributed to the formation of additional Si nanocrystals as a result of irradiation-induced crystallization of Si nanoprecipitates. An increase in the number of Si nanocrystals was detected using direct electron-microscopy observations [9] and was later corroborated through the example of nc-Ge [10]. It was assumed that crystallization of nanoprecipitates was of impact origin and initiated by individual displacements [9]. This mechanism is plausible if some of the phase Si nanoprecipitates are not crystallized and are in a stressed state after the first annealing at 1100°C. There are indications [11, 12] that Si nanoprecipitates are indeed subjected to compression by surface layers.

The fact that the efficiency of heat treatments at temperatures lower than 1000°C is low after irradiation with P doses higher than 3×10^{14} cm^{-2} is apparently caused by amorphization of nc-Si. In fact, the number of displacements in an Si nanocrystal at the aforementioned dose can be as large as ~1500, which exceeds the amorphization threshold determined previously [9] as corresponding to ~1000 displacements per Si nanocrystal or ~0.2 displacements per atom. Kachurin *et al.* [9] determined the amorphization threshold in the case of irradiation with light (He) ions, which produce only mobile point defects. In this study, we used heavier P ions, which can introduce defect complexes into nc-Si; these complexes can act as sinks for mobile defects. However, taking into account incomplete overlap of the distributions of P atoms and elastic losses (displacements), this circumstance did not profoundly affect the amorphization threshold. In conventional Si, a decrease in ion masses below 30 amu leads to a rapid increase in the amorphization dose at 20°C, so that amorphization becomes completely impossible for the lightest ions. Approximate agreement between the energy losses of He and P ions for amorphization of nc-Si indicates that the nc-Si surface is an efficient sink for defects. A sharp intensification of the band peaked at 780 nm after heat treatment at 1000 and 1100°C with the simultaneous disappearance of the orange-emission band is consistent with the concept of transformation of noncrystalline Si nanoprecipitates into Si nanocrystals. It is worth noting that the crystallization temperature of preliminarily formed but amorphized Si nanocrystals is comparable to the crystallization temperature of bulk amorphous Si (~500–600°C). Thus, heat treatments at temperatures higher than 1000°C are needed mainly for the phase transition rather than just for the diffusion-limited growth of particles. Apparently, the above variation in the amorphization temperatures is also caused by the strong effect of the surface layer on the crystallization of nanoprecipitates [13].

We believe that the effect of the impurity manifests itself in the acceleration of PL recovery, which is noticeable after irradiation with doses higher than 10^{15} cm^{-2} when the calculated P content exceeds ~0.1 at. %. It is well known that highly soluble impurities (such as the elements of Groups III and V) with the content on the order of 0.1–1.0 at. % promote Si crystallization [14]. An increase in the PL intensity with increasing P concentration is more clearly pronounced at relatively low heat-treatment temperatures (600–1000°C) (see Figs. 2, 3a), which is consistent with the published data [7, 15, 16]. As can be seen from Figs. 1–3, a variation in the dose of P ions leads to virtually no shift of the 780-nm band, which indicates that the number of emitting centers (rather than their properties) has changed. In addition, according to the electron-microscopy data [4], introduction of P does not affect the sizes of Si nanocrystals. Apparently, the high level of doping also manifested itself in the course of irradiation when the PL intensity increased immediately after irradiation with high doses of P ions (Fig. 1). It is worth noting here that the ion-stimulated formation of Si nanocrystals was observed previously for undoped nc-Si as well, but at irradiation temperatures higher than 500°C [17]. High concentrations of P can facilitate the formation of nanocrystals at lower temperatures. The target temperature can be as high as about 100°C by the end of high-dose irradiations. It is also important that the PL intensity can increase owing to passivation of nonradiative-recombination centers by P atoms.

The effect of P on the formation of Si nanocrystals indirectly indicates that a high concentration (>10^{20} cm^{-2}) of P atoms can be found in these nanocrystals. The pronounced dependence of the PL intensity on the dose of P ions is also indicative of the penetration of P into Si nanocrystals. However, this dependence contradicts the results of calculations [8]; according to the latter, the presence of even a single additional charge carrier in an Si nanocrystal should completely quench the PL owing to the Auger process, in which case the energy released in the recombination of an excited electron–hole pair is spent on heating a third charge carrier rather than on the generation of a photon. However, the increase in the dose by three orders of magnitude in our experiments reduced the PL intensity to a much lesser extent. Even if the calculated number of P atoms in a Si nanocrystal is as large as 50, the PL intensity will decrease by a mere 50% (Fig. 3b). Similar high levels of doping were reported previously [2–7]; nevertheless, the PL intensities for doped and undoped nc-Si are comparable. The discrepancy between theoretical estimates and experimental data can apparently be caused by the following factors. Lannoo *et al.* [8] considered the interaction between free charge carriers generated in nc-Si as a result of illumination or an applied electric field. In the case of doping, the charge carriers are found to be in a Coulomb field of impurity atoms. In nc-Si, the Cou-

lomb interaction between charge carriers and nuclei is expected to be stronger than in bulk single-crystal Si owing to a decrease in the permittivity [18]. For example, it is well known that free charge carriers cannot be detected at room temperature in porous Si produced from a heavily doped material [19, 20]. We believe that the wave functions of charge carriers change appreciably in nc-Si containing P; as a result, the applicability of theoretical estimates [8] to the case under consideration is questionable. A slight decrease in the PL intensity with the dose of P ions increasing is most probably caused by the gradual accumulation of various imperfections in nc-Si rather than by Auger recombination.

5. CONCLUSION

We studied the effect of P-ion implantation and subsequent annealing on the photoluminescence (PL) of Si nanocrystals preliminarily formed in SiO_2. The observed quenching of the main PL band immediately after implantation at a dose of 10^{13} cm^{-2} is consistent with estimates indicating that nonradiative recombination is dominant even if isolated defects are introduced into the nanocrystals. At the same time, implantation of P ions at low doses brings about an increase in the PL intensity for the samples annealed at 1000 and 1100°C, which can be attributed to an increase in the number of Si nanocrystals as a result of the crystallization of nanoprecipitates initiated by atomic displacements. The PL recovery in the samples implanted with phosphorus-ion doses lower than 3×10^{14} cm^{-2} is readily noticeable even after heat treatments at 600–800°C. However, heat treatments at 1000–1100°C are required for the recovery of PL in the samples irradiated with higher doses of P ions. According to estimates, this fact is due to the amorphization of nc-Si. The high temperatures needed for the recovery of PL in amorphized nc-Si indicate that high-temperature heat treatments are required not only for the diffusion-limited growth of Si nanocrystals during their formation but also for the phase transition itself. High crystallization temperatures during heat treatments and an increase in the number of Si nanocrystals, which is initiated by isolated displacements, are the results of the effect of the surface on phase transformations of nanoparticles. The impurity effects themselves are clearly pronounced as the enhanced recovery of the nc-Si PL at the calculated P concentrations greater than 0.1 at. %. The manifestation of the impurity-related enhancement of PL recovery and the evident dependence of the PL intensity on the dose of P ions indicate that P atoms penetrate into Si nanocrystals. However, variation in the PL intensity with the dose of P ions is inconsistent with previous inferences about the inevitable quenching of PL due to Auger recombination if even a single additional charge carrier appears in an Si nanocrystal. These discrepancies can be attributed to the fact that charge carriers are subjected to Coulomb interaction with the nuclei of impurity atoms in doped Si nanocrystals.

ACKNOWLEDGMENTS

We are grateful to A.V. Chaplik, M.V. Éntin, and V.A. Burdov for their helpful participation in discussions and to V.A. Volodin, S.N. Vasilenko, and V.K. Vasil'ev for their assistance in carrying out the experiments.

This study was supported by the Russian Foundation for Basic Research (project no. 00-02-17963) and INTAS (grant no. 00-0064).

REFERENCES

1. Y. Kanzawa, M. Fujii, S. Hayashi, and K. Yamamoto, Solid State Commun. **100**, 227 (1996).
2. M. Fujii, S. Hayashi, and K. Yamamoto, J. Appl. Phys. **83**, 7953 (1998).
3. M. Fujii, A. Mimura, S. Hayashi, and K. Yamamoto, Appl. Phys. Lett. **75**, 184 (1999).
4. M. Fujii, A. Mimura, S. Hayashi, *et al.*, J. Appl. Phys. **87**, 1855 (2000).
5. A. Mimura, M. Fujii, S. Hayashi, *et al.*, Phys. Rev. B **62**, 12625 (2000).
6. L. Patrone, D. Nelson, V. I. Safarov, *et al.*, J. Appl. Phys. **87**, 3829 (2000).
7. D. I. Tetel'baum, I. A. Karpovich, M. V. Stepikhova, *et al.*, Poverkhnost, No. 5, 31 (1998).
8. M. Lannoo, C. Delerue, and G. Allan, J. Lumin. **70**, 170 (1996).
9. G. A. Kachurin, S. G. Yanovskaya, M.-O. Ruault, *et al.*, Fiz. Tekh. Poluprovodn. (St. Petersburg) **34**, 1004 (2000) [Semiconductors **34**, 965 (2000)].
10. M. Klimenkov, W. Matz, S. A. Nepijko, and M. Lehman, Nucl. Instrum. Methods Phys. Res. B **179**, 209 (2001).
11. D. K. Yu, R. Q. Zhang, and S. T. Lee, Phys. Rev. B **65**, 245417 (2002).
12. H. Kohno, T. Iwasaki, Y. Mita, and S. Takeda, J. Appl. Phys. **91**, 3232 (2002).
13. G. A. Kachurin, S. G. Yanovskaya, V. A. Volodin, *et al.*, Fiz. Tekh. Poluprovodn. (St. Petersburg) **36**, 685 (2002) [Semiconductors **36**, 647 (2002)].
14. L. Czepregi, E. F. Kennedy, T. J. Gallaher, *et al.*, J. Appl. Phys. **48**, 4234 (1977).
15. D. I. Tetelbaum, O. N. Gorshkov, S. A. Trushin, *et al.*, Nanotechnology **11**, 295 (2000).
16. D. I. Tetelbaum, S. A. Trushin, V. A. Burdov, *et al.*, Nucl. Instrum. Methods Phys. Res. B **174**, 123 (2001).
17. G. A. Kachurin, M.-O. Ryuo, S. G. Yanovskaya, *et al.*, in *Interaction of Ions with Surface: Proceedings of 14th International Conference, Zvenigorod, 1999* (Moscow, 1999), Vol. 2, p. 69.
18. R. Tsu, Appl. Phys. A **71**, 391 (2000).
19. H. J. von Bardeleben, C. Ortega, A. Grosman, *et al.*, L. Lumin. **57**, 301 (1993).
20. G. Mauckner, W. Rebitzer, K. Thonke, and R. Sauer, Solid State Commun. **91**, 717 (1994).

Translated by A. Spitsyn

Semiconductors, Vol. 37, No. 6, 2003, pp. 718–722. Translated from Fizika i Tekhnika Poluprovodnikov, Vol. 37, No. 6, 2003, pp. 743–747.

LOW-DIMENSIONAL SYSTEMS

Interband Absorption of Light in Semiconductor Nanostructures

S. I. Pokutnyi

Il'ichevsk Scientific Training Center at the Mechnikov Odessa National University, ul. Danchenko 17a, Il'ichevsk, 68001 Ukraine

e-mail: univer@ivt.ilyichevsk.odessa.ua

Submitted November 18, 2002; accepted for publication November 25, 2002

Abstract—Interband absorption of light in a small semiconductor microcrystal was investigated theoretically within the dipole approximation. An expression for the light-absorption coefficient was derived for the situation where the polarization-related interaction of an electron and hole with the microcrystal surface is dominant. It is shown that the edge of absorption in a microcrystal shifts to shorter wavelengths if the polarization-related interaction of electrons and holes with the microcrystal surface is taken into account. It is ascertained that the absorption edge for small microcrystals is formed by two transitions comparable in intensity; these transitions occur from different levels of size-related quantization for a hole to the lower level of size-related quantization for an electron. *© 2003 MAIK "Nauka/Interperiodica".*

1. INTRODUCTION

Quasi-zero-dimensional structures represented by spherical semiconductor microcrystals (SCMCs) with radii of $a \approx 1$–10^2 nm and grown in transparent insulating media [1–5] attract attention due to the nonlinear optical properties of these structures and possible applications of SCMCs in optoelectronics (in particular, as promising new materials for the development of components that can control optical signals [2]). Since the band gap of a semiconductor is much narrower than that of an insulator, the charge-carrier transport in an SCMC (a quantum dot) is confined to its volume. Notably, the radii a are comparable with characteristic sizes of quasiparticles in semiconductors. In these conditions, the effect of an interface between an SCMC and an insulating medium can give rise to size-related quantization of the energy spectrum of electrons and holes; this quantization is associated both with purely spatial confinement of the quantization region [3] and with polarization-related interaction of charge carriers with the SCMC surface [6–10].

It was found experimentally [1, 2] that the structure of the interband-absorption spectrum of light in a small SCMC was governed by size-related quantization of the energy spectrum of corresponding quasiparticles.

At present, the interband absorption of light by small SCMCs is poorly understood. The theory of interband absorption of light in an SCMC [3] does not account for the contribution of the polarization-related interaction of charge carriers with the SCMC surface to the spectra of electrons and holes in SCMCs. Previously [4, 5], the optical absorption and luminescence in nonspherical cadmium selenide nanocrystals was studied theoretically. However, the effect of polarization-related interaction of electrons and holes with the surface of a small SCMC on the absorption and luminescence in such SCMCs was ignored [3–5].

In order to fill this gap in the theory, in this study we consider the effect of the polarization-related interaction of electrons and holes with the surface of a small SCMC on the interband absorption of light in a small SCMC. We derived an expression for the light-absorption coefficient in relation to the SCMC radius a and problem variables in situations where the polarization-related interaction of electrons and holes with the SCMC surface is important. It is shown that the threshold of absorption in a small SCMC shifts to shorter wavelengths if the polarization-related interaction of electrons and holes with the SCMC surface is taken into account. It is ascertained that the absorption edge in small SCMCs is formed by two transitions from different levels of size-related quantization for holes to the lowest levels of size-related quantization for electrons, with the intensities of these two transitions being comparable.

2. THE SPECTRUM OF AN ELECTRON–HOLE PAIR IN A SMALL MICROCRYSTAL

A simple model of a quasi-zero-dimensional structure has been examined previously [6–10]. In this model, a neutral spherical SCMC with a radius a and relative permittivity ε_2 in an insulating medium with relative permittivity ε_1 is considered; it is assumed that $\varepsilon_1 \ll \varepsilon_2$. An electron e and a hole h with effective masses m_e and m_h, respectively, move within the volume of the aforementioned SCMC; in what follows, r_e and r_h are the distances of an electron and hole from the SCMC center. It is also assumed that the energy bands of electrons and holes in an SCMC are parabolic.

1063-7826/03/3706-0718$24.00

We will also assume that the condition

$$m_e \ll m_h \tag{1}$$

is satisfied. The validity of inequality (1) makes it possible to consider the motion of a heavy hole in the electronic potential averaged over the electron motion (the adiabatic approximation). In this approximation, the wave function of an electron–hole pair in a small SCMC can be written as [11]

$$\Psi(\mathbf{r}_e, \mathbf{r}_h) = \Psi_{n_e, l_e, m_e}(r_e, \Theta, \varphi)\chi^{n_e, l_e, m_e}_{n_h, l_h, m_h}(r_h, \Theta, \varphi), \tag{2}$$

where $\Psi_{n_e, l_e, m_e}(r_e, \Theta, \varphi)$ and $\chi^{n_e, l_e, m_e}_{n_h, l_h, m_h}(r_h, \Theta, \varphi)$ are the wave functions of an electron and hole, respectively (n_e, l_e, and m_e and n_h, l_h, and m_h are the radial, orbital, and azimuthal quantum numbers of an electron and hole, respectively; and Θ and φ are the corresponding azimuthal and polar angles).

The following energy spectrum of an electron–hole pair was obtained in the context of the aforementioned approximations and also in adiabatic approximation (1), as well as in the effective-mass approximation using only the first order of the perturbation theory on the basis of the wave functions $\Psi_{n_e, l_e, m_e}(r_e, \Theta, \varphi)$ (2) of an infinitely deep potential well [6–9]:

$$E^{n_h, l_h, m_h}_{n_e, l_e = m_e = 0}(S) = E_g + \frac{\pi^2 n_e^2}{S^2}\frac{m_h}{m_e} + \frac{1}{S}\left(Z_{n_e, 0} + P_{n_e, 0} + \frac{\varepsilon_2}{\varepsilon_1}\right) + \omega_0(S, n_e)\left(t_h + \frac{3}{2}\right), \tag{3}$$

$$Z_{n_e, 0} = 2\int_0^1 dx \sin^2(\pi n_e x)/(1 - x^2),$$

$$P_{n_e, 0} = 2\mathrm{Ci}(2\pi n_e) - 2\ln(2\pi n_e) - 2\gamma + (\varepsilon_2/\varepsilon_1) - 1, \tag{4}$$

$$\omega_0(S, n_e) = 2(1 + (2/3)\pi^2 n_e^2)^{1/2} S^{-3/2}.$$

In the expression for the hole oscillation frequency $\omega_0(S, n_e)$ (4), the first term in the parenthesis accounts for the energy of polarization-related interaction, whereas the second term accounts for the energy of the Coulomb interaction between an electron and a hole in an SCMC; this interaction [3] leads to the following frequency of hole oscillations:

$$\tilde{\omega}_0(S, n_e) = 2((2/3)\pi^2 n_e^2)^{1/2} S^{-3/2}. \tag{4a}$$

The SCMC radius is defined by the inequality

$$(a_0/a_h) \ll 1 < S \leq (a_e/a_h) \approx (a_{\mathrm{ex}}/a_h) \tag{5}$$

in the state (n_e, $l_e = m_e = 0$; n_h, l_h, m_h). In (3)–(5), $t_h = 2n_h + l_h$ is the principal quantum number of a hole; $S = a/a_h$ is the dimensionless SCMC radius; $a_e = \varepsilon_2\hbar^2/m_e e^2$, $a_h = \varepsilon_2\hbar^2/m_h e^2$, and $a_{\mathrm{ex}} = \varepsilon_2\hbar^2/\mu e^2$ are the Bohr radii of an electron, hole, and exciton in a semiconductor with a relative permittivity ε_2; $\mu = m_e m_h/(m_e + m_h)$ is the exciton's reduced mass; and a_0 is the characteristic size, which, in its order of magnitude, is equal to the interatomic spacing [12]. Henceforth, the energy is expressed in units of $\mathrm{Ry}_h = \hbar^2/2m_h a_h^2$; E_g is the band gap of the semiconductor with relative permittivity ε_2; $\mathrm{Ci}(y)$ is the integral cosine; and $\gamma = 0.577$ is the Euler constant.

The fulfillment of condition (5) results in the fact that the contribution of polarization-related interaction of electrons and holes with the SCMC surface ($\sim e^2/\varepsilon_2 a$) [the last two terms in expression (3)] to the spectrum of electron–hole pair becomes comparable in its order of magnitude with the exciton-binding energy ($E_b = \hbar^2/2\mu a_{\mathrm{ex}}^2$) in an SCMC.

The last term in the spectrum of the electron–hole pair (3) corresponds to the spectrum of the heavy hole that oscillates with the frequency $\omega_0(S, n_e)$ (4) in the field of the adiabatic electron potential in an SCMC [7, 8]. Notably, the hole wave function $\chi^{n_e, l_e, m_e}_{t_h}(\mathbf{r}_h)$ (2) is expressed in terms of odd Hermitian polynomials [11].

It is noteworthy that the spectrum of electron–hole pair (3) is applicable only to the lowest states of this pair (n_e, 0, 0; t_h), for which the following inequality is satisfied:

$$E^{t_h}_{n_e, 0, 0}(S) - E_g \ll \Delta V(S). \tag{6}$$

Here, $\Delta V(S)$ is the depth of the potential well for electrons in an SCMC; for example, $\Delta V = 2.3$–2.5 eV in a CdS microcrystal with the radius satisfying condition (5) [13].

It is worth noting that the expression for the frequency of hole oscillations $\omega_0(S, n_e)$ (4) was derived [7, 8] on the assumption that there is a great difference ($\varepsilon_2/\varepsilon_1 \gg 1$) between the permittivities of an SCMC (ε_2) and the surrounding matrix (ε_1); due to this difference, the energy of polarization-related interaction makes a significant relative contribution ($1/(2/3)\pi^2 n_e^2$) to the aforementioned oscillation frequency $\omega_0(S, n_e)$. As the principal quantum number of an electron n_e increases, this contribution decreases as n_e^2 (this contribution is considerable for $n_e = 1$ and amounts to $1/(2/3)\pi^2 \simeq 0.15$, whereas the contribution is negligible ($1/(2/3)4\pi^2 \simeq 0.04$) for $n_e = 2$).

The latter circumstance indicates that, if we take into account the polarization-related interaction, the hole-oscillation frequency $\omega_0(S, n_e)$ (4) becomes higher than a similar frequency $\tilde{\omega}_0(S, n_e)$ (4a) [3], which is governed only by the Coulomb interaction of electrons with holes in an SCMC. In other words, the great difference ($\varepsilon_2/\varepsilon_1 \gg 1$) between the permittivities of SCMCs and the surrounding matrix brings about an increase in the spacing between equidistant levels of the

hole $\omega_0(S, n_e)$ compared to that given by $\tilde{\omega}_0(S, n_e)$ (4a) [3], which, in turn, leads to a more pronounced localization of the hole in the adiabatic electron potential in an SCMC.

3. INTERBAND ABSORPTION OF LIGHT IN A SMALL MICROCRYSTAL

We now use the aforementioned approximations and a simple model of a quasi-zero-dimensional structure [6–9] to study the interband absorption of light in an SCMC whose radius S satisfies condition (5). In addition, we use the dipole approximation; i.e., we assume that the absorption length is large compared with the SCMC radius a. Relative intensities of dipole-allowed optical interband transitions in an SCMC are defined by the squared overlap integral for the electron $\Psi_{n_e, l_e, m_e}(\mathbf{r}_e)$ (2) and hole $\chi^{n_e, l_e, m_e}_{n_h, l_h, m_h}(\mathbf{r}_h)$ (2) wave functions [3, 14]; i.e.,

$$K(S, \omega) = A \sum_{n_e n_h l_e l_h m_e m_h} \left| \int \Psi_{n_e, l_e, m_e}(\mathbf{r}_e) \chi^{n_e, l_e, m_e}_{n_h, l_h, m_h}(\mathbf{r}_h) \times \delta(\mathbf{r}_e - \mathbf{r}_h) dr_e dr_h \right|^2 \delta(\Delta - E^{n_e, l_e, m_e}_{n_h, l_h, m_h}(S)), \quad (7)$$

where $\Delta = \hbar\omega - E_g$, ω is the frequency of incident light, and A is a quantity which is proportional to the squared absolute value of the dipole-moment matrix element (this absolute value is calculated on the basis of the Bloch functions).

The quantity $K(S, \omega)$ defined by (7) relates the energy absorbed by an SCMC per unit time to the time-average squared electric field of an incident wave. In addition, the quantity $K(S, \omega)$ multiplied by the number of SCMCs in a unit volume of insulating matrix represents the electrical conductivity observed at the field frequency in the quasi-zero-dimensional system under consideration and conventionally related to the absorption coefficient of light.

The orthogonality of the wave functions of electrons $\Psi_{n_e, l_e, m_e}(\mathbf{r}_e)$ (2) and holes $\chi^{n_e, l_e, m_e}_{n_h, l_h, m_h}(\mathbf{r}_h)$ (2) results in the orbital quantum numbers of electrons and holes being conserved ($l_e = l_h$) in the course of transition, whereas the azimuthal quantum number changes its sign ($m_e = -m_h$). It should be noted that the radial quantum numbers n_e and n_h can be arbitrary.

It is noteworthy that allowance made for the Coulomb and polarization-related interactions of an electron and hole in a small SCMC results in a change in the selection rules for dipole transitions compared to similar rules obtained in the approximation where the Coulomb and polarization-related interactions are disregarded. In this approximation, the radial and orbital quantum numbers are conserved ($n_e = n_h$ and $l_e = l_h$), whereas the azimuthal quantum numbers change their sign ($m_e = -m_h$) [3].

Let us determine the quantity $K(S, \omega)$ defined by formula (7) and related to optical transitions of holes from the levels with $t_h = 2n_h$ (in this case, $l_h = m_h = 0$) to the lowest electron level ($n_e = 1$, $l_e = m_e = 0$). In this situation, the squared overlap integral for the electron $\Psi_{1,0,0}(\mathbf{r}_e)$ (2) and hole $\chi^{1,0,0}_{t_h}(\mathbf{r}_h)$ (2) wave functions was previously calculated [3] as

$$L_{n_h}(S) = \left| \int_0^a \Psi_{1,0,0}(r) \chi^{1,0,0}_{t_h}(r) r^2 dr \right|^2 = 2\pi^{5/2} \left[\frac{\hbar^2}{m_h \omega_0(S, n_e = 1) a^2} \right]^{3/2} \frac{(n_h + 1)}{2^{2n_h}(n_h!)}. \quad (8)$$

Taking into account the expression for $\omega_0(S, n_e = 1)$ (4), the quantity $L_{n_h}(S)$ can be written as

$$L_{n_h}(S) = \frac{2\pi^{5/2}}{(1 + (2/3)\pi^2)^{3/4}} \frac{(n_h + 1)}{2^{2n_h}(n_h!)} S^{-3/4}. \quad (9)$$

Substituting expressions (8), (9), and (3) into formula (7), we obtain the following expression for the quantity $K(S, \omega)$:

$$\frac{K(S, \omega)}{A} = \sum_{n_h} L_{n_h}(S) \delta\left[\Delta - \frac{\pi^2}{S^2} \frac{m_h}{m_e} - \frac{1}{S}\left(Z_{1,0} + P_{1,0} + \frac{\varepsilon_2}{\varepsilon_1} \right) - \omega_0(S, n_e = 1)\left(2n_h + \frac{3}{2} \right) \right]. \quad (10)$$

It follows from formula (10) that, if the Coulomb and polarization-related interactions of an electron and hole in a small SCMC whose radius S satisfies equation (5) are taken into account, each line appearing in the interband optical-absorption spectrum and corresponding to the given values of the radial n_e and orbital l_e quantum numbers of the electron transforms into a series of closely spaced equidistant lines; the latter correspond to various values of the principal quantum number t_h of a hole. Notably, according to formula (4) for $\omega_0(S, n_e)$, the spacing between the equidistant series of lines depends on both the quantum number n_e and the SCMC radius S. As the radial quantum number of an electron n_e increases, the spacing between the equidistant series of lines $\omega_0(S, n_e)$ increases ($\omega_0 \sim n_e$), whereas this spacing decreases with increasing SCMC radius S ($\omega_0 \sim S^{-3/2}$).

It follows from formula (10) that, when considering the interband absorption of light by a small SCMC, the

absorption threshold corresponds to the frequency of light of $\bar{\omega}(S)$ given by

$$\bar{\omega}(S) = E_g + \frac{\pi^2}{S^2}\frac{m_h}{m_e} + \frac{1}{S}\left(Z_{1,0} + P_{1,0} + \frac{\varepsilon_2}{\varepsilon_1}\right) + \frac{3}{2}\omega_0(S, n_e = 1). \quad (11)$$

It follows from the analysis of the formula for $\bar{\omega}(S)$ (11) and a similar formula for $\bar{\omega}(S)$ in [3], which describes the light-absorption threshold in an SCMC taking into account only the Coulomb interaction of electrons and holes, that consideration of the polarization-related interaction of electrons and holes with the SCMC surface along with the Coulomb interaction of electrons with holes results in a larger shift of the light–absorption threshold to shorter wavelengths than in the situation where only the Coulomb interaction is taken into account [3]. The value of this relative shift is given by

$$\Delta\omega_0(S) = \bar{\omega}(S) - \tilde{\bar{\omega}}(S) = \frac{1}{S}\left(Z_{1,0} + P_{1,0} + \frac{\varepsilon_2}{\varepsilon_1} + 2\beta_{n_e=1}\right) + \frac{3}{2}(\omega_0(S, n_e = 1) - \tilde{\omega}(S, n_e = 1)), \quad (12)$$

where

$$\beta_{n_e=1} = 2\int_0^\pi \frac{\sin^2 y}{y}dy.$$

Expression (11) represents the law according to which the effective band gap of an SCMC increases as the SCMC radius S decreases. Notably, the polarization-related interaction [the term $S^{-1}(Z_{1,0} + P_{1,0} + (\varepsilon_2/\varepsilon_1))$ in (11) makes a positive contribution to (11), in contrast with the negative contribution (the term $2\beta_{n_e=1}S^{-1}$) in [3] that appears if only the Coulomb interaction is taken into account.

Thus, consideration of the polarization-related interaction of electrons with the SCMC surface brings about an increase in the effective band gap of the SCMC; this increase is described by expression (11). In other words, if the polarization-related interaction of charge carriers with the SCMC surface is taken into account, the light-absorption threshold $\bar{\omega}(S)$ (11) experiences a larger shift (compared with the similar quantity $\tilde{\bar{\omega}}(S)$ obtained in [3] disregarding the polarization-related interaction) to shorter wavelengths. Notably, the relative shift of the light-absorption threshold $\Delta\omega_0(S)$ (12) in an SCMC is a positive quantity.

4. COMPARISON OF THEORY WITH EXPERIMENT

The low-temperature ($T \sim 4.2$ K) interband-absorption spectra of cadmium sulfide SCMCs (with the relative permittivity $\varepsilon_2 = 9.3$ and the radii $a \le a_{ex}$) embedded in a silicate-glass matrix (with the relative permittivity $\varepsilon_1 = 1.5$) were studied experimentally in [15, 16]. In the region of transitions to the lowest dimensional-quantization level ($n_e = 1$, $l_e = 0$) of an electron, a structure consisting of equidistant series of lines with the interline spacing (i.e., the magnitude of splitting) equal to $\Delta E(a) \propto a^{-3/2}$ was observed. This structure is formed owing to the quantization of the heavy-hole energy spectrum in an adiabatic electron potential. The effective masses of an electron and hole in CdS are equal to $m_e = 0.205m_0$ and $m_h = 5m_0$ (i.e., $m_e/m_h \ll 1$), where m_0 is the electron mass in free space.

In fact, the heavy-hole motion in the electronic potential in the range of SCMC radii (5) including those studied in [15, 16] also gives rise to an equidistant series of levels in the energy spectrum of a hole; the spacing between these levels is given by $\omega_0(S, n_e = 1)$ (4) [7, 8]. For SCMSs with radii $a \le a_{ex}$, the values of splitting $\omega_0(S, n_e = 1)$ (4) are in good agreement with the experimental data on $\Delta E(a)$ obtained in [15, 16]; the difference between experiment and theory is insignificant (≤6%) [7, 8].

We will now use formula (9) for the same experimental conditions as in [15, 16] to obtain the following squared values of the overlap integral $(K(S, \omega)/A)$ (10) for transitions of a hole from an equidistant series of levels ($n_h = 0$; $l_h = m_h = 0$), ($n_h = 1$; $l_h = m_h = 0$), ($n_h = 2$; $l_h = m_h = 0$), and ($n_h = 3$; $l_h = m_h = 0$) to the lower level of the electron size-related quantization ($n_e = 1$; $l_e = m_e = 0$):

$$K(S, \omega)/A = \sum_{n_h=0}^{3} L_{n_h}(S) = 7.659S^{-3/4}(1 + 0.5 + 9.4\times10^{-2} + 1.0\times10^{-2}). \quad (13)$$

It follows from (13) that

$$L_0 = 7.659S^{-3/4}, \quad L_1 = 0.5L_0, \quad L_2 = 9.4\times10^{-2}L_0, \quad L_3 = 10^{-2}L_0. \quad (14)$$

Formulas (13) and (14) indicate that the major contribution to the coefficient of light absorption $(K(S, \omega)/A)$ (10) by small CdS SCMCs with sizes S (5) is made by the states of holes with quantum numbers ($n_h = 0$; $l_h = m_h = 0$) and ($n_h = 1$; $l_h = m_h = 0$); these states feature the highest oscillator strengths for the transitions under consideration [17, 18]. Notably, the contributions of highly excited hole states ($n_h \ge 2$; $l_h = m_h = 0$) relative to the contribution of the state ($n_h = 0$; $l_h = m_h = 0$) are negligible ($\le 9\times10^{-2}$). It is noteworthy that inequality (6) is well satisfied for the states of the electron–hole pair $E^{t_h}_{1,0,0}(S)$ (3) (where $t_h = 2n_h = 0, 2, 4, 6$).

Let us estimate the relative shift $\Delta\omega_0(a)$ (12) of the light-absorption threshold in SCMCs with radii $a \le a_{ex}$ for the conditions corresponding to experiments performed in [14, 15]. The relative shifts $\Delta\omega_0(a)$ (12) become significant in comparison with the potential-well depth $\Delta V(S)$ (6) for electrons in an SCMC. As the SCMC radius a increases from $a = 3$ nm to $a = 5$ nm, the relative shift $\Delta\omega_0(a)$ (12) of the light-absorption edge in an SCMC decreases from 232.9 to 141.3 meV.

5. CONCLUSION

Thus, in the context of the considered model of a quasi-zero-dimensional system and in the range of SCMC sizes $a_h \le a \simeq a_{ex}$ (in which case, the polarization-related interaction of electrons and holes with the SCMC surface is dominant), it is shown that the absorption edge of an SCMC is formed by two transitions (comparable in intensity) from various levels of the hole dimensional-quantization levels of a hole to the lowest dimensional-quantization level of an electron. It is ascertained that the light-absorption threshold for an SCMC undergoes a larger shift to shorter wavelengths ($\simeq$200 meV) compared to that obtained in [3] disregarding the polarization-related interaction.

REFERENCES

1. A. I. Ekimov and A. A. Onushchenko, Pis'ma Zh. Éksp. Teor. Fiz. **40**, 337 (1984) [JETP Lett. **40**, 1136 (1984)].
2. Yu. V. Vandyshev, V. S. Dneprovskiĭ, and V. I. Klimov, Zh. Éksp. Teor. Fiz. **101**, 270 (1992) [Sov. Phys. JETP **74**, 144 (1992)].
3. Al. L. Éfros and A. L. Éfros, Fiz. Tekh. Poluprovodn. (Leningrad) **16**, 1209 (1982) [Sov. Phys. Semicond. **16**, 772 (1982)].
4. A. L. Efros and A. V. Rodina, Phys. Rev. B **47**, 10005 (1993).
5. M. Nirmal, D. Norris, and A. L. Efros, Phys. Rev. Lett. **75**, 3728 (1995).
6. N. A. Efremov and S. I. Pokutniĭ, Fiz. Tverd. Tela (Leningrad) **27**, 48 (1985) [Sov. Phys. Solid State **27**, 27 (1985)]; Fiz. Tverd. Tela (Leningrad) **32**, 1637 (1990) [Sov. Phys. Solid State **32**, 955 (1990)].
7. S. I. Pokutniĭ, Fiz. Tekh. Poluprovodn. (Leningrad) **25**, 628 (1991) [Sov. Phys. Semicond. **25**, 381 (1991)]; Fiz. Tekh. Poluprovodn. (Leningrad) **30**, 1952 (1996) [Semiconductors **30**, 1015 (1996)].
8. S. I. Pokutnyi, Phys. Lett. A **168**, 433 (1992).
9. S. I. Pokutniĭ, Fiz. Tverd. Tela (St. Petersburg) **38**, 2667 (1996) [Phys. Solid State **38**, 1463 (1996)].
10. N. V. Tkach and V. A. Golovatskiĭ, Fiz. Tverd. Tela (Leningrad) **32**, 2512 (1990) [Sov. Phys. Solid State **32**, 1461 (1990)].
11. L. D. Landau and E. M. Lifshitz, *Course of Theoretical Physics*, Vol. 3: *Quantum Mechanics: Non-Relativistic Theory*, 3rd ed. (Nauka, Moscow, 1974; Pergamon, New York, 1977).
12. V. M. Agranovich, *The Theory of Excitons* (Nauka, Moscow, 1968).
13. V. Ya. Grabovskis, Ya. Ya. Dzenis, and A. I. Ekimov, Fiz. Tverd. Tela (Leningrad) **31** (7), 272 (1989) [Sov. Phys. Solid State **31**, 149 (1989)].
14. G. B. Grigoryan, É. M. Kazaryan, and Al. L. Éfros, Fiz. Tverd. Tela (Leningrad) **32**, 1772 (1990) [Sov. Phys. Solid State **32**, 1031 (1990)].
15. A. I. Ekimov, A. A. Onushchenko, and Al. L. Éfros, Pis'ma Zh. Éksp. Teor. Fiz. **43**, 292 (1986) [JETP Lett. **43**, 376 (1986)].
16. D. Chepic, A. Efros, and A. Ekimov, J. Lumin. **47** (3), 113 (1990).
17. S. I. Pokutniĭ, Fiz. Tverd. Tela (St. Petersburg) **39**, 606 (1997) [Phys. Solid State **39**, 528 (1997)].
18. S. I. Pokutniĭ, Fiz. Tverd. Tela (St. Petersburg) **39**, 720 (1997) [Phys. Solid State **39**, 634 (1997)].

Translated by A. Spitsyn

Semiconductors, Vol. 37, No. 6, 2003, pp. 723–726. Translated from Fizika i Tekhnika Poluprovodnikov, Vol. 37, No. 6, 2003, pp. 748–752.

AMORPHOUS, VITREOUS, AND POROUS SEMICONDUCTORS

Modification of the Nanostructure of Diamond-Like Carbon Films by Bombardment with Xenon Ions

I. A. Faizrakhmanov*, V. V. Bazarov*, A. L. Stepanov, and I. B. Khaibullin***

**Kazan Physicotechnical Institute, Kazan Scientific Center, Russian Academy of Sciences, Kazan, Tatarstan, 420029 Russia*
e-mail: fiak@kfti.kcn.ru
***Physikalisches Institut der Aachen Technische Universität (RWTH) D-52056 Aahen, Germany*
e-mail: stepanov@physik.rwth-aachen.de

Submitted September 2, 2002; accepted for publication November 6, 2002

Abstract—The effect of bombardment with heavy Xe ions (energy E_i = 80 keV) on the optical properties, low-temperature conductivity, and nanostructure of diamond-like carbon (DLC) films is studied. A number of specific features have been ascertained in the behavior of graphite-like nanoclusters which are not observed upon bombardment of the films with light ions. At low irradiation doses ($D < 6 \times 10^{13}$ cm^{-2}), the concentration and size of nanoclusters decrease. At relatively high bombardment doses ($D > 1.2 \times 10^{15}$ cm^{-2}) the effective optical gap, found from the Tauc plot, becomes negative, which is due to the high density of electronic defect states within the gap. In this range, the temperature dependence of conductivity changes, although the conduction mechanism itself remains of the hopping type. The width of the band of defect states, which is formed upon irradiation and in which charge transport occurs, is 0.07 eV, which is close to a value obtained previously by the authors. © *2003 MAIK "Nauka/Interperiodica".*

1. INTRODUCTION

Diamond-like carbon (DLC) films are a nanostructured material in which nanosize fragments of graphite planes—graphite-like nanoclusters—act as nanoparticles. The presence of these nanoclusters predetermines most of the properties of DLC films. In particular, the optical properties in the visible spectral range and the low-temperature electrical conductivity are determined by the concentration and mean size of graphite-like nanoclusters in a sample, which is a manifestation of the quantum-confinement effect. This circumstance allows one to control the properties of DLC films via the parameters of nanoparticles. A similar opportunity also exists for other nanostructured materials. Therefore, the development of appropriate methods for controlling the parameters of nanoclusters is a topical task. Ion implantation, which, in addition, enables synthesis of nanoparticles may become a method of this kind [1, 2].

As shown in previous studies of the authors [3, 4], graphite-like nanoclusters are quite stable against bombardment with light ions (C^+ ions with an energy E_i = 20 keV). The mechanism of amorphization through accumulation of radiation defects, which is characteristic of bombardment of solids with light ions, is inefficient for DLC films.

This study is concerned with the influence exerted on the microstructure of diamond-like films from bombardment with heavy Xe^+ ions (E_i = 80 keV). The specific loss of energy by these ions in a carbon targetis — dE_i/dx = 240 eV/Å, which exceeds the specific energy loss (14 eV/Å) of carbon ions with E_i = 20 keV by more than an order of magnitude. The energy required to displace a carbon atom in graphite is ~40 eV, and in diamond, ~80 eV. Thus, the specific energy loss of energy by xenon ions exceeds these values, being, in contrast, much lower in the case of carbon ions. Such a difference in the energy loss between xenon and carbon ions leads to a pronounced difference between structural changes in diamond-like carbon films, which are induced by bombardment with these two kinds of ions, and which may be even more significant than that in the amorphization of silicon.

2. EXPERIMENTAL

Diamond-like carbon films $d \approx$ 60–80 nm thick, obtained on glass substrates through ion sputtering of graphite [5], had optical and electrical properties typical of diamond-like films (energy gap E_g = 1.1–1.2 eV, refractive index $n \approx 2.0$, resistance $R \gtrsim 10^5$ MΩ). The implantation was done with Xe ions with E_i = 80 keV at doses in the range 6×10^{12}–3×10^{16} cm^{-2}. The ion current density did not exceed 2 μA/cm^2. The samples were mounted on a water-cooled holder.

As in the previous studies of the authors [3, 4], the optical properties and low-temperature conductivity of DLC films were investigated. It was demonstrated in [4] that, in terms of the cluster model of the structure of DLC films, the Tauc parameters (E_{gT}, B_1), which appear in the spectral dependence of the absorption coefficient $\alpha(E)$ in the visible spectral region, are determined by

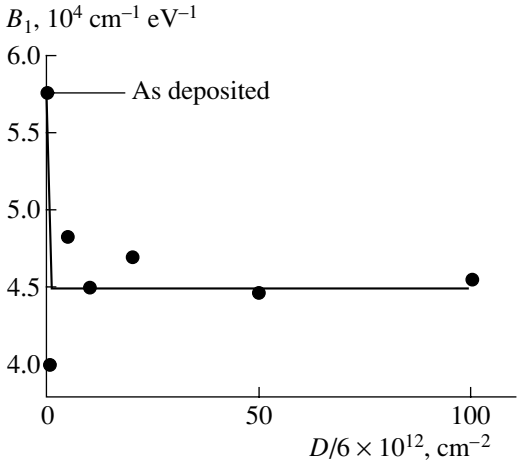

Fig. 1. Parameter B_1 vs. dose of bombardment with Xe^+ ions.

the mean size of clusters (E_{gT}) and their concentration (B_1):

$$\alpha E = B_1(E - E_{gT})^2, \quad (1)$$

$$B_1\ [\text{eV cm}^{-1}] \approx 5.2 \times 10^{16} N_0, \quad (2)$$

$$E_{gT} \approx 6/n_0^{0.5}. \quad (3)$$

Here, N_0 is the concentration (in cm^{-3}) of graphite-like nanoclusters in a film, n_0 is the average number of hexagonal rings constituting a cluster, and E is the photon energy.

The low-temperature conduction in DLC films occurs by variable-range hopping described by the classical Mott expression [6]:

$$R = R_0 \exp(T_0/T)^{1/4}, \quad (4)$$

where R is the sample resistance and T is temperature. In this case, T_0 is determined by the tunneling parameter a and by the density of localized states near the Fermi level, $N(E_F)$:

$$T_0 = 16a^3/kN(E_F). \quad (5)$$

In [4], it was demonstrated that, similarly to the Tauc optical gap E_{gT}, T_0 can be determined by the mean size of nanoclusters via the tunneling parameter a, this being more pronounced for T_0 than for E_{gT}. Thus, the results of optical and electrical measurements furnish information about the size and concentration of graphite-like nanoclusters in DLC films and make it possible to monitor their changes under various treatments.

Previously [3, 4], the film thickness was chosen as $d \approx R_p + \Delta R_p$ and remained virtually unchanged during bombardment (sputtering factor $S < 1$). In contrast, the film thickness in the present study greatly exceeded the thickness of the implanted layer (average projective range of ions, $R_p \approx 40$ nm; rms deviation $\Delta R_p \approx 7$ nm). This is due to the fact that, during bombardment with Xe ions, the sputtering factor $S > 1$ and the sputtering effect is noticeable even at doses $D > 10^{15}$ cm^{-2}. Therefore, it was assumed that the film under study comprises two layers:an implanted layer of thickness d_1 and an unimplanted layer whose thickness d_2 depends both on the thickness of the initial sample and on the implantation dose. In the effective-medium approximation,

$$\alpha = a\alpha^i + b\alpha^0, \quad (6)$$

where α is the absorption coefficient determined from reflection and transmission spectra, α^i is the absorption coefficient of the implanted layer, and α^0 is that of the initial sample;

$$a = d_1/(d_1 + d_2), \quad (7)$$

$$b = d_2/(d_1 + d_2). \quad (8)$$

Using these relations, the absorption coefficient α^i was calculated and E_{gT} and B_1 were determined for the implanted layer.

The optical parameters of the films were found from the reflection $\tilde{R}(\lambda)$ and transmission $\tilde{T}(\lambda)$ spectra, which were measured on a Hitachi-330 double-beam spectrophotometer at wavelengths $350 \leqslant \lambda \leqslant 900$ nm. From the film thickness d and the $\tilde{R}(\lambda)$ and $\tilde{T}(\lambda)$ spectra, the spectral dependences of the refractive index $n(\lambda)$, extinction coefficient $k(\lambda)$, and absorption coefficient $\alpha(\lambda) = 4\pi k/\lambda$ were calculated in the approximation of a "thin film on transparent substrate."

The temperature dependences of electrical resistance were measured in the temperature range $T = 20$–300 K by the two-probe method. Since the resistance of the implanted layer $R_i \ll R_0$, the double-layer structure of the films was disregarded. Silver contacts were deposited by thermal evaporation in a vacuum. The temperature dependences of the electrical resistance were used to determine the activation energy and the conduction mechanism.

The thickness of the initial films was determined by the interference method. Change in the film thickness as a result of ion sputtering was evaluated by the position of the first interference peak in the reflection spectra. In addition, the experimental results obtained demonstrated that, at doses of $\sim 3 \times 10^{16}$ cm^{-2}, a film of thickness ~65 nm is almost completely removed by sputtering. This result also yields an approximate estimate of the rate of sputtering of a DLC film bombarded with xenon ions.

3. EXPERIMENTAL RESULTS AND DISCUSSION

Figure 1 and 2 show the dose dependences of B_1 and E_{gT}. A significant difference is seen in the behavior of the optical parameters and, correspondingly, the microstructure of DLC films for the case of bombardment with light carbon ions [4]. First of all, even at doses of

6×10^{12} cm^{-2}, a noticeable decrease in the concentration of graphite-like particles is indicated by a decrease in the parameter B_1. No noticeable change in the nanocluster size is observed in this stage. At higher doses, the concentration of nanoclusters remains unchanged (Fig. 1). In the authors' opinion, this fact indicates that the initial film contains a certain amount of nanoclusters whose structure becomes unstable under conditions for the generation of dense radiation cascades. Chainlike or other structurally similar clusters can act as these clusters. This process is most effective at doses lower than that at which radiation cascades of separate ions start to overlap. Estimating this dose (rms deviation of xenon ions in the transverse direction is 6 nm) gives a value of ~10^{12} cm^{-2}. This range was not studied for technical reasons; however, it can be stated that, at least in the range $D > 6 \times 10^{12}$ cm^{-2}, a decrease in the concentration of nanoclusters is no longer observed.

The stage in which a decrease in the nanocluster size is the most significant effect is the next (Fig. 2). Of course, in no way means that this process does not occur at lower irradiation doses:, the concentration of such clusters is low and, as a result, they exert no noticeable influence on the mean size of nanoparticles. The decrease in the nanocluster size is due, in the authors' opinion, to the effect of ballistic dissolution under the conditions of a dense radiation cascade. Several vacancies are created in a nanocluster which partly recombine with atoms of the surrounding matrix and partly diffuse toward the boundary of a cluster, thus reducing its size.

At doses $D > 2 \times 10^{14}$ cm^{-2}, the fast growth of nanoclusters is observed, and this stage is a common stage in the implantation of any ion, with only the characteristic doses of bombardment being different. It is clear that the growth of nanoclusters occurs via the addition of carbon atoms with a diamond-like matrix, since there are no other sources of carbon atoms. After this source is exhausted, the rate of nanocluster growth first decreases and then the growth ceases altogether. However, in contrast to the case of bombardment with carbon ions, further irradiation with xenon ions ($D > 2 \times 10^{15}$ cm^{-2}) leads to a further decrease in the E_{gT} value, which even becomes negative. Nothing of the kind was previously observed by the authors. It is understood that negative E_{gT} has no physical meaning and cannot be related to nanocluster size.

In the authors' opinion, the most important process in this range of irradiation doses is the accumulation of radiation defects in nanoclusters. This gives rise to a state within the energy gap of a separate nanocluster. As a result, the effective optical gap of a sample is filled with defect states making additional contributions to the optical absorption. Therefore, in the spectral range studied (350 nm < λ < 900 nm), the Tauc dependence of the absorption coefficient should be modified:

$$E\alpha = B_1(E - E_g)^2 + EC(E), \quad (9)$$

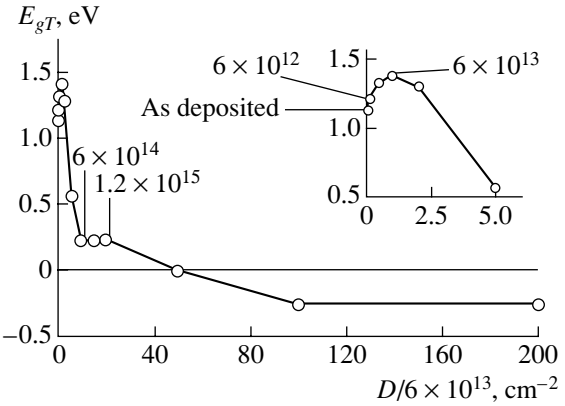

Fig. 2. Optical gap E_{gT} of DLC films vs. dose of bombardment with Xe^+ ions. Insert: low-dose range. The doses are given in cm^{-2}; the same for Fig. 3.

where $C(E)$ is the absorption associated with defect states. If it is now assumed that $C(E)$ is weakly dependent on energy, i.e., is approximately constant, at high energies of incident radiation ($E > E_g$), then the absorption spectrum can be approximated by a linear function in the Tauc coordinates:

$$\begin{aligned}(E\alpha)^{1/2} &= [B_1(E - E_g)^2 + EC(E)]^{1/2} \\ &\approx B_1^{1/2}[E - (E_g - C/2B_1)],\end{aligned} \quad (10)$$

$$E_{gT} = E_g - C/2B_1. \quad (11)$$

It follows from this expression that, at high concentrations of radiation defects, the experimentally measured optical gap is determined not only by nanocluster size, but also by the defect concentration. In the case when $C/2B_1 > E_g$, the optical gap E_{gT}, found from the Tauc plot, becomes negative. Since C is approximately proportional to the defect concentration N_d, the dose dependence of E_{gT} at $D > 2 \times 10^{15}$ cm^{-2} is determined by the kinetics of accumulation of radiation defects. It can be seen from Fig. 2 that the concentration of radiation defects eventually reaches a limiting value. Thus, the final stage is associated with the generation and accumulation of radiation defects in nanoclusters; this stage is shifted, compared with that in structurally homogeneous materials, to the range of higher doses as in the cage of irradiation with carbon ions. The model suggested is supported by data on thermal annealing in a vacuum of samples with $E_{gT} < 0$. Annealing at T = 350°C for 15 min leads to an increase in the optical gap to ~0.7 eV and a decrease in conductivity by several orders of magnitude. In the process, a noticeable decrease in the film thickness is observed and the refractive index increases from ~1.9 to ~2.3. The stage of defect formation in nanoclusters is characteristic not only of bombardment with heavy xenon ions as similar dose dependences are observed in the bombardment of DLC films with lighter ions, such as copper or argon.

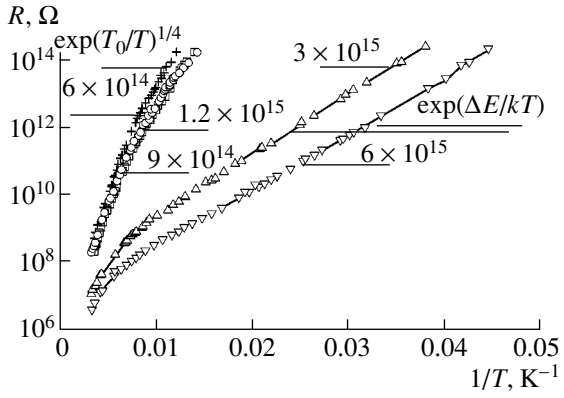

Fig. 3. Temperature dependence of the resistance of DLC films bombarded with xenon ions.

Figure 3 presents temperature dependences of the electrical resistance of carbon films subjected to irradiation with different doses of Xe ions. In the dose range in which nanoclusters grow ($D < 10^{15}$ cm^{-2}), conduction occurs by the variable-range hopping mechanism ($R \propto \exp(T_0/T)^n$, where $n = 1/4$). Similarly to the case of irradiation with carbon ions [4], the parameter T_0 decreases with increasing irradiation dose, which is due to an increase in the nanocluster size. In the defect-formation range ($D > 1.2 \times 10^{15}$ cm^{-2}), a dramatic decrease in resistance (by approximately two orders of magnitude) is observed, together with a change in the temperature dependence of the electrical resistance, which can now be described by an exponential dependence with $n = 1$; i.e., it becomes thermally activated. However, the mechanism of conduction retains its hopping nature. In this dose range, conduction occurs by carrier hopping via the nearest defect states [6]. This conclusion is in agreement with the above interpretation of the data obtained in optical measurements for the given range of irradiation doses.

The activation energy of low-temperature electrical conductivity $\Delta E = 0.034$ eV and is virtually independent of the irradiation dose. This value coincides with that previously obtained for samples bombarded with carbon ions [4]. Consequently, the width of the band of defect states via which the charge transport occurs, which is formed as a result of irradiation, is independent of the mass of the bombarding ions and equals ~0.07 eV.

Thus, bombardment of DLC films with heavy ions creating radiation cascades with a high density of displaced ions leads to more complex structural changes than bombardment with light ions. Studying how the optical properties and low-temperature electrical conductivity of DLC films depend on the irradiation dose made it possible to distinguish several characteristic stages:

(1) $D < 6 \times 10^{12}$ cm^{-2}, disintegration of a part of nanoclusters;

(2) $6 \times 10^{12} < D < 6 \times 10^{13}$ cm^{-2}, decrease in the mean size of nanoclusters;

(3) $6 \times 10^{13} < D < 6 \times 10^{14}$ cm^{-2}, increase in the mean size of nanoclusters;

(4) $6 \times 10^{14} < D < 1.2 \times 10^{15}$ cm^{-2}, strong decrease in the rate of nanocluster growth;

(5) $D > 1.2 \times 10^{15}$ cm^{-2}, generation and accumulation of radiation defects in nanoclusters.

Stages 1 and 2 are not observed in bombardment with light ions, and stage 5 is much less effective in this case.

Another important result is that the optical gap E_{gT} is governed not only by the size of graphite-like nanoclusters, but also by the concentration of structural defects in nanoclusters.

ACKNOWLEDGMENTS

This study was supported by the Russian Foundation for Basic Research program “Leading Scientific Schools” (grant no. 00-15-96615).

REFERENCES

1. G. F. Kachurin, I. E. Tyschenko, V. Skorupa, *et al.*, Fiz. Tekh. Poluprovodn. (St. Petersburg) **31**, 730 (1997) [Semiconductors **31**, 626 (1997)].
2. A. L. Stepanov and D. Hole, Recent Res. Dev. Appl. Phys. **5**, 1 (2002).
3. I. A. Faizrakhmanov, V. V. Bazarov, V. A. Zhikharev, and I. B. Khaibullin, Nucl. Instrum. Methods Phys. Res. B **127–128**, 719 (1997).
4. I. A. Faĭzrakhmanov, V. V. Bazarov, V. A. Zhikharev, and I. B. Khaĭbullin, Fiz. Tekh. Poluprovodn. (St. Petersburg) **35**, 612 (2001) [Semiconductors **35**, 591 (2001)].
5. I. A. Faĭzrakhmanov and I. B. Khaĭbullin, Poverkhnost, No. 5, 88 (1996).
6. N. F. Mott and E. A. Davis, *Electronic Processes in Non-Crystalline Materials* (Clarendon Press, Oxford, 1971; Mir, Moscow, 1974).

Translated by M. Tagirdzhanov

Semiconductors, Vol. 37, No. 6, 2003, pp. 727–729. Translated from Fizika i Tekhnika Poluprovodnikov, Vol. 37, No. 6, 2003, pp. 753–755.

AMORPHOUS, VITREOUS, AND POROUS SEMICONDUCTORS

Effect of Illumination on the Rate of Relaxation of Light-Induced Metastable States in *a*-Si:H(B)

I. A. Kurova*, N. N. Ormont*, and A. L. Gromadin**

**Department of Physics, Moscow State University, Moscow, 119992 Russia*

e-mail: scon282@phys.msu.su

***GIREDMET (State Research Institute for the Rare-Metals Industry), Moscow, 109017 Russia*

Submitted September 24, 2002; accepted for publication November 6, 2002

Abstract—Time dependences of the rates of relaxation of light-induced metastable states of electrically active impurity atoms in boron-doped *a*-Si:H films have been studied in the dark and under illumination. It has been established that under illumination the rate of relaxation of light-induced metastable states of boron atoms grows in the initial stage when the rate of light-induced relaxation of these states exceeds that of their light-induced generation. © *2003 MAIK "Nauka/Interperiodica".*

In [1–3], the effect of illumination on the kinetics of relaxation of metastable dangling bonds of silicon in undoped films of amorphous hydrogenated silicon (*a*-Si:H) was studied. It was demonstrated that illumination of the films leads to a higher rate of their isothermal relaxation in the initial stage of relaxation compared with that in the dark. This points to the occurrence of light-induced annealing of metastable dangling bonds in undoped films. No investigations of this kind have been carried out for metastable states in doped *a*-Si:H films.

It is known that two types of metastable states (MS) are formed in doped *a*-Si:H films: metastable dangling bonds (MDB) and metastable electrically active impurity atoms (MEAI). This study is concerned with the effect of illumination on the rate of isothermal relaxation of light-induced MEAI in boron-doped *a*-Si:H films.

The kinetics of MEAI relaxation was studied by recording the kinetics of variation of the dark conductivity of the films. It was shown in [4–6] that, for each type of MS, the variation of their concentration with time *t* causes an upward or downward shift of the Fermi level from its equilibrium position in the band gap. This leads to a decrease or increase in the dark conductivity of the film, $\sigma_d(t)$. If the density of localized states in the region across which the Fermi level moves is constant, $\rho(E) = \rho_0$, then the dark conductivity of a film in the course of MS relaxation is related to the MS concentration $N(t)$ by

$$N(t) = kT\rho_0|\log[\sigma_d(t)/\sigma_{d0}]|. \quad (1)$$

Here, $\sigma_{d0}(T)$ is the equilibrium dark conductivity of a film, T is temperature, and k is the Boltzmann constant.

a-Si:H films lightly doped with boron were studied. The concentration of boron in the films was determined by SIMS to be $(3–4) \times 10^{17}$ cm^{-3}. The Fermi level position in the films was ~0.8 eV above the valence band top in the region of a rather broad minimum in the density of states, where $\rho(E)$ can be considered virtually constant and equal to ρ_0. This allowed use of the above formula (1) in studying the kinetics of MS relaxation. It should also be noted that the ρ_0 value is smaller in films of *a*-Si:H lightly doped with boron, than that in a heavily doped material [7]. This leads to a stronger variation of the dark conductivity of a film at a given value of $N(t)$ and, consequently, to higher accuracy in determining the MS concentration as a function of time.

The experiment was performed as follows. Prior to each run, an *a*-Si:H(B) film was annealed at $T = 200$°C for 1 h in a nitrogen cryostat and then slowly cooled to a certain temperature and kept at this temperature for a time sufficient for the corresponding equilibrium to be attained. Then, to generate light-induced MS, the film was exposed to white light from a halogen lamp with an IR filter, with the density of incident power equal to 90 mW/cm^2. After the light was switched off, the kinetics of variation of the dark conductivity was recorded in the dark and under weak illumination (8 mW/cm^2). In the latter case, the dark conductivity in the course of MS relaxation was measured with the illumination switched off for a short time. The measurement temperature was 410 K, which is required for a sufficiently high concentration of light-induced MS to be generated [5, 6]. During the measurements, the temperature of a film was maintained constant to within 0.5 K.

Figure 1 shows experimental data (points) on the kinetics of variation of the dark conductivity for film no. 1, beginning at the instant when its preliminary illumination with a power density of 90 mW/cm^2 for 600 s is switched off. It can be seen that the dependence $\log[\sigma_d(t)/\sigma_{d0}]$ is nonmonotonic. The dependence can be represented, similarly to the case of MS relaxation in

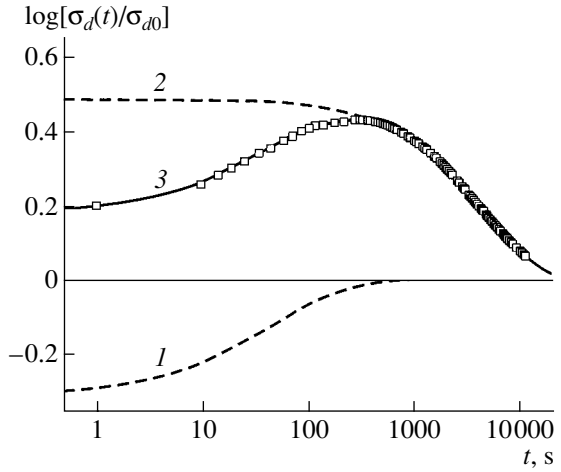

Fig. 1. Kinetics of variation of $\sigma_d(t)$ of an *a*-Si:H(B) film at $T = 410$ K in the dark after its preliminary illumination for 600 s. *Points*, experiment; *lines*, calculation: (*3*) sum of two stretched exponentials reflecting the isothermal relaxation of light-induced (*1*) MDB and (*2*) MEAI. Parameters of stretched exponentials: $a_1 = -0.31$, $\tau_{01} = 51$, $\beta_1 = 0.66$, $a_2 = 0.49$, $\tau_{02} = 4800$, and $\beta_2 = 0.85$.

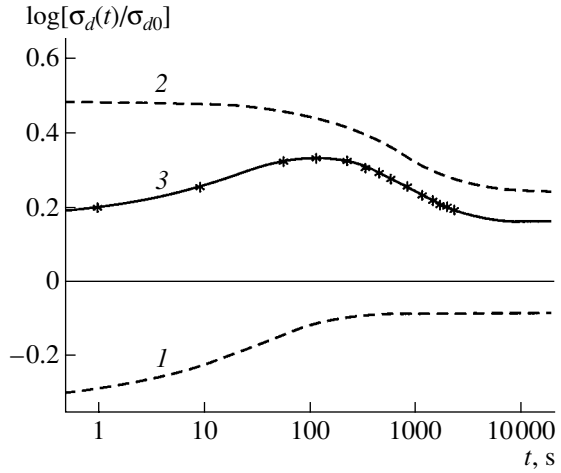

Fig. 2. Kinetics of variation of $\sigma_d(t)$ of an *a*-Si:H(B) film at $T = 410$ K under weak illumination after preliminary exposure to light for 600 s. *Points*, experiment; *lines*, calculation: (*3*) calculation by formula (3), the sum of curves *1* and *2* reflecting the relaxation of light-induced (*1*) MDB and (*2*) MEAI under illumination. Calculation parameters: $h_1 = -0.08$, $\tau_{01} = 31$, $\beta_1 = 0.6$; $h_2 = +0.24$, $\tau_{02} = 970$, $\beta_2 = 0.78$.

heavily doped films [6], as the sum (curve *3*) of two stretched exponentials (curves *1* and *2*) reflecting the dark relaxation of two ensembles of light-induced MS—MDB and MEAI:

$$\log[\sigma_d(t)/\sigma_{d0}] = a_1\exp[-(t/\tau_{01})^{\beta_1}] + a_2\exp[-(t/\tau_{02})^{\beta_2}]. \quad (2)$$

Here, a_1, τ_{01}, β_1 and a_2, τ_{02}, β_2 are parameters of stretched exponentials which have the following meaning: a_1 and a_2 are the initial concentrations of, respectively, MDB and MEAI in relative units; τ_{01} and τ_{02} are the effective times of relaxation of, respectively, the MDB and MEAI ensembles, which are equal to the times at the peaks of the MDB and MEAI distributions with respect to $\tau_{1,2}$; $1/\beta_{1,2}$ characterize the halfwidths of the distribution functions.

Curve *1* reflects the fast relaxation of light-induced MDB predetermining the increase in the conductivity of the film to the equilibrium value σ_{d0}. Curve *2* reflects the slow relaxation of light-induced MEAI, which results in a decrease in the conductivity of the film to its equilibrium value σ_{d0}.

Figure 2 shows experimental data on the kinetics of variation of the conductivity of the same film under weak illumination, beginning at the instant when the preliminary illumination of the film (incident power density of 90 mW/cm^2 for 600 s) was switched off. It can be seen that the experimental dependence $\log[\sigma_d(t)/\sigma_{d0}]$ is also nonmonotonic (curve *3*) and the conductivities at the initial instant of time are close for the curves describing relaxation in the dark and under illumination (compare curves *3* in Figs. 1 and 2). This is due to similar conditions of preliminary illumination of the film, which result in the same concentrations of light-induced MDB and MEAI being generated. Further, at $t > 0$, curves *3* in Figs. 1 and 2 differ significantly in the rate of variation of the dark conductivity with time. In addition, at large times, the steady-state value attained by the conductivity in MS relaxation under illumination exceeds the equilibrium value σ_{d0}. This is due to the fact that, in the second case, a steady-state value is eventially reached by the concentration of MDB and MEAI. This value is determined by the equality of the rates of generation and relaxation of MDB and MEAI under illumination.

The curve describing conductivity relaxation under weak illumination (Fig. 2, curve *3*) can be represented as the sum of two terms:

$$\log[\sigma_d(t)/\sigma_{d0}] = \{(-0.31 - h_1)\exp[-(t/\tau_{01})^{\beta_1}] + h_1\} + \{(0.49 - h_2)\exp[-(t/\tau_{02})^{\beta_2}] + h_2\}. \quad (3)$$

The first term (curve *1*) reflects the relaxation of MDB under illumination, and the second, the relaxation of MEAI. The initial concentrations of MDB and MEAI in relative units (0.31 and 0.49) are equal to the initial concentrations of MDB and MEAI. These concentrations are found from curves *1* and *2* in Fig. 1, which reflect the relaxation of MDB and MEAI in the dark.

To determine the rates of relaxation of light-induced MDB and MEAI in the dark and under illumination, curves *1* and *2* in Figs. 1 and 2 are differentiated with respect to time. Figures 3a and 3b show the thus-obtained time dependences of the relaxation rates of, respectively, MDB and MEAI in the dark (curves *1*) and under illumination (curves *2*). It can be seen from

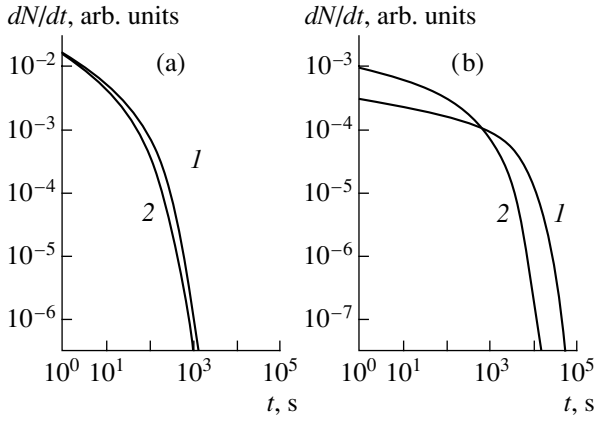

Fig. 3. Rates of relaxation of light-induced (a) MDB and (b) MEAI (*1*) in the dark and (*2*) under weak illumination vs. relaxation time. $T = 410$ K.

Fig. 3b that, at a certain instant of time $t = t_C$, the rates of variation of the MEAI concentration in the dark and under illumination are the same. This means that the rates of light-induced generation and relaxation of MEAI, determined by illumination, are equal. Indeed, the rate of variation of the MEAI concentration under illumination is determined by the thermal and light-induced rates of MEAI generation and relaxation [8]:

$$(dN/dt)_{\text{ill}} = G_T + G_{\text{ill}} - R_T - R_{\text{ill}}. \quad (4)$$

Here, G_T, G_{ill} and R_T, R_{ill} are, respectively, the rates of thermal and light-induced generation and relaxation. In the dark, the rate of variation of the MEAI concentration is determined only by the rates of thermal generation and relaxation of MEAI:

$$(dN/dt)_T = G_T - R_T. \quad (5)$$

From (4) and (5), it follows that, at the instant of time $t = t_C$, the rates of light-induced generation and relaxation of MEAI are equal, $G_{\text{ill}} = R_{\text{ill}}$; at $t < t_C$, the rate of light-induced relaxation exceeds that of light-induced generation, $R_{\text{ill}} > G_{\text{ill}}$; at $t > t_C$, the rate of light-induced generation is higher than that of light-induced relaxation, $G_{\text{ill}} > R_{\text{ill}}$.

It can be seen from Fig. 3a that no light-induced relaxation is observed for MDB in the region of the measurement times ($t \geq 1$ s): only the region $t > t_C$ manifests itself, in which the rate of light-induced relaxation of MDB is lower than that of their light-induced generation under illumination. Comparison of the time dependences of MEAI relaxation in the dark and under illumination (Fig. 3b) with analogous dependences obtained for MDB relaxation in undoped films [2] shows that the dependences are similar. This may point to the similar nature of the mechanisms by which light-induced relaxation of MDB and MEAI occurs in *a*-Si:H films. However, further studies are necessary for elucidating the mechanisms of light-induced relaxation of MEAI and MDB in amorphous hydrogenated silicon.

ACKNOWLEDGMENTS

We thank I.P. Zvyagin for discussions of the results obtained. This study was supported by the program "Universities of Russia" and by the scientific program of GIREDMET State Scientific Center.

REFERENCES

1. R. Meaudre and M. Meaudre, Phys. Rev. B **45**, 12134 (1992).
2. H. Gleskova, P. A. Morin, and S. Wagner, Appl. Phys. Lett. **62**, 2063 (1993).
3. C. F. O. Graeff, R. Buhleir, and M. Stutzmann, Appl. Phys. Lett. **62**, 3001 (1993).
4. J. K. Rath, W. Fuhs, and H. Mell, J. Non-Cryst. Solids **137–138**, 279 (1991).
5. I. A. Kurova, É. V. Larina, N. N. Ormont, and D. V. Senashenko, Fiz. Tekh. Poluprovodn. (St. Petersburg) **31**, 1455 (1997) [Semiconductors **31**, 1257 (1997)].
6. A. G. Kazanskii, I. A. Kurova, N. N. Ormont, and I. P. Zvyagin, J. Non-Cryst. Solids **227–230**, 306 (1998).
7. S. Sheng, X. Liao, and G. Kong, Appl. Phys. Lett. **78**, 2509 (2001).
8. D. Redfield, Appl. Phys. Lett. **52**, 492 (1988).

Translated by M. Tagirdzhanov

Semiconductors, Vol. 37, No. 6, 2003, pp. 730–735. Translated from Fizika i Tekhnika Poluprovodnikov, Vol. 37, No. 6, 2003, pp. 756–761.

PHYSICS OF SEMICONDUCTOR DEVICES

Efficient Silicon Light-Emitting Diode with Temperature-Stable Spectral Characteristics

A. M. Emel'yanov*, N. A. Sobolev*, T. M. Mel'nikova, and S. Pizzini*****

**Ioffe Physicotechnical Institute, Russian Academy of Sciences, St. Petersburg, 194021 Russia*

***SME Orion, Moscow, 111123 Russia*

****INFM and Department of Materials Science, l-20126 Milan, Italy*

Submitted September 25, 2002; accepted for publication November 4, 2002

Abstract—The influence of temperature on the parameters of the band-to-band emission spectrum of a light-emitting diode based on single-crystal silicon was investigated; the unprecedentedly high stability against variations in temperature was observed for both the electroluminescence intensity at the peak of the spectral distribution (I_{EL}^{m}) and the wavelength corresponding to this peak (λ_m). The internal quantum efficiency of the light-emitting diode at room temperature is estimated as no lower than 0.1%. The value of I_{EL}^{m} varies by no more than ~10% as the temperature is varied from 120 to 300 K. The value of λ_m remains virtually constant in the temperature range of 200–300 K. The unprecedentedly high stability of λ_m is related to interference effects in the oxide film through which the radiation of the light-emitting exits. It is shown that one of the important factors that govern the temperature stability of I_{EL}^{m} is a decrease in the lifetime of the minority charge carriers with decreasing temperature. © *2003 MAIK "Nauka/Interperiodica".*

1. INTRODUCTION

Single-crystal silicon belongs to the class of indirect-gap semiconductors in which the radiative band-to-band recombination can generally occur with involvement of phonons. This circumstance brings about a much lower (by several orders of magnitude) probability of band-to-band transitions in indirect-gap semiconductors compared to that in direct-gap semiconductors. In this context, single-crystal silicon had generally been considered as a material that has no potential for the development of efficient light-emitting diodes (LEDs) with a spectrum characteristic of the band-to-band emission. This misconception was refuted only in 2001, when it was reported that silicon LEDs were developed that emit in the spectral region of band-to-band recombination and have a quantum efficiency at room temperature almost as high as the quantum efficiency of LEDs made of direct-gap semiconductors [1, 2].

As is well known, the internal quantum efficiency of the band-to-band emission η_i can be defined by the formula

$$\eta_i = \tau_p/\tau, \tag{1}$$

where τ_p is the lifetime of minority charge carriers, which is mainly controlled in Si by nonradiative recombination; and τ is the radiative lifetime. In both publications [1] and [2], the high quantum efficiency was, in general, related to long lifetimes τ_p. Green *et al.* [1] used special technology that ensured the minimization of nonradiative-recombination losses both in the bulk and at the surface of a semiconductor. It was also believed [2] that nonradiative recombination was suppressed to a great extent by restrictions on the charge-carrier diffusion, which were introduced by potential barriers of dislocation loops whose presence was confirmed by electron-microscopy studies. It should also be noted that another possible mechanism for the beneficial effect of dislocations on the efficiency of radiative band-to-band recombination has been considered. The dislocation-related stresses and corresponding distortions of the energy-band structure can reduce the radiative lifetime of charge carriers [3]. Consequently, in order to gain insight into both the causes of the attainment of high quantum efficiency in silicon LEDs and the possible role of dislocations, one should study experimentally and theoretically the effects of various factors on the physical parameters that characterize the band-to-band emission. Experimental studies of the radiative band-to-band recombination in single-crystal silicon at room temperature have been scarce (in addition to [1, 2], see also [3–10]). A theoretical expression for the radiative lifetime of charge carriers was first derived by van Roosbroeck and Shockley [11] back in the 1950s; it was mentioned in [11] (see also [12, 13]) that the resulting formula for the lifetime had been obtained for the case of a small deviation of the charge-carrier concentration from the equilibrium concentration. As far as we know, the theory for determining the radiative lifetime has not changed since that time; however, the formula derived by van Roosbroeck and Shockley [11] was later used (see, for example, [3, 8])

in the situation where the concentration of injected nonequilibrium charge carriers exceeded that of the doping impurity (the case of a so-called high injection level [14]). If we extend the expression derived in [11] to the case of a high injection level, the quantity reciprocal to the radiative lifetime will be directly proportional to the concentration of injected charge carriers. Further studies of band-to-band recombination radiation in silicon diodes fabricated by different technologies and operating in different modes are required in order to either validate or disprove the aforementioned physical concepts and to develop corresponding light-emitting devices for practical applications. The results of one of these studies are reported in this publication. In particular, we will describe here for the first time the fabrication, characteristics, and physical principles of operation of a silicon LED, in which a high temperature stability of both the electroluminescence (EL) intensity and the peak in the distribution of the band-to-band emission over the wavelengths λ is observed.

2. EXPERIMENTAL CONDITIONS

The diodes under investigation were fabricated using the planar technology for a single-crystal *n*-Si wafer; the latter had a thickness of ~0.35 mm and a doping-impurity concentration of $\sim 6 \times 10^{13}$ cm^{-3}. After final rinsing in an ammonia peroxide solution, the wafer was oxidized in a wet oxygen atmosphere for 2 h at 1150°C. The *p–n* junctions were formed by diffusion through square windows (with a side of 2 mm) in an oxide film in two stages: first by predeposition of boron from boron nitride for 1 h at 950°C and then by the drive-in diffusion of boron for 2 h at 1150°C in a dry oxygen atmosphere. Before the drive-in diffusion of boron, a borosilicate-glass layer was removed using a special etchant. After removal of the oxide film from the rear surface and final rinsing, this side of the wafer was additionally doped with phosphorus by diffusion from a liquid PCl_3 source in a nitrogen atmosphere for 1 h at 1000°C. The concentrations of boron and phosphorus were equal to $\sim 3 \times 10^{19}$ cm^{-3} in the surface p^+- and n^+-type layers, respectively. Ohmic contacts were formed by the evaporation of Al in vacuum without additional fusing. A continuous Al layer was deposited onto the rear surface of the wafer; the Al contact to the front surface was formed using photolithography and had the form of a thin strip over the perimeter of the *p–n* junction area. We used a lens system to focus the emission from the central part of the *p–n* junction area (not shielded by Al) either onto the entrance slit of an MDR-23 monochromator (when measuring the EL spectra) or onto the entrance window an FD-10 AG germanium photodiode (when measuring the EL kinetics and the quantum efficiency). The radiation at the exit from the monochromator was detected by an uncooled InGaAs photodiode using a selective nanovoltmeter. All of the spectral characteristics shown below were corrected for the spectral responses of both the photodetector and the entire optical system. In order to excite the EL, we used a pulsed voltage with a frequency of 32 Hz and a duration of the forward-current pulses of t_0 = 0.2–5 ms. The time constant of the detection system was 2.7 μs in measurements of the EL decay and rise kinetics. The samples were mounted on a massive copper cylinder. The temperature dependences were measured in the temperature range from 80 to 300 K.

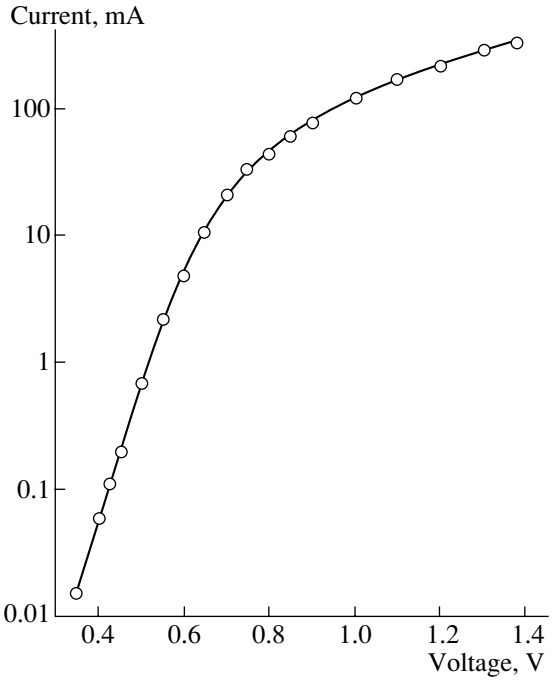

Fig. 1. Forward current–voltage characteristic of the diode.

The charge-carrier lifetimes were determined using the method suggested by Lax and Neustadter [15]. With the condition $0.1 < I_1/I_0 < 1$ satisfied, the quantity τ_p was calculated from the simplified formula [16]

$$\tau_p \approx t_1 I_1 / 0.2 I_0, \quad (2)$$

where I_0 is the amplitude of the forward-current pulse; and I_1 and t_1 are the amplitude and duration of a fraction of the reverse-current pulse which corresponds to the stage of high reverse conduction in the diode, respectively. As a result of the low dopant concentration in the diode's *n*-type region, the conditions for a high injection level were satisfied in all experiments related to the determination of τ_p [14]. It is also noteworthy that, according to [14], the effect of an electric field (appearing in the diffused *p–n* junction owing to gradual variation in the impurity concentration) on the results of determining the value of τ_p by the method suggested by Lax and Neustadter [15] can be ignored under conditions of a high injection level.

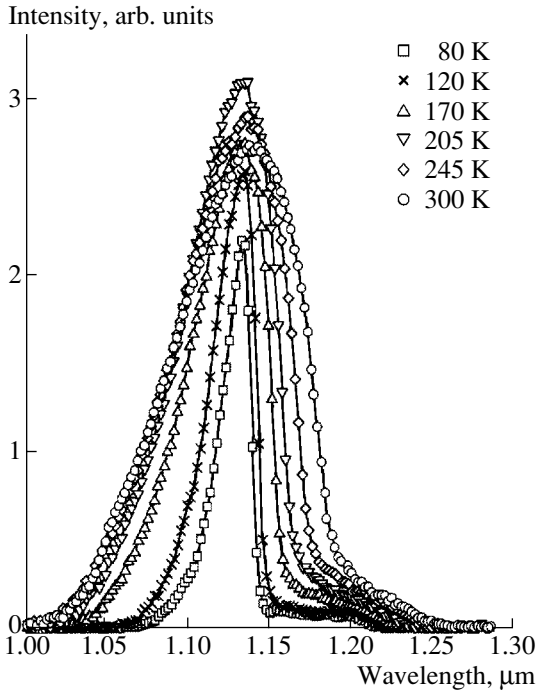

Fig. 2. Electroluminescence spectra of the silicon light-emitting diode; the spectra were measured at a current of 300 mA and at various temperatures.

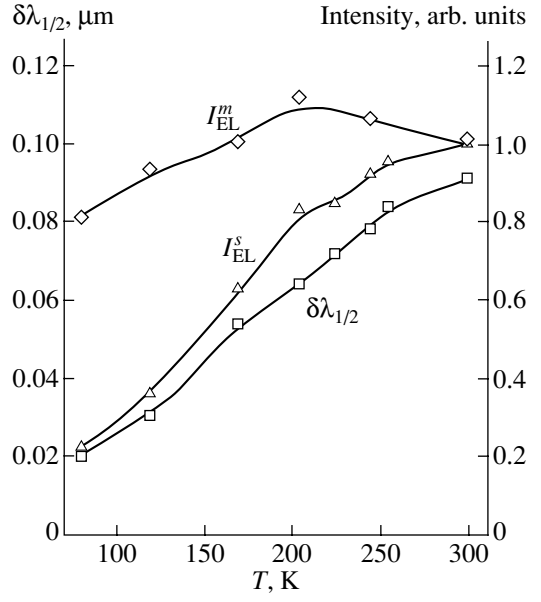

Fig. 3. Temperature dependences of the electroluminescence (EL) intensity at the peak of the spectral distribution (I^m_{EL}), the area under the EL spectral curve (I^s_{EL}), and the half-width of the EL peak ($\delta\lambda_{1/2}$).

3. RESULTS AND DISCUSSION

The forward current–voltage characteristic of the diode is shown in Fig. 1. The EL spectra measured at various temperatures are shown in Fig. 2; the amplitude and duration of current pulses were equal to 300 mA and t_0 = 1 ms, respectively. The spectral resolution of the monochromator amounted to 3 nm. For t_0 = 1 ms, the position of the peak in the EL spectrum of the diode under investigation in the region of band-to-band radiation of silicon was virtually independent of current both at 80 and 300 K in the entire range of currents under consideration (20–500 mA). The absence of a shift of the spectral-characteristic peak indicates that the sample is not appreciably heated during measurements; this circumstance is due both to the short relative pulse duration and a good heat sink. As can be seen from Fig. 2, the EL spectra feature a high stability against temperature variations; this stability concerns both the radiation intensity at the peak of the spectral distribution (I^m_{EL}) and the wavelength corresponding to I^m_{EL} (λ_m). For example, λ_m = 1.136 μm in the temperature range T = 200–300 K; as T decreases to 80 K, λ_m decreases by a mere 4 nm. The temperature dependences of I^m_{EL} and the half-width of the EL band ($\delta\lambda_{1/2}$) are shown in Fig. 3. The temperature dependence of the integrated EL intensity I^s_{EL} (the area under the spectral curve) is also shown in Fig. 3. As can be seen from Fig. 3, the variations in I^s_{EL} do not exceed ~10% at $T \gtrsim$ 120 K and ~20% in the entire temperature range under investigation. Variations in I^s_{EL} do not exceed ~20% in the narrower temperature range (~200–300 K). As can be seen from Fig. 3, more appreciable variations in I^s_{EL} compared to those in I^m_{EL} are related to the temperature-induced variation in the EL spectrum width. The temperature stability of λ_m in the obtained spectra is virtually no lower (and the temperature stability of I^m_{EL} is even higher) than those in the most temperature-stable spectra of silicon LEDs; in the latter, the radiation is caused by transitions within the *f* core of ions of rare-earth elements (Er^{3+} or Ho^{3+}) excited in the conditions of breakdown of the *p–n* junction [17, 18]. It is noteworthy that the high temperature stability of I^m_{EL} (but not of λ_m) for the band-to-band radiation was also noticed in silicon LEDs studied by Wai Lek Ng *et al.* [2]. Since the LEDs were fabricated in [2] using significantly different technology (ion implantation with subsequent annealing), our results show that the temperature stability of I^m_{EL} in the region of the band-to-band radiation can be attained in a wide range of fabrication technologies for silicon LEDs. As follows from expression (1), the temperature dependence of the integrated EL intensity (I^s_{EL}) at a fixed value of current is governed by the temperature dependences of τ_p and τ. In this study, we measured the dependence of τ_p on tem-

perature T at a forward current of 300 mA; this dependence, along with experimental curve $I^s_{EL}(T)$ obtained for the same value of the current, is shown in Fig. 4. As can be seen from Fig. 4, the curves under comparison are close to each other (if we take into account the chosen scale of I^s_{EL} and τ_p and the experimental accuracy) when the values of both τ_p and I^s_{EL} vary severalfold. This circumstance indicates that a decrease in I^s_{EL} with decreasing temperature in the diode under investigation is caused to a great extent by a decrease in τ_p, which, in combination with other factors, in particular, those capable of stimulating an increase in I^m_{EL} (narrowing of the EL spectrum and onset of recombination via excitons), can give rise to a high temperature stability of I^m_{EL}.

It is worth noting that we failed in this study to detect the band-to-band photoluminescence when the diode was exposed to visible-region illumination with a power of ~50 mW. This fact can be attributed to a high rate of nonradiative recombination in the heavily doped p-type region of the diode.

In Fig. 5, curve *1* represents the temperature dependence of λ_m plotted using the published data [2]. The dependence $\lambda_m(T)$ for the LED studied by us is also shown (curve *2*). It can be seen that, at $T \lesssim 200$ K, dependences *1* and *2* are virtually indistinguishable from one another. The observed insignificant discrepancy (2 nm) is within the experimental accuracy. At $T >$ 200 K, curves *1* and *2* in Fig. 5 begin to diverge appreciably. We attribute this divergence to the specific conditions of extraction of radiation from the semiconductor bulk for the two different diodes under consideration. In the course of fabrication of the diode under investigation (mainly, during the drive-in diffusion of boron), an oxide film was formed on the silicon surface from which the radiation was collected; the interference-related phenomena in this film could affect the observed emission spectrum. This assumption was validated by comparative measurements of the reflection spectra of the unoxidized silicon surface for an almost normal angle of incidence (with deviation from the normal smaller than 30°). Experimental dependence of the ratio between the reflectivity of the silicon surface with the oxide film (R) and that of an unoxidized silicon (R_{Si}) on the wavelength of incident radiation in the region of the band-to-band emission in silicon is shown in Fig. 6 (curve *1*). We can note that, first, the reflectivity of the silicon surface with oxide film is higher than that of unoxidized silicon surface at wavelengths 1.05 μm ≤ $\lambda \le 1.2$ μm. Second, the value of R/R_{Si} decreases with decreasing wavelength. Since the effect of oxide film on the reflection of radiation, which is incident on the silicon surface from inside, is qualitatively similar, we may expect that the formation of oxide film will bring about an increase in the ratio between the intensity of radiation in the region of shorter wavelengths and the corresponding intensity at longer wavelengths. This inference is confirmed by comparison of the diode's EL spectra measured at room temperature before and after etching off of the oxide film from the light-emitting sur-

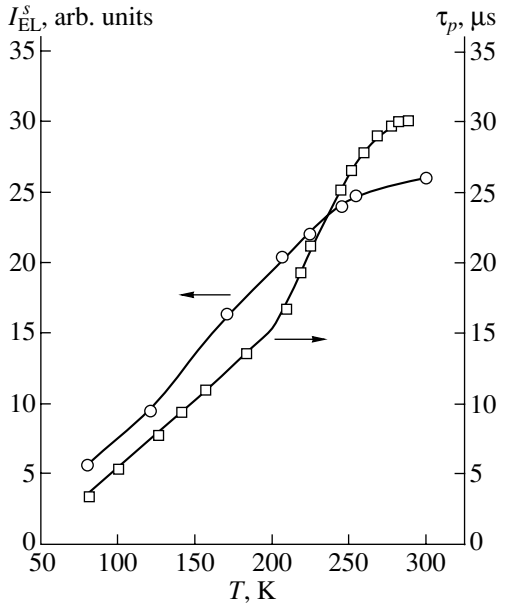

Fig. 4. Temperature dependences of the lifetime of minority charge carriers (τ_p) and the area under the spectral EL curve in the region of the band-to-band recombination (I^s_{EL}).

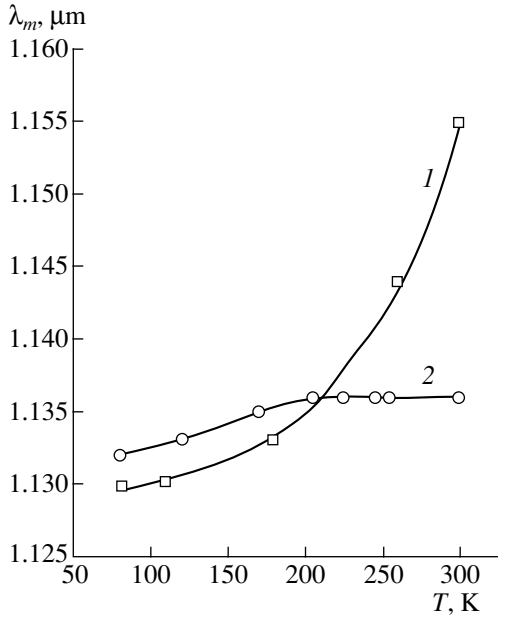

Fig. 5. Temperature dependences of the wavelength corresponding to the peak in the EL spectral distribution (λ_m) for (*1*) the light-emitting diode investigated in [2] and (*2*) the light-emitting diode investigated in this study.

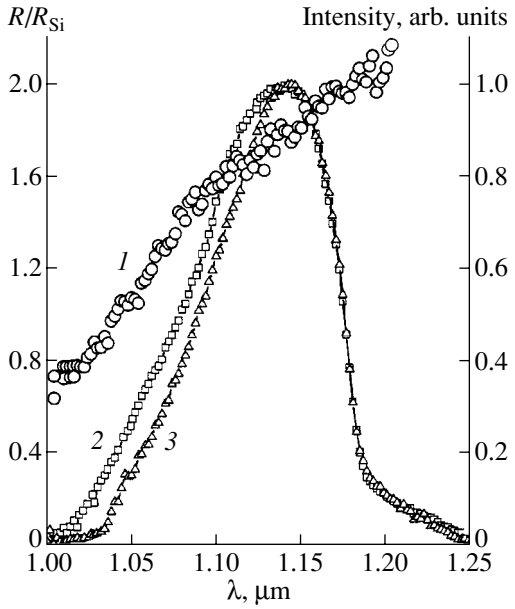

Fig. 6. (*1*) Spectral characteristic of the ratio between the coefficient of reflection of light from the surface of the studied diode with the surface oxide film (R) and the reflection coefficient for an unoxidized silicon surface (R_{Si}) under almost normal incidence of light and the EL spectra (normalized to the maximal intensity) for the investigated light-emitting diode (*2*) before and (*3*) after etching off of the oxide film; the spectra were measured at a current of 300 mA at room temperature.

face of the diode (see curves *2*, *3* in Fig. 6). The value of λ_m increased by $\delta\lambda_1 \approx 7$ nm after etching off of the oxide film. However, the effects of interference in the oxide film of the LED under investigation do not allow us to satisfactorily explain the differences between the values of λ_m at room temperature for curves *1* and *2* in Fig. 5. Another important difference in the conditions of radiation extraction from the semiconductor between this study and [2] is the fact that, in [2], the EL radiation was collected (to then be directed to a photodetector) from the semiconductor-wafer side which was opposite with respect to the formed *p*–*n* junction. It was shown previously [9] that, if radiation is detected at room temperature from the rear surface of the wafer, the peak in the band-to-band EL spectrum is shifted to longer wavelengths compared with the situation where the radiation is detected from the *p*–*n*-junction side. This shift is caused by an increase in the absorption coefficient for shorter wavelengths and amounts to $\delta\lambda_2 \approx$ 12 nm for the diode studied in [9]. The value of $\delta\lambda_1 + \delta\lambda_2$ are in satisfactory agreement with the difference between curves *1* and *2* in Fig. 5 at room temperature. As temperature decreases, the EL spectrum narrows and becomes more and more controlled by recombination via excitons [12]. Simultaneously, the effects of the reflection spectrum of the oxide film and the absorption spectrum of the silicon wafer on the position of the peak in the EL spectrum become much less profound; as follows from Fig. 5, these effects become negligible at $T \lesssim 200$ K.

The external quantum efficiency at room temperature (η_{ex}) for the silicon LED under investigation was calculated from measurements of photocurrent in the germanium photodiode, its current–radiant-power characteristic, and the solid angle within which the LED radiation was focused onto the entrance window of the Ge photodiode. We assumed that the spatial distribution of the LED radiation was isotropic. In addition, we assumed that all of the radiation focused onto the photodiode's entrance window, which had the shape of a minilens mounted on the photodiode case, was collected by the photosensitive area of the photodiode. The value of η_{ex} was equal to ~0.006% at a current of 300 mA and at room temperature. This value of η_{ex} is an order of magnitude smaller than that for the planar silicon LED described by Green *et al.* [1], which can be attributed to the much longer lifetimes of minority charge carriers in the experiments conducted in [1]. In addition, the smaller values of η_{ex} can be partially caused by a larger coefficient of internal reflection of radiation due to the presence of an oxide film (see Fig. 6). In this context, it is possible that deposition of an insulator film with other (antireflecting) properties can, under certain conditions, allow one to increase by severalfold the value of η_{ex} for the LED of the type we used while retaining the temperature stability of the diode's spectral characteristics. The ratio η_i/η_{ex} is very large (as a result of the large value of the refractive index in Si) in a silicon LED, in which the structure is not specially designed for an increase in the external quantum efficiency (see, for example, [13]). On the basis of the foregoing, the internal quantum efficiency of the silicon LED under investigation can be estimated as being no lower than 0.1%. Special texturing of the silicon surface using selective etching (see [1]) can, for example, bring the external quantum efficiency close to the aforementioned value. This texturing allowed Green *et al.* [1] to increase the value of η_{ex} in a silicon LED by an order of magnitude compared to that in a planar diode. It is worth noting that the value of η_{ex} obtained in [2] was ~0.1%; i.e., this value was larger than that for the planar LED described in [1]. This increase in η_{ex} was attained notwithstanding the fact that, apparently, no special efforts were taken in [2] (in contrast with [1]) to minimize the recombination losses at the semiconductor surface. This observation confirms the importance of studying the effect of dislocations on the band-to-band luminescence of silicon.

At a current of 300 mA, the EL intensity in the diode under investigation attained a value which amounted to 0.63 of the maximum value in ~35 μs; this intensity then decreased with the time constant of ~18 μs. The results of studying the kinetics of the rise and decay of EL in the LED under consideration will be reported and discussed in detail in our next publication.

4. CONCLUSION

We considered the fabrication technology and the effect of temperature on the spectral parameters of the band-to-band radiation of a highly efficient (an internal quantum efficiency at room temperature no lower than 0.1%) silicon light-emitting diode; an unprecedentedly high stability of both the electroluminescence intensity at the peak in the spectral distribution and the position of the peak λ_m against variations in temperature is observed in this diode. It is shown that one of the causes of the high stability is a decrease in the lifetime of minority charge carriers with decreasing temperature. The unprecedentedly high stability of λ_m against variations in temperature is related to the interference effects in the oxide film that covers the light-emitting diode surface.

ACKNOWLEDGMENTS

This study was supported in part by the INTAS (grant no. 01-0194), the Russian Foundation for Basic Research (project no. 02-02-16374), and the Russian Foundation for Basic Research together with the Office for International Cooperation in Research and Technology Cooperation, Austria (grant no. 01-02-02000 BNTS_a).

REFERENCES

1. M. A. Green, J. Zhao, A. Wang, *et al.*, Nature **412**, 805 (2001).
2. Wai Lek Ng, M. A. Lourenco, R. M. Gwilliam, *et al.*, Nature **410**, 192 (2001).
3. Th. Dittrich, V. Yu. Timoshenko, J. Rappich, and L. Tsybeskov, J. Appl. Phys. **90**, 2310 (2001).
4. W. Michaelis and M. H. Pilkuhn, Phys. Status Solidi **36**, 311 (1969).
5. T.-C. Ong, K. W. Terrill, S. Tam, and C. Hu, IEEE Electron Device Lett. **4**, 460 (1983).
6. A. M. Emel'yanov and A. N. Yakimenko, in *Proceedings of 7th International Meeting on Radiation Physics of Solids* (Sevastopol, 1997), p. 56.
7. V. Yu. Timoshenko, J. Rappich, and Th. Dittrich, Appl. Surf. Sci. **123–124**, 111 (1998).
8. R. D. Altukhov and E. G. Kuzminov, Solid State Commun. **111**, 379 (1999).
9. A. M. Emel'yanov, Yu. A. Nikolaev, and N. A. Sobolev, Fiz. Tekh. Poluprovodn. (St. Petersburg) **36**, 454 (2002) [Semiconductors **36**, 430 (2002)].
10. C. W. Liu, M. H. Lee, Miin-Jang Chen, *et al.*, Appl. Phys. Lett. **76**, 1516 (2000).
11. W. van Roosbroeck and W. Shockley, Phys. Rev. **94**, 1558 (1954).
12. R. A. Smith, *Semiconductors*, 2nd ed. (Cambridge Univ. Press, Cambridge, 1978; Mir, Moscow, 1982).
13. A. A. Bergh and P. J. Dean, *Light Emitting Diodes* (Clarendon Press, Oxford, 1976; Mir, Moscow, 1979), Chap. 3.
14. Yu. R. Nosov, *Switching in Semiconductor Diodes* (Nauka, Moscow, 1968; Plenum, New York, 1969), Chaps. 1, 2, 5.
15. B. Lax and S. F. Neustadter, J. Appl. Phys. **25**, 1148 (1954).
16. I. M. Vikulin and V. I. Stafeev, *Physics of Semiconductor Devices* (Sovetskoe Radio, Moscow, 1980), Chap. 1, p. 50.
17. N. A. Sobolev, A. M. Emel'yanov, and K. F. Shtel'makh, Appl. Phys. Lett. **71**, 1930 (1997).
18. N. A. Sobolev, A. M. Emel'yanov, and Yu. A. Nikolaev, Fiz. Tekh. Poluprovodn. (St. Petersburg) **34**, 1069 (2000) [Semiconductors **34**, 1027 (2000)].

Translated by A. Spitsyn

Semiconductors, Vol. 37, No. 6, 2003, pp. 736–739. Translated from Fizika i Tekhnika Poluprovodnikov, Vol. 37, No. 6, 2003, pp. 762–766.

PHYSICS OF SEMICONDUCTOR DEVICES

Mid-Infrared (λ = 2.775 μm) Injection Laser Based on AlGaAsSb/InAs/CdMgSe Hybrid Double Heterostructure Grown by Molecular-Beam Epitaxy

S. V. Ivanov, K. D. Moiseev, V. A. Kaĭgorodov, V. A. Solov'ev, S. V. Sorokin, B. Ya. Meltser, E. A. Grebenshchikova, I. V. Sedova, Ya. V. Terent'ev, A. N. Semenov, A. P. Astakhova, M. P. Mikhaĭlova, A. A. Toropov, Yu. P. Yakovlev, P. S. Kop'ev, and Zh. I. Alferov

Ioffe Physicotechnical Institute, Russian Academy of Sciences, St. Petersburg, 194021 Russia

e-mail: irina@beam.ioffe.ru

Submitted November 14, 2002; accepted for publication November 20, 2002

Abstract—The lasing of an injection-pumped *p*-AlGaAsSb/n^0-InAs/*n*-CdMgSe double hybrid heterostructure in the mid-IR range is demonstrated for the first time. The lasing wavelength λ is 2.775 μm, and the threshold current density J_{th} = 3–4 kA/cm^2 at T = 77 K. The structure grown by two-stage molecular-beam epitaxy is characterized by extremely high (~1.5 eV) asymmetric potential barriers for electrons and holes in the InAs active region. The output power of spontaneous emission for round-mesa diodes at T = 300 K was no less than 0.3 mW.

In recent years, intensive efforts in the fabrication of semiconductor lasers operating at room temperature in the mid-IR range (3–5 μm) have revealed several basic types of promising materials and heterostructures. The highest working temperature in the CW mode (230 K, λ = 4.2 μm) was achieved for PbSe laser diodes [1], though the relatively low thermal conductivity of this material does not promise high output emission power even at cryogenic temperatures. Recently, stimulated CW generation at $\lambda \sim 9$ μm was obtained near 300 K in AlInAs/GaInAs quantum-cascade lasers (QCL) [2]; however the maximum temperature achieved for the 3–5 μm range was only T_{max} = 175 K [3]. It seems probable that a relatively high threshold current density and operating voltage might preclude the significant extension of the temperature range of CW lasing in type-I QCL. At the same time, III–V antimonide type-II heterostructures with a *W*-like arrangement of quantum wells (QWs) exhibited lasing at λ = 3.25 μm at T = 310 K under pulsed injection pumping; this was achieved due to an optimized design that essentially suppressed the nonradiative Auger-recombination losses and intraband absorption and provided maximum possible electron confinement of holes for this system and maximum overlapping of the electron and hole wave functions, close to that in type-I QWs [4]. However, to date T_{max} in CW mode has only been 195 K. It is worth noting that, a few months ago, type-II QCLs based on antimonide heterostructures also demonstrated lasing under pulsed pumping at 300 K in the wavelength range 3.3–3.5 μm [5].

In our opinion, the reason for such a slow progress along the way to III–V laser operation at higher temperatures is the specific mutual position of energy bands of narrow-gap III–V compounds having lattice constants close to $a_{latt} \approx 6.1$ Å (AlSb, GaSb, InAs), with the valence band lying at the maximum depth for the semiconductor with the narrowest gap, which is InAs (E_g = 0.41 eV at T = 77 K). Attempts to use this semiconductor as the active region of a laser heterostructure collide with the problem of strong leakage of the injection current of holes across the *p–n* junction because of an insufficient barrier height at elevated temperatures, even if the barriers are formed by AlAsSb or InAsSbP solid solutions with the maximum possible lattice mismatch, and the active region, by strained InAsSb layers [6].

To solve this problem, we recently proposed an original AlGaAsSb/InAs/CdMgSe hybrid double heterostructure with a heterovalent (III–V)/(II–VI) interface at the boundary of the active region [7], which provides a barrier of more than 1.5-eV for holes in the InAs active region, due to a giant valence band offset. Additional advantages of this structure are ideal lattice matching between $Cd_{0.9}Mg_{0.1}Se$ and InAs and a large difference between the refractive indices (n_{InAs} = 3.4, n_{CdSe} = 2.55), which enables strong optical confinement of emitted light in InAs. Furthermore, these heterostructures can be regarded as a key element in spintronics, a new branch in microelectronics, which uses the electron spin instead of charge as an information carrier. Spin-polarized electrons are injected from a semimagnetic semiconductor, e.g., CdMnSe [8], into the nonmagnetic InAs, in which the spin orientation is detected by measuring the circular polarization of the emitted light [9]. Similar LED heterostructures with a circular polarization of about 80% at 5 K in a magnetic

field of ~1 T were recently fabricated for the first time using the ZnBeMnSe/AlGaAs system [10]. At the same time, the use of a heterovalent InAs/CdMgSe interface in the active region poses serious technological problems [11], because it imposes strict limitations on the structural and electronic perfection defined by the density of extended and point defects, i.e., electronic traps and centers of nonradiative recombination. The first structures containing only comparatively thin *p*-AlGaAs and *n*-CdMgSe barriers around a 0.6-μm-thick undoped InAs layer demonstrated rather strong photoluminescence (PL) in the visible and IR spectral regions [12], and intense electroluminescence (EL) at 300 K at a wavelength of 3.12 μm [13] with a relatively high density (~10^7 cm^{-2}) of extended defects (stacking faults and dislocations) originating at the InAs/CdMgSe heterointerface.

We report the first observation of lasing at a wavelength of ~2.78 μm (T = 77–100 K) under pulsed injection pumping in an AlGaAsSb/InAs/CdMgSe double heterostructure with thick wide-bandgap emitter layers grown by two-stage molecular-beam epitaxy (MBE).

The laser heterostructure was grown successively on (100) p^+-InAs substrate in two MBE machines. The III–V part of the structure consisted of a 50-nm-thick *p*-InAs:Be buffer layer ($p \approx 10^{18}$ cm^{-3}); a 2.3-μm-thick $Al_{0.5}Ga_{0.5}As_{0.12}Sb_{0.88}Be$ *p*-emitter ($p \approx 10^{17}$ cm^{-3}), with its composition varying smoothly in the last 0.1 μm closest to the 20-nm-thick $AlAs_{0.2}Sb_{0.8}$ layer in order to minimize the barrier for the forward current of holes into InAs; and an undoped 0.5-μm-thick n^0-InAs layer ($n \approx 3 \times 10^{16}$ cm^{-3}). The II–VI part of the structure included a 2-μm-thick CdMgSe:Cl *n*-emitter with an electron density $n = (5–8) \times 10^{17}$ cm^{-3} and 10% Mg content corresponding to ternary CdMgSe solid solution lattice-matched with InAs [12]. A 100-nm-thick heavily doped n^+-CdSe:Cl layer ($n \approx 5 \times 10^{18}$ cm^{-3}) was used as an *n*-contact layer.

On completion of the growth of the III–V part at T_S = 480°C, a thin polycrystalline As layer was deposited onto the surface of the top InAs layer at $T_S \approx 3$°C and under a standard As_4 flux. The epitaxial structure was then transferred through open atmosphere to the annealing chamber connected with the II–VI growth chamber by a high-vacuum sample transfer system. Annealing in the As_4 flow at T_S = 500°C led to the desorption of the polycrystalline As layer, and a distinct striped (2 × 4) RHEED pattern corresponding to a planar As-stabilized surface was observed. Further, the structure was transferred to the growth chamber for II–VI compounds. The growth of CdMgSe was initiated at a lowered temperature $T_S \approx 200$°C by migration-enhanced epitaxy described elsewhere [12]. The subsequent (Cd,Mg)Se part of the heterostructure was grown in the standard MBE mode at $T_S \approx 280$°C in (2 × 1) Se-stabilized conditions.

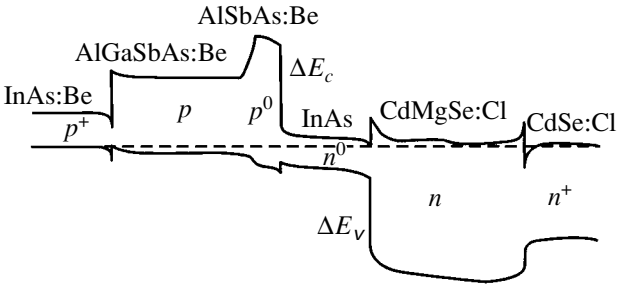

Fig. 1. The energy-band diagram of a p^+-InAs/*p*-AlGaSbAs/n^0-InAs/*n*-CdMgSe/n^+-CdSe laser heterostructure.

Mesa-stripe laser structures with a double-channel profile were produced using the standard post-growth chemical etching technique. The length of the laser cavity was L = 500 μm, and the stripe width d = 30 μm. An ohmic contact to *p*-InAs was produced by successive sputtering of a three-layer Cr/Au + Zn/Au coating. Metallic In was used as a contact of acceptable quality to *n*-CdMgSe:Cl. Laser diodes were mounted onto a copper heat sink, which served also as a contact, and the second contact was a gold wire soldered to the contact pad of the mesa-stripe.

Figure 1 shows the band diagram of a hybrid laser heterostructure. As established earlier by theoretical calculations [13] and preliminary experimental study [14], an InAs/CdSe heteropair grown under appropriate conditions is, in all probability, a type-II heterojunction in which the conduction band of InAs lies ~60 meV above that of CdSe. At the same time, $InAs/Cd_{0.8}Mg_{0.1}Se$ forms a type-I heterojunction in which the conduction band of solid solution lies ~120 meV above the InAs conduction band bottom, according to the data on the band offset in CdSe/CdMgSe system [15], and the valence band offset at the interface $\Delta E_V \approx 1.6$ eV. The conduction band offset at the InAs/AlSbAs heterointerface is $\Delta E_C \approx 1.45$ eV. Thus, this heterostructure, with sharply asymmetric band offsets at opposite interfaces of the InAs active region, contains extremely high potential barriers for electrons and holes, which offers possibilities for a drastic suppression of injection losses at elevated temperatures and high injection currents, which is necessary for the design of high-power low-threshold injection lasers operating in the IR range at room temperature [16].

Figure 2a shows a typical cross-sectional image of a laser heterostructure obtained by scanning electron microscopy (SEM) using secondary electrons. It confirms the high quality and planarity of heterojunctions, as well as the good reproducibility of the epitaxial layer thickness. The current–voltage (*I–V*) characteristics were recorded independently for each heterojunction and for the laser structure as a whole. A diode-type *I–V* characteristic was obtained for an *n*-InAs/*p*-AlGaAsSb heterostructure with a rather thick (0.7 μm) AlGaAsSb layer, while the *n*-InAs/*n*-CdMgSe heterojunction dem-

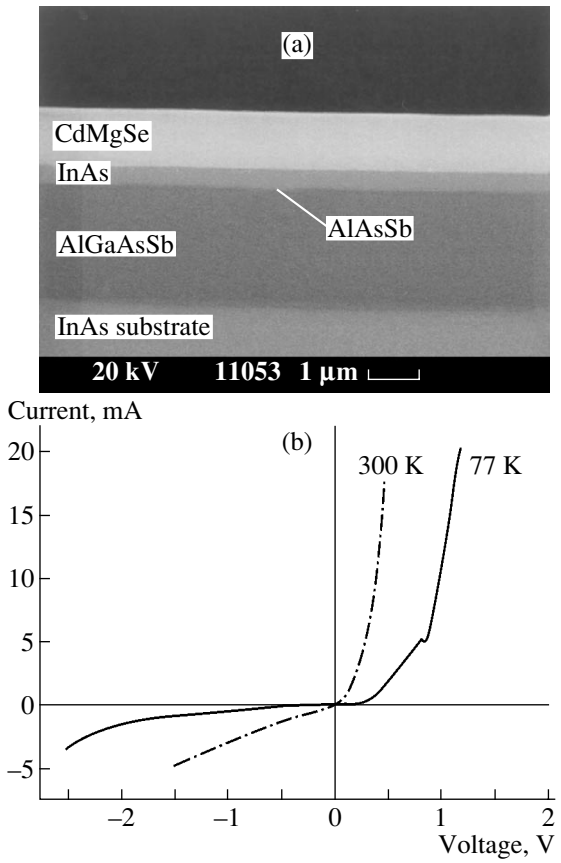

Fig. 2. (a) Cross-sectional secondary-electron SEM image of a laser heterostructure; (b) *I–V* characteristics of a hybrid laser diode at 77 and 300 K.

onstrated an ohmic *I–V* characteristic. Hence, it follows that the major part of the bias across the structure drops near the AlAsSb/InAs interface. Figure 2b shows the *I–V* characteristics of a p^+-InAs/*p*-(Al,Ga)AsSb/n^0-InAs/*n*-CdMgSe/n^+-CdSe laser diode at two different temperatures. At room temperature, the cutoff voltage of the forward *I–V* characteristic ($U_{300} \approx 0.25$ V) is apparently defined by the InAs band gap, while at 77 K it increases to $U_{77} \approx 0.8$ V, which indicates that the space charge layer is shifted to wide-bandgap AlAsSb, probably due to its insufficient doping. The kink in the forward *I–V* curve at 77 K may be assigned to the presence of some additional barrier in the wide-bandgap or contact regions of the diode.

EL under quasi-static pumping was observed in the temperature range from 77 to 300 K. The pumping current reached 200 mA, the pulse width $\tau = 1$ ms, and the pulse repetition rate $f = 500$ Hz. At room temperature, EL was observed in the spectral range of 0.3–0.5 eV (Fig. 3a). The EL spectrum demonstrates a pronounced emission band with a peak energy of 0.365 eV corresponding to E_g(InAs). A shoulder appears at 0.423 eV on the short-wavelength side at high injection levels. With the pumping current rising, a slight (2–3 meV) blue shift of the emission peak $h\nu_1$ is observed at 300 K,

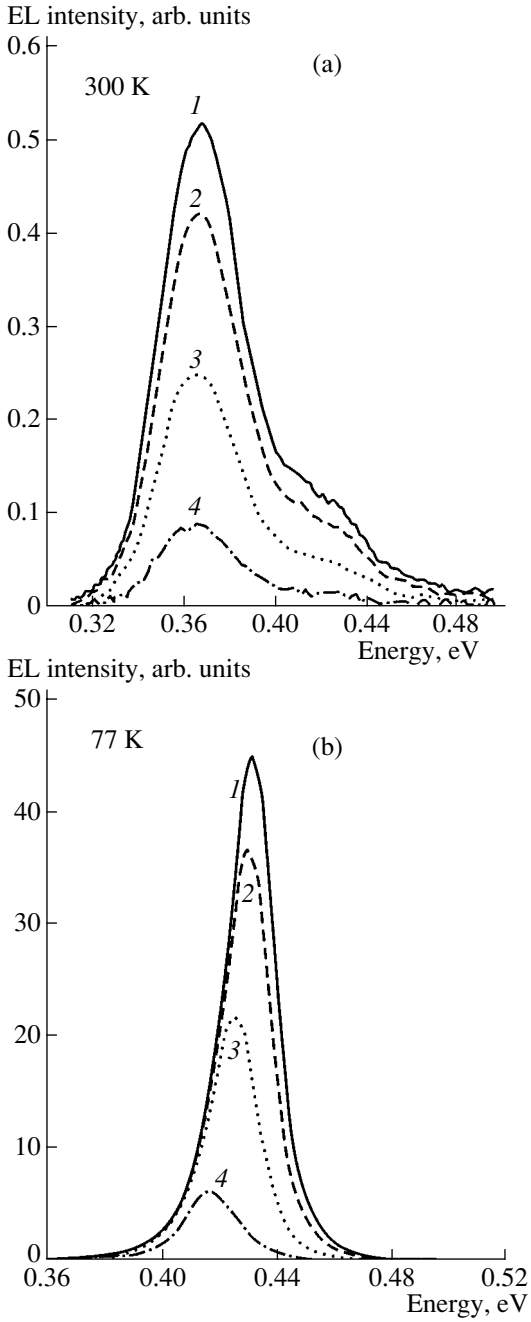

Fig. 3. EL spectra of a hybrid laser heterostructure at 77 and 300 K. Pumping current: (*1*) 180, (*2*) 150, (*3*) 100, and (*4*) 50 mA.

while at 77 K this shift is 18 meV, from 0.418 to 0.436 eV. It is necessary to also stress that at 77 K the EL spectrum contains only one clearly pronounced asymmetric band without additional peaks even at high injection levels (Fig. 3b). When the temperature was lowered from 300 to 77 K, the intensity of spontaneous EL increased by factor of ~70. It is worth noting that the output power of a round mesa-diode structure at 300 K was not less than 0.3 mW.

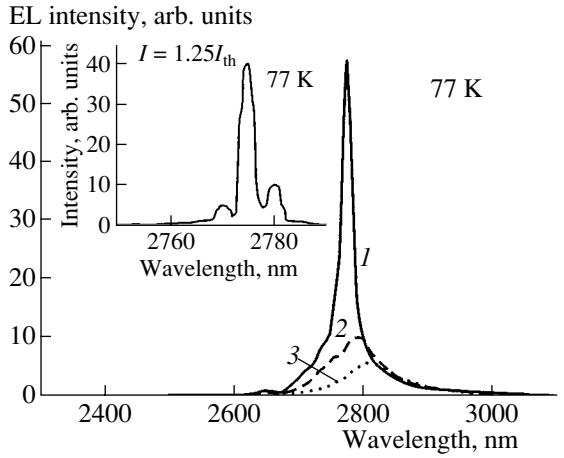

Fig. 4. EL spectra at the threshold of stimulated emission in a stripe diode (d = 30 μm, L = 500 μm) based on the hybrid AlGaAsSb/InAs/CdMgSe heterostructure recorded at 77 K under pulsed pumping (τ = 500 ns, f = 32 kHz). Insert: the lasing spectrum at I = 850 mA. Pumping current: (*1*) 820, (*2*) 610, and (*3*) 488 mA.

Stimulated emission was obtained at T = 77 K under pulsed pumping (Fig. 4). The width of current pulses varied from 125 ns to 2 μs, the repetition rate was 32 kHz. The main emission band $h\nu_1$ was blue-shifted from 0.436 to 0.442 eV with the pumping current rising, which points to the formation of a self-consistent QW in the conduction band near the InAs/AlAsSb heterointerface. At the pulse width τ_1 = 500 ns, the threshold current was I_{th} = 680 mA, which corresponds to the threshold current density j_{th} = 3–4 kA/cm^2. Lasing was observed at the wavelength λ = 2.775 μm. The average intermode distance was 5 nm, and the FWHM of the main laser peak did not exceed 3 nm (see the insert in Fig. 4). We believe that the relatively high values of the threshold current are due to the insufficient *p*-doping of the emitted wide bandgap, the relatively high density of extended defects, and the high level of nonradiative losses associated with Auger recombination and intraband absorption in the InAs bulk layer.

The lasing in the mid-IR range (λ = 2.775 μm) at 77 K under injection pumping of the (Al,Ga)SbAs/InAs/(Cd,Mg)Se double hybrid heterostructure with a (III–V)/(II–VI) heterovalent interface at the boundary of the InAs active region was demonstrated for the first time. It is expected that further optimization of MBE technology for all structure components and its development with the use of type-II QWs (e.g., (Ga,In)Sb/InAs) in the active region so as to suppress nonradiative losses will make it possible to apply this promising structure in the design of high-power IR lasers operating in the 3–5 μm range near room temperature.

ACKNOWLEDGMENTS

This study was supported by the International Science & Technology Center (grant no. 2044), INTAS (grant no. 01-2375), the Russian Foundation for Basic Research (project nos. 00-02-17047 and 02-02-17643), and the Volkswagen Foundation.

REFERENCES

1. U. P. Schliessl and J. Rohr, Infrared Phys. Technol. **40**, 325 (1999).
2. D. Hofstetter, M. Beck, T. Aellen, *et al.*, Appl. Phys. Lett. **78**, 1964 (2001); S. Slivken, Z. Huang, A. Evans, and M. Razeghi, Appl. Phys. Lett. **80**, 4091 (2002).
3. C. Gmachl, A. M. Sergent, A. Tredicucci, *et al.*, IEEE Photonics Technol. Lett. **11**, 1369 (1999).
4. W. W. Bewley, H. Lee, I. Vurgaftman, *et al.*, Appl. Phys. Lett. **76**, 256 (2000).
5. R. Q. Yang, J. L. Bradshaw, J. D. Bruno, *et al.*, Appl. Phys. Lett. **81**, 397 (2002).
6. G. G. Zegrya, M. P. Mikhaĭlova, T. N. Danilova, *et al.*, Fiz. Tekh. Poluprovodn. (St. Petersburg) **33**, 110 (1999) [Semiconductors **33**, 350 (1999)].
7. S. V. Ivanov, K. D. Moiseev, A. M. Monakhov, *et al.*, in *Proceedings of 8th International Symposium on Nanostructures: Physics and Technology* (St. Petersburg, 2000), p. 109.
8. P. Grabs, G. Richter, R. Fiederling, *et al.*, Appl. Phys. Lett. **80**, 3766 (2002).
9. A. G. Aronov and G. E. Pikus, Fiz. Tekh. Poluprovodn. (Leningrad) **10**, 1177 (1976) [Sov. Phys. Semicond. **10**, 698 (1976)].
10. R. Fiederling, M. Keim, G. Reuscher, *et al.*, Nature **402**, 787 (1999).
11. N. Samarth, H. Luo, J. K. Furdyna, *et al.*, Appl. Phys. Lett. **54**, 2680 (1989).
12. V. A. Solov'ev, I. V. Sedova, A. A. Toropov, *et al.*, Fiz. Tekh. Poluprovodn. (St. Petersburg) **35**, 431 (2001) [Semiconductors **35**, 419 (2001)].
13. S. V. Ivanov, V. A. Solov'ev, K. D. Moiseev, *et al.*, Appl. Phys. Lett. **78**, 1655 (2001).
14. S. Ivanov, S. Sorokin, K. Moiseev, *et al.*, Mater. Res. Soc. Symp. Proc. **692**, H8.8.1-6 (2002).
15. V. A. Kaygorodov, I. V. Sedova, S. V. Sorokin, *et al.*, Phys. Status Solidi B **229**, 19 (2002).
16. Yu. P. Yakovlev, S. V. Ivanov, K. D. Moiseev, *et al.*, Proc. SPIE **4651**, 203 (2002).

Translated by D. Mashovets